
**THE DESIGN AND ANALYSIS OF SUGAR-BASED
CARRIER SYSTEMS FOR THE PROTECTION OF
NUCLEIC ACIDS**

BAHIJJA TOLULOPE RAIMI – ABRAHAM

**A THESIS PRESENTED FOR THE DEGREE OF DOCTOR OF PHILOSOPHY AT
THE SCHOOL OF PHARMACY, UNIVERSITY OF EAST ANGLIA, NORWICH
RESEARCH PARK, NORWICH, UK**

MAY 2012



© This copy of the thesis has been supplied on condition that anyone who consults it is understood to recognise that its copyright rests with the author and that no quotation from this thesis, nor any information derived therefrom, may be published without the author's prior, written consent.

ABSTRACT

The overall aim of the work detailed in this thesis was to design and analyse sugar-based (trehalose, raffinose and sucrose) carrier systems for the protection of naked plasmid DNA formulations generated by spray drying.

Trehalose exists in multiple crystalline anhydrous and hydrated forms and is thought to exist in two different amorphous forms. Reported thermal transitions of trehalose dihydrate vary with environmental conditions and particle size. The first area of this thesis focused on investigating the inter-conversion properties of trehalose dihydrate to observe if an in-depth understanding of its physical properties will provide an insight into its bio-protective properties. Within this area, two standardised forms of α,α -trehalose dihydrate were generated and characterised by performing a series of thermal, spectroscopic and X-ray diffraction techniques. This resulted in the identification of an intermediary anhydrous form.

Within the second area of this thesis the use of the fragility parameter m and the strength parameter D as predictors of amorphous stability of generated co-spray dried sucrose-raffinose and sucrose-trehalose samples was investigated. Results showed addition of both raffinose and trehalose improved predicted amorphous stability, with the greatest effect seen at highest additive concentrations.

The third area of the thesis was to evaluate the degree of degradation of plasmid DNA spray dried in the presence of amorphous sugars. Spray-drying can be used to develop biopharmaceutical particles for the pulmonary delivery. However, it runs the risk of loss of

Abstract

biological activity, sample instability as well as thermal degradation of the biopharmaceutical. Results showed that plasmid DNA degradation was reduced when co-spray dried in the presence of raffinose and to a greater extent with trehalose. Co-spray drying of plasmid DNA in the presence of sucrose, sucrose-raffinose and sucrose-trehalose formulations offered less protection than trehalose and raffinose.

Overall, two key messages are concluded from the work detailed in this thesis. Firstly, the thermal transitions of trehalose dihydrate can be influenced by environmental factors as well as inter-batch variability. This can affect authenticity of polymorphous and amorphous forms identified. Secondly, addition of raffinose and trehalose to amorphous sucrose formulations improved the predicted amorphous stability of the formulations however; these co-spray dried samples offered less protection compared to plasmid DNA co-spray dried in the presence of trehalose and raffinose alone.

ACKNOWLEDGEMENTS

I would like to thank my supervisors Professor Duncan Craig, Dr Susan Barker and Dr Anja Mueller for their guidance and support throughout the course of my PhD. I would also like to express my gratitude to Professor Pete Belton, Dr Jonathan Moffat, Mr Bertrand Leze and Dr Chris Morris for their invaluable time and expertise.

My thanks go to members of the drug delivery group at UEA. A special mention must go to the following people; Dr Sarah Otun (aka my Mento) and Mr Dereck Gondongwe (and our mutual acquaintances “Sauv”, Pinot and Chianti!) who have been a constant source of laughter, support and friendship over the years.

I would like to thank Miss Janet Mabayoje and Mr Jerome Jefferson for all their kind words of encouragement and understanding over the past few years. I would also like to thank Mr Lee Wyatt who has provided me with food (aka ‘The Lee Burger’) during my thesis writing process.

I would like to thank my family for all their love, understanding and support. Finally, I would like to say a special thank you to my darling mother who without her patience, understanding, support and guidance I would not have been able to complete my PhD!

Acknowledgements

For my mummy

TABLE OF CONTENTS

TITLE	1
ABSTRACT	2
ACKNOWLEDGEMENTS	4
TABLE OF CONTENTS	6
LIST OF FIGURES	15
LIST OF TABLES	29
LIST OF SYMBOLS	32
LIST OF ABBREVIATIONS	34
CHAPTER ONE	36
1.1 GENERAL INTRODUCTION	37
1.2 USE OF NUCLEIC ACIDS AS THERAPEUTIC AGENTS (DNA-BASED THERAPEUTICS)	37
1.2.1 OLIGONUCLEOTIDES FOR ANTISENSE AND ANTIGENE APPLICATIONS	40
1.2.2 PLASMID DNA	40
1.2.3 SHORT INTERFERING RNA (siRNA)	43
1.3 DELIVERY OF NUCLEIC ACIDS	45
1.3.1 VIRAL VECTORS.....	46
1.3.2 NON-VIRAL VECTORS	48
<i>1.3.2.1 Liposomal non-viral delivery systems</i>	48

Table of contents

1.3.2.2	<i>Polymeric non-viral delivery systems</i>	49
1.4	PULMONARY DELIVERY	50
1.4.1	FUNCTIONAL ANATOMY AND PHYSIOLOGY OF THE RESPIRATORY SYSTEM ...	50
1.4.1.1	<i>Functional Anatomy of the Respiratory System</i>	50
1.4.1.2	<i>Physiology of the Respiratory System</i>	52
1.4.2	BARRIERS TO PULMONARY DELIVERY.....	53
1.4.3	IDEAL PARTICLE CHARACTERISTICS FOR PULMONARY DELIVERY	55
1.4.4	PULMONARY DELIVERY OF NUCLEIC ACIDS	56
1.4.5	OTHER ROUTES OF DELIVERY OF NUCLEIC ACIDS.....	59
1.4.5.1	<i>Ocular Delivery</i>	59
1.4.5.2	<i>Topical Delivery</i>	59
1.5	ANHYDROBIOSIS	60
1.6	MAILLARD REACTIONS	61
1.7	DELIQUESCENT	62
1.8	SOLID STATE	63
1.9	THE AMORPHOUS STATE	64
1.9.1	GLASS TRANSITION THEORIES	69
1.9.1.1	<i>Free volume theories</i>	69
1.9.1.2	<i>Thermodynamic phase transition theory</i>	70
1.9.1.3	<i>Entropy theories</i>	71
1.9.2	GLASS FRAGILITY	72

Table of contents

1.9.3	THE FICTIVE TEMPERATURE	77
1.9.4	PLASTICIZATION.....	77
1.9.5	CRYSTALLIZATION/NUCLEATION.....	79
1.9.6	POLYAMOPHORMISM.....	80
1.9.7	PHARMACEUTICAL RELEVANCE OF THE AMORPHOUS STATE	80
1.9.7.1	<i>Vapour condensation</i>	82
1.9.7.2	<i>Quench cooling</i>	82
1.9.7.3	<i>Milling</i>	82
1.9.7.4	<i>Precipitation from solution</i>	83
1.9.7.5	<i>Dehydration of crystalline hydrates</i>	84
1.10	THE CRYSTALLINE STATE	85
1.10.1	POLYMORPHISM	86
1.10.2	CRYSTAL HYDRATES	87
1.10.2.1	<i>The Gibbs' Phase rule</i>	88
1.10.3	STRUCTURE ASPECTS	89
1.11	RESEARCH OBJECTIVES.....	90
CHAPTER TWO	92
2.1	MATERIALS	93
2.1.1	SUGARS	93
2.1.1.1	<i>Trehalose</i>	95
2.1.1.2	<i>Raffinose</i>	103

Table of contents

2.1.1.3	<i>Sucrose</i>	106
2.1.2	PLASMID DNA.....	107
2.1.2.1	<i>Plasmid DNA Purification using Qiagen Plasmid Giga Kit</i>	108
2.1.2.2	<i>DNA quantification using ultraviolet spectroscopy</i>	113
2.1.3	HYDROXYPROPYLMETHYLCELLULOSE	114
2.2	METHODS	116
2.2.1	SPRAY DRYING	116
2.2.2	BIOLOGICAL EXPERIMENTS	119
2.2.2.1	<i>Gel Electrophoresis</i>	119
2.2.2.2	<i>Cell Culture of HeLa and A549 Cells</i>	121
2.2.2.3	<i>Transfection of Plasmid DNA</i>	122
2.2.2.4	<i>MTT (3-(4,5-Dimethylthiazol-2-yl)-2,5-diphenyltetrazolium bromide) assay</i>	123
2.2.3	SCANNING ELECTRON MICROSCOPY.....	125
2.2.4	PARTICLE SIZE ANALYSIS	125
2.2.4.1	<i>Laser particle sizing</i>	125
2.2.4.2	<i>Particle size analysis using the dry sieving method (mechanical agitation)</i>	127
2.2.5	X-RAY POWDER DIFFRACTION	128
2.2.6	HOT STAGE MICROSCOPY	129
2.2.7	VARIABLE TEMPERATURE FOURIER TRANSFORM INFRARED SPECTROSCOPY	129
2.2.7.1	<i>The Michelson Interferometer</i>	130

Table of contents

2.2.7.2	<i>Exploratory Data Analysis</i>	132
2.2.7.2.1	Hierarchical Cluster Analysis	132
2.2.7.2.2	Principal Component Analysis	134
2.2.8	DYNAMIC VAPOUR SORPTION.....	135
2.2.9	THERMOGRAVIMETRIC ANALYSIS	138
2.2.10	CONVENTIONAL DIFFERENTIAL SCANNING CALORIMETRY	139
2.2.10.1	<i>Heat Flux DSC</i>	140
2.2.10.2	<i>Power Compensation DSC</i>	141
2.2.11	MODULATED TEMPERATURE DIFFERENTIAL SCANNING CALORIMETRY	143
2.2.12	QUASI-ISOTHERMAL MODULATED TEMPERATURE DIFFERENTIAL SCANNING CALORIMETRY.....	147
2.2.12.1	<i>Lissajous Figures</i>	150
2.2.13	HYPERDSC®	151
CHAPTER THREE.....		153
3.1	BACKGROUND.....	154
3.2	PRELIMINARY WORK.....	158
3.2.1	STUDY OBJECTIVES	158
3.2.2	GENERAL METHODOLOGY	158
3.2.3	RESULTS AND DISCUSSION.....	159
3.2.3.1	<i>Particle size and morphology analysis</i>	159
3.2.3.2	<i>XRPD analysis</i>	161

Table of contents

3.2.3.3	<i>Spectroscopic analysis</i>	164
3.2.3.4	<i>Thermal analysis</i>	165
3.2.3.4.1	Using the dry sieving method to separate Sigma B particles	173
3.2.4	CONCLUSION.....	176
3.3	GENERATION AND CHARACTERISATION OF STANDARDISED SAMPLES OF α,α-TREHALOSE DIHYDRATE	178
3.3.1	STUDY OBJECTIVE.....	178
3.3.2	SAMPLE PREPARATION	179
3.3.2.1	<i>Method I, α,α-trehalose dihydrate crystals generated by slow evaporation of a 46.6%w/w saturated solution</i>	179
3.3.2.2	<i>Method II, α,α-trehalose dihydrate crystals generated by exposure of amorphous trehalose to 75%RH at room temperature</i>	179
3.3.3	METHODOLOGY.....	180
3.3.4	RESULTS AND DISCUSSION.....	181
3.3.4.1.	<i>Particle morphology and size analysis of standardised trehalose dihydrate batches</i>	181
3.3.4.2	<i>X-Ray Diffraction Analysis</i>	183
3.3.4.3	<i>Spectroscopic analysis</i>	185
3.3.4.4	<i>Thermal analysis</i>	186
3.3.4.4.1	Effect of pan type on thermal response: pin holed pans	186
3.3.4.4.2	Effect of pan type on thermal response: closed pan	189

Table of contents

3.3.4.4.3	Effect of heating rate on thermal response of standardized forms of α,α -trehalose dihydrate	194
3.3.4.4.4	Visualisation of thermal events using hot stage microscopy	216
3.3.4.5	<i>Variable temperature ATR-FTIR at 2°C/min</i>	219
3.3.4.6	<i>Generation and basic characterisation of T_{hx} form</i>	226
3.4	SECTION SUMMARY	234
3.5	CONCLUSION	238
CHAPTER FOUR	240
4.1	BACKGROUND.....	241
4.2	STUDY OBJECTIVE.....	241
4.3	GENERAL METHODOLOGY	241
4.4	RESULTS AND DISCUSSION.....	242
4.3.1	PARTICLE SIZE AND MORPHOLOGY ANALYSIS OF CRYSTALLINE AND AMORPHOUS SAMPLES.....	242
4.3.2.	X-RAY DIFFRACTION ANALYSIS OF CRYSTALLINE AND AMORPHOUS SAMPLES 250	
4.3.3.	SPECTROSCOPIC ANALYSIS OF CRYSTALLINE AND AMORPHOUS SAMPLES ...	252
4.3.3.1	<i>Crystalline Samples</i>	252
4.3.3.2	<i>Amorphous Samples</i>	253
4.3.4	THERMAL ANALYSIS OF AMORPHOUS AND CRYSTALLINE SAMPLES	255
4.3.4.1	<i>Raffinose pentahydrate and amorphous raffinose</i>	255
4.3.4.2	<i>Amorphous trehalose</i>	259

Table of contents

4.3.4.3	<i>Crystalline sucrose and amorphous sucrose</i>	261
4.3.5	DYNAMIC VAPOUR SORPTION ANALYSIS OF AMORPHOUS SAMPLES	265
4.3.5.1	<i>Amorphous Trehalose</i>	266
4.3.5.2	<i>Amorphous Raffinose</i>	267
4.3.5.3	<i>Amorphous Sucrose</i>	269
4.5	CONCLUSION	271
CHAPTER FIVE		274
5.1	BACKGROUND	275
5.1.1	STUDY OBJECTIVES	278
5.1.2	GENERAL METHODOLOGY	278
5.2	RESULTS AND DISCUSSION	279
5.2.1	X-RAY DIFFRACTION ANALYSIS OF AMORPHOUS SAMPLES	279
5.2.2	SPECTROSCOPIC ANALYSIS OF CRYSTALLINE AND AMORPHOUS SAMPLES	281
5.2.3	SAMPLE WATER CONTENT	283
5.2.4	CALCULATION OF AMORPHOUS STABILITY PARAMETERS	287
5.2.4.1	<i>Determination of activation enthalpy (ΔE_{T_g}) for structural relaxation around T_g (ΔE_{T_g}), calculated from the heat rate dependency of T_g</i>	287
5.2.4.2	<i>Calculation of fragility and strength parameters</i>	307
5.2.4.4	<i>Characterisation using quasi-isothermal modulated temperature dsc</i>	309
5.3	CONCLUSION	317
CHAPTER SIX		319

Table of contents

6.1	BACKGROUND.....	320
6.2	STUDY OBJECTIVE.....	321
6.3	METHODOLOGY.....	322
6.4	RESULTS AND DISCUSSION.....	323
6.4.1	MTT ASSAY AND TRANSFECTION STUDIES	323
6.4.2	CO-SPRAY DRYING pDNA WITH TREHALOSE AND RAFFINOSE AT 125°C	327
6.4.3	CO-SPRAY DRYING SR2.5, SR11.11, ST2.5 AND ST11.11 WITH pDNA AT 125°C	330
6.5	CONCLUSION	332
CHAPTER SEVEN		334
7.1	THESIS CONCLUSIONS	335
7.2	RECOMMENDATIONS FOR FUTURE WORK	341
REFERENCES		344
APPENDIX.....		366
APPENDIX 2.1 PREPARATION OF [x1] TBE BUFFER		366
APPENDIX 2.2 COUNTING CELLS USING A HAEMOCYTOMETER (PROTOCOL TAKEN FROM ABCAM[®])		366
APPENDIX 2.3 RESULTS FROM MTT ASSAY.....		367
APPENDIX 2.4 PREPARING A 6-WELL PLATE.....		369
APPENDIX 2.5 TRANSFECTION OF A549 CELLS		370
APPENDIX 2.6 TRANSFECTION OF HE LA CELLS.....		371

LIST OF FIGURES

CHAPTER ONE

FIGURE 1.1	Illustration showing deoxyribonucleic acid which consists of two anti-parallel polynucleotides consisting of a sugar phosphate backbone and purine and pyrimidine base pairing (Take from http://ghr.nlm.nih.gov/handbook/basics/dna)	40
FIGURE 1.2	Schematic showing differences with super-coiled and open-circular DNA (taken from Redway,2012)	43
FIGURE 1.3.	Schematic illustration of the RNAi pathway (taken from Gewirtz (2007))	45
FIGURE 1.4	Illustration showing a liposome and a multilamellar vesicle (taken from http://www.britannica.com/EBchecked/media/92244/Phospholipids-can-be-used-to-form-artificial-structures-called-liposomes and http://www.encapsula.com/products_01.html)	49
FIGURE 1.5	Regions of the human respiratory system (taken from Seville et al.,(2007))	52
FIGURE 1.6	Schematic showing the inhalation and exhalation process (Taken from http://blm1128.blogspot.co.uk/2011/04/objective-49-contrast-inspiration-and.html)	54
FIGURE 1.7	Schematic representation of the structure of a crystalline solid, an amorphous solid and a gas (taken from Yu, (2001))	65
FIGURE 1.8	Schematic depiction of the variation of enthalpy (or volume) with temperature (taken from Hancock and Zografi (1996))	68
FIGURE 1.9	Schematic illustration of the enthalpy or the free volume as a function of temperature showing the effect of cooling on the T_g where Glass 1 has been cooled at a faster rate than Glass 2 (taken from Ediger et al., 1996)	68
FIGURE 1.10	Schematic of the change in thermal expansivity (α) or the heat capacity (C_p) upon cooling from the equilibrium liquid state to the glassy state (taken from Badrinarayanan et al.,(2007))	69
FIGURE 1.11	Schematic of the evolution of specific volume (v) or enthalpy (H) with temperature upon cooling from the equilibrium liquid state to the glassy state	69
FIGURE 1.12	A plot of viscosity versus temperature scaled to T_g for Boron Trioxide (+); sorbitol (x), o-terphenyl (✱) and IMC (◆) (taken from Crowley and Zografi 2001)	74

FIGURE 1.13	Schematic of the parameters controlling crystallization from the amorphous state (taken from Hancock and Zografi (1996) who adapted from Jolley (1970))	81
--------------------	---	-----------

CHAPTER TWO

FIGURE 2.1	α,α -Trehalose dihydrate	97
FIGURE 2.2	i) DSC trace of α,α -trehalose dihydrate under different conditions: a) hermetically sealed; b) covered pan; c), open pan; d) open pan and vacuum (1 mmHg) (Taken from Shafizad and Susott (1973)) ii) DSC and TGA response for α,α -trehalose dihydrate in pin-holed pans (10°C/min) (taken from McGarvey et al., (2003))	102
FIGURE 2.3	A schematic of trehalose crystalline anhydrous, hydrous and amorphous forms, showing the inter-conversion between each form	105
FIGURE 2.4	Raffinose Pentahydrate	106
FIGURE 2.5	Crystal structure of raffinose pentahydrate showing location of water molecules (taken from Bates et al.,(2007))	107
FIGURE 2.6	Schematic illustrating a proposed process of dehydration of raffinose pentahydrate and the generation of an anhydrate form (taken from Cheng and Lin (2006))	108
FIGURE 2.7	Schematic illustrating a proposed process of dehydration resulting in the generation of amorphous raffinose (taken from Chamrathy et al., (2010))	108
FIGURE 2.8	Crystalline Sucrose	110
FIGURE 2.9	Plasmid DNA Restriction Map and Multiple Cloning Site (MCS) of pEGFP Arrestin-2 (plasmid DNA encoding enhanced green fluorescent protein gene and the intracellular protein β -Arrestin)	110
FIGURE 2.10	a) Insufficient mixing after addition of Buffer P2 (lysis buffer). b) Correct mixing after addition of Buffer P2 (lysis buffer) (Taken from Qiagen®, 2005)	113
FIGURE 2.11	Addition of neutralization buffer (Buffer P3) causes LyseBlue to turn colourless. A homogeneous solution with no traces of blue indicates that the SDS has been effectively precipitated a) Insufficient mixing after addition of neutralization buffer. b) Correct mixing after addition of neutralization buffer. (Taken from Qiagen®, 2005)	114
FIGURE 2.12	Schematic summarizing plasmid DNA extraction and purification using a Qiagen Plasmid Giga Kit	115
FIGURE 2.13	(Hydroxypropyl)methylcellulose	116
FIGURE 2.14	The Büchi Mini Spray Dryer B-290, a typical laboratory-size model	119

List of figures

	(taken from Büchi, 2003)	
FIGURE 2.15	Schematic showing co-current flow (taken from Büchi, 2003)	120
FIGURE 2.16	Diffraction patterns of a) small particle and b) large particle c) example of a calculated diffraction pattern for a non-spherical particle (taken from Sympatec (2012))	122
FIGURE 2.17	The Michelson Interferometer consisting of fixed mirror, movable mirror and a semi-transparent mirror (adapted from Bruker Optics, 2008)	124
FIGURE 2.18	A multiple reflection ATR system (taken from the PerkinElmer Technical information (2005))	126
FIGURE 2.19	A dendrogram with 75 samples with four clusters at a similarity value of 0.5 (taken from Infometrix, 2008)	128
FIGURE 2.20	Example of a two dimensional PCA scores plot (taken from Infometrix, 2008)	133
FIGURE 2.21	The internal organisation of a typical DVS instrument MFC = Mass Flow Controllers (taken from Q5000SA product literature from TA instruments 2010)	134
FIGURE 2.22	The internal organisation of a typical TGA instrument (taken from Q5000IR product literature from TA instruments 2007)	135
FIGURE 2.23	DSC Thermograph of PET showing a) a glass transition, b) a cold crystallisation exotherm and c) a melting endotherm taken from Coleman and Craig (1996)	136
FIGURE 2.24	Heat Flux DSC Schematic showing sample (S) and reference (R) pan location within the same furnace (taken from http://www.anasys.co.uk/library/dsc1.htm)	138
FIGURE 2.25	Power compensation schematic DSC Schematic showing sample and reference (R) pan location in separate furnace (taken from http://www.fchpt.stuba.sk/generate_page.php?page_id=2890)	140
FIGURE 2.26	Temperature as a function of time for a typical DSC and MTDSC experiment (taken from Verdonck et. al.,(1999))	142
FIGURE 2.27	Deconvoluted signals (total heat flow, reversing heat flow and the non-reversing heat flow which is calculated by subtracting the reversing heat flow signal from the total heat flow signal) for MTDSC experiments of a quenched PET sample (taken from Thomas (2005))	143
FIGURE 2.28	A schematic for Qi-MTDSC using a TA instruments 2920 DSC (taken from Judovits and Gupta (2011))	144
FIGURE 2.29	Heat capacity changes at a glass transition followed by crystallisation using Qi-MTDSC (taken from Verdonck et al 1999)	146

List of figures

FIGURE 2.30	Example of Lissajous figures produced by plotting the Modulated Heat Flow (W/g) and Derivative Modulated Temperature (°C/min) of various ratios and phase differences (adapted from Kett, (2000))	147
FIGURE 2.31	Schematic summarising the gel electrophoresis procedure (taken from http://www.molecularstation.com/agarose-gel-electrophoresis/)	150
FIGURE 2.32	Schematic showing electroporation of a cell (taken from http://www.utwente.nl/ewi/bios/research/Cells-on-chips/cell%20electroporation.doc/)	151
FIGURE 2.33	Schematic illustration of a 96-well plate used in an MTT assay where C = cells with media only, MA = media (RPMI – 1640) alone, C = control solutions, T = trehalose solutions, R = raffinose solutions and H = HPMC solutions, ■ = phosphate buffered saline solution	153

CHAPTER THREE

FIGURE 3.1.	a) DSC traces of different particle size fractions of trehalose dihydrate heated at 10 °C min ⁻¹ . b) Dynamic TGA traces of different particle size fractions of trehalose dihydrate heated at 10 °C min ⁻¹ . From left to right: <45, 45-75, 75-150, 150-250, 250-425, >425µm. The dashed line shows the material as supplied. (Taken from Taylor and York (1998a))	159
FIGURE 3.2	Route of crystallisation for large (>425 µm) particles and small (<45µm) particles (Adapted from Horvat (2003) and Taylor and York, (1998a))	159
FIGURE 3.3	Plot showing particle size distributions for all batches (1.5 – 801.5µm)	162
FIGURE 3.4.	SEM images of un-fractionated a) Sigma A b) Sigma B c) Acros particles. Scale bar corresponds to a) 100µm b) 200µm and c) 200µm	163
FIGURE 3.5	XRPD diffractogram of Trehalose dihydrate obtained from the Cambridge Structural Database (CSD) (Brown et al., 1972)	164
FIGURE 3.6	XRPD diffractogram of Sigma A	165
FIGURE 3.7	XRPD diffractogram of Sigma B	165

List of figures

FIGURE 3.8	XRPD diffractogram of Acros Batch	166
FIGURE 3.9	ATR-FTIR spectra of Sigma A (pink), Sigma B (red), Acros (blue)	167
FIGURE 3.10	Typical TGA and DSC heat flow signal for un-fractionated Sigma A at 2°C/min using a pin-holed pan	168
FIGURE 3.11.	Typical TGA and DSC heat flow signal for un-fractionated Sigma B at 2°C/min using a pin-holed pan	169
FIGURE 3.12	Typical TGA and DSC heat flow signal for un-fractionated Acros at 2°C/min using a pin-holed pan	169
FIGURE 3.13	Hot stage microscopy images captured at specific temperatures for Sigma A sample heated at 2°C/min	171
FIGURE 3.14	Hot stage microscopy images captured at specific temperatures for Sigma B sample heated at 2°C/min	172
FIGURE 3.15	Hot stage microscopy images captured at specific temperatures for Acros sample heated at 2°C/min	173
FIGURE 3.16	Typical DSC heat flow signal for fractionated Sigma B <63µm, 63 to 125µm, 125 to 180 µm, 180 to 250µm and 250 to 355µm at 2°C/min using a pin-holed pan	177
FIGURE 3.17	SEM image of a) T _{h1} c) Th2 Cross section showing grain boundaries b)T _{h1} d)T _{h2} Cross section showing grain boundaries. Scale bar corresponds to 500µm (a, c and d) and 100 µm (b)	183
FIGURE 3.18	Plot showing particle size distribution from T _{h1}	185
FIGURE 3.19	Plot showing particle size distribution from T _{h2}	185
FIGURE 3.20	XRPD diffractogram of T _{h1} standardised form generated by slow evaporation (method I)	186
FIGURE 3.21	XRPD diffractogram of T _{h2} standardised form generated by exposure of amorphous trehalose to 75%RH at room temperature (Method II)	186
FIGURE 3.22	ATR-FTIR spectra of T _{h1} (blue) and T _{h2} (red)	187
FIGURE 3.23	Typical MTDSC total, non-reversing and reversing heat flow signals for T _{h1} at 2°C/min ±0.212°C modulation over a 60 second period using a pin-holed pan	189
FIGURE 3.24	Typical TGA weight loss profile of T _{h1} heated at 2°C/min to 250°C	189

List of figures

FIGURE 3.25	Typical MTDSC total, non-reversing and reversing heat flow signals for T_{h2} at $2^{\circ}\text{C}/\text{min} \pm 0.212^{\circ}\text{C}$ modulation over a 60 second period using a pin-holed pan	190
FIGURE 3.26	Typical TGA weight loss profile of T_{h2} heated at $2^{\circ}\text{C}/\text{min}$ to 250°C using pin-holed pan	191
FIGURE 3.27	Typical MTDSC total, non-reversing and reversing heat flow signals for T_{h1} at $2^{\circ}\text{C}/\text{min} \pm 0.212^{\circ}\text{C}$ modulation over a 60 second period using a closed pan system	192
FIGURE 3.28	Typical TGA weight loss profile of T_{h1} heated at $2^{\circ}\text{C}/\text{min}$ to 250°C using a closed pan system	193
FIGURE 3.29	a) Typical MTDSC total, non-reversing and reversing heat flow signals for T_{h2} at $2^{\circ}\text{C}/\text{min} \pm 0.212^{\circ}\text{C}$ modulation over a 60 second period using a closed pan system b) a close up of possible crystallisation seen after low temperature endotherm.	194
FIGURE 3.30	Typical TGA weight loss profile of T_{h2} heated at $2^{\circ}\text{C}/\text{min}$ to 250°C using a closed pan system	195
FIGURE 3.31	Typical DSC heat flow signal for T_{h1} at 2, 20, 50 and $100^{\circ}\text{C}/\text{min}$ using a pin-holed pan	198
FIGURE 3.32	Typical DSC heat flow signal for T_{h2} at 2, 20, 50 and $100^{\circ}\text{C}/\text{min}$ using a pin-holed pan	198
FIGURE 3.33	Typical HyperDSC [®] heat flow signal for T_{h1} at 500 and $750^{\circ}\text{C}/\text{min}$ using a pin-holed pan	200
FIGURE 3.34	Typical HyperDSC [®] heat flow signal for T_{h2} at 500 and $750^{\circ}\text{C}/\text{min}$ using a pin-holed pan	202
FIGURE 3.35	Typical MTDSC total heat flow signal (1 st heat) for T_{h1} at 0.5, 1 and $2^{\circ}\text{C}/\text{min} \pm 0.212^{\circ}\text{C}$ modulation over a 60 second period using a pin-holed pan	202
FIGURE 3.36	Typical MTDSC (cooling) reversing heat flow signal for T_{h1} at a) $0.5^{\circ}\text{C}/\text{min}$ b) $1^{\circ}\text{C}/\text{min}$ c) $2^{\circ}\text{C}/\text{min} \pm 0.212^{\circ}\text{C}$ modulation over a 60 second period using a pin-holed pan	203
FIGURE 3.37	Typical MTDSC (2 nd heat) reversing heat flow signal for T_{h1} at a) $0.5^{\circ}\text{C}/\text{min}$ b) $1^{\circ}\text{C}/\text{min}$ c) $2^{\circ}\text{C}/\text{min} \pm 0.212^{\circ}\text{C}$ modulation over a 60 second period using a pin-holed pan	204
FIGURE 3.38	Typical MTDSC (2 nd heat) Total heat flow signal for T_{h1} at a) $0.5^{\circ}\text{C}/\text{min}$ b) (in total, reversing and non-reversing heat flow) $1^{\circ}\text{C}/\text{min}$ c) $2^{\circ}\text{C}/\text{min} \pm 0.212^{\circ}\text{C}$ modulation over a 60 second	205

	period using a pin-holed pan	
FIGURE 3.39	Typical MTDSC (1 st heat) total heat flow signal for T _{h2} at 0.5, 1 and 2°C/min ±0.212°C modulation over a 60 second period using a pin-holed pan	207
FIGURE 3.40	Typical MTDSC (2 nd heat) total heat flow and cooling (insert) in reversing heat flow signal for T _{h2} at 0.5, 1 and 2°C/min±0.212°C modulation over a 60 second period using a pin-holed pan	207
FIGURE 3.41	Typical MTDSC (2 nd heat) Total heat flow signal for T _{h2} at 0.5, 1, 2 °C/min ±0.212°C modulation over a 60 second period using a pin-holed pan	208
FIGURE 3.42	Typical Qi-MTDSC reversing heat capacity (as a function of time) signal of T _{h1} at a temperature modulation of ±1°C, 20 minute isothermal periods with 2°C increments using a pin-holed pan	212
FIGURE 3.43	Typical Qi-MTDSC reversing heat capacity (as a function of time) signal of T _{h2} at a temperature modulation of ±1°C, 20 minute isothermal periods with 2°C increments using a pin-holed pan	213
FIGURE 3.44	Typical Lissajous figure in Qi-MTDSC as modulated heat flow (as a function of time derivative of modulated temperature) signal for T _{h1} at 80°C (black) and 96°C (red) using pin-holed pans	215
FIGURE 3.45	Typical Lissajous figure in Qi-MTDSC as modulated heat flow (as a function of time derivative of modulated temperature) signal for T _{h2} at 80°C (black) and 86°C (red) using a pin-holed pan	216
FIGURE 3.46	a) Typical Qi-MTDSC Reversing heat capacity (as a function of time) signal for un-fractionated T _{h2} at 90°C b) Typical Lissajous figure in Qi-MTDSC as modulated heat flow (as a function of time derivative of modulated temperature)signal for un-fractionated T _{h2} at 90°C showing different changes in heat capacity when held isothermal for 20 minutes	217
FIGURE 3.47	Hot stage microscopy images captured at specific temperatures for T _{h1} sample heated at 2°C/min	219
FIGURE 3.48	Hot stage microscopy images captured at T _{h2} sample which at 2°C/min	219
FIGURE 3.49	A hierarchical cluster analysis dendrogram of T _{h1} for variable temperature ATR-FTIR spectra obtained from 30°C to 198°C at a heating rate of 2°C/min spectra at 1 minute intervals	224
FIGURE 3.50	Variable temperature ATR-FTIR spectra of T _{h1} showing two clusters as identified in HCA data. (black) correlates to spectra at 30°C to 116°C, (red) correlates to spectra at 118°C to 198°C	224

List of figures

FIGURE 3.51	A hierarchical cluster analysis dendrogram of T_{h2} for variable temperature ATR-FTIR spectra obtained from 30°C to 198°C at a heating rate of 2°C/min spectra at 1 minute intervals	225
FIGURE 3.52	ATR-FTIR spectra of T_{h2} showing three clusters as identified in HCA data. (green) correlates to spectra at 30°C to 116°C, (red) correlates to spectra at 118°C to 134°C (black) correlates to spectra at 136°C to 198°C	226
FIGURE 3.53	Two dimensional PCA scores plot of T_{h1}	227
FIGURE 3.54	Two dimensional PCA scores plot of T_{h2}	277
FIGURE 3.55	ATR- FTIR Spectra of T_{h2} at 120°C (blue), T_{h2} held isothermal for 12hours (red)	229
FIGURE 3.56	ATR- FTIR Spectra of T_{h2} at 120°C (blue), T_{h2} held isothermal for 12hours (red), T_{hx} generated at 120°C in an oven (blue)	229
FIGURE 3.57	a) SEM image of T_{hx} b) Cross section showing grain boundaries. Scale bar corresponds to a) 50µm b) 10 µm	230
FIGURE 3.58	XRPD diffractogram of T_{hx}	231
FIGURE 3.59	Typical MTDSC total and reversing heat flow signals for T_{hx} at 2°C/min $\pm 0.212^\circ\text{C}$ modulation over a 60 second period using a pin-holed pan	232
FIGURE 3.60	Typical MTDSC reversing heat flow signals for T_{hx} at 2°C/min $\pm 0.212^\circ\text{C}$ modulation over a 60 second period using a pin-holed pan	232
FIGURE 3.61	Typical TGA profile for T_{hx}	233
FIGURE 3.62	Typical MTDSC (cooling cycle) reversing heat flow signals for T_{hx} at 2°C/min $\pm 0.212^\circ\text{C}$ modulation over a 60 second period using a pin-holed pan	234
FIGURE 3.63	Typical MTDSC (heating cycle) reversing heat flow signals for T_{hx} at 2°C/min $\pm 0.212^\circ\text{C}$ modulation over a 60 second period using a pin-holed pan	235
FIGURE 3.64	DSC (plan line) and TGA (dotted line) curves for T_{h1} taken from Dupray et al., (2009) at a heating rate of 1°C/min	238
FIGURE 3.65	Schematic illustrating the thermal transitions of T_{h1} , T_{h2} and T_{hx}	240

CHAPTER FOUR

FIGURE 4.1	SEM images of raffinose pentahydrate. Scale bar corresponds to a) 500 μ m b) 100 μ m.	244
FIGURE 4.2	SEM images of crystalline sucrose. Scale bar corresponds to 100 μ m.	245
FIGURE 4.3	SEM images of a) amorphous trehalose. Scale bar corresponds 5 μ m	246
FIGURE 4.4	SEM images of amorphous raffinose. Scale bar corresponds to 10 μ m	247
FIGURE 4.5	SEM image amorphous sucrose. Scale bar corresponds to 50 μ m	248
FIGURE 4.6	Average particle size distribution for raffinose pentahydrate	249
FIGURE 4.7	Average particle size distribution for crystalline sucrose	250
FIGURE 4.8	Average particle size distribution for amorphous trehalose, amorphous raffinose and amorphous sucrose	251
FIGURE 4.9	XRPD diffractogram of raffinose pentahydrate	252
FIGURE 4.10	XRPD diffractogram of crystalline sucrose	253
FIGURE 4.11	XRPD diffractogram of a) amorphous raffinose b) amorphous sucrose c) amorphous trehalose	254
FIGURE 4.12	ATR-FTIR spectra of raffinose pentahydrate (blue) and crystalline sucrose (red)	255
FIGURE 4.13	ATR- FTIR Spectra of amorphous raffinose (blue), amorphous sucrose (red) and amorphous trehalose (green)	256
FIGURE 4.14	A typical MTDSC (in the total heat flow) for raffinose pentahydrate at 2 $^{\circ}$ C/min \pm 0.212 $^{\circ}$ C modulation over a 60 second period and b) A typical TGA weight loss profile for raffinose pentahydrate heated at 2 $^{\circ}$ C/min using a pin-holed pan	258
FIGURE 4.15	A typical MTDSC in the reversing heat flow signal for amorphous raffinose at 2 $^{\circ}$ C/min \pm 0.212 $^{\circ}$ C modulation over a 60 second period showing a)plasticized T _g at 51.2 $^{\circ}$ C (first heat) b) un-plasticized T _g at 116.1 $^{\circ}$ C using pin holed pans	260
FIGURE 4.16	Typical TGA weight loss profile of amorphous raffinose heated at 2 $^{\circ}$ C/min using a pin holed pan system	261
FIGURE 4.17	A typical MTDSC in the reversing heat flow signal for amorphous trehalose at 2 $^{\circ}$ C/min \pm 0.212 $^{\circ}$ C modulation over a 60 second period showing a)plasticized T _g at 51.8 $^{\circ}$ C (first heat) b)	262

	un-plasticized T_g at 119.9°C using pin holed pan	
FIGURE 4.18	Typical TGA weight loss profile of amorphous trehalose heated at 2°C/min using a pin holed pan system	263
FIGURE 4.19	A typical MTDSC (in the total heat flow) for crystalline sucrose at 2°C/min $\pm 0.212^\circ\text{C}$ modulation over a 60 second period (black line) and a typical TGA weight loss profile for raffinose pentahydrate heated at 2°C/min (blue line) using a pin-holed	264
FIGURE 4.20	A typical MTDSC in the reversing heat flow signal for amorphous sucrose at 2°C/min $\pm 0.212^\circ\text{C}$ modulation over a 60 second period showing a) plasticized T_g at 36.5°C (first heat) b) un-plasticized T_g at 63.1°C using pin holed pans	265
FIGURE 4.21	Typical TGA weight loss profile of amorphous sucrose heated at 2°C/min using a pin holed pan system	266
FIGURE 4.22	Sorption isotherm curve for amorphous trehalose exposed to 10 to 90%RH at sequential increments of 5%RH steps at 25°C	269
FIGURE 4.23	Sorption isotherm curve for amorphous raffinose exposed to 10 to 90%RH at sequential increments of 5%RH steps at 25°C b) close up crystallisation transition	270
FIGURE 4.24	Sorption isotherm curve for amorphous sucrose exposed to 10 to 90%RH at sequential increments of 5%RH steps at 25°C	271
 CHAPTER FIVE		
FIGURE 5.1	XRPD diffractogram of amorphous sucrose	282
FIGURE 5.2	XRPD diffractogram of amorphous sucrose-trehalose samples	282
FIGURE 5.3	XRPD diffractogram of amorphous sucrose-raffinose samples	283
FIGURE 5.4	ATR-FTIR Spectra of amorphous sucrose and ST samples	284
FIGURE 5.5	ATR-FTIR Spectra of amorphous sucrose and SR samples	284
FIGURE 5.6	Typical TGA weight loss profile of amorphous sucrose heated at 2°C/min using a pin holed pan system	285
FIGURE 5.7	Typical TGA weight loss profile of ST2.5 heated at 2°C/min using a pin holed pan system	286
FIGURE 5.8	Typical TGA weight loss profile of ST4 heated at 2°C/min using a pin holed pan system	286

List of figures

FIGURE 5.9	Typical TGA weight loss profile of ST5.26 heated at 2°C/min using a pin holed pan system	286
FIGURE 5.10	Typical TGA weight loss profile of ST11.11 heated at 2°C/min using a pin holed pan system	287
FIGURE 5.11	Typical TGA weight loss profile of SR2.5 heated at 2°C/min using a pin holed pan system	287
FIGURE 5.12	Typical TGA weight loss profile of SR4 heated at 2°C/min using a pin holed pan system	288
FIGURE 5.13	Typical TGA weight loss profile of SR5.26 heated at 2°C/min using a pin holed pan system	288
FIGURE 5.14	Typical TGA weight loss profile of SR11.11 heated at 2°C/min using a pin holed pan system	288
FIGURE 5.15	A typical DSC heat flow signal for amorphous sucrose at 2,5,10 and 20°C/min	290
FIGURE 5.16	Activation energy determination from DSC heating rate experiments on amorphous sucrose.	291
FIGURE 5.17	A typical DSC heat flow signal for ST2.5 a) at 2,5,10 and 20°C/min b) close up of DSC heat flow signal at 2°C/min and at c)5°C/min	292
FIGURE 5.18	Activation energy determination from DSC heating rate experiments on ST2.5.a) with 2.5,10 and 20°C/min values plotted b) with 2,10 and 20°C/min values plotted	293
FIGURE 5.19	A typical DSC heat flow signal for ST4 a) at 2,5,10 and 20°C/min b) close up of DSC heat flow signal at 2°C/min	294
FIGURE 5.20	Activation energy determination from DSC heating rate experiments on ST4	295
FIGURE 5.21	A typical DSC heat flow signal for ST5.26 a) at 2,5,10 and 20°C/min b) close up of DSC heat flow signal at 2°C/min	296
FIGURE 5.22	Activation energy determination from DSC heating rate experiments on ST5.26.a) with 2.5,10 and 20°C/min values plotted b) with 2, 5 and 10°C/min values plotted	298
FIGURE 5.23	A typical DSC heat flow signal for ST11.11 a) at 2,5,10 and 20°C/min b) close up of DSC heat flow signal at 2°C/min	298
FIGURE 5.24	Activation energy determination from DSC heating rate experiments on ST11.11	299
FIGURE 5.25	A typical DSC heat flow signal for SR2.5 a) at 2,5,10 and	301

	20°C/min b) close up of DSC heat flow signal at 2°C/min	
FIGURE 5.26	Activation energy determination from DSC heating rate experiments on SR2.5	302
FIGURE 5.27	A typical DSC heat flow signal for SR4 a) at 2,5,10 and 20°C/min b) close up of DSC heat flow signal at 2°C/min	303
FIGURE 5.28	Activation energy determination from DSC heating rate experiments on SR4	303
FIGURE 5.29	A typical DSC heat flow signal for SR5.26 a) at 2,5,10 and 20°C/min b) close up of DSC heat flow signal at 2°C/min	304
FIGURE 5.30	Activation energy determination from DSC heating rate experiments on SR5.26	305
FIGURE 5.31	A typical DSC heat flow signal for SR11.11 at 2,5,10 and 20°C/min	306
FIGURE 5.32	Activation energy determination from DSC heating rate experiments on SR11.11	307
FIGURE 5.33	Typical Qi-MTDSC reversing heat capacity (as a function of time) signal of amorphous sucrose at a temperature modulation of $\pm 1^\circ\text{C}$, 20 minute isothermal periods with 2°C increments using a pin-holed pan	312
FIGURE 5.34	Typical Qi-MTDSC reversing heat capacity (as a function of time) signal of ST2.5 at a temperature modulation of $\pm 1^\circ\text{C}$, 20 minute isothermal periods with 2°C increments using a pin-holed pan	313
FIGURE 5.35	Typical Qi-MTDSC reversing heat capacity (as a function of time) signal at a temperature modulation of $\pm 1^\circ\text{C}$, 20 minute isothermal periods with 2°C increments for a) ST4 b) ST5.26 using a pin-holed pan	314
FIGURE 5.36	Typical Qi-MTDSC reversing heat capacity (as a function of time) signal of ST11.11 at a temperature modulation of $\pm 1^\circ\text{C}$, 20 minute isothermal periods with 2°C increments using a pin-holed pan	315
FIGURE 5.37	Typical Qi-MTDSC reversing heat capacity (as a function of time) signal at a temperature modulation of $\pm 1^\circ\text{C}$, 20 minute isothermal periods with 2°C increments for a) SR2.5 b) SR5.26 using a pin-holed pan	317
FIGURE 5.38	Typical Qi-MTDSC reversing heat capacity (as a function of time) signal of SR4 at a temperature modulation of $\pm 1^\circ\text{C}$, 20 minute isothermal periods with 2°C increments using a pin-	318

- holed pan
- FIGURE 5.39** Typical Qi-MTDSC reversing heat capacity (as a function of time) signal of SR11.11 at a temperature modulation of $\pm 1^\circ\text{C}$, 20 minute isothermal periods with 2°C increments using a pin-holed pan **318**
- CHAPTER SIX**
- FIGURE 6.1** Cytotoxicity of a) trehalose b) raffinose and c) HPMC on A549 cells (24hour MTT exposure) assessed by MTT assay. The % cell viability was compared to control cells (n =3, error bars represent standard deviation of mean) **326**
- FIGURE 6.2** a) Showing unsuccessful transfection studies using A549 cells (control using $10\mu\text{g}$ of pEGFP Arrestin 2) showing non-specific fluorescence b) Showing successful transfection of HeLa cells (control using $10\mu\text{g}$ of pEGFP Arrestin 2) showing low transfection efficiency c) Showing successful transfection of HeLa cells using $10\mu\text{g}$ of pEGFP Arrestin 2 spray dried in the presence of 10% w/v trehalose (in the presence of $20\mu\text{L}$ of sodium butyrate) d) Showing unsuccessful transfection studies using HeLa cells $10\mu\text{g}$ of pEGFP Arrestin 2 spray dried in the presence of 10% w/v raffinose e) $10\mu\text{g}$ of pEGFP Arrestin 2 spray dried in the presence of 2% w/v HPMC **328**
- FIGURE 6.3** 2% agarose gel electrophoresis of spray dried powders containing linearized pEGFP-Arrestin-2 by digestion with restriction enzymes. Lane 1 HPMC co-spray dried with pDNA; Lane 2; Raffinose co-spray dried with pDNA lane 3: Trehalose co-spray dried with pDNA; lane 4 pEGFP Arrestin 2 (without spray drying) at 125°C **330**
- FIGURE 6.4** Degradation of pDNA co-spray dried with HPMC, trehalose and raffinose at 125°C spray drying inlet temperature (n =3, error bars represent standard deviation of mean). **331**
- FIGURE 6.5** 2% agarose gel electrophoresis analysis of pDNA co-spray dried (at 125°C inlet temperature) with sucrose (lane 1), ST2.5 (lane 2), ST11.11 (lane 3), SR2.5 (lane 4) and SR11.11 (lane 5) **332**

List of figures

FIGURE 6.6 Percentage degradation plot of sucrose, ST2.5, SR2.5, ST11.11 and SR11.11 co-spray dried with pDNA at 125 °C spray drying inlet temperature (n =3, error bars represent standard deviation of mean) **333**

APPENDIX

FIGURE A.1 Haemocytometer with cells for counting (taken from <http://www.cf.ac.uk/biosi/staffinfo/kille/Methods/Cellculture/HAEMO.html>) **369**

FIGURE A.2 Schematic illustration of a 96-well plate used in an MTT assay where C = cells with media only, MA = media (RPMI – 1640) alone, C = control solutions, T = trehalose solutions, R = raffinose solutions and H = HPMC solutions, ■ = phosphate buffered saline solution **370**

LIST OF TABLES

CHAPTER ONE

TABLE 1.1	Examples of current DNA-based therapeutics in various stages of clinical development <small>*http://silence-therapeutics.com/pipeline/ *A http://www.alnylam.com/Programs-and-Pipeline/index.php <small>*http://www.isispharm.com/Pipeline/index.htm</small></small>	47
TABLE 1.2	Properties of viral vector systems commonly used in gene therapy (taken from Walker and Stein, (2000))	48
TABLE 1.3	Critical relative humidities (RH ₀) for crystalline sucrose, raffinose and trehalose (taken from Hancock and Shamblin, (1998))	64

CHAPTER TWO

TABLE 2.1.	Basic composition and safety of common sugars	96
TABLE 2.2	Reported crystalline forms of trehalose	101
TABLE 2.3	Reported amorphous forms of trehalose	104
TABLE 2.4	Composition of buffer solutions used in DNA purification	112
TABLE 2.5	General recommendations to select optimised MTDSC parameters for all thermal events (Taken from Guinot and Leveiller (1999))	123
TABLE 2.6	Components used in restriction enzyme digestion of plasmid DNA	126
TABLE 2.7	Concentrations of sugar and media solutions used in MTT assay	148

CHAPTER THREE

TABLE 3.1.	Particle size distribution of Sigma B obtained by the dry sieving method	176
-------------------	--	------------

TABLE 3.2	Summary of Sigma A, B and Acros batches results	179
TABLE 3.3	Summary of endotherm values (°C) for T _{h1} and T _{h2} MTDSC heat flow experiments at 2°C/min ±0.212°C modulation over a 60 second period and TGA weight loss data of T _{h1} and T _{h2} heated at 2°C to 250°C (n=3)	196
TABLE 3.4	Endotherm values (°C) for T _{h1} and T _{h2} DSC heat flow experiments at heating rates of experiments at 2, 20, 50 and 100°C/min ±0.212°C modulation over a 60 second period using a pin-holed pan (n=3)	199
TABLE 3.5	Endo- and exotherm values (°C) for T _{h1} and T _{h2} DSC heating rate experiments at 500 and 750°C/min using a pin-holed pan (n=3)	201
TABLE 3.6	Summary of endotherm and T _g values for T _{h1} and T _{h2} MTDSC heat flow experiments at 0.5,1, and 2°C/min using a pin-holed pan (n=3)	210
CHAPTER FOUR		
TABLE 4.1	Reported literature T _g values of amorphous sucrose	267
TABLE 4.2	Summary of physico-chemical properties of crystalline samples (n=3)	273
TABLE 4.3	Summary of physico-chemical properties of amorphous samples (n=3)	274
CHAPTER FIVE		
TABLE 5.1	Summary of T _g values obtained from DSC heat flow signal for amorphous sucrose at 2, 5, 10 and 20°C/min (n=3)	290
TABLE 5.2	Summary of T _g values obtained from DSC heat flow signal for ST2.5 at 2, 5, 10 and 20°C/min (n=3)	292
TABLE 5.3	Summary of T _g values obtained from DSC heat flow signal for ST4 at 2, 5, 10 and 20°C/min	295
TABLE 5.4	Summary of T _g values obtained from DSC heat flow signal for ST5.26 at 2, 5, 10 and 20°C/min (n=3)	297
TABLE 5.5	Summary of T _g values obtained from DSC heat flow signal for ST5.26 at 2, 5, 10 and 20°C/min (n=3)	299

List of tables

TABLE 5.6	ΔE_{T_g} calculated from the heating rate dependency of T_g for Amorphous Sucrose and ST samples	300
TABLE 5.7	Summary of T_g values obtained from DSC heat flow signal for SR2.5 at 2, 5, 10 and 20°C/min (n=3)	301
TABLE 5.8	Summary of T_g values obtained from DSC heat flow signal for SR4 at 2, 5, 10 and 20°C/min (n=3)	303
TABLE 5.9	Summary of T_g values obtained from DSC heat flow signal for SR5.26 at 2, 5, 10 and 20°C/min (n=3)	305
TABLE 5.10	Summary of T_g values obtained from DSC heat flow signal for SR11.11 at 2, 5, 10 and 20°C/min (n=3)	306
TABLE 5.11	ΔE_{T_g} calculated from the heating rate dependency of T_g for Amorphous Sucrose and SR samples	307
TABLE 5.12	ΔE_{T_g} calculated from the heating rate dependency of T_g for Amorphous Sucrose with or without sugar additive	308
TABLE 5.13	Calculated fragility parameter, m (Eq.5.1) using ΔE_{T_g} calculated from the heating rate dependency of T_g for Amorphous Sucrose, ST and SR samples	310
TABLE 5.14	Calculated strength parameter, D (Eq.5.2) using ΔE_{T_g} calculated from the heating rate dependency of T_g for Amorphous Sucrose, ST and SR samples using $m_{\min}=16$	310
TABLE 5.15	Calculated strength parameter, D (Eq.5.2) using ΔE_{T_g} calculated from the heating rate dependency of T_g for Amorphous Sucrose, ST and SR samples using m_{\min} from data	312

LIST OF SYMBOLS

T_m	Melting temperature
T_g	Glass transition temperature
T_K	Kauzmann temperature
T_{oc}	calorimetric ideal glass transition temperature
C_p	Heat capacity
α	thermal expansivity
v	Specific volume
H	Enthalpy
η	viscosity
V	Volume
V_f	Free volume
S	Entropy
T	Temperature
	Activation energy
R	Gas constant
D	Strength parameter
τ	mean molecular relaxation time
	zero mobility temperature
	relaxation time constant
S_c	configurational entropy
	configurational heat capacity
M	Fragility parameter
ΔH^*	Arrhenius activation energy
ΔE_{T_g}	activation enthalpy for structural relaxation at temperatures around the glass transition
	minimum value for m

List of symbols

T_f	Fictive temperature
W	Weight fraction
K	sample specific parameter
ΔH_{fus}	Specific Heat of Fusion
F	degrees of freedom
C	number of independent components
N	number of non-compositional variables
Φ	number of phases
d_A	aerodynamic diameter
Re	Reynolds number
$RH\%$	Relative humidity
RH_0	Critical relative humidity
T_h	Trehalose dihydrate
T_β	stable crystalline anhydrous form of trehalose
T_α	isomorph desolvate of T_h
T_ϵ, T_k	Anhydrous polymorphic forms of trehalose
T_γ	transient” crystalline metastable form of trehalose
T_{am1}, T_{am2}	Amorphous forms of trehalose
A_λ	absorbance at a particular wavelength
C	concentration of the nucleic acid
ϵ_λ	extinction coefficient
d_{ab}	multivariate distance between two samples a and b
d_{max}	largest distance in the data set
ΔQ	Heat

LIST OF ABBREVIATIONS

VTF	Vogel-Tamman-Fulcher
LDA	low-density amorphous ice
HDA	High-density amorphous ice
AIDS	Acquired Immunodeficiency Syndrome
DNA	Deoxyribonucleic acid
siRNA	short interfering RNA
mRNA	messenger RNA
pDNA	Plasmid DNA
FDA	U.S Food and Drug Administration
biomolecules	biological molecules
<i>E.coli</i>	<i>Escherichia coli</i>
LB medium	Luria-Bertani medium
SDS	sodium dodecyl sulfate
HPMC	Hydroxypropylmethylcellulose
SEM	Scanning electron microscopy
DSC	differential scanning calorimetry
MTDSC	Modulated temperature DSC

List of abbreviations

Qi-MTDSC	Quasi-Isothermal MDSC
TGA	Thermogravimetric analysis
XRPD	X-ray powder diffraction
PCA	Principle component analysis
HCA	Hierarchical cluster analysis
HSM	Hot stage microscopy
FTIR	Fourier Transform Infrared spectroscopy
ATR	attenuated total reflection
2D	two dimensional
DVS	Dynamic Vapour Sorption
MTT	(3-(4,5-Dimethylthiazol-2-yl)-2,5-diphenyltetrazolium bromide)
T _{h1} , T _{h2}	Standardised forms of trehalose dihydrate
T _{hx}	Generated from T _{h2}
SR	Mixed sugar glasses containing sucrose and raffinose
ST	Mixed sugar glasses containing sucrose and trehalose

CHAPTER ONE
INTRODUCTION

1.1 GENERAL INTRODUCTION

The relevance of amorphous and polymorphic states in biological, pharmaceutical and food science is well recognised. It is important to accurately define thermodynamic transitions (at equilibrium) as well as study kinetically metastable transformations which characterize the physical properties of the material under different experimental conditions (Sussich et al., 1998).

Sugars are found at relatively high concentrations in anhydrobiotic organisms (Crowe et al., 1992) where they exert a protective effect. There has been considerable interest in amorphous sugars specifically regarding their hydration, glass transition and bio-preservation properties.

The work presented in this thesis details the generation and characterisation of two standardised forms of trehalose dihydrate, the effect sugar additives on amorphous sucrose stability and an evaluation of the degree of degradation of plasmid DNA spray dried in the presence of amorphous sugars. In the following sections a comprehensive review of key areas in this study are explored followed by the research objectives.

1.2 USE OF NUCLEIC ACIDS AS THERAPEUTIC AGENTS (DNA-BASED THERAPEUTICS)

Nucleic acids are fundamental “molecules of life” and play key roles in gene expression and regulation (Li et al., 2011). Gene therapy involves the introduction of a gene into target cells in a patient to induce a therapeutic effect or to correct or modulate a disease

(Durland and Eastman, 1998). A biopharmaceutical is a protein or nucleic acid based pharmaceutical substance used for therapeutic or *in vivo* diagnostic purposes, which is produced by means other than direct extraction from a native (non engineered) biological source (Walsh, 2002). Effective gene delivery requires targeted delivery of deoxyribonucleic acid (DNA) to a sufficient amount of target cells and high expression of the gene at concentrations high enough to induce a pharmacological effect. Overall, gene delivery is a clinical strategy that has the potential to treat an array of genetic and non-genetic disease (Sakurai et al., 2008).

DNA (*Figure 1.1*) is comprised of two anti-parallel polynucleotide chains comprised of nucleotides monomer units with an alternating phosphate and deoxyribose (monosaccharide) backbone. These strands are wound around each other with a right-handed helical symmetry (Watson and Crick, 1953). The deoxyribose sugars are joined at 3'-hydroxyl and 5'-hydroxyl groups to phosphate groups in ester linkage referred to as phosphodiester bonding. There are four different nucleotides found within a DNA molecule. They are the purine bases (adenine and guanine) and the pyrimidine bases (cytosine and thymine) (*Figure 1.1*). With adenine and thymine only forming hydrogen bonds together whilst guanine and cytosine only forming hydrogen bonds together.

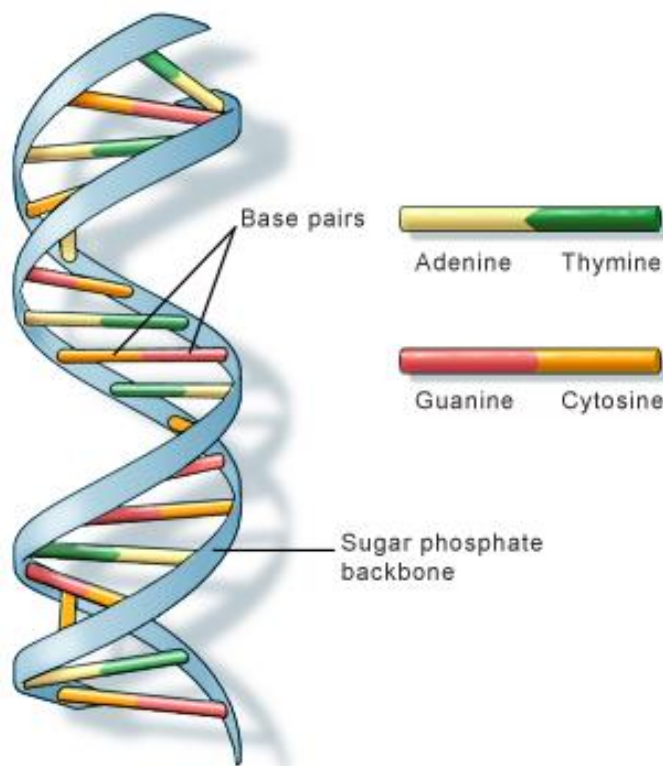


Figure 1.1 Illustration showing deoxyribonucleic acid which consists of two anti-parallel polynucleotides consisting of a sugar phosphate back bone and purine and pyrimidine base pairing
(Take from <http://ghr.nlm.nih.gov/handbook/basics/dna>)

The majority of DNA is located within the nucleus of a cell. Some DNA is located within the mitochondria and referred to as mitochondrial DNA. DNA holds essential genetic information for cell and organism function. The DNA molecule is an important source for not only understanding of fundamental basis of human life but also for the development of a novel group of therapeutics modelled on its endogenous structure. DNA-based therapeutics includes but is not limited to oligonucleotides for antisense and antigene applications, plasmids DNA and short interfering ribonucleic acid (siRNA). A significant advantage of DNA-based drugs over low molecular weight drugs is their selective recognition of molecular targets and pathways with incredible specific of action.

1.2.1 OLIGONUCLEOTIDES FOR ANTISENSE AND ANTIGENE APPLICATIONS

Oligonucleotides are short-single stranded segments of DNA once taken up by the cell they selectively inhibit the expression of a single protein. For antisense applications, oligonucleotides interact with messenger RNA (mRNA) or precursor mRNA and forms a duplex inhibiting their translation or processing in turn inhibiting protein biosynthesis. Using antigene applications, oligonucleotides are required to enter the nucleus where it forms a triplex with double stranded genomic DNA. It inhibits translation as well as the transcription of the target protein (Crooke, 1999). For therapeutic purposes, antisense oligonucleotides are used to downregulate gene expression. This approach is very successful, though extensive experimental investigation is required to identify effective target sites within the gene which can prove not only expensive but time consuming (Thomas et al., 2007).

1.2.2 PLASMID DNA

Plasmid DNA (pDNA) is a high molecular weight double stranded DNA polyanion which contains transgenes encoding for specific proteins (Uherek and Wels, 2000). pDNA can be thought of as pro-drug on a molecular level, as upon cellular internalization it facilitates DNA transcription and translation within the cell to biosynthesis a protein (the therapeutic entity) (Patil et al., 2005). The role of pDNA in gene delivery is to introduce transgenes into the cell to produce the required protein that the transgene is sequenced to generate. In order to exert a therapeutic effect pDNA is required to be delivered directly to the nucleus.

DNA condensation is a process by which the molecular volume of pDNA is dramatically reduced by its interaction with multivalent cationic agents. It is characterised by molecular collapse that protects pDNA from nucleases and chemical degradation. This process is limited to polynucleotides greater than approximately 400 bases (Bloomfield, 1991). DNA condensation bears some similarities to protein folding. The similarities include improbability of the formation of compact, ready reversibility, several non-covalent interactions that drive the processes and the requirement of the collapsed state for biological function. However, DNA condensation does differ from protein folding in that no unique compact structure is formed, hydrophobic interactions do not drive collapse and a functional assay is not available for analysis of the condensed state (Bloomfield, 1996). The term “condensation” is often misused to describe electrostatic association of nucleic acids with a delivery agent regardless of polynucleotide size, valency of the cation or ability of the delivery system to affect molecular collapse. The complexation of poly- and oligonucleotides with a cationic delivery agent results in nuclease resistance however condensation is rarely achieved (Xu and Anchordoquy, 2010).

To obtain optimal biological effectiveness, pDNA should ideally be in its supercoiled circular form, as this form is important for genetic transfection into cells (be it prokaryotic or eukaryotic) and offers the highest transfection efficiency (Tse et al., 2009; Walther et al., 2003). This also aides transport into the cell for successful gene expression. Structural changes will convert the super-coiled circular form to an open-circular and/or linear form. Open-circular DNA has a "nick" in one of its strands (*Figure 1.2*). The degradation of these forms can occur at near neutral pH by the two step process of depurination and β -elimination, leading to cleavage of the phosphodiester backbone (Evans et al., 2000;

Suzuki et al., 1994). The supercoiled form can be maintained when plasmid DNA solutions are stored at -80°C (Quaak et al., 2010). Przybylowski et al., (2007) demonstrated plasmid DNA stability and biological functionality after storage for 3 years at -20°C .

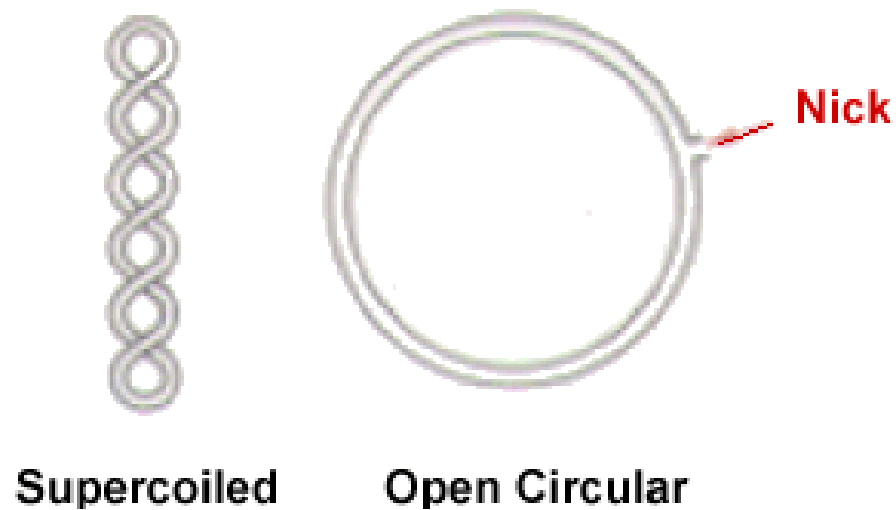


Figure 1.2 Schematic showing differences with super-coiled and open-circular DNA (taken from Redway,2012)

pDNA based gene expression delivery systems are composed of three genetic components i) a prokaryotic plasmid vector allowing plasmid to be propagated in an appropriate host, usually the bacteria *Escherichia coli*; ii) eukaryotic regulatory elements that control the location, level and duration of therapeutic protein production in the target cells iii) a gene usually encoding for a therapeutic protein (Durland and Eastman, 1998). Extensive research has been conducted on the design and engineering of pDNA to achieve optimal transfection. pDNA contain regulatory signals which play an important role in regulating gene expression (Patil et al., 2005). These regulatory signals are often endogenously present on viral delivery vectors, or can be artificially engineered in the viral genome (Anderson, 1984).

1.2.3 SHORT INTERFERING RNA (siRNA)

Research into the use of short interfering RNA (siRNA) as a sequence selective inhibitor of gene expression in mammalian cells is rapidly developing. siRNAs are small double stranded ribonucleic acid (dsRNA) that are functional mediators of post transcriptional gene silencing of a specific target protein, by disrupting messenger RNAs (mRNAs) which contains the complementary sequence. This is a naturally occurring mechanism that regulates gene expression and is called RNA interference (RNAi). RNAi is a post-transcriptional gene process, in which dsRNA trigger the degradation of homologous mRNA. RNAi was originally observed as an inherent property of plants, and is believed to play a role in the body's natural defence against a viral attack. RNAi (*Figure 1.3*) involves the cleavage of dsRNA to short 20-25bp siRNAs which is catalyzed by DICER (a member of the RNase III family of ds-RNA specific ribonucleases) resulting in siRNAs that have 5' phosphate and 3' hydroxyl termini and are recognised by RNA-induced silencing complex (RISC) (Thomas et al., 2007; Gewirtz, 2007; Aigner, 2007). RISC has a helicase activity that unwinds the two strands of RNA molecules, allowing the antisense strand to bind to the targeted RNA molecule. RISC also has an endonuclease activity which hydrolyzes the target mRNA at the site where the antisense strand is bound (Fattal and Bochot, 2006). Active RISC complexes (RISC*) promote the unwinding of siRNA through an adenosine triphosphate (ATP) dependent process. The unwound antisense strand that is produced, guides RISC* towards complementary mRNA which is cleaved by RISC* at a single site defined by the location of the 5' end antisense strand bound to the mRNA target sequence. In order for RNA-mediated mRNA cleavage and degradation to occur successfully 5' phosphorylation of this antisense strand must occur. This process highlights the role of siRNA in RNAi initiation and its potential function in RNAi induction.

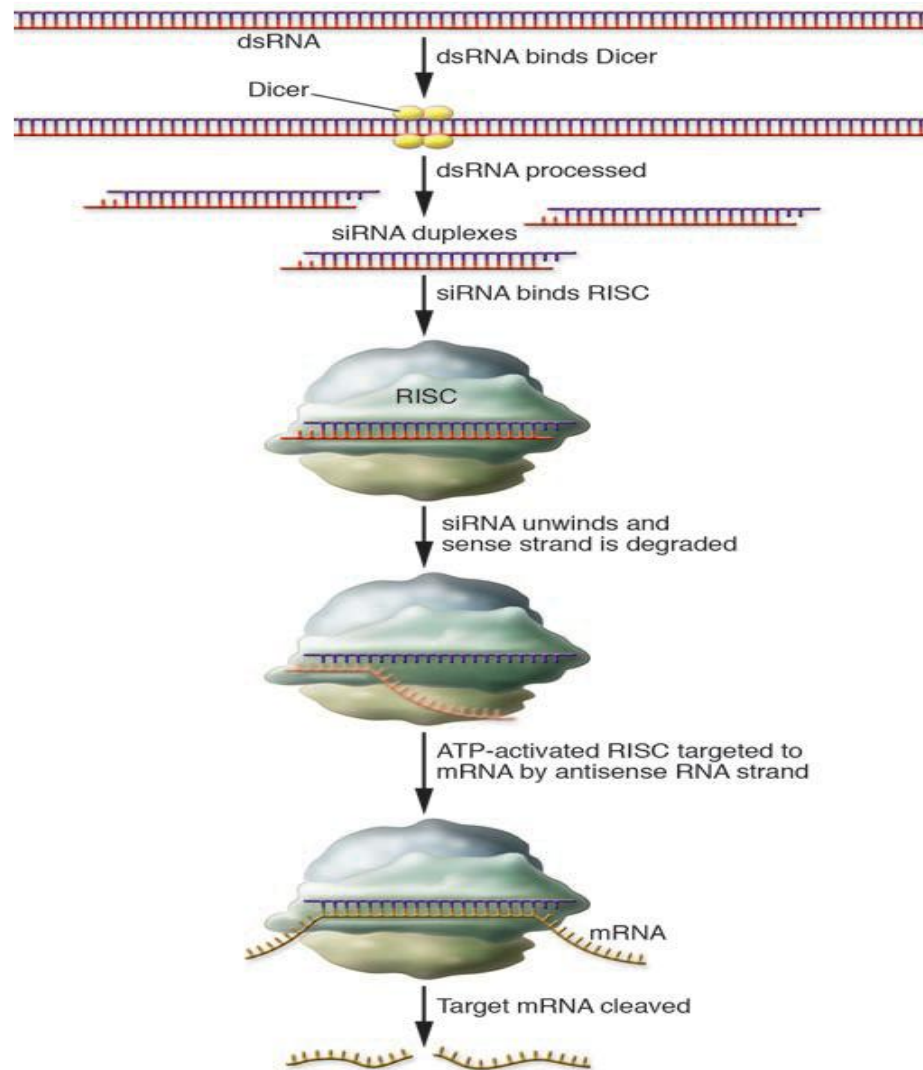


Figure 1.3 Schematic illustration of the RNAi pathway (taken from Gewirtz (2007))

Endogenous siRNA (produced by DICER mediated cleavage of dsRNAs) as well as exogenous (chemically synthesised) siRNA can be introduced into cells. Each approach has its unique advantages and disadvantages. SiRNAs can be synthesized directly against its target with high specificity and can be prepared against any gene known (Sklan and Glenn, 2007). Chemically synthesized siRNA are of defined length and composition however, they are expensive and their effects are often transient (Kettner-Buhrow et al., 2006).

1.3 DELIVERY OF NUCLEIC ACIDS

Most debilitating illnesses have an underlying genetic cause which pharmacological approaches can fail to treat effectively. Gene therapy provides the opportunity for the correction of dysfunctional or deleted genes by supplying the lacking component. This approach can be used as a means to treat or reverse such disorders. Several pharmaceutical companies are actively trying to get nucleic acids into formulation and into the clinic with some success. *Table 1.1* provides examples of current DNA-based therapeutics in various stages of clinical development.

For effective gene delivery it is imperative for the DNA-based therapeutic be delivered to its required site of action. For example, comparing antisense oligonucleotides, pDNA and siRNA all are required to cross the cell membrane and escape lysosomal degradation. The negative charge of these molecules suggests they are unable to bind to the cell surface or cross the cell membrane by passive diffusion. pDNA requires entry into the nucleus to initiate transcription of encoded genes, whilst antisense oligonucleotides and siRNA is able to exert its therapeutic effect in the cytosol.

Overall, for successful, efficient and safe gene delivery (and gene silencing) the nucleic acid e.g. pDNA, siRNA or antisense oligonucleotides must be delivered safely to its site of action at a sufficient concentration to exert its therapeutic effect. Delivery methods can be classified into three general types, electrical techniques (such as electroporation (Regnier et al., 2000)), mechanical transfection (e.g. microinjection techniques (Pearson et al., 2008)) and vector assisted delivery.

Table 1.1 Examples of current DNA-based therapeutics in various stages of clinical development

*s<http://silence-therapeutics.com/pipeline/> *A <http://www.alnylam.com/Programs-and-Pipeline/index.php> *I<http://www.isispharm.com/Pipeline/index.htm>

COMPANY	TYPE OF DNA-BASED THERAPEUTIC	DRUG NAME	TARGET DISEASE	STATUS
SiBono Genetech	Plasmid pDNA	Gendicine	Head and neck squamous cell carcinoma	Chinese-FDA approved
Alnylam and partners	Naked siRNA	ALN-RSV01	Respiratory syncytial virus infection	Phase IIb * ^A
		ALN-VSP01	Liver cancer	Phase I * ^A
		ALN-APC	Hemophilia	Preclinical * ^A
Isis Pharmaceuticals and partners	Antisense oligonucleotide	Kynamro (mipomersen sodium)	Reduction of LDL cholesterol	Phase III* ^I
Silence /Quark	Naked siRNA	QPI-100	Acute kidney injury	Phase II * ^s
Silence/Quark/Pfizer	Naked siRNA	PF-04523655	Diabetic macular oedema	Phase II * ^s

Ideal properties of a nucleic acid delivery vector include high transfection efficiency (accompanied with high specificity), low toxicity and immunogenicity, easy modifiable for customized nucleic acid release and good gene expression. Vector assisted delivery can be categorised into two main groups, viral and non-viral and will be discussed in the following sections.

1.3.1 VIRAL VECTORS

The concept of viral vectors for gene delivery is relatively straightforward. It involves insertion of genetic material into a viral genome taking advantage of the inherent ability of

the virus to transduce cells from a desired therapeutic outcome (Patil et al., 2005). Unfortunately viral based delivery holds disadvantages, including the possibility of inflammatory, oncogenic transformations, immune and toxicity reactions. Common viruses used as vectors for gene delivery are adenoviruses, adeno-associated virus, retrovirus and lentivirus (subclass of retrovirus). Retroviral vectors infect only dividing cells whilst adenoviral vectors and adeno-associated viral vectors are able to infect non-dividing cells. Lentiviral vectors are able to infect dividing and non-dividing cells. Adeno-associated viral vectors are the most superior in terms of their gene transfer abilities. Adeno-associated viral vectors appear to have the best safety profile as all viral genes have been removed as well as long lasting high level of gene expression (Walther and Stein, 2000). Properties of commonly used viral vectors in gene delivery are summarised in *Table 1.2* (taken from Walther and Stein, (2000)).

Table 1.2 Properties of viral vector systems commonly used in gene therapy (taken from Walker and Stein, (2000))

Viral vector	Advantages	Disadvantages
Retroviral vectors	Insert capacity for transgene <7-8kb, stable integration into host DNA, recombinant virus titers of 10^2 - 10^7 pfu/ml, broad cell tropism of infectivity, relatively easy manipulation of viral genome for vector engineering	Difficult targeting of viral infection, no infection of non-dividing cells, random integration into host genome, instability of vectors
Lentiviral vectors	Infect dividing and non-dividing cells, stable gene expression, insert capacity of 10kb	Potential insertional mutagenesis, presence of regulatory (tat, rev) and of accessory protein sequences in the packaging constructs
Adenovirus vectors	Generation of high virus titers of 10^{10} pfu/ml, high level gene expression, large insert capacity (7-8kb), infects dividing and non-dividing cells	Immune response to viral proteins, no integration into host genome, transient gene expression
AAV vectors	Infect dividing and non-dividing cells, broad cell tropism, potential of targeted integration, low immunogenicity and nonpathogenic	Limited capacity for transgenes (4kb), difficult generation of high virus titers, requirement of adenovirus or herpesvirus for AAV replication
Herpesvirus vectors	Infects a wide variety of cell types, high insertion capacity (up to 50 kb), natural tropism to neuronal cells, stable viral particles allow generation of high virus titers (10^{12} pfu/ml)	Possible toxicities, risk of recombination, no viral integration into host DNA,
Poxvirus vectors	High insertion capacity, insertion of large DNA fragments possible, high transgene expression level, suited for live recombinant vaccine	Potential cytopathic effects
Epstein-Barr virus vectors	Infects dividing and non-dividing cells with preference for B-cells, high insert capacity (<150kb)	Difficult access to packaging cell lines

AAV = adeno-associated virus; pfu = plaque forming units.

1.3.2 NON-VIRAL VECTORS

Non-viral vectors have several advantages over viral vectors mainly safety. The downside of non-viral vectors however is that their level of gene expression and transfection efficiency is low compared to viral vectors. Non-viral vectors can be modified and be incorporated by ligands for cell specific targeting to improve the transfection efficiency. The two major vector types for non-viral nucleic delivery are liposomal and polymeric based delivery systems.

1.3.2.1 Liposomal non-viral delivery systems

A liposome is a vesicle which consist of an aqueous compartment enclosed in a phospholipid bilayer (*Figure 1.4*). When multiple lipid bilayers are formed around a primary core in a concentric fashion the complexes generated are known as multilamellar vesicles (*Figure 1.4*).

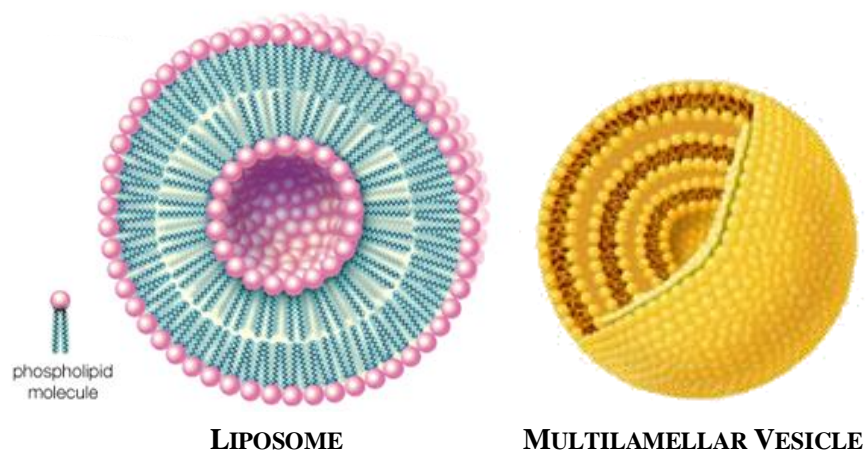


Figure 1.4 Illustration showing a liposome and a multilamellar vesicle (taken from <http://www.britannica.com/EBchecked/media/92244/Phospholipids-can-be-used-to-form-artificial-structures-called-liposomes> and http://www.encapsula.com/products_01.html)

Liposomes can be used as DNA drug delivery systems either by entrapping the DNA-based therapeutics inside the aqueous core or complexing them to the phospholipid lamellae. Liposomes offer significant advantages over viral delivery options for the delivery of DNA therapeutics as they are generally non-immunogenic, can be easier easily engineered to yield a desired size, surface charge, composition, and morphology. A variety of cationic, anionic and synthetically modified lipids have been used to deliver a wide range of DNA-based therapeutics.

Cationic lipids commonly used are 1,2-dioleoyl-3-trimethylammonium propane (DOTAP) and N-[1-(2,3-dioleoyloxy)propyl]-N,N,N-trimethylammonium chloride (DOTMA). Commonly used helper lipids (also referred to as zwitterionic lipids) are DOPE and cholesterol. The cationic surface charge of lipids like DOTAP can aid in DNA complexation during the formation of the lipoplex (DNA and liposome complex). The positive charge also aids in cellular entry. Helper lipids help in membrane perturbation and fusion (Patil et al., 2005).

1.3.2.2 Polymeric non-viral delivery systems

Cationic polymers are commonly used as non-viral gene delivery systems because of their ability to easily complex with DNA molecules leading to the formation of polymer-DNA complexes (polyplexes). Commonly used polymers include polyethyleneimine (PEI), dendrimers and chitosan. Chitosan (1,4-2 amino-2-deoxy-b-D-glucan) is a linear biodegradable polymer derived from chitin (a polysaccharide abundant in nature) and is extracted from crustacean shells. Chitosan is a weak base polysaccharide that contains amino acid groups which are protonated in an acid medium, resulting in a high positive

charge. Chitosan based carriers are non-viral vectors that have gained an increased interest in recent times as a safer and more cost effective delivery system for gene materials including plasmid DNA, oligonucleotides as well as proteins and peptides. Chitosan also has advantages as a non-viral vector as it has a low toxicity and immunogenicity profile, good biodegradability, biocompatibility, mucoadhesiveness, a high positive charge and can be used as an absorption enhancer (Katas and Alpar, 2006). Chitosan forms polyelectrolyte complexes with negatively charged nucleotides by an electrostatic interaction (Katas and Alpar, 2006).

1.4 PULMONARY DELIVERY

Pulmonary delivery is used to deliver a variety of therapeutics including DNA based for the treatment of many localised diseases like respiratory tract infections, asthma, chronic obstructive pulmonary disease and cystic fibrosis. In this section, the functional anatomy and physiology of the lung (including physiological barriers to pulmonary delivery), ideal particle characteristics and pulmonary delivery of nucleic acids are discussed.

1.4.1 FUNCTIONAL ANATOMY AND PHYSIOLOGY OF THE RESPIRATORY SYSTEM

1.4.1.1 Functional Anatomy of the Respiratory System

The lungs occupy the thoracic cavity with the left lung being smaller than the right lung due to the position of the heart, which extends into the left thoracic space. The lungs are almost pyramidal in shape, with an approximate height of 20cm, a density (when fully inflated) of approximately 0.2kg dm^{-3} and surface area of $72\text{-}140\text{m}^2$ in adults (Kumar and Clark, 2005). The respiratory system consists of two functional sections, the airways

(nose, nasopharynx, oropharynx, trachea, bronchi and bronchioles) and the alveoli. The upper airways (the nose, nasopharynx and the oropharynx) are lined by ciliated cubical or columnar epithelium, interspersed with goblet cells and receptors or free nerve endings. The trachea is 10-12cm in length. It lies slightly to the right of the midline and divides into the right and left main bronchi. The right main bronchus is more vertical than the left, because of this inhaled material is more likely to end up in the right lung than the left (Yang et al., 2008). At the tracheobronchial region, a mucus layer protects the epithelium.

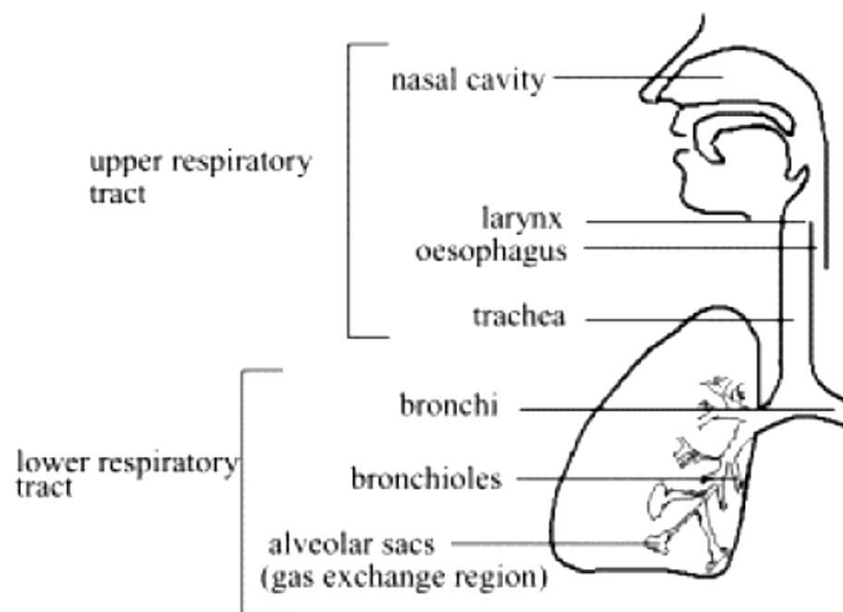


Figure 1.5 Regions of the human respiratory system (taken from Seville et al.,(2007))

The mucus is a thick gelatinous substance that is secreted from goblet cells and mucous glands, under normal conditions the tips of the cilia are in contact with the under surface of the gel phase and coordinate their movement to push the mucus upwards. It takes approximately 30-60minutes for mucus to be cleared from the large bronchi; however, there is delay of several days before clearance is achieved from the bronchioles. Any particle deposited in this area is transported away from the lung by mucocilliary clearance

or diffused through the mucus layer to reach the epithelium cells. Ciliated epithelium is a key defence mechanism of the lung. Pseudostratified epithelia act as a barrier to absorption into the bloodstream; it is markedly different in airways and alveoli of the lungs. Alveoli are not well protected against inhaled substances compared to the airways, because of the large alveoli surface area and the intimate air-blood contact. The pulmonary artery is the main blood supply to the lung. It divides into the right and left pulmonary arteries and these in turn subdivide to provide up to eight generations of elastic walled vessels with a diameter of more than 2mm. Pulmonary receptors contribute to the pattern of breathing in a wide range of circumstances. Their role in the upper airways is mainly protective.

1.4.1.2 Physiology of the Respiratory System

Lung ventilation is a two-part mechanical process of inspiration and expiration that control respiration to an appropriate level to satisfy metabolic needs (*Figure 1.6*). Inspiration is an active process and results from the descent of the diaphragm and movement of the ribs upwards and outwards by the contraction of the intercostals muscles. Expiration follows passively because of gradual relaxation of the intercostals muscles, allowing the lungs to collapse under the influence of their own elastic forces. The lungs have a tendency to collapse away from the thoracic wall, generating a negative pressure within the pleural space. The strength of the force relates to the lung volume. At high lung volumes, the lung is stretched more, and a greater negative intrapleural pressure is generated.

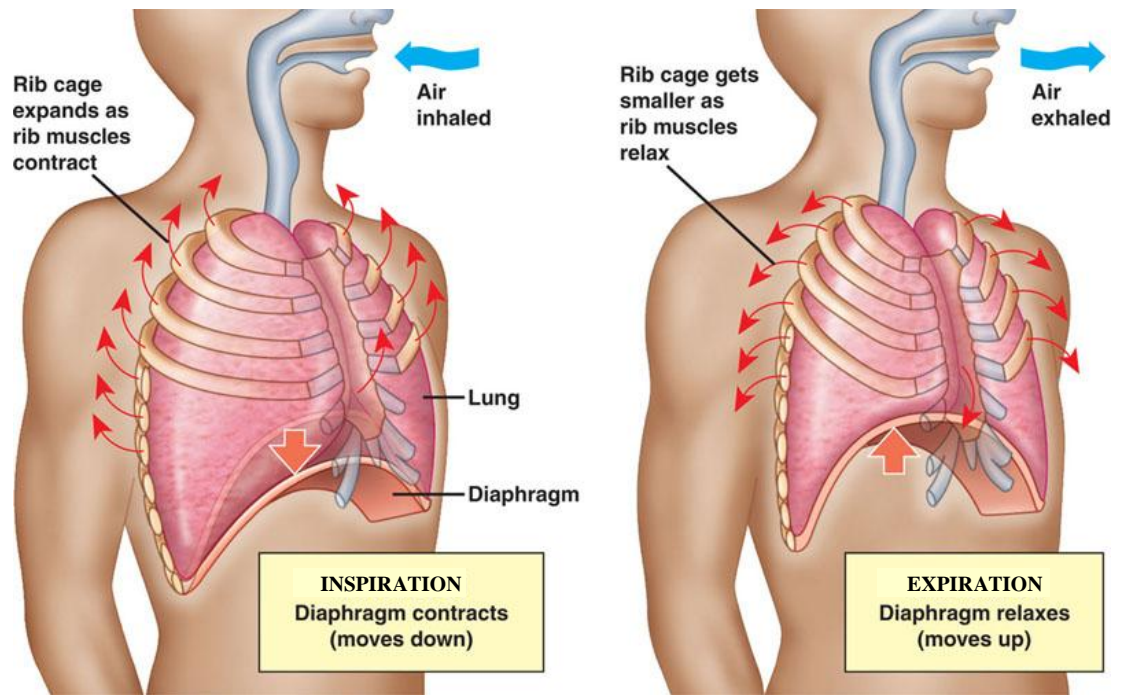


Figure 1.6 Schematic showing the inhalation and exhalation process (taken from <http://blm1128.blogspot.co.uk/2011/04/objective-49-contrast-inspiration-and.html>)

1.4.2 BARRIERS TO PULMONARY DELIVERY

The lung has evolved both physical and immunological barriers that can hinder effective transduction of epithelial cells. Pulmonary disease is often due to the failure of the lungs' defence mechanisms which can be divided into physical, physiological, humoral and cellular mechanisms. Once a particle is deposited onto the lining of the respiratory tract, it comes into contact with a thick gelatinous mucus water impermeable layer located within the airways or the surfactant-lining fluid layer in the alveolar region. Airway mucus is about 5 μ m in depth and consists of electrolytes, proteins, glycoproteins (e.g. mucins, high-molecular-weight glycosylated protein) and cell debris (varies on environmental and disease states). The surfactant lining layer, also referred to as the airway surface liquid (ASL) is 10-20nm in thickness and covers the alveolar surface. It consists of phospholipids, specific proteins and mucins. These components are likely to affect the

transfer of nucleic acids. In order to maintain lung function, facilitate gaseous exchange and prevent alveoli collapse phospholipids (in the ASL) form liquid crystals but not micelles in aqueous media therefore reducing the lung air interface surface tension (Yang et al., 2008).

The negative charge of the surfactant lining constituents are capable of directly binding to positively charged complexes, altering their size and switching their overall charge density (to negative) affecting their diffusion to the target cells or cellular uptake. DNA-based therapeutic agents may be displaced and delivery efficiency lowered. Such effects have been seen by cationic liposome-mediated DNA transfection (Ernst et al., 1999).

Defence mechanisms, include (but are not limited to) a mucocilliary escalator transport, phagocytosis by macrophages and pinocytosis are involved in the removal of deposited particles and the maintenance of the lung mucosal surface. Particles consisting of slowly dissolving or insoluble materials in the airway mucus can be partially moved by the action of ciliated epithelial cells pushing the mucus either to the gastro-intestinal tract or excreted through the mouth. Deposited particles may also be removed by coughing within a few days.

Pulmonary alveolar macrophages are derived from precursors in the bone marrow and migrate to the lungs via the bloodstream. They phagocytise particles, these are then removed by the mucocilliary escalator, lymphatics and the blood stream. Macrophage phagocytosis mainly clears slow dissolving and insoluble particles from the alveoli. The

uptake of deposited particles by alveolar macrophages depends on the particle size and composition of the coating material.

1.4.3 IDEAL PARTICLE CHARACTERISTICS FOR PULMONARY DELIVERY

The aerodynamic diameter d_A , is the diameter of a sphere of unit density which achieves the same velocity in an air stream as a non-spherical particle of arbitrary density. d_A is dependent on the morphology, density and size of the particle. The correct aerodynamic particle size is often expressed as the mass median aerodynamic diameter (MMAD). d_A defines the mechanism of particle deposition of the respiratory system and generally depends on the airflow (particle Reynolds number, Re) as well as particulate properties (geometric, size, morphology and density) (Chow et al., 2007).

There are three principal mechanisms that lead to pulmonary deposition; inertial impaction, gravitational sedimentation and diffusion (Brownian diffusion). Particles with a MMAD of more than $5\mu\text{m}$ are subject to inertial impaction; 1 to $5\mu\text{m}$ are subject to sedimentation by gravitational forces; $0.5\mu\text{m}$ (less or equal to) are subject to diffusion by Brownian motion (Yang et al., 2008). The size, extent and efficacy of particle deposition after inhalation is influenced by several factors such as aerosol properties and physiology during breathing, particle/droplet diameter, density, surface properties or shape and anatomy of the upper and lower airways. Successful deposition into the deep lung requires the particle to be small enough to avoid deposition by inertial impaction at the upper airways but large enough to avoid exhalation. The optimal particle size for achieving

delivery deep into an alveolar region has been established to be d_A between 1 to $3\mu\text{m}$ (Yang et al., 2008).

1.4.4 PULMONARY DELIVERY OF NUCLEIC ACIDS

Pulmonary delivery offers a non-invasive route for the administration of DNA-based therapeutics. The lungs have a large surface area and a good blood supply therefore pulmonary administration of small hydrophobic molecules results in rapid local and systemic effects. Therefore this route can be used to treat local conditions like chronic obstructive pulmonary disease, asthma and upper respiratory tract infections.

Particle engineering for DNA-based therapeutics for pulmonary delivery requires particles to be within the respirable range (1 to $5\mu\text{m}$). Formulation strategies are employed to reduce the particle size to within the respirable range whilst preventing loss of biological activity. Popular techniques include spray drying, spray freeze drying and freeze drying which have been discussed in *Section 1.9.7*. Currently there are three types of inhalation devices for pulmonary delivery they are nebulizers, metered dose inhalers (MDIs) and dry powder inhalers (DPIs).

Jet nebulisers uses compressed gases to produce aerosol droplets in the respirable size range. Ultrasonic nebulisers use ultrasonic energy to convert liquids into a spray, they have been less studied and characterised than jet nebulisers. Nebulisers deliver large volumes of drug solutions and suspensions for inhalation. They are more commonly used for drugs that cannot be easily formulated into a MDI or DPI. The temperature of the drug

solution in the ultrasonic nebulisers can rise up to about 20°C above ambient temperature during use. The heat generated can cause degradation of heat liable materials like nucleic acids.

Pressurised MDIs have the active substance dissolved or suspended in a propellant system, which contains at least one liquefied gas in a pressurised container that is sealed with a metering valve. The activation of the valve delivers a metered dose of the medicament in the form of an aerosol spray, which is directed by a suitable adaptor or actuator for administration via oral or nasal inhalation. MDIs are advantageous due to their portability, low cost and disposability. Up to 200 doses are stored in one canister and drug delivery is reproducible. However, instability of biological molecules is a problem.

DPIs are favoured for pulmonary delivery of nucleic acids and other delicate molecules because of instability issues with MDIs and nebulisers. DPIs are portable, simple formulation, easy to operate, propellant free and inexpensive. DPIs impart energy into the powder formulation to overcome gravitation and electrostatic forces. This process also disrupts aggregates that may form as a result of inter-particulate forces. This ensures that the particles that are inhaled and deposited are at their primary particle size (Son and McConville, 2008).

Delivery of DNA-based therapeutic molecules relevant to lung diseases has been attempted through multiple routes and using various carriers in animal models. An influenza pandemic occurs annually due to the development of a new strain of the influenza virus that the population does not have immunity to. The vaccine is formulated yearly because

viral antigens (HA and NA) change therefore previous year's vaccines are ineffective against new strains. It can take up to 6 months to produce vaccines and early on in the formulation processes a calculation is made as to which strain to include. The ability of synthetic siRNAs to inhibit influenza virus production in cell culture has been extensively reviewed (Thomas et al., 2007). Experiments conducted by Ge et al., (2004) using polycation mediated intratracheal delivery of siRNAs specific for genes encoding the nucleocapsid protein and components of the influenza virus in mice, overall saw promising results implying there may be potential for the use of siRNAs as a prophylactic therapeutic agent to inhibit influenza virus production in humans.

Other experiments have looked at formulation strategies and the potential to produce respirable dry powders for stable and efficient non-viral gene delivery to the lung (Seville et al., 2002; Li et al., 2005; Colonna et al., 2008; Kuo, 2003).

For example, Seville et al., (2002) produced respirable lipid-peptide-DNA complexes (LPD) (lipid used was DOTAP, cationic peptide was protamine) by either freeze drying or spray drying. Transfection studies conducted on A549 (human lung epithelial carcinoma) cells saw that formulated DNA was able to mediate β -Galactosidase reporter gene expression interestingly with spray-dried formulations proving superior even when compared to freshly prepared LPD complexes.

1.4.5 OTHER ROUTES OF DELIVERY OF NUCLEIC ACIDS

1.4.5.1 Ocular Delivery

The negative charge of nucleic acids make them strong potential candidates for ocular delivery using iontophoresis. Iontophoresis is a non-invasive technique commonly used to transfer ionized drugs using an electric field into the skin and more recently the eye (Halhal et al., 2004). Using this technique delivery of antisense oligonucleotides have been explored with great success (Fattal and Bochot, 2006).

1.4.5.2 Topical Delivery

The transdermal entry of DNA has been studied liposomes (Li et al., 2010) and electrical techniques (e.g. electroporation) mechanical transfection (e.g. microneedles (DeMuth et al., 2010)). The size of sweat pores and the follicular openings of the skin are 30 μ m to 100 μ m in size therefore it is reasonable to assume that DNA or small oligonucleotides such as siRNA would be able to penetrate through the skin. Wang et al., (2008) developed a topical siRNA delivery system based on chitosan nanoparticles. The target was a natriuretic peptide receptor and was chosen because it was recently found that this receptor when silenced prevented lung inflammation in mouse models for allergic asthma. Transdermal delivery of siRNA significantly decreased lung inflammation (mice model) confirmed by evidence produced from lung section staining, eosinophil counting and quantification of inflammatory markers (Wang et al., 2008).

1.5 ANHYDROBIOSIS

Anhydrobiosis (a form of cryptobiosis) involves the partial or total desiccation of living organisms resulting in a reduction in metabolism however, upon exposure to moisture vital functions are restored (Crowe et al., 1992). Many organisms like plants, fungi or insects are able to thrive in essentially complete dehydration and may exist without water for decades and sometimes centuries these organisms are called anhydrobiotic organisms. Surprisingly, they are able to survive even when greater than 99% of their body water is removed resulting in dry but viable tissues containing at least 0.1% water content (Crowe et al., 1998). Their metabolic processes are reduced as concentration of water within the cells decreases. Upon rehydration full functionality is resorted along with metabolic processes. It has been found that anhydrobiotic organisms usually contain high concentrations of sugars in particular trehalose. An example of such an organism is the nematode *Aphelenchus avenae*. When this organism was slowly dehydration, 20% of its dry weight was converted to trehalose. It appears as though survival of anhydrobiotic molecules in the absence of water is correlated to the synthesis of sugars like trehalose or sucrose. There are two main hypothesis proposed for this effect they are i) the water replacement hypothesis and ii) the vitrification hypothesis.

The Water Replacement Hypothesis

The water replacement hypothesis is a thermodynamically based theory which suggests that protective sugars interact with anhydrobiotic organisms through hydrogen bonding in a similar manner to replaced water (removed by drying). The sugar in an amorphous or anhydrate form is thought to stabilise biological molecules by absorbing surrounding

water, crystallising and then phase separating therefore acting as a desiccant (Moran and Buckton, 2007).

Vitrification of Carbohydrates

According to this hypothesis, vitrified sugars form an amorphous matrix surrounding the anhydrobiotic organisms preventing any conformational distortion (i.e. degradation). The higher the glass transition of the protecting sugar, the greater the physical stability of the system (Simperler et al., 2006). Crowe et al., 1998 concluded that vitrification alone was insufficient to achieve complete stabilization and maintenance of a dry cell in an anhydrobiotic organism. Direct and specific interactions were also required. Therefore vitrification and was not mutually exclusive with the water replacement hypothesis.

1.6 MAILLARD REACTIONS

Maillard reaction (also known as the amino-carbonyl cascade) is a cascade initiated by Schiff base formation which leads to cross-linking and fragmentation of a protein and browning via the generation of melanoid pigments (Kett, 2000). Its reaction is well known in food science to cause not only browning of colour and flavour change as well as a loss of nutritional or functional value (Kawai et al., 2004). The non-reducing character of these sugars like trehalose is crucial in the stabilization of a biological molecule to avoid Maillard reactions which can lead to detrimental effects on the biological molecule (Schebor et al., 2010).

1.7 DELIQUESCENT

The presence of atmospheric water whether it is behaving as a reactant, a product, a reaction medium or enhancing the molecular mobility at disordered sites can cause undesirable changes to the physical and chemical properties of a pharmaceutical material (e.g. sugars). These effects can include phase transformations or chemical degradation. Deliquescence is a property exhibited by a variety of different compounds including some inorganic salts, sugars and drugs (Crowe, 2002). When a material undergoes deliquescence, phase transformation occurs whereby the material absorbs water vapour from the atmosphere leading to dissolution of the solid and presence of bulk water in the system at a partial vapour pressures less than 1 (Hernandez Garcia, 2011).

The relative humidity (RH%) at which deliquescence occurs is a characteristic of the material and has been found to be the same as the RH% produced by a saturated aqueous solution. At elevated water vapour pressures (generally >65% RH) crystalline sugars and sugar derivatives may experience deliquescence. Where sugar molecules at the material surface start to dissolve in adsorbed water vapour and form a saturated sugar solution (Hancock and Shamblin, 1998). The RH% at which deliquescence first occurs is commonly referred to as the 'critical relative humidity' (RH_0) (Hancock and Shamblin, 1998). RH_0 is an important parameter for pharmaceutical systems as above RH_0 formation of a liquid phase can occur leading to accelerated chemical reactions or physical changes. *Table 1.3* provides examples of RH_0 for common sugars.

Table 1.3 Critical relative humidities (RH_0) for crystalline sucrose, raffinose and trehalose (taken from Hancock and Shamblin, (1998))

MATERIAL	CRITICAL RELATIVE HUMIDITIES (RH_0)
Sucrose	84% at 25 °C
Raffinose	~100% at 23 °C
Trehalose	~98% at 23 °C
Lactose	~99% at 24°C
Glucose	81% at 25°C

1.8 SOLID STATE

The three states of matter are solids, liquids and gases. Molecular arrangement between these states differs greatly. Materials in the solid state can be crystalline, amorphous or a combination of both. *Figure 1.7* is a schematic representation of the molecular arrangement of a crystalline solid, amorphous solid and gas. Molecules in the crystalline state are located in a fixed position, closely bound together by different inter-molecular forces (such as van der Waals forces and hydrogen bonding). They exhibit long-range translational, rotational and conformational order. This is in contrast to the molecular arrangement within an amorphous solid (also termed glass) which are located in a random order (not to the same extent as molecules in the gaseous phase) and feature short-range translational, rotational and conformational order. Molecules in the gaseous phase are random and do not exhibit any order.

energy levels of a solution. The average time scale of molecular motions within a glass is usually in excess of 100s and viscosity is typically greater than 10^{12} Pa·s (Angell, 1995).

Amorphous materials are thermodynamically unstable as a result of their high energy state making them more prone to recrystallise to a lower energy crystalline state over time. From a pharmaceutical perspective, due to its higher internal energy, the amorphous state would be expected to possess enhanced thermodynamic properties relative to the crystalline state (such as solubility, vapour pressure), greater molecular mobility and greater chemical reactivity (potential for spontaneous crystallisation above and below T_g) (Hancock and Zograf, 1996).

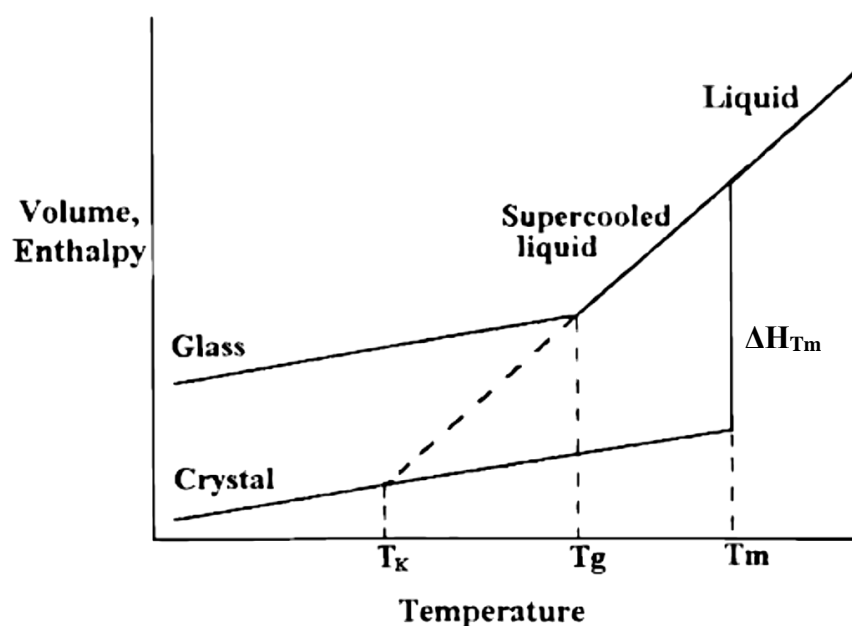


Figure 1.8 Schematic depiction of the variation of enthalpy (or volume) with temperature (taken from Hancock and Zograf (1996))

T_g is defined as the temperature at which the extrapolated glass and liquid equilibrium lines cross (*Figure 1.8*) and is accurately measured on cooling from the equilibrium state. *Figure 1.8* is a schematic plot of the enthalpy or specific volume of a solid material as a function of its temperature. *Figure 1.8* also depicts the relationship between the enthalpy and temperature for a liquid, supercooled liquid, glass and crystalline phases (taken from Hancock and Zografi (1996)). As a viscous liquid is cooled below its T_m it is described as being “supercooled”. The discontinuity observed in the enthalpy at T_m illustrates the first-order phase transition to the liquid state. Cooling of the melt results in enthalpy values which may follow the equilibrium line for the liquid beyond the temperature into a “supercooled liquid” region. At T_g , a change in the slope is observed as the properties of the glass deviate from the properties of the equilibrium supercooled liquid. T_g appears to be a thermodynamic requirement for a supercooled liquid as without T_g , the glass will reach a lower enthalpy than the crystalline state at a critical temperature resulting in a negative enthalpy. The critical temperature is known as the Kauzmann temperature (T_K). Walter Kauzmann (1948) conducted a series of experiments exploring the properties of supercooled liquids at low temperatures below their T_g . Experimental entropy versus temperature curves were extrapolated to below T_g and it was discovered that the extrapolated entropy of some supercooled liquids appeared to fall below that of a crystal as shown in *Figure 1.8*. This phenomenon was in conflict with Newton’s third law of thermodynamics which states “*The entropy of a perfect crystal at absolute zero is exactly equal to zero*”. As the crystalline state is the most ordered system (in terms of molecular arrangement) it is expected to have the lowest entropy. T_K (also termed the calorimetric ideal glass transition temperature, T_{oc}) represents the lower limit to the T_g where the configuration entropy of the system reaches zero, this is known as the Kauzmann paradox. In practice, experimental T_g occurs 20K or more above T_K (Craig et al., 1999).

The glass transition differs from a change in state as T_g values are dependent on the cooling rate of the system with slower rates resulting in lower transition values and denser glasses. *Figure 1.9* is a schematic illustration of the enthalpy or specific volume of a solid material as a function of its temperature (as in *Figure 1.8*) showing the effect that cooling rate has on T_g and the more thermodynamically favorable path taken on slow cooling that allows for re-crystallization to occur.

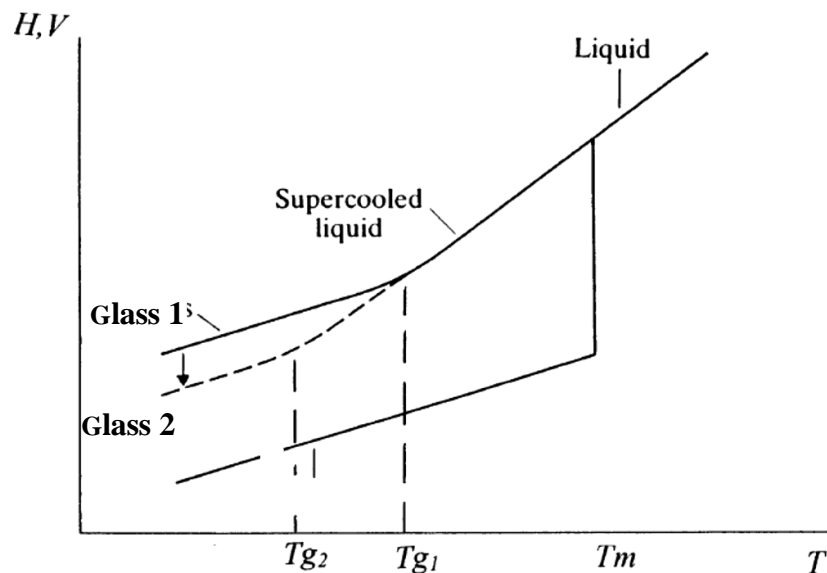


Figure 1.9 Schematic illustration of the enthalpy or the free volume as a function of temperature showing the effect of cooling on the T_g where Glass 1 has been cooled at a faster rate than Glass 2 (taken from Ediger et al., 1996)

T_{g1} shows the T_g of a rapidly cooled glass (*Glass 1*) which has been cooled at a faster rate than *Glass 2* and has deviated from the equilibrium at a higher temperature. *Glass 2* has been cooled at a slow rate and has a lower T_g value as it deviated from the equilibrium of the supercooled liquid at a lower temperature. The cooling process is too fast in both glasses for crystallization to occur, this could be due to a rapid cooling rate or crystallization not favored because of sample molecular size or shape.

The basic physico-chemical parameter used to characterize amorphous materials is the T_g . It can be used to predict the physical and chemical stability, as well as the rheological properties (temperature dependent) of an amorphous sample. T_g is characterised by a step change in the heat capacity (C_p) or thermal expansivity (α) and is often determined using calorimetric techniques like differential scanning calorimetry (DSC) by measuring the heat flow or heat capacity as a function of time. Using this technique, T_g can be measured as the point in the transition region where the step change in the heat capacity, C_p (a derivative of enthalpy) or thermal expansivity attains half the value of the total step change (*Figure 1.10*). The T_g can also be determined by measurement of the volume as a function of temperature using dilatometry techniques. T_g is evaluated as shown in *Figure 1.11*.

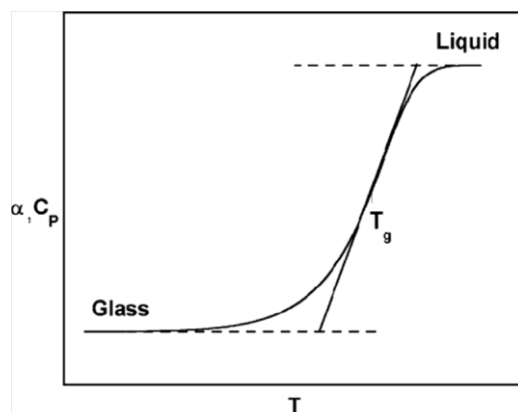


Figure 1.10 Schematic of the change in thermal expansivity (α) or the heat capacity (C_p) upon cooling from the equilibrium liquid state to the glassy state (taken from Badrinarayanan et al.,(2007))

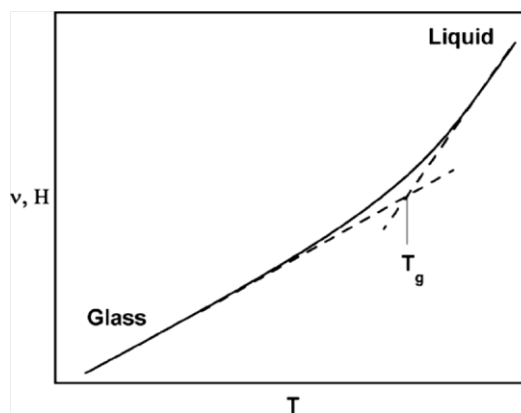


Figure 1.11 Schematic of the evolution of specific volume (v) or enthalpy (H) with temperature upon cooling from the equilibrium liquid state to the glassy state

1.9.1 GLASS TRANSITION THEORIES

The complex nature of a glass and its T_g is still poorly understood and several theories exist that can be used to describe the physical changes that occur during the transition. The three main theories are the free volume theory, entropy theories and thermodynamic phase transition theory.

1.9.1.1 Free volume theories

Fox and Flory (1950) first proposed the free volume theory for understanding transport properties of a liquid i.e. viscosity. It was speculated that the transport properties of a liquid were determined by its free volume defined as the unoccupied space available within a liquid which is free to be filled by molecules. T_g therefore occurs due to a gradual reduction in the occupied volume of a material.

The Doolittle equation (1951) depicted in *Eq.1.1* relates the viscosity of a liquid to its volume and free volume temperature above T_g . It predicts that an increase in pressure will result in a reduced T_g and at a temperature below T_g the free volume will be equal to zero.

$$\eta = \eta_o \exp \frac{c(v-v_f)}{v_f} \quad \text{Eq. 1.1}$$

where η is the viscosity, η_o and C are adjustable parameters. V is the volume and V_f is the free volume.

Cohen and Turnbull (1959) later further developed the free volume theory by defining a relation between the diffusion constant, D in a liquid of hard spheres and the free volume,

V_f . This was based on the concept that statistical redistribution of the free volume occasionally opens up voids large enough for diffusive displacement. The relationship is depicted in *Equation 1.2*. The equation is of the same form as the Doolittle equation (*Eq.1.1*)

$$D = A \exp \left[-\frac{\gamma v^*}{v_f} \right] \quad \text{Eq. 1.2}$$

where v^* is the minimum required volume of the void and A and γ are constants. This theory assumes that the total volume of a liquid is made up of two parts with one part occupied by a series of hard spheres or molecules. The second portion of the liquid is made up of unoccupied space where spheres are free to move randomly by diffusion (Cohen and Turnbull, 1959). Therefore, as the temperature decreases the occupied and free volume within a liquid will also decrease.

Assumptions based on this model are that the free volume within a liquid is dependent on its geometrical arrangements, molecular size and intermolecular interactions. It also assumes that thermal expansion will remain linear even for a small free volume.

1.9.1.2 Thermodynamic phase transition theory

According to the Ehrenfest classification scheme, a phase transition is a second derivative of the free energy and is discontinuous at a critical point. The glass transition is therefore classified as a second-order phase transition according to this classification. At the glass transition a sample demonstrates a continuation of thermodynamic properties which are associated with the first derivatives (of free energy) like the specific volume or enthalpy

however; the sample demonstrates a discontinuity in the second derivative (of free energy) like the specific heat or thermal expansion coefficient. The thermodynamic phase transition theory overall states that latent heat is not associated with the glass transition. However, as the glass transition can be kinetically influenced (i.e. by factors such as the cooling rate) this weakens the concept that the glass transition is a genuine second-order phase transition.

1.9.1.3 Entropy theories

The step change seen at the heat capacity can also be related to the entropy (S) of the system at constant pressure (Eq.1.3)

$$C_p = T \left(\frac{\partial S}{\partial T} \right)_p \quad \text{Eq.1.3}$$

The glass transition occurs because of excess entropy within the system. As discussed in *Section 1.9*, experiments conducted by Kauzmann (1948) found that the extrapolated entropy of some supercooled liquids fell below that of a crystal (*Figure 1.8*) which was in conflict with the third law of thermodynamics (Kauzmann paradox). These results showed that the glass transition was a thermodynamic requirement in preventing the volume (or enthalpy) of the supercooled liquid from reaching Kauzmann temperature, T_k . Gibbs and Di Marzio (1958) developed an entropy model to avoid the Kauzmann paradox. Experiments were conducted with a focus on the bonding energy of straight chained polymers. Their model assumed that a true second-order thermodynamic phase transition with decreasing entropy existed below the glass transition temperature. It was then possible to relate the relaxation time of an amorphous system to the configurational

entropy where the larger the entropy the faster the material will relax. Unfortunately this model was limited to polymers.

1.9.2 GLASS FRAGILITY

The fragility of a liquid is a measure of the temperature dependence of the viscosity (or molecular motions) approaching T_g . It can also be defined as the sensitivity of a liquid structure to temperature fluctuations describing the kinetic behaviour of an undercooled liquid. This property has been linked to its glass forming ability where glass formers are classified as being either “strong” or “fragile”. Strong glass formers are typically inorganic, they possess high viscosities at T_m and are resistant to structural changes which is shown by their characteristic small heat capacity changes at T_g (Angell 1995). Viscosity changes above T_g is described using *Equation 1.4* which is based on the Arrhenius equation which shows that strong glass formers show linear dependence of their viscosity on temperature (*Figure 1.12*).

$$\frac{-d\eta}{dt} = k \exp \frac{-E_A}{RT}$$

Eq.1.4

where η is the viscosity, $\frac{-d\eta}{dt}$ is the rate of decreasing viscosity, k is a rate constant, $-E_A$ is the activation energy for the deterioration process and R is the gas constant ($8.314 \text{ JK}^{-1} \text{ mol}^{-1}$).

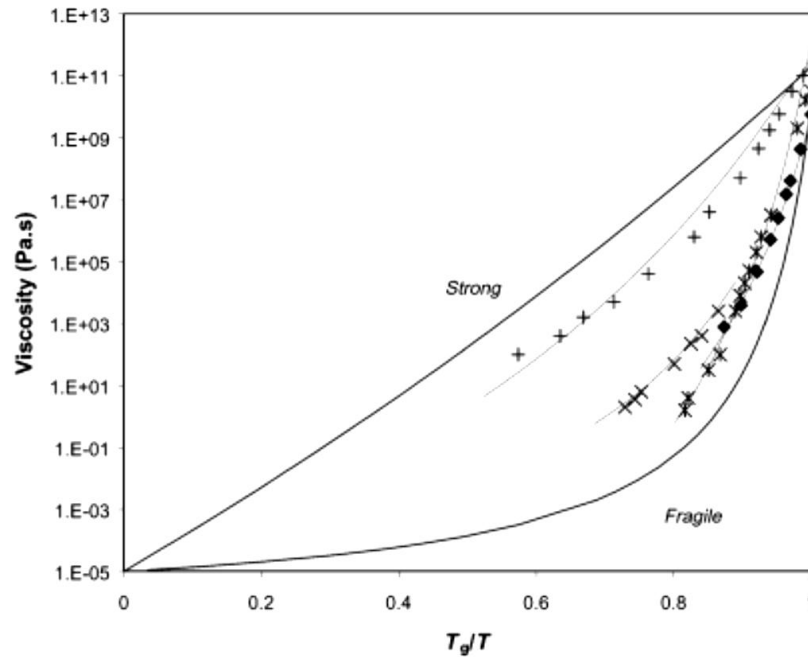


Figure 1.12 A plot of viscosity versus temperature scaled to T_g for Boron Trioxide (+); sorbitol (x), *o*-terphenyl (*) and IMC (◆) (taken from Crowley and Zografis 2001)

Figure 1.12 shows that strong liquids exhibit Arrhenius like behaviours whilst fragile liquids deviate from this and exhibit non-Arrhenius like behaviour. The Vogel-Tamman-Fulcher (VTF) equation (Eq. 1.5) in its modified form describes the non-Arrhenius behaviour of fragile liquids. It describes the relationship between η and temperature (T) in the supercooled region.

$$\eta(T) = \eta_0 \exp\left(\frac{DT_0}{T-T_0}\right) \quad \text{Eq.1.5}$$

where $\eta(T)$ is the temperature dependence of viscosity above the glass transition temperature, T is the temperature and η_0 , D and T_0 constants. D is a variable termed the strength parameter; a large D value (i.e. greater than 30) represents a strong liquid whilst a

low value (i.e. less than 10) represents fragile behaviour. Changes in molecular dynamics can be described using the structural relaxation time.

Structural relaxation (also referred to as aging or annealing) is a process where an amorphous solid is held below its T_g , the material relaxes towards the metastable supercooled liquid state, therefore decreasing in energy, entropy and free volume (Ediger et al., 1996). This process occurs because the amorphous solid is in a non-equilibrium state with significant molecular mobility. Structural relaxation is an indicator of molecular mobility and if it occurs exponentially at a characteristic time (τ) can be defined and used to measure the molecular mobility within a material. Both η and τ have comparable relationships with temperature and so the VTF equation can also be presented as in *Equation 1.6* (using a pre-exponential constant τ_0)

$$\tau = \tau_0 \exp\left(\frac{DT_0}{T-T_0}\right) \quad \text{Eq.1.6}$$

where τ is the mean molecular relaxation time (or viscosity), T_0 is the zero mobility temperature, τ_0 is the relaxation time constant for the unrestricted material, and D is a variable termed the strength parameter. Estimations of T_K using free volume calculations have shown to match VTF T_0 with some accuracy (Hodge, 1996). This is not entirely surprising as T_0 represents the temperature at which either η or τ become infinite, a point which can be conceptually related to T_K (Crowley and Zografi, 2001). When T is equal to T_0 (this is usually 50K below T_g), the viscosity goes to infinity (Angell, 1995).

The Adam-Gibbs (1965) theory identifies that the non-Arrhenius behaviour within the supercooled region could be due to the presence of co-operative molecular motions. The

size of these co-operative regions can be defined using the configurational entropy (S_c) by the use of the Adam-Gibbs equation (Eq.1.7).

$$\tau = \tau_0 \exp\left(\frac{C}{TS_c}\right) \quad \text{Eq.1.7}$$

where C is a constant. S_c can be defined as in Equation 1.8.

$$S_c = \int_{T_2}^T \left(\frac{C_p^{conf}}{T}\right) dT \quad \text{Eq.1.8}$$

where C_p^{conf} represents the configurational heat capacity, i.e. the difference in heat capacity (C_p) between liquid and crystalline states, T_2 the temperature at which configurational entropy reaches zero so is taken to represent the Kauzmann temperature

$$(T_2 \equiv T_K) \quad (\text{Kauzmann, 1948}).$$

The fragility parameter (also termed the steepness parameter (Plazek 1991)) m is related to the VTF parameters by Eq.1.9.

$$m = \frac{DT_0/T_g}{(\ln 10) (1-T_0/T_g)^2} \quad \text{Eq.1.9}$$

m can also be determined from the slope of a plot at T_g of $\log \tau$ versus T_g/T and can also be related to the Arrhenius activation energy, ΔH^* (Eq.1.10)

$$m = \left. \frac{d \log_{10}(\tau)}{d \frac{T_g}{T}} \right|_{T=T_g} = \frac{\Delta H^*}{2.303RT_g} \quad \text{Eq.1.10}$$

By replacing ΔH^* with ΔE_{T_g} at a single temperature, an alternative fragility parameter is defined (Eq.1.11).

$$m = \frac{\Delta E_{T_g}}{2.303RT_g} \quad \text{Eq.1.11}$$

where ΔE_{T_g} is the activation enthalpy for structural relaxation at temperatures around the glass transition and R is the gas constant ($8.314 \text{ JK}^{-1}\text{mol}^{-1}$). Strong liquids have m values less than 40 whilst fragile liquids have m values greater than 75. ΔE_{T_g} can be calculated using the glass width or the scanning rate dependency of T_g . Solving *Eq.1.10* requires a minimum value for m (*Eq.1.12*)

$$m_{min} = \log\left(\frac{\tau(T_g)}{\tau_0}\right) = \frac{DT_0/T_g}{(\ln 10)(1-T_0/T_g)} \quad \text{Eq.1.12}$$

τ at T_g is approximately 100s (measured using DSC at 10K/min) (Moynihan 1974) whilst τ_0 represents a timescale of vibrational motions of approximately 10^{-14} s (Crowley and Zografi, 2001). Using these approximations $m_{min}=16$. Combining *Eq.1.10* and *Eq.1.12* an alternative equation for D is provided (*Eq.1.13*).

$$D = \frac{\ln(10) m_{min}^2}{m - m_{min}} \quad \text{Eq.1.13}$$

The Williams-Landel-Ferry (1955) equation (*Eq.1.14*) was developed to illustrate the temperature dependence of the viscosity for fragile materials. It is an alternative to the VTF equation to describe the non-Arrhenius behavior of a fragile liquid

$$\eta(T) = \eta_g \exp\left(\frac{C_1(T-T_g)}{C_2+(T-T_g)}\right) \quad \text{Eq.1.14}$$

where η_g is the mean viscosity at T_g and C_1 is related to the inverse of the free volume in the system at T_g . C_2 is proportional to the ratio of the free volume at T_g over the increase in free volume caused by thermal expansion above T_g . C_1 and C_2 are both constants are related to $DT_0/(T-T_0)$ and $T_g - T_0$ respectively and will be different depending on the system that is being studied.

1.9.3 THE FICTIVE TEMPERATURE

The fictive temperature (T_f) was first introduced by Tool and Eichlin (1931) and is defined as the temperature at the intersection between the equilibrium liquid curve and the linear extrapolation of the glass line. T_f provides the “true” glass transition temperature irrespective of heating rate and can be measured on heating. T_g can be replaced by using T_f as they have similar values (Borde et al., 2002).

1.9.4 PLASTICIZATION

A plasticizer is a molecule that fits in-between molecules of an amorphous solid. This action leads to an increase in molecular mobility, which as a result lowers the T_g of the system. Water acts not only as a plasticizer to amorphous materials, but can also act as a reactant or medium. The complicated effects of water may be responsible for an apparent lack of relationship between chemical stability and molecular mobility (Yoshioka and Aso, 2007). The presence of water in an amorphous formulation can affect the crystallisation tendency of the formulation. In this event water can act as both a plasticizer (reducing the T_g) as well as a building unit for hydrated crystals impacting the stability of the formulation. An anti-plasticizer is a molecule that possesses a high T_g (higher than the T_g of material used). Adding an anti-plasticizer to a formulation not only increases T_g but reduces structural mobility, therefore increasing the stability of the formulation (Shamblin and Zografi, 1998). The presence of low levels of low molecular weighted contaminants or additives (which include water vapour) are predicted and observed to have a plasticizing effect (Hancock and Zografi, 1994) on amorphous pharmaceutical formulations. Whilst, the addition of low levels of high molecular weighted additives results in anti-plasticizing effects on pharmaceutical formulations (Shamblin and Zografi, 1998).

The Fox equation (Fox and Flory, 1950) and the Gordon-Taylor Equation (Gordon and Taylor, 1952) are models commonly used to predict the plasticising effect of water on the T_g . The Fox equation is described in *Equation 1.15*.

$$\frac{1}{T_g} = \frac{W_1}{T_{g1}} + \frac{W_2}{T_{g2}} \quad \text{Eq.1.15}$$

where T_{g1} is the T_g of the first component of the sample and W_1 is the weight fraction of this sample (Fox and Flory, 1950). T_{g2} is the second component of the sample and W_2 is its weight fraction. The accuracy of the Fox equation in predicting T_g for low molecular weight glass formers (e.g. sugars) is debatable due to densities difference in amorphous samples which are not accounted for in the Fox equation (Hancock and Zografi, 1994). The plasticizing effect of water on various amorphous pharmaceutical solids can be accurately described using the Gordon-Taylor equation (*Equation 1.16*) (Hancock and Zografi, 1994; Gordon and Taylor, 1952).

$$T_{gmix} = \frac{W_1 T_{g1} + K W_2 T_{g2}}{W_1 + K W_2} \quad \text{Eq.1.16}$$

$$K = \frac{\rho_1 T_{g1}}{\rho_2 T_{g2}} \quad \text{Eq.1.17}$$

Where ρ is true density kg/m^3 and K (*Equation 1.17*) is a sample specific parameter which can be considered to be the ratio of the free volumes of the two components. *Equation 1.16* is the simplified Gordon-Taylor/Kelley-Bueche equation allowing for the calculation of K from the densities of two components. Water in its amorphous state has a confirmed T_g of 136K (-137°C) (Angell, 2002) it is expected when absorbed by an amorphous sample with a different T_g value, it would produce mixtures with intermediate T_g values (Gordon and Taylor, 1952). For two amorphous materials with the same T_g , the material with the

higher density will be plasticized the most by any given amount of water. Whereas for two materials with the same density, the one with the higher dry T_g should experience the greatest plasticization (Hancock and Zografi, 1994).

1.9.5 CRYSTALLIZATION/NUCLEATION

Metastability by definition requires that there be intermediate states of higher free energy than the metastable state along all possible routes between the metastable and stable states of a thermodynamic system (Kauzmann, 1948). Intermediate states give rise to free energy barriers which prevent the transformation of the metastable state to the stable state. When a glass undergoes crystallisation it must go through intermediate states with higher free energies than the crystal. Spontaneous crystallisation can occur and be interpreted as a result of random accumulation (by thermal fluctuations) of sufficient free energy for the glass to pass over these barriers. Crystallization from an amorphous material involves two steps, crystal nuclei formation followed by crystal/nuclei growth. The rate of spontaneous crystallization is determined by the temperature and the starting material itself. Nucleation must occur before crystallization can occur, therefore preventing, inhibiting or retarding nucleation could result in a more stable amorphous system. *Figure 1.13* is a schematic illustrating the parameters controlling crystallization from the amorphous state. A maximal crystallization rate occurs at a temperature between T_g and T_m which is caused by a lowering of the temperature and an increased viscosity (that accompanies the temperature reduction). The crystallization temperature of an amorphous sample in particular amorphous sugars, is reduced by the presence of absorbed water and can be raised by the incorporation of high T_g additives (Hancock and Shamblin, 1998).

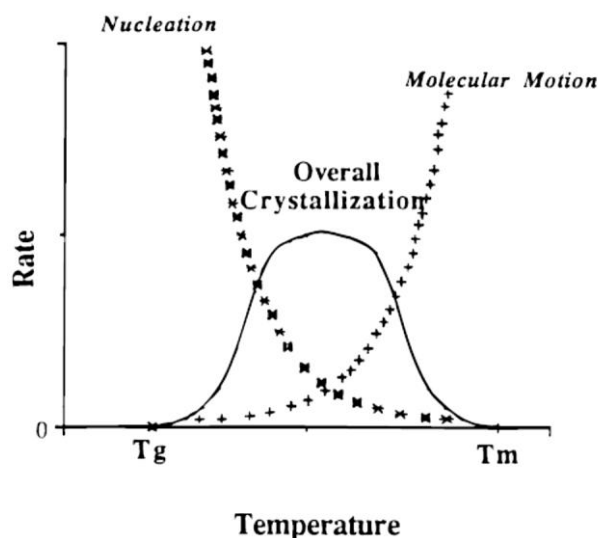


Figure 1.13 Schematic of the parameters controlling crystallization from the amorphous state
(taken from Hancock and Zografi (1996) who adapted from Jolley (1970))

1.9.6 POLYAMOPHORPHISM

“Polyamorphism” is an analogue of crystalline polymorphism meaning that a pure amorphous material can exist in more than one amorphous state. An example of polyamorphism is the behavior of water. Water exists as glassy water referred to as amorphous ice which exists in two different forms, low-density amorphous ice (LDA) (Hallbrucker et al., 1989) and high density amorphous ice (HDA) (Mishima et al., 1985). In general terms, for any glassy materials abrupt changes in density and glass structure with changing pressure resembles behaviour associated with first-order phase transitions and are termed as being "polyamorphic" (Poole et al., 1997). Polyamorphism can also occur in amorphous solids produced by different annealing times or preparative routes.

1.9.7 PHARMACEUTICAL RELEVANCE OF THE AMORPHOUS STATE

Most pharmaceutical solids have an amorphous state either induced as a result of processing or due to their large molecular size (in the case of peptides and proteins). In the

pharmaceutical industry, the amorphous state possesses useful and desirable properties such as higher solubility and dissolution rate and occasionally possessing better compression characteristics compared to crystalline products (for example with lactose (Lerk, 1993)). However, as the amorphous state is a high-energy state it is not as stable as its corresponding crystalline form. It is therefore important that storage of amorphous materials are ideal to suppress its tendency to undergo unwanted physical changes like crystallisation, aggregation of protein or chemical degradation over the product shelf life (Shamblin et al., 1999). An example of an Active Pharmaceutical Ingredient (API) formulated in the amorphous form is the synthetic lipid lowering drug (also known as a “statin”) rosuvastatin (amorphous salt, rosuvastatin calcium), manufactured by AstraZeneca and is marketed under the brand name Crestor[®] in tablet form.

In the preparation of nucleic acid, protein and peptide formulations, the drying stage is very important. Delicate molecules under drying conditions can be detrimental. It has been observed that addition of certain excipients like sugars their amorphous form can have stabilising effects on the formulations though a clear mechanism for the stabilising effects have not been established. They are suspected to involve vitrification and direct interactions between the sugars and delicate molecule via hydrogen bonding. This is further discussed in *Section 1.5*.

Partially or wholly amorphous solids may be generated via a number of methods, so long as the method prevents crystals from forming within the product. Common methods are vapour condensation, supercooling of the melt (quench cooling), mechanical activation of the crystalline mass (milling), precipitation from solution and dehydration from a crystal hydrate. These methods are briefly discussed in the following sections.

1.9.7.1 Vapour condensation

Vapour deposition is a useful method for preparing an amorphous solid from the vapour of a corresponding liquid with poor glass-forming ability. Many liquids with poor glass-forming ability require an ultra-fast cooling technique in order to by-pass undesirable crystallisation. This process can rapidly extract the thermal energy of molecules during production of the amorphous solid in a molecule by molecule fashion and avoid the passage in which crystallisation might take place (Takeda et al 1994).

1.9.7.2 Quench cooling

Quench cooling is a technique used to generate amorphous matter by rapid cooling of the melt and by-passing crystallization. Once all of sample has melted the sample is then rapidly cooled using liquid nitrogen to form a glassy material. Below the melting temperature the generated liquid becomes metastable due to the existence of a thermodynamic barrier which controls nucleation of supercritical clusters of the stable crystalline phase (Willart and Descamps, 2008). The cooling process is too fast for crystallisation to occur because of the rapid rate of cooling.

1.9.7.3 Milling

Phase transformation of crystalline materials can occur during sample processing. Milling is generally the last processing step in the production of bulk drug substance to reduce particle size. Due to high levels of mechanical energy used this can cause a reduction in crystallinity due to the creation of lattice defects occurring at the crystal surface. Lattice

defects would contribute to lattice disorder therefore inducing phase transformation of the crystalline material. Thermodynamically, as a result of high levels of mechanical energy this can also generate heat causing a local heating effect which is followed by rapid quenching.

1.9.7.4 Precipitation from solution

Freeze drying also known as lyophilisation is commonly used to generate amorphous samples. A typical freeze-drying process involves three stages, freezing, primary drying and secondary drying. The first stage (freezing stage) is a separation of the solvent (water) from the solute results in the formation of ice. The solute phase becomes concentrated and is termed the “freeze concentrate”. The second stage (primary drying) starts when the chamber pressure decreases (to below the vapour pressure of ice) and the shelf temperature is raised facilitating sublimation of ice. During this stage, ice is transferred from the product to the condenser by sublimation and crystallisation onto cold coils (set at -50°C). Primary drying is the longest stage of the freeze drying process. The final stage is the secondary drying stage. During this stage water is desorbed from the freeze concentrate at low pressure and elevated temperature. Freeze drying in the presence of suitable stabilizing agents and cryopreservatives is a common method for generating dry protein formulations (Johnson, 1997) as well as non-viral gene delivery vectors (Talsma et al., 1997)

Spray drying is a rapid solidification process used to yield amorphous samples and can be used to generate respirable nucleic acid powders (Kuo, 2003). The spray drying process involves four stages i) atomization of the feed solution into a spray ii) spray air contact

(mixing) iii) drying of spray dried droplets at elevated temperatures iv) separation of dried product from the air. Unfortunately with this technique there is a risk of sample degradation (especially biological molecules) during the atomization step which requires high shear rates. This technique is discussed in great detail in *Chapter 2, Section 2.2.1*.

Spray freeze drying involves the atomization of an aqueous drug solution via a two-fluid or an ultrasonic nozzle into a spray chamber filled with a cryogenic liquid (liquid nitrogen) or halocarbon refrigerant such as chlorofluorocarbon or fluorocarbon (Rogers et al., 2001). Spray freeze drying can be performed below (spray-freezing into liquid) or above the surface of the cryogenic liquid, depending on the position of nozzle (Yu et al., 2004). The level of cryogenic liquid will inevitably drop due to evaporation therefore; continuous addition of fresh cryogenic liquid is required. This is particularly important when a lengthy atomization process or a large spray volume is used. On contact with the cryogenic medium, the liquid droplets solidify rapidly (in milliseconds time scale) because of the high heat-transfer rate (Chow et al., 2007). Stirring of cryogenic liquid may be required to prevent possible aggregation of newly formed frozen particles. Particles produced from this process are porous and spherical suitable for inhalation. The main issue with this technique when formulating proteins is the risk of adsorption of the protein at the air-liquid interface during atomization which accounts for loss of activity during spray freeze drying (as seen in spray drying) (Shoyele and Cawthome, 2006).

1.9.7.5 Dehydration of crystalline hydrates

Phase transformations can occur when a crystalline hydrate or solvate is dehydrated resulting in the formation of an amorphous form. This is a feasible and gentle method of

generating an amorphous form of an organic solid. Within a crystal hydrate, water molecules occupy definite positions in the crystal lattice forming hydrogen bond(s) and/or co-ordinate covalent bond(s) with the anhydrate molecules (Khankari and Grant, 1995). Removal of these water molecules would result in structural collapse leading to structural re-organisation either towards a stable or metastable crystalline anhydrous form or towards an amorphous state.

1.10 THE CRYSTALLINE STATE

Molecules in the crystalline state are packed in a defined order and exhibit long range molecular order. A crystalline solid can be characterised by its melting temperature (T_m) and Specific Heat of Fusion (ΔH_{fus}). At T_m , the crystal lattice is disrupted when the molecules within the lattice have gained sufficient energy from heating to overcome the attractive forces holding the molecules together. Generally, a low T_m is observed in crystals with weak inter-molecular forces such as van der Waals forces, whilst crystals with stronger intermolecular forces such as extensive hydrogen bonding have high T_m (Aulton M E and Taylor, 2001). Crystals are produced by inducing a change from the liquid to the solid state. Crystallisation is a multi-step process, molecules with structures resembling the mature crystals referred to as “pre-nucleation aggregates” assemble in crystal nuclei. The crystal nuclei then grow into mature crystals. There are several factors affecting the rate and mechanism of crystal formation, these include but are not limited to the solubility, rate of supersaturation, temperature and the reactivity of surfaces towards nucleation (Vippagunta et al., 2001). Crystallisation from the amorphous state has been discussed in detail in *Section 1.3.4.2*.

Pharmaceutical solids exist in different physical forms; the two most common forms are polymorphs and solvates (also known as pseudomorphs). Polymorphism can be characterised as the ability of a crystal (or a drug) to exist as two or more crystalline phases possessing different molecular arrangements and conformations within the crystal lattice. Polymorphs and crystal hydrates differ in crystal packing, molecular arrangement, lattice energy and entropy. They also have different physical properties such as density, T_m , ΔH_{fus} , and other thermodynamic and kinetic properties.

1.10.1 POLYMORPHISM

A polymorph is a solid crystalline phase of a given compound resulting from the possibility of at least two different molecular arrangements of that compound in the solid state (Haleblija.J and McCrone, 1969). Pharmaceutical polymorphs of the same chemical compound differ in their internal structure and have different chemical and physical properties (i.e. packing, thermodynamic, spectroscopic, kinetic and mechanical properties). Such properties have a direct impact on drug processability and product performance (Raw et al., 2004) and affect drug stability, dissolution and bioavailability. Polymorphs are classified as being either enantiotropes or monotropes. An enantiotropic system allows for a reversible transformation between polymorphs at a definite transition temperature below its T_m . In a monotropic system a reversible transition is not observed between the polymorphs below T_m (Vippagunta et al., 2001). Unexpected appearance or disappearance of a polymorphic form may result in serious pharmaceutically relevant consequences as in the case of ritonavir. Ritonavir is a protease inhibitor and was first marketed for the treatment of Acquired Immunodeficiency Syndrome (AIDS) in 1996. Only one crystal

form of ritonavir was identified during its development with no apparent stability problems. In 1998, several batches of capsules containing ritonavir failed dissolution testing. Further examination identified a new polymorph of ritonavir with reduced solubility compared to the parent crystal form. This was an example of conformational polymorphism which can occur when different conformational isomers of a compound crystallise as distinct polymorphs. As a result of this ritonavir had to be reformulated as the sudden appearance of this new less soluble form (which was also very difficult to crystallise) made the initial formulation un-manufacturable. This phenomenon is further discussed in great detail elsewhere (Bauer et al., 2001).

1.10.2 CRYSTAL HYDRATES

A pseudomorph is a crystalline solid that contains solvent molecules within its crystal structure. Crystal hydrates are formed when water is the solvent of crystallisation. Water molecules within crystal hydrates occupy definite positions within the crystal lattice usually by forming hydrogen bonds or co-ordinate covalent bonds with the anhydrate molecule. The solvent molecules can be located in either stoichiometric or non-stoichiometric proportions which results in unique differences in the physical and pharmaceutical properties. Hydrates have different physical properties to the anhydrate due to the incorporation of water molecules into the crystal lattice of the anhydrate which produces a new unit cell. At the negatively charged region, water molecules interact with neighbouring molecules via covalent (dative) bonding or acts as a hydrogen bond acceptor. At the positively charged region, the water molecule interacts with its neighbouring molecule by a donated hydrogen bond. Therefore neighbouring molecules within a crystal

hydrate include electron acceptor groups (or proton donors) and electron donor groups (or proton acceptors) (Khankari and Grant, 1995).

At least two main types of hydrates are said to exist, stoichiometric hydrate and non-stoichiometric hydrates. Stoichiometric hydrates have well defined water contents and a different crystal structure to the anhydrate or other hydrates. Whilst non-stoichiometric hydrates have a continuously variable composition within a certain range, without any significant change in the crystal structure except when required to accommodate additional water molecules. It is also common for a non-stoichiometric hydrate to lose its crystallinity when the last water molecule is lost. Mineral hydrates differ from organic hydrates by the nature and intensity of water-substrate interaction. This is because water in mineral hydrates is mainly linked by chemical sorption as oppose to hydrogen bonding in organic hydrates (Authelin, 2005).

1.10.2.1 *The Gibbs' Phase rule*

A system is said to be in thermodynamic equilibrium when it is in thermal, mechanical, and chemical equilibrium. For a system in equilibrium, the phase rule relates the number of components (substances), variables (temperature, pressure) and phases to the degree of freedom or variance F . *Equation 1.21* describes the Gibb's Phase rule.

$$F = C + N - \phi \qquad \text{Eq.1.18}$$

Where F is the degrees of freedom, i.e. the number of independent variables used to establish the state of the system; C the number of independent components, i.e. the number of components minus the number of stoichiometric relationships; ϕ the number of phases

and N is the number of non-compositional variables i.e. $N=2$ (pressure and temperature).

The Gibbs' Phase rule can be used to correlate the stoichiometric and non-stoichiometric behavior with variance of the hydrate system (Authelin, 2005).

1.10.3 STRUCTURE ASPECTS

Pharmaceutical hydrates are classified (from a structural viewpoint) into three categories.

- i. Class I are the isolated site hydrates, where water molecules are located at well-defined and isolated crystallographic sites.
- ii. Class II are channel hydrates or planar hydrates where water molecules are included in the crystal next to each other, forming either channels or planar networks.
- iii. Class III are ion-associated hydrates.

Class I hydrates are generally stoichiometric, whilst Class II are generally non-stoichiometric however can be sub-classified into two sub-categories. One category are non-stoichiometric hydrates that are able to take up additional moisture when exposed to high humidities. The crystal lattice can expand or contract as the hydration or dehydration process effects changes in the dimension of unit cell. The second sub-category consist of channel hydrates where water is localized in a two dimensional order. Class III hydrates can be stoichiometric or non-stoichiometric and involve the bonding of metal ions with water.

Phase transformation of hydrates occurs due to hydration, dehydration and solvation (or dissolution). These changes occur in response to changes in environmental conditions. Crystal hydrates convert to an amorphous phase or anhydrate when dehydrated or can convert from a lower to a higher state of hydration producing forms with lower solubility. It is important to note, the dehydration kinetics of a hydrate system are dependent to an extent on its class as well as particle size and morphology.

1.11 RESEARCH OBJECTIVES

The overall aim of the research detailed in this thesis was to design and analyze sugar-based (trehalose, raffinose and sucrose) carrier systems for the protection of nucleic acids. The work detailed in this thesis is comprised of three main areas.

The first area focused on investigating the inter-conversion properties of trehalose dihydrate with a view to gain further understanding of its bio-protective properties. Within this area, the first objective was address the influence of inter-batch variation on the thermal response of trehalose dihydrate by performing a series of thermal, spectroscopic and X-ray diffraction techniques on α,α -trehalose dihydrate batches obtained from two different manufacturers, Sigma-Aldrich and Acros Organics. This work described in *Chapter 3, Section 3.2* highlighted the need for standardised forms of α,α -trehalose dihydrate to, in effect “erase” processing history of manufactured α,α -trehalose dihydrate. The second objective (based on results from *Chapter 3, Section 3.2*) was to generate and characterise two standardised forms of α,α -trehalose dihydrate by performing a series of thermal, spectroscopic and X-ray diffraction techniques. This work described in *Chapter*

3, *Section 3.3*, led to the identification of a polymorphic form of α,α -trehalose dihydrate which was characterised and is described in *Chapter 3, Section 3.3.4.5*

Within the second area of this thesis, the first objective described in *Chapter 4*, was to characterise the physicochemical properties and behaviour of amorphous trehalose, raffinose and sucrose (generated by spray drying) with reference to their crystalline counterparts. The second objective described in *Chapter 5*, was to investigate the inhibition of non-isothermal crystallisation of amorphous sucrose using sugar additives (trehalose and raffinose) and identify quantitative and qualitative relationships connecting T_g and the crystallisation onset temperature to the strength and fragility parameters.

The third area of this thesis was to evaluate the degree of degradation of plasmid DNA spray dried in the presence of amorphous sugars. Within this area (detailed in *Chapter 6*), the first objective was to evaluate the percentage degradation of plasmid DNA spray dried in the presence of trehalose and raffinose. The second objective was to observe the effects of trehalose and raffinose on A549 cells was explored by performing an MTT assay. A549 cells were used as pDNA formulations generated were intended for pulmonary delivery therefore, it was important to ensure the materials used did not cause any cell cytotoxicity. Transfection studies were then performed using A549 cells and HeLa cells. The third objective within this area was to evaluate the percentage degradation of pDNA spray dried in the presence of sucrose, sucrose-raffinose and sucrose-trehalose co-spray dried formulations designed in *Chapter 5*.

CHAPTER TWO
MATERIALS AND METHODS

2.1 MATERIALS

α,α -Trehalose dihydrate (batch number 108K7354, $\geq 99\%$), crystalline sucrose (batch number 058K00541, $\geq 99.5\%$), and raffinose pentahydrate (batch number 039K0016, $\geq 98\%$) were obtained from Sigma-Aldrich and were used without any further purification. As previously discussed in *Chapter 1*, an amorphous phase can be generated using a variety of methods. In this study, amorphous sugars (trehalose, raffinose and sucrose) were generated by spray drying and they along with their crystalline counterparts were analysed using a variety of thermal and analytical techniques. *Section 2.2* details theories behind the techniques used, experimental set up as well as methodologies used. This section provides a background to each sugar and their common characteristics.

2.1.1 SUGARS

Simple carbohydrates (i.e. mono-, di-saccharides and oligosaccharides) are commonly referred to as sugars. These sugars are characteristically sweet and are composed of carbon, hydrogen and oxygen. Sugars are usually the main constituent of a biological system. In such systems, they exist as a mixture of other sugars to protect cells or membranes. Sugar alcohols or polyols (e.g. mannitol and sorbitol) are hydrogenated carbohydrates (usually mono- or disaccharide sugars). Sugars and their derivatives (including mono-, di-, tri-saccharides, polyols, and esters) are common excipients incorporated into pharmaceutical dosage forms. They possess low toxicity, are available in a highly purified state, available at low cost and are reasonably stable under storage and processing conditions comparable to pharmaceutical products (Hancock and Shamblin, 1998). “Generally Recognised As Safe” (GRAS) substances are those that are not subject to pre-market review and approval by The U.S Food and Drug Administration (FDA) as

they are generally recognised and evaluated as safe. Many sugars and other pharmaceutical excipients fall under this characterisation. Lactose, sucrose, trehalose, glucose, mannitol and sorbitol are sugars and polyols commonly used as food ingredients and pharmaceutical excipients. *Table 2.1* details the basic composition, safety category and common uses of these materials.

Table 2.1 Basic composition and safety of common sugars

SUBSTANCE	COMPOSITION	SAFETY	COMMON USES
LACTOSE	Reducing disaccharide consisting of galactose and glucose monosaccharides linked via a glycosidic bond, anhydrous and mono-hydrate	GRAS, FDA approved	Crystal –tableting aid Amorphous – tableting aid, pulmonary delivery carrier
GLUCOSE	Reducing monosaccharide, monohydrate	GRAS	Sweetener
MANNITOL	Non-reducing acyclic/polyol sugar, 3 main polymorphic forms (alpha, beta, delta)	GRAS	Stabiliser, sweetener, tableting aid
SORBITOL	Non-reducing acyclic/polyol sugar, structurally similar to mannitol, 2/3 hydrate	GRAS	Suspending agent, sweetener
SUCROSE	Non reducing disaccharide consisting of glucose and fructose monosaccharides linked via a glycosidic bond, hygroscopic, anhydrous crystal	GRAS	Tablet coating aid (crystal and amorphous), use in food industry
TREHALOSE	Non-reducing disaccharide consisting of two glucose units, linked via a glycosidic bond, dihydrate and several anhydrous polymorphs	GRAS	Cryo-protectant Use in food industry

2.1.1.1 Trehalose

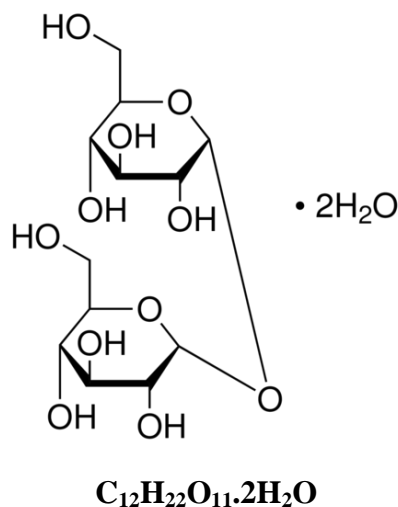


Figure 2.1 α,α -Trehalose dihydrate

α,α -Trehalose dihydrate (chemical name α -D-glucopyranosyl, α -D-glucopyranoside) is a non-reducing disaccharide, consisting of two α,α units of glucopyranose linked together by a α,α -1 \rightarrow 1-glycosidic linkage (Brown et al., 1972). α,β -trehalose (α -D-glucopyranosyl- β -D glucopyranoside) is an isomer of α,α -trehalose where two glucose molecules are linked through α - β 1 \rightarrow 1-glycosidic bond.

The name trehalose is derived from a desert manna 'Trehala manna'. High concentrations of trehalose (as high as 30%) was found in the cocoon of the parasitic beetle Trehala manna. Trehalose is also found at high concentrations (~20%) in anhydrobiotic organisms such as the larvae of *Polypedilum vanderplanki* which breed in temporal rock pools and frequently dry out during the larvae lifetime in Northern Nigeria and Uganda (Furuki et al., 2005; Gil et al., 1996). Upon hydration these organisms rapidly resume active metabolism. On an industrial scale, trehalose is mainly prepared by extraction from the yeast *Saccharomyces cerevisiae*, also known as Brewer's yeast.

Water and trehalose molecules are held together within the crystal structure by a complex hydrogen bond arrangement, where hydroxyl groups of trehalose molecules act as both bond donor and acceptors in the hydrogen bond network (Cesaro et al., 2006). The two water molecules in trehalose dihydrate are said to be isolated from each other within the crystal lattice, occupying adjacent positions along channels (Ahlqvist and Taylor, 2002). The expected water content for trehalose dihydrate is 9.5 % which equates to two moles of water (molecular weight of water, 18.02 g/mol, molecular weight of trehalose dihydrate, 378.33g/mol).

Computer simulations conducted by Sussich et al., (2001) suggested that water molecules were liberated from the trehalose crystal by movement from site to site locations along its channels at such a rate that the structure of the sugar is not able to relax to a more compact form. Therefore, the architecture of trehalose is maintained in several anhydrous forms as inter-molecular forces between the sugar molecules within the lattice can energetically support the structure after the removal of water.

Trehalose is often added to protein formulations because of its special properties as a stabilizer of biological molecules (biomolecules). These properties are suspected to be because trehalose exists as a stable dihydrate in its crystalline form. Therefore in its amorphous form it is able to act as a “sink”, maintaining a high T_g within the remaining amorphous matrix (in the dried state) by removing the plasticizing water (Aldous et al., 1995). The amorphous matrix formed on dehydration between trehalose and the biomolecule (such as a protein) restricts mobility of the biomolecule, which reduces the rate of chemical degradation and prevents aggregation which may occur in the absence of trehalose (and other stabilizing sugars) (Crowe et al., 1996).

Trehalose exists in multiple crystalline and amorphous forms. Trehalose dihydrate (T_h) is the most common and stable (at room temperature) crystalline form. The dehydration behavior of T_h has been extensively studied and is of particular interest due to its relevance in desiccation tolerance of anhydrobiotic organisms. These studies have yielded information confirming the existence of hydrous and anhydrous polymorphic forms of trehalose. A stable crystalline anhydrous form (T_β) and an unstable crystalline anhydrous form, T_α were first identified by Reisener et al., (1962). T_α is an isomorph desolvate of the stable dihydrate generated by gentle dehydration of the dihydrate. Anhydrous polymorphic forms of trehalose (T_k) (Nagase et al., 2002) and T_ϵ (Furuki et al., 2005) also exist. Finally, a crystalline form (T_γ), generated by cold crystallization of the partially dehydrated dihydrate, has also been identified (Sussich et al., 1998), which is reported to be a “transient” crystalline metastable form of trehalose. These forms are summarized in *Table 2.2*. T_β , T_α , T_k , T_ϵ , T_γ anhydrous and hydrous polymorphs will be briefly discussed below.

T_β , Stable anhydrous form of trehalose

T_β is generated by rapid heating of T_h . It is less hygroscopic than T_h however it is stable at room temperatures and has a reported melting point of 210°C.

T_α , Isomorph desolvate of trehalose dihydrate

T_α is produced as a result of slow dehydration of T_h . It has a reported melting point of 130°C. As mentioned above, T_α is an isomorph desolvate of T_h . The term isomorph desolvate accurately defines a desolvate which retains the crystal structure of its parent crystal (in this case trehalose dihydrate). This indicates that the desolvated structure

retains the three dimensional (3D) order of the original crystal as defined by space group symmetry and lattice parameters (Stephenson et al., 1998). Isomorph desolvates tend to be hygroscopic when re-exposed to elevated humidities.

T_γ, Crystalline metastable form of trehalose

T_γ was first reported by Sussich et al., (1998). It was identified during a DSC experiment where T_h was heated from room temperature at a heating rate 5 to 20°C/min. An exothermic peak was observed after water depletion which was ascribed to the molecular re-arrangement resulting in the formation of a new structural order, T_γ. It was suggested that T_γ contained a mixture of T_h and T_β. It is speculated that this form possible comprises of an anhydrous shell around a dihydrate core on a particulate basis (McGarvey et al., 2003) . This form appears to “melt” at temperatures about its formation (120-130°C) confirming that it is not a stable form. Sussich et al., (1998) proposed and later confirmed (Sussich et al., 1999) the following explanation for the formation of T_γ. “A delicate kinetic balance exists between water leaving the T_h crystal structure and its structural collapse into a disordered state. Unless there is enough time or enough amorphous water still encapsulated to allow the trehalose molecules to become structurally organized the water depletion may produce either an amorphous state or an unstable open cage water-free network.”

T_K, generated from T_h by vacuum heating and heating in hot air

T_K is a hygroscopic anhydrous form of T_h and it was prepared by heating the dihydrate to 100 °C at 4.5°C/min under vacuum, then further heating at 100°C for a further 30 minute under vacuum (Nagase et al., 2002). It is stable at room temperature and does not appear

to transform to other crystalline forms. Thermal analysis of T_K in a sealed pan system saw a characteristic endothermic peak at 127°C. Further studies by Nagase et al., (2008) concluded that T_K was identical to T_α though generated by a different route. Further details of this form are discussed elsewhere (Nagase et al., 2002; Nagase et al., 2008).

T_ϵ , anhydrous form generated by dehydration of T_h

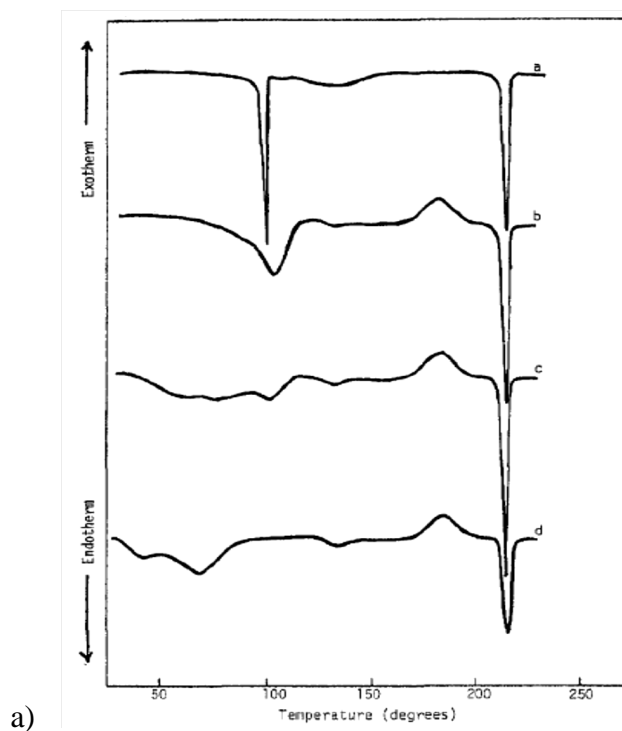
T_ϵ is formed upon complete dehydration of T_h . Upon hydration it transforms to T_β (Furuki et al., 2005). It is a dehydrated state with low crystallinity. Interestingly with this form, humidity conditions have a notable effect on its crystallinity in that crystallinity is higher in a high humid environment.

Table 2.2 Reported crystalline forms of trehalose

FORM	DESCRIPTION
T_h	Stable Dihydrate (Brown et al.,1972)
T_β	Stable Anhydrate (Reisener et al., 1962)
T_α	Isomorph desolvate of T_h (Reisener et al., 1962)
T_γ	Crystalline metastable form (Sussich et al., 1998)
T_K	Generated from T_h by vacuum heating and hot air (Nagase et al., 2002)
T_ϵ	Intermediate anhydrate (Furuki et al., 2005)

Thermal transitions of trehalose dihydrate appear to be dependent on pan type (closed pan (Shafizad.F and Susott, 1973), pin-holed (McGarvey et al., 2003) and open-pan (Dupray et al., 2009)) and particle size (Taylor and York, 1998; Horvat, 2003). Depending on experimental conditions the observed thermal response of trehalose dihydrate can give rise to the observation of an amorphous phase (characterised by the identification of a T_g), one, two or three endotherms and/or a crystallisation exotherm. *Figure 2.2* provides literature

examples taken from Shafizad and Susott (1973) and McGarvey et al., (2003) of differential scanning calorimetry (DSC) traces of α,α -trehalose dihydrate under different conditions. In experiments where three endotherms have been observed, for example in a study by McGarvey et al., (2003) (*Figure 2.2ii*), the first two low temperature endotherms have been attributed to the initial partial dehydration of the dihydrate to the T_γ form (said to be a mixture of the dihydrate and stable anhydrate T_β (Sussich et al., 1998)), then subsequent further dehydration of T_γ resulting in the formation of the stable anhydrate T_β . This then melts at $\sim 210^\circ\text{C}$. The single endotherm seen between 40°C and 160°C ((Macdonald and Johari, 2000) and *Figure 2.2ia* and *b*) is attributed to several processes involving the decomposition of the dihydrate crystal resulting in molecular rearrangement leading to the formation of the stable anhydrate followed by the re-organization of the molecules to an anhydrous form of trehalose.



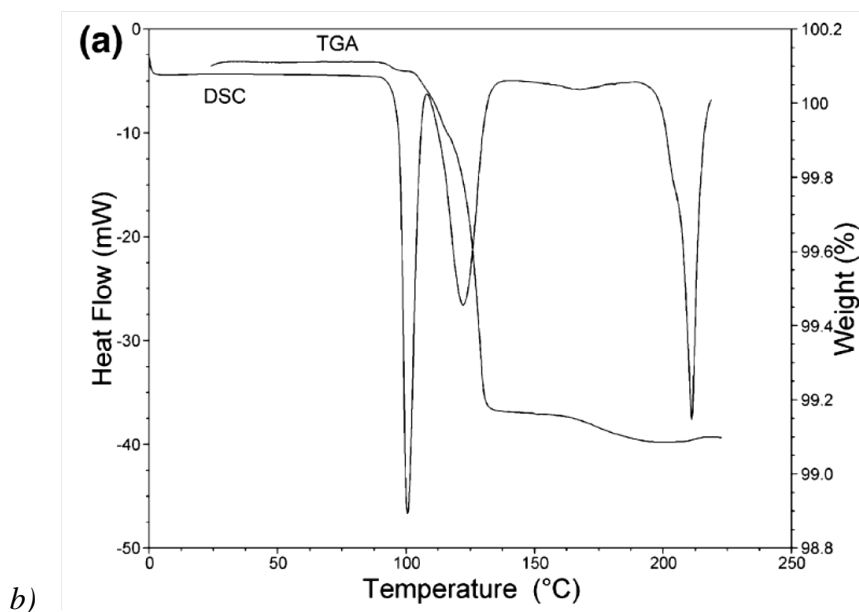


Figure 2.2 i) DSC trace of α - α -trehalose dihydrate under different conditions: a) hermetically sealed; b) covered pan; c), open pan; d) open pan and vacuum (1 mmHg) (Taken from Shafizad and Susott (1973)) ii) DSC and TGA response for α , α -trehalose dihydrate in pin-holed pans (10°C/min) (taken from McGarvey et al., (2003))

Amorphous trehalose exists with a known reported high glass transition temperature (T_g) of 120°C. De Giacomo (2008) has proposed the existence of two amorphous phases referred to as T_{am1} and T_{am2} summarized in *Table 2.3*. T_{am2} is a non-crystallisable amorphous phase said to be the undercooled liquid obtained from the melt of T_β . By these methods the undercooled liquid is unable to crystallise. Whilst a crystallisable amorphous phase, T_{am1} is generated from the melt of the isomorph desolvate of the dihydrate T_α . The T_g 's of T_{am1} and T_{am2} were evaluated by subjecting samples to different cooling rates (from 0.02°C/min to 20°C/min) and a constant heating rate of 20°C/min. The extrapolated T_g (using both the T_f and T_g onset temperature) observed in the total heat flow was 117.3°C for T_{am1} and 117.9°C for T_{am2} (De Giacomo, 2008). Characterizations of these amorphous forms were performed by studying the process of physical aging with the result that different molecular mobility and different activation energies are deduced for the two

amorphous forms. T_α is a monotropic form of T_β , upon melting of T_α the liquid phase generated is an undercooled liquid metastable with respect to T_β (Sussich and Cesaro, 2008). In these conditions the undercooled liquid produced from the melt of T_α crystallizes to T_β .

Table 2.3 Reported amorphous forms of trehalose

FORM	DESCRIPTION
T_{am1}	Crystallisable amorphous phase generated from the melt of T_α
T_{am2}	Non-crystalline amorphous phase generated from the melt of T_β

Trehalose's ability to interchange between its various forms, as well as its thermal behaviour, is of interest because of its protective and stabilizing properties. In the literature there is considerable uncertainty as to how the physical properties of these forms relate to the bio-protective properties of trehalose. *Figure 2.3* shows a summary of the proposed theories for the interchange between the crystalline anhydrous, hydrous and amorphous forms based on literature reports discussed in this section.

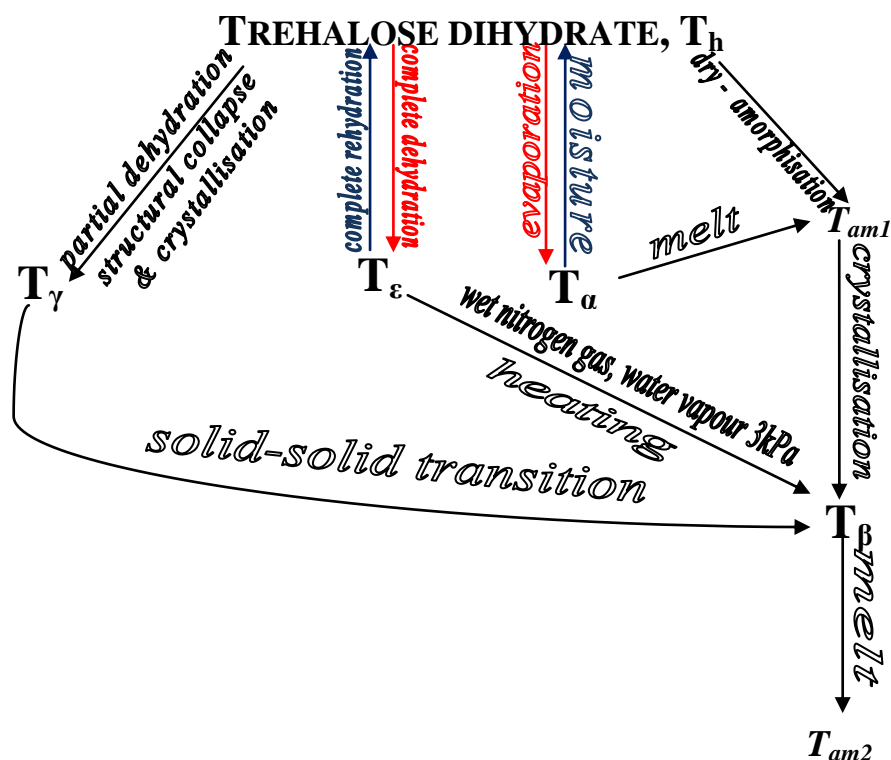


Figure 2.3 A schematic of trehalose crystalline anhydrous, hydrous and amorphous forms, showing the inter-conversion between each form

2.1.1.2 Raffinose

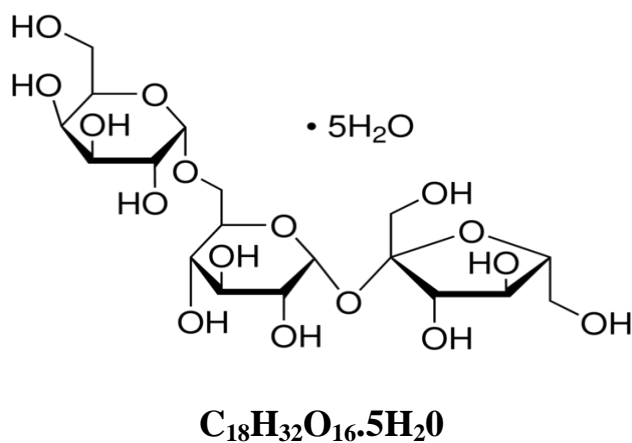


Figure 2.4 Raffinose Pentahydrate

Raffinose pentahydrate (also known as melitose) is a non reducing trisaccharide (chemical name β -D-fructofuranosyl- o- α -D galactopyranosyl-(1 \rightarrow 6)- α -gluco -pyranosidel) (Berman,

1970). Raffinose is often found in plants and food of plant origin like beans and melons. The expected weight loss for raffinose pentahydrate is 15.27%, which is equal to five moles of water (molecular weight of water: 18.015g/mol, molecular weight of raffinose pentahydrate: 594.5g/mol). In addition to existing as a stable pentahydrate, upon its dehydration it forms less stable intermediate crystalline states (both hydrate and anhydrate). Three of raffinose's water molecules are both proton donors and acceptors, whilst the remaining two act as donors forming a hydrogen bond complex (Hogan and Buckton, 2001). The hydration and dehydration characteristics of crystalline forms of raffinose correlate with what would be expected based on the location of water molecules within the pentahydrate crystalline lattice (*Figure 2.5*). It is thought that the three water molecules in the structure (water molecules 1,2 and 4) of the crystal lattice play a more integral role compared to the latter two water molecules (water molecules 3 and 5) (Salekigerhardt et al., 1995; Bates et al., 2007) (*Figure 2.5*).

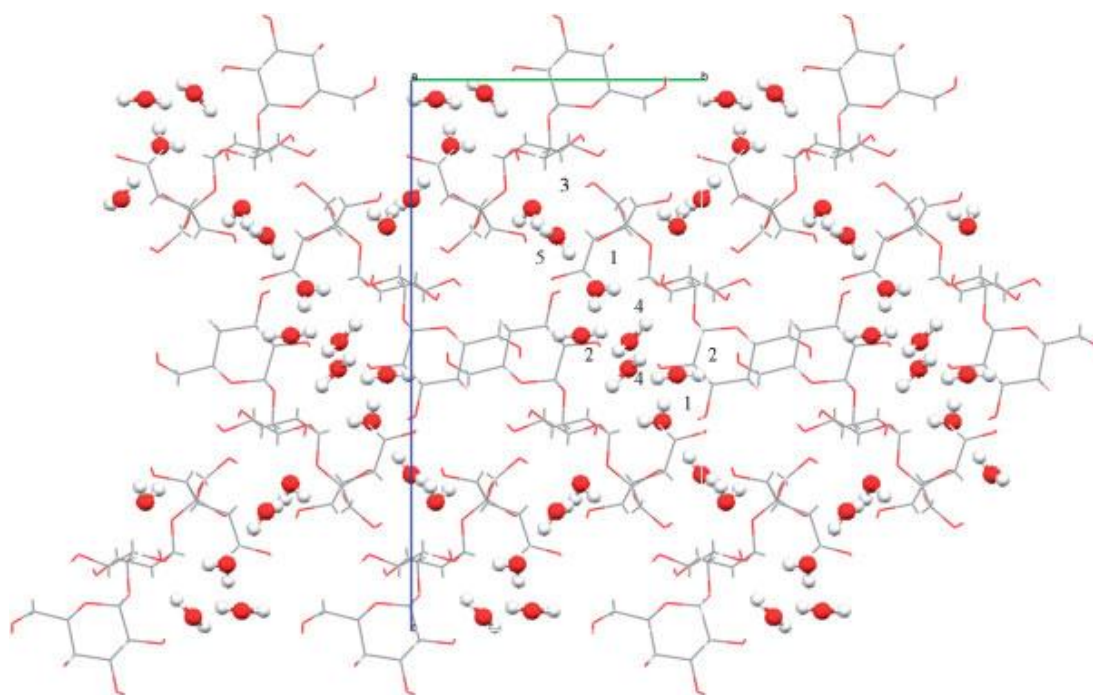


Figure 2.5 Crystal structure of raffinose pentahydrate showing location of water molecules (taken from Bates et al.,(2007))

The existence of a trihydrate form has been identified said to be generated by storing raffinose pentahydrate at 30°C in a vacuum oven for 24hours resulting in the loss of two water molecules whilst the crystal structure remains unchanged. Increasing the temperature to 60°C resulted in the removal of the remaining three water molecules causing the crystal to collapse into an amorphous form (Salekigerhardt et al., 1995).

A proposed process of dehydration of raffinose pentahydrate is illustrated in *Figure 2.6*. Where initially one molecule of water is lost at 62°C, further heating results in the loss of two water molecules at 81°C and 125°C respectively resulting in the formation of an anhydrate form (Cheng and Lin, 2006).

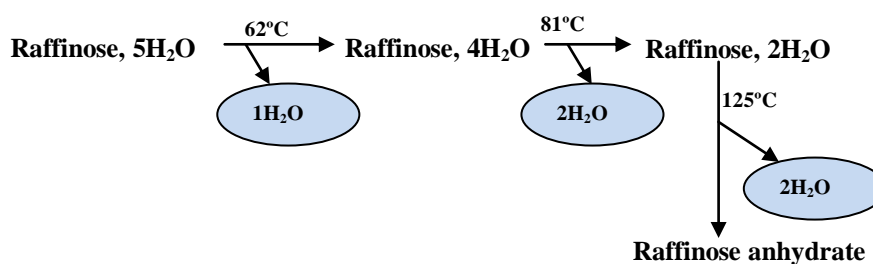


Figure 2.6 Schematic illustrating a proposed process of dehydration of raffinose pentahydrate and the generation of an anhydrate form (taken from Cheng and Lin (2006))

Salekigerhardt et al., (1995) were not able to generate a completely non-solvated anhydrous form of raffinose, but an anhydrous methanolate was generated by re-crystallizing raffinose from a saturated solution of raffinose pentahydrate in anhydrous methanol heated to 50°C. Upon complete dissolution, the sample was cooled to room temperature (24hours) and allowed to re-crystallize at room temperature for a further 48hours. Sample had a melting point of 152°C with decomposition. Other theories suggest that upon complete dehydration raffinose pentahydrate converts to its amorphous

form (Chamarthy et al., 2010; Kajiwarra and Franks, 1997; Salekigerhardt et al., 1995) (Figure 2.7).

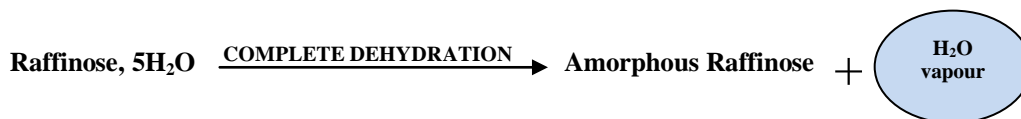


Figure 2.7 Schematic illustrating a proposed process of dehydration resulting in the generation of amorphous raffinose (taken from Chamarthy et al., (2010))

Amorphous raffinose has comparable T_g values to trehalose (at low water content) (expected T_g : 100 to 116°C (Chamarthy et al., 2010; Miller and Lechuga-Ballesteros, 2006; Kajiwarra et al., 1999) and appears to be a better water scavenger because of its ability to form pentahydrate crystals when crystallised (Sun et al., 1998). However even with these desirable properties raffinose has a lesser protective ability compared to trehalose (Sun et al., 1998).

2.1.1.3 Sucrose

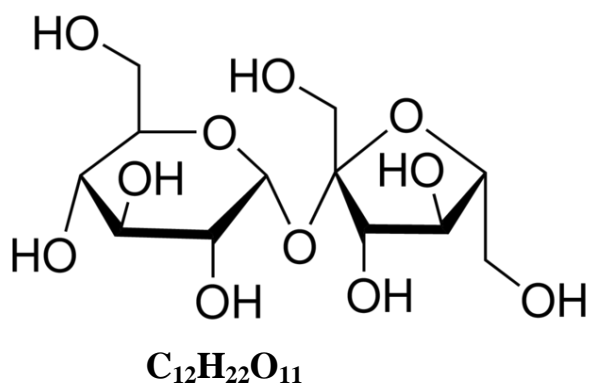


Figure 2.8 Crystalline Sucrose

Sucrose, a commonly used food ingredient, is a non reducing disaccharide. It is often present in combination with other saccharides in seeds (Wolkers et al., 1998) and in

desiccation tolerate (functional) pollens. Sucrose can be obtained as a pure anhydrous crystalline solid (molecular weight of sucrose: 342.30g/mol) and can easily be formulated into a completely amorphous state using a variety of methods including lyophilisation (freeze-drying) and spray drying. Amorphous sucrose easily crystallises at temperatures above its glass transition or upon exposure to increasing relative humidity (%RH). Both trehalose (Roe and Labuza, 2005) and raffinose (Leinen and Labuza, 2006; Salekigerhardt and Zografi, 1994) are reported to inhibit crystallisation of amorphous sucrose. Though the mechanism of this occurrence by trehalose is not confirmed, it is thought that raffinose is able to inhibit crystallisation by the attachment of the fructose (β -D-fructofuranosyl) portion of the raffinose molecule to the corresponding fructose (β -D-fructofuranoside) portion of the sucrose crystal (Cue et al., 2001).

2.1.2 PLASMID DNA

Plasmid DNA (pDNA) was used in this study to evaluate the ability of sucrose; trehalose and raffinose to preserve the structural integrity of spray dried pDNA. The plasmid used in this study was pEGFP-Arrestin-2, pDNA (*Figure 2.9*) encoding for enhanced green fluorescent protein gene and the intracellular protein β -Arrestin.

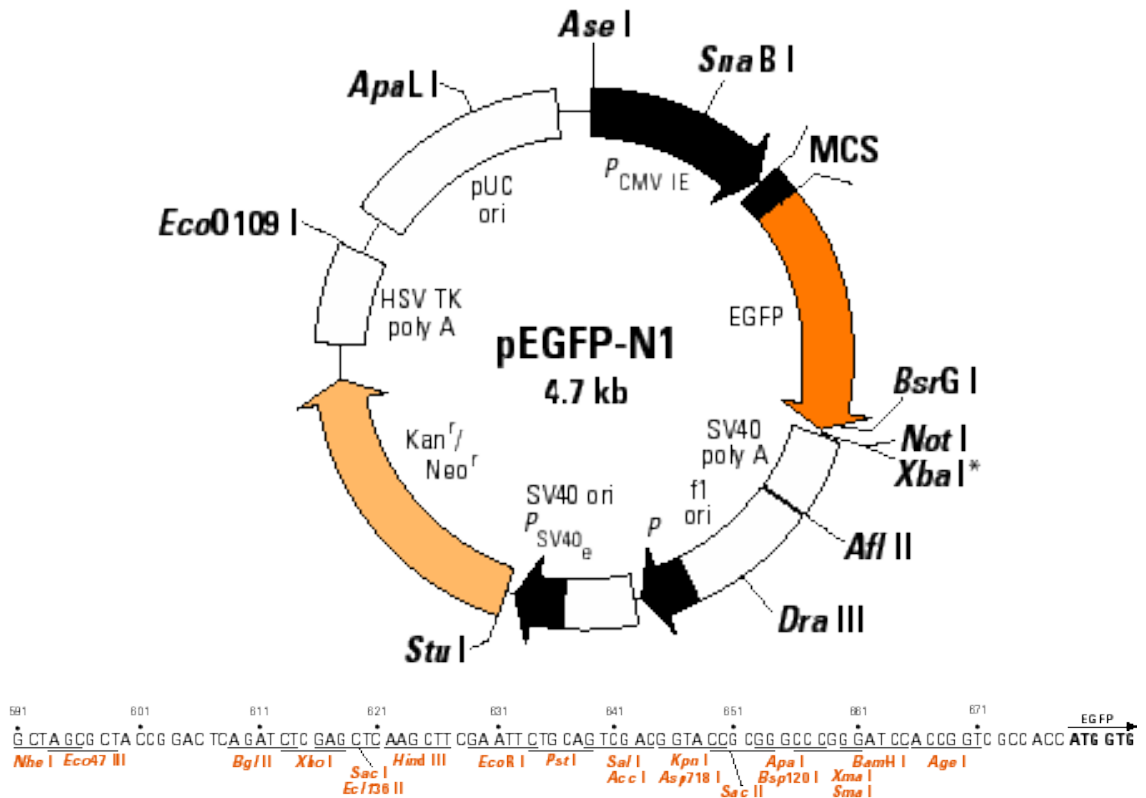


Figure 2.9 Plasmid DNA Restriction Map and Multiple Cloning Site (MCS) of pEGFP Arrestin-2 (plasmid DNA encoding enhanced green fluorescent protein gene and the intracellular protein β -Arrestin)

pEGFP-Arrestin-2 was amplified in *Escherichia coli* (strain DH5 α) grown in Luria-Bertani (LB) medium. pDNA was extracted and purified following steps outlined in the protocol for ‘Plasmid DNA Purification using Qiagen Plasmid Giga Kit’ which is based on a modified alkaline lysis procedure which yields transfection grade pDNA (QIAGEN®, 2005).

2.1.2.1 Plasmid DNA Purification using Qiagen Plasmid Giga Kit

This procedure involves the binding of plasmid DNA to an anion-exchange resin under appropriate low salt and pH conditions. A summary of the components of buffer solution used in the extraction of pDNA is detailed in *Table 2.4*. pEGFP-Arrestin-2 was amplified

in *Escherichia coli* (*E.coli*) (strain DH5 α) grown in Luria-Bertani (LB) medium. LB medium consists of tryptone, yeast extract, and sodium chloride. Tryptone provides a source for amino acids to promote bacterial growth, whilst vitamins and trace elements are provided by the yeast extract. Addition of sodium ions aids osmotic balance. LB medium was prepared by suspending 20g of LB broth powder (obtained from Sigma-Aldrich,) in one litre of distilled water. This solution was then autoclaved at 131.5°C using an Astell swiftlock autofill sterilizer. Once solution was cooled 100 μ g of kanamycin (aminoglycoside antibiotic) was added. A starter culture of 100mL LB medium and *E.coli* DH5 α strain was incubated for approximately eight hours at 37°C with vigorous shaking. The culture was then diluted in 2.5L of LB medium and then incubated for a further 16 hours at 37°C with vigorous shaking. It was important to have sufficient shaking of culture as this promotes good bacterial growth. Bacterial cells were harvested by centrifugation of the culture solution for 15 min at 4°C. A bacterial pellet was produced and was re-suspended in 125mL of Buffer P1 containing the ribonuclease RNase A which degrades RNA. For efficient lysis it was important to use a vessel that was large enough to allow for complete mixing of the lysis buffer, Buffer P2 containing sodium hydroxide and sodium dodecyl sulfate (SDS) which a strong anionic detergent. 125mL of Buffer P2 was added to facilitate cell lysis. The lysate suspension was mixed thoroughly by vigorously inverting the flask 6 times and allowed to incubate at room temperature for 5 minutes.

Table 2.4 Composition of buffer solutions used in DNA purification

BUFFER SOLUTION	COMPOSITION
Buffer P (resuspension buffer)	Contains DNase-free RNase A (a ribonuclease used to degrade RNA), contains LyseBlue a color indicator which provides visual identification of optimum buffer mixing
Buffer P2 (lysis buffer)	Contains sodium hydroxide and SDS which is a strong anionic detergent
Buffer P3 (neutralization buffer)	Contains acetic acid
Buffer QBT (equilibration buffer)	Contain isopropanol, 0.15% Triton® X-100 (v/v) (a non-ionic surfactant), 750 mM NaCl
Buffer QC (wash buffer)	Contain isopropanol, 1.0 M NaCl
Buffer QF (elution buffer)	Contain isopropanol and 1.25 M NaCl

As the colour indicator, LyseBlue had previously been added to Buffer P1 (re-suspension buffer) on addition of Buffer P2 (lysis buffer) the cell suspension turned blue (*Figure 2.10*). Mixing resulted in a homogeneously coloured suspension. If the suspension contained localised colourless regions or brown cell clumps this would indicate insufficient mixing and solution will need to be mixed further until a homogeneously colored suspension was achieved. 125mL of Buffer P3, a neutralization buffer (containing acetic acid) was added to the lysate suspension. This resulted in precipitation of SDS (the anionic detergent), proteins, and other cellular debris whilst plasmid DNA (pDNA) in its super-coiled structure was in solution. The suspension was immediately mixed by inverting 6 times and allowed to incubate on ice for 30 minutes. The precipitated matter (proteins and cellular debris) was seen as a fluffy white material.

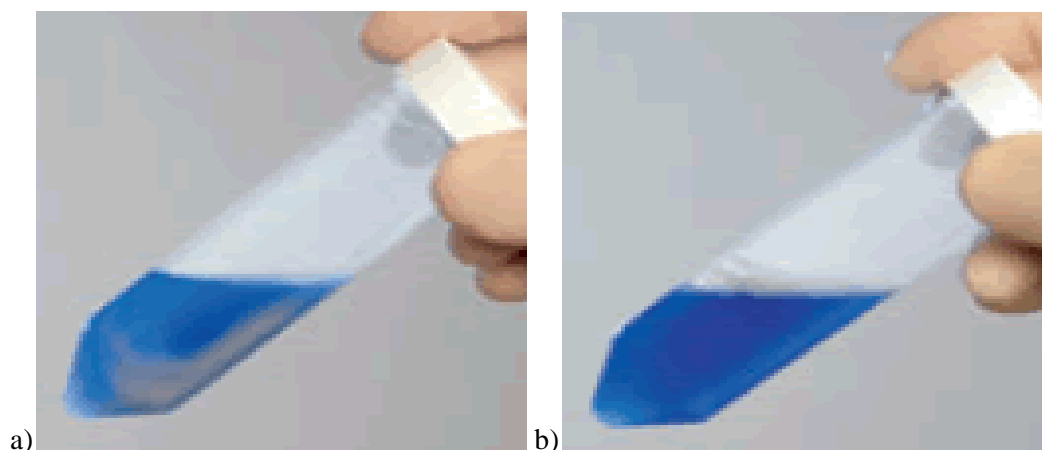


Figure 2.10 a) Insufficient mixing after addition of Buffer P2 (lysis buffer). b) Correct mixing after addition of Buffer P2 (lysis buffer) (Taken from Qiagen®, 2005)

The suspension was mixed until all traces of blue had disappeared, producing a colourless suspension (Figure 2.11). A homogenous colourless suspension indicated that the anionic detergent SDS had been effectively precipitated. The solution was centrifuged twice for 30 minutes at 4°C to avoid applying suspended or particulate material to the Qiagen-tip as suspended material could clog the tip and reduce or eliminate the gravity flow. Qiagen-tip 10000 was equilibrated by applying 75mL of Buffer QBT (equilibration buffer). Once the tip was drained completely, the solution was loaded onto the Qiagen-tip and allowed to enter the resin by gravity flow. The tip was washed by adding 600mL of Buffer QC (wash buffer). The first half of the volume of Buffer QC is sufficient to remove any contaminants whilst the second half of the volume is necessary to ensure highest yields with best achievable purity. DNA was eluted from Qiagen-tip by adding 100mL of Buffer QF (elution buffer) which had high sodium chloride content. Under high salt conditions and by a shift of pH from neutral to 9.0 these alkaline conditions cause the positive charge of the anion-exchange resin to be neutralized allowing for the release of pDNA.

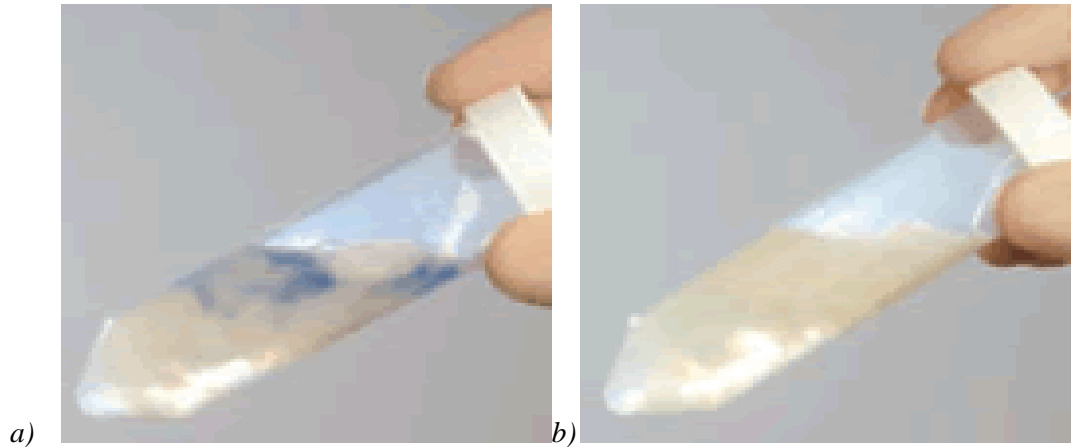


Figure 2.11 Addition of neutralization buffer (Buffer P3) causes LyseBlue to turn colourless. A homogeneous solution with no traces of blue indicates that the SDS has been effectively precipitated a) Insufficient mixing after addition of neutralization buffer. b) Correct mixing after addition of neutralization buffer. (Taken from Qiagen®, 2005)

Addition of room temperature isopropanol (70mL) to the eluted pDNA precipitated pDNA. Solution was mixed and centrifuged for 1 hour and 30 minutes at 4°C. The solution was carefully decanted leaving a pDNA pellet. 10mL of room-temperature 70% ethanol was added. After removal of ethanol, the pDNA pellet was air-dried for 20 min, and re-dissolved in TE buffer, pH 8.0. It was necessary to precipitate the DNA and remove salts and all traces of alcohol as these can disturb or enzymatically inhibit activity require for restriction or sequencing reactions. A summary of the process described is provided in *Figure 2.12*.

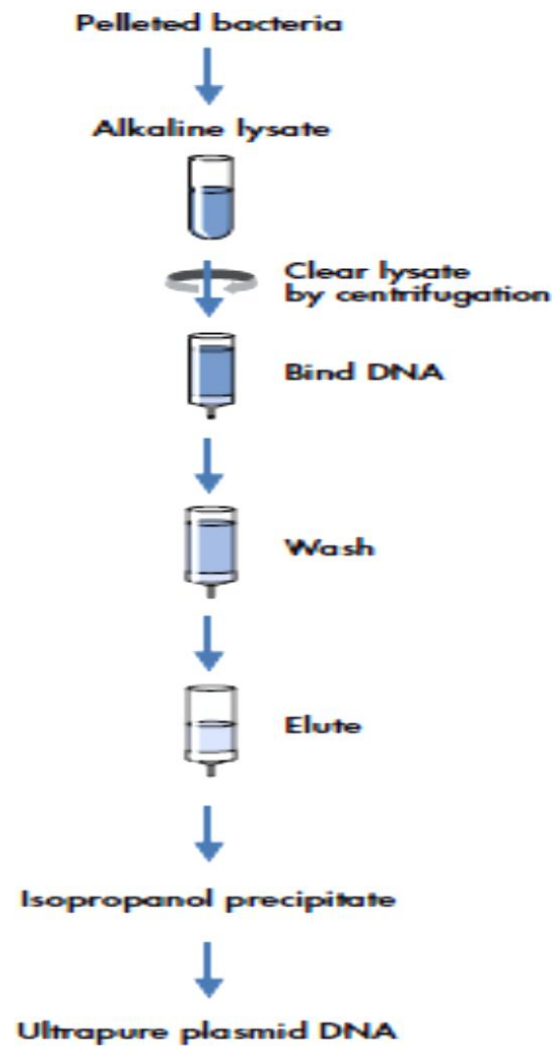


Figure 2.12 Schematic summarizing plasmid DNA extraction and purification using a *Qiagen Plasmid Giga Kit*

2.1.2.2 DNA quantification using ultraviolet spectroscopy

Ultraviolet spectroscopy is an accepted method for evaluating nucleic acid concentration and purity. It was first described by Warburg and Christian (1942) as a means to measure protein purity in the presence of nucleic acid contamination. Nucleic acid concentration is calculated using the Beer-Lambert law, which predicts a linear change in absorbance with concentration (*Equation 2.1*).

$$A_{\lambda} = \epsilon_{\lambda} lc \quad \text{Eq.2.1}$$

where A_λ is the absorbance at a particular wavelength, c the concentration of the nucleic acid, l the path length (which is typically 1cm) and ϵ_λ which is the extinction coefficient. Average extinction coefficients for 1 mg/ml nucleic acid solutions at 260nm and 280nm are 20 and 10 respectively. To determine the purity of pure nucleic acid, a ratio of the average extinction coefficient of the nucleic acids at 260nm and 280nm (20 and 10 respectively) is used. Therefore pure nucleic acid samples would have a ratio of 2. As a general rule nucleic acid samples with an A_{260}/A_{280} greater than approximately 1.7 are considered “pure” (Granske, 2008).

pDNA was quantified using a Thermo Scientific NanoDrop 3300 Fluorospectrometer. 1 μ L of sample was pipetted onto the instrument. A pulsed xenon flash lamp provides the ultraviolet light source and an internal spectrometer analyzes the light after passing through the sample to quantify pDNA. The instrument was controlled using NanoDrop 1000 Spectrophotometer Version 3.7 software.

2.1.3 HYDROXYPROPYLMETHYLCELLULOSE

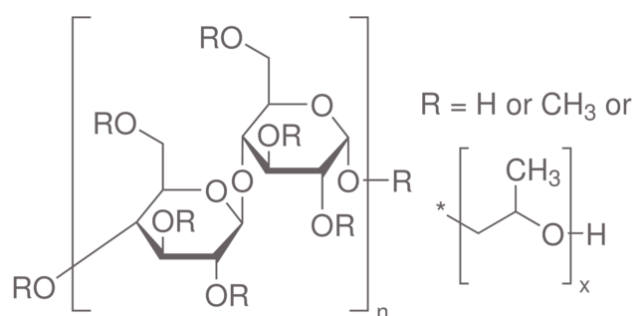


Figure 2.13 (Hydroxypropyl)methylcellulose

Hydroxypropylmethylcellulose (HPMC) is an inert hydrophilic polymer, with a wide application of use within the pharmaceutical (e.g. tablet coating, granulation, sustained

release and liquid formulations) and food industry (e.g. bakery, salads dressings). HPMC is commonly used in capillary gel electrophoresis experiments for the separation of proteins and DNA fragments (Garcia-Canas et al., 2002; Kang et al., 2005) and (to date) is not known to protect DNA in any way.

In this study, HPMC was co-spray dried with pDNA where it was used as a carrier for pDNA as spray drying pDNA alone did not result in visible particles in the spray drying collecting chamber. This is likely to be due to low mass (500µg of extracted pEGFP Arrestin 2 pDNA) used.

Methocel E5 and Methocel K4M Premium were obtained from Colorcon®. However, Methocel E5 was chosen for further experiments as it had a lower viscosity of 5mPa·s (in water at 20°C at 2%) compared with Methocel K4M Premium viscosity of 2903mPa·s (in water at 20°C at 2°C). It was also chosen because its viscosity and consistency were suitable for spray drying experiments. A 2%w/v solution was prepared using the “hot/cold” technique, where a third of the required volume of water was heated above 90°C. HPMC powder was added and mixed using a magnetic stirrer. Once all the particles were thoroughly wetted, to complete solubilisation the remainder of the water (cold) was added, solution was spray dried using a Büchi mini spray dryer B-290 with a Büchi dehumidifier B-296 attached using parameters detailed in *Section 2.2.1*.

2.2 METHODS

2.2.1 SPRAY DRYING

Spray drying is a particle processing technique used to dry aqueous or organic solutions, suspensions or pastes into a dry particulate form (powders, granules, or agglomerates. This is achieved by spraying the feed into a hot drying medium (usually air). Spray drying allows for the production of precisely defined powders, of which the size, geometry and morphology can be determined by the processing parameters used. The first significant industrial use of spray drying was demonstrated for detergents in the 1920s (Masters, 1976). It was later used in the pharmaceutical industry around the 1940s for the preparation of spray-dried infusions for reconstitution and more recently is used to formulate antibiotics, dry powder inhaler formulations and tablet excipients. A typical spray drying process consists of four steps i) atomization of the liquid feed, ii) contact of spray and drying medium with heat and mass transfer, iii) drying of spray dried droplets at elevated temperatures (removal of moisture) and finally iv) separation of the dried product from the air (recovery) (Büchi, 2003). These processes are indicated on the Büchi Mini Spray Dryer B-290 in *Figure 2.14*.

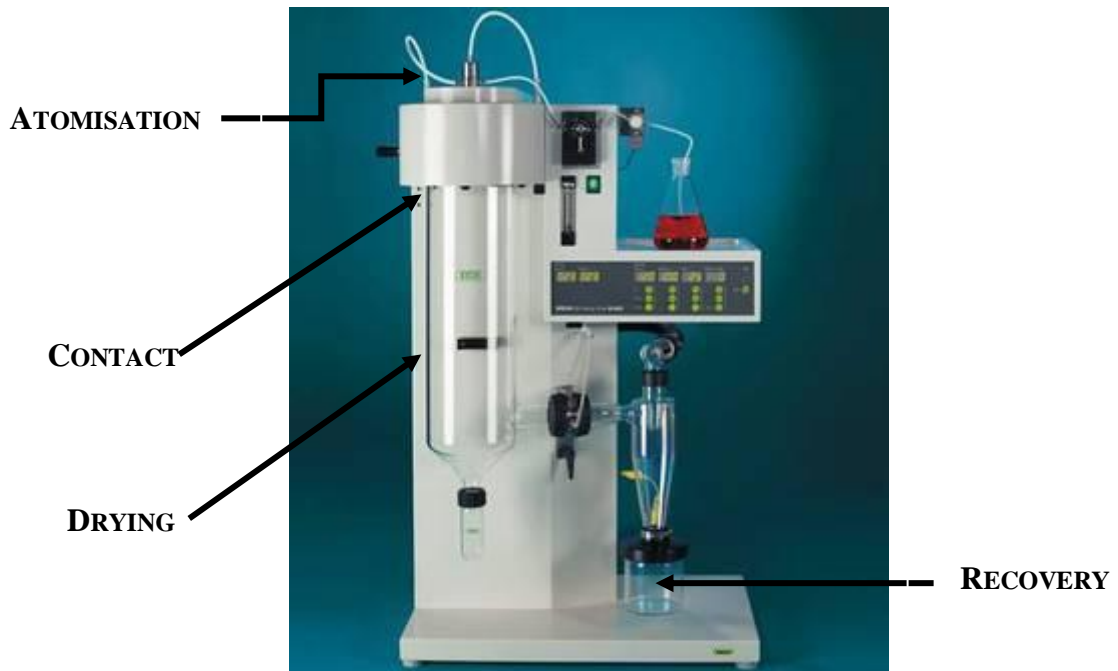


Figure 2.14 The Büchi Mini Spray Dryer B-290, a typical laboratory-size model (taken from Büchi, 2003)

Atomization involves the break-up of the liquid feed into small droplets forming a spray. There are four types of atomizers available, a pressure nozzle, a two fluid nozzle (used in this experiment), a rotary disk atomizer and an ultrasonic nozzle (Moller and Fredsted, 2009). The choice of atomizer is dependent on the nature, amount of feed and the desired characteristics of the spray dried product. Typical droplet mass median diameters in pharmaceutical spray dryers range from less than $10\mu\text{m}$ for pulmonary applications to upwards of $100\mu\text{m}$, which translates to a typical dry particle diameter range of 0.5 to $50\mu\text{m}$ (Vehring, 2008). An atomizer is generally located at the top of the drying chamber; the heated drying medium is introduced through a roof-mounted air/gas dispenser around the atomizer which creates a co-current flow of gas and droplets/particles (*Figure 2.15*). This method of drying takes advantage of evaporative cooling and decreasing temperatures downwards; ensuring droplets come into contact with hot drying medium when they are at their most moist.

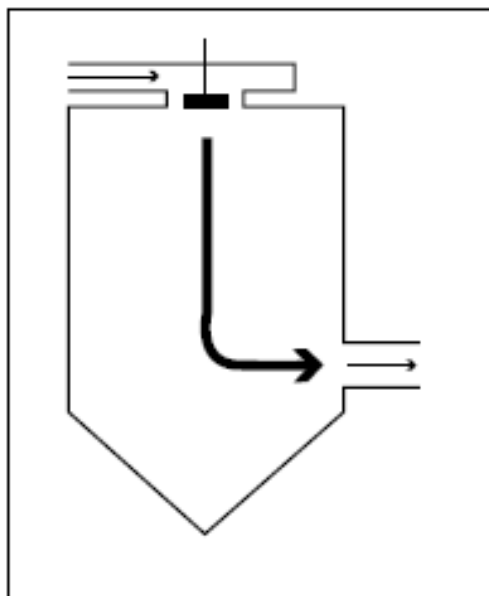


Figure 2.15 Schematic showing co-current flow (taken from Büchi, 2003)

For each sugar a 100mL 10% w/v solution was prepared using filtered (0.44 μ m) distilled water. As both trehalose and raffinose are hydrates in their crystalline form, when preparing spray drying solutions it was important to ensure that the concentration was calculated as 10% w/v of the anhydrous sugar and not 10% w/v of the hydrated sugar. The solution was first stirred using a magnetic stirrer on a plate for 30minutes to ensure full dissolution, then was spray dried using a Büchi mini spray dryer B-290 with a Büchi dehumidifier B-296 attached. Trehalose, raffinose and sucrose were co-spray dried with 100 μ g of extracted pDNA (mixed by pipeting). Both samples were spray dried using the following parameters: inlet temperature of 125 $^{\circ}$ C, an average pump flow rate of 3.7mL/min, 100% aspirator setting and an outlet temperature ranging from 60-80 $^{\circ}$ C (not controlled). An inlet temperature of 125 $^{\circ}$ C was chosen as previous studies (Naini et al., 1998) obtained a crusty product at higher inlet temperatures. Samples were stored at -80 $^{\circ}$ C until use. This temperature was used as it was over 100 $^{\circ}$ C below the lowest glass

transition temperature and therefore it was reasonable to assume that no further changes in the glass would take place (Hunter, 2009b). pDNA loaded samples were stored at -20°C.

2.2.2 BIOLOGICAL EXPERIMENTS

2.2.2.1 Gel Electrophoresis

Gel electrophoresis is a technique based on charge migration. It allows for the separation and identification of DNA fragments ranging from 0.1kB to 25kB. The concentration of agarose used for a gel depends primarily on the size of the DNA fragments to be analyzed. Low agarose concentrations are used to separate large DNA fragments, whilst high agarose concentrations allow resolution of smaller DNA fragments. Ethidium bromide can be added to the agarose gel before or after electrophoresis. Addition of ethidium bromide leads to complexes with plasmid DNA which increases fluorescence. This means that illumination of a stained gel under UV light (254–366nm) allows bands of DNA to be visualized against a background of unbound dye (Sauer P, 1998). *Figure 2.16* is a schematic summarizing the gel electrophoresis procedure.

In this study gel electrophoresis experiments were conducted using 2% agarose gels to separate pDNA. To make 300mL of a 2% agarose gel, 6g of agarose powder was dissolved in [1X] TBE buffer and microwaved for 30 seconds to ensure all of the agarose powder was fully dissolved, indicated by a clear solution. Details of method used to prepare [1X] TBE buffer are detailed in *Appendix 2.1*. Once the solution temperature had reduced to around 55°C ethidium bromide was added to give a final concentration of 0.5µg/mL.

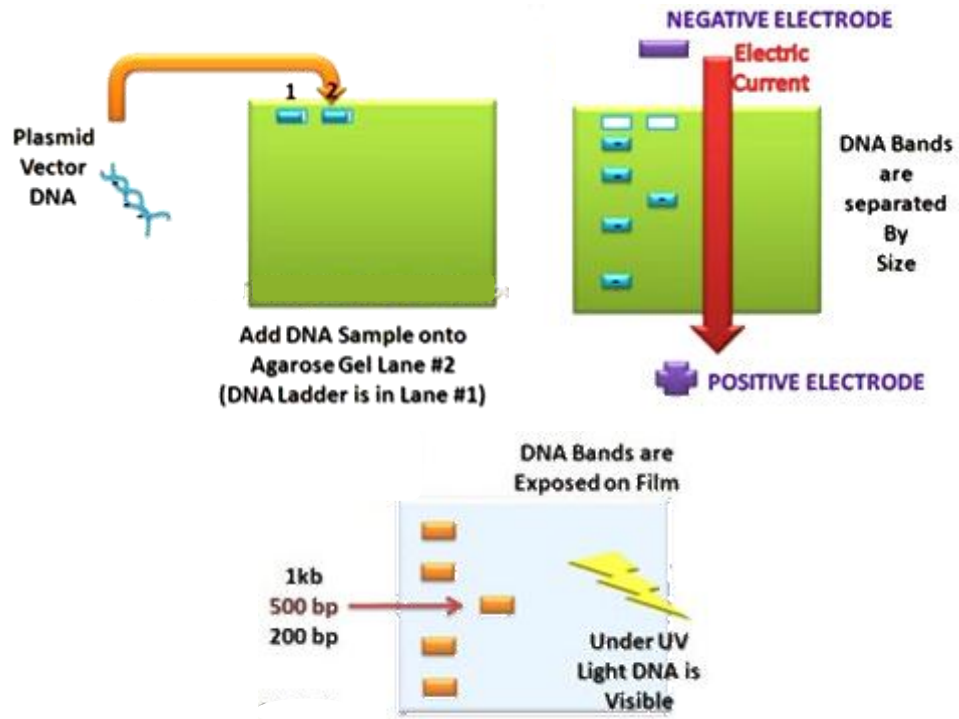


Figure 2.16 Schematic summarising the gel electrophoresis procedure (taken from <http://www.molecularstation.com/agarose-gel-electrophoresis/>)

It was important to ensure ethidium bromide was added once solution was cooled to prevent inhalation of fumes as it is carcinogenic. Therefore this process was conducted in a fume cupboard. The solution was then added to a gel tray and a comb was vertically placed approximately an inch from the end of the tray ensuring air bubbles were not present. The gel was allowed to solidify at room temperature. Once solidified, the comb was gently removed and the tray was placed in the electrophoresis chamber and covered by [1X] TBE buffer. Purified plasmid DNA (pDNA) was cut using *StuI*, *HindIII*, *BamH* and *NotI* restriction enzymes (obtained from Promega). An analytical scale restriction enzyme digestion was performed of a 25 μ L maximum volume using 1 μ g of pDNA. In a sterile tube, the components listed in *Table 2.1* were assembled in the order listed. The components were then mixed by gentle pipetting and were incubated at 37 $^{\circ}$ C for 3 hours. After this [1X] loading buffer was added and mixed by gentle pipetting. The sample was

then added to the well (in the previously prepared gel). Gel electrophoresis experiments were run at 100 volts until the dye markers had migrated an appropriate distance to allow DNA to be visualised. Gels were visualised using a G:Box gel imaging system using the GeneSnap software version 7.09. Gels were analysed using GeneTools version 4.01 and ImageJ 1.45s

Table 2.5 Components used in restriction enzyme digestion of plasmid DNA

COMPONENT	VOLUME
Sterile, deionised water	16.3 μ L
MC Buffer (restriction enzyme buffer)	4 μ L
Acetylated BSA (Bovine serum albumin), 10μg/μL	0.2 μ L
DNA	1 μ g
Mix by pipeting then add	
StuI	0.5 μ L
HindIII	0.5 μ L
BamH	0.5 μ L
NotI	0.5 μ L
Total Volume (dependant on DNA concentration)	~ 22.5 - 25 μ L

2.2.2.2 *Cell Culture of HeLa and A549 Cells*

Tissue culture is a general term used to describe the removal of cells, tissues or organs from any animal or plant and their subsequent placement into an artificial environment conducive to growth. HeLa cell is a cervical cancer cell line that originated from Henrietta Lacks, a patient who died of cancer on October 4th 1951. A549 cells are human alveolar basal epithelial cells and are grow adherently as a monolayer.

HeLa cells are adherent cells and stick to the bottom of the flask used. Cells were passaged when they were 70-80% confluent using PBS-EDTA (Phosphate buffered saline-Ethylenediaminetetraacetic acid) 37°C solution and were re-suspended in complete DMEM (Dulbecco's Modified Eagle Medium).

A549 cells were passaged when they were 70-80% confluent using trypsin solution (at 37°C) and were re-suspended in complete RPMI - 1640 (Roswell Park Memorial Institute) medium.

2.2.2.3 Transfection of Plasmid DNA

Transfection studies involve the induction of exogenous molecules and gene encoding molecules (e.g. plasmid DNA or short interfering RNA) to the cell. Electroporation is a transfection technique used to physically alter the cell membrane permeability by applying short electrical pulses (over a specified period of time) to the membrane therefore allowing exogenous molecules to enter the cell (*Figure 2.17*) (Rabussay et al., 2003).

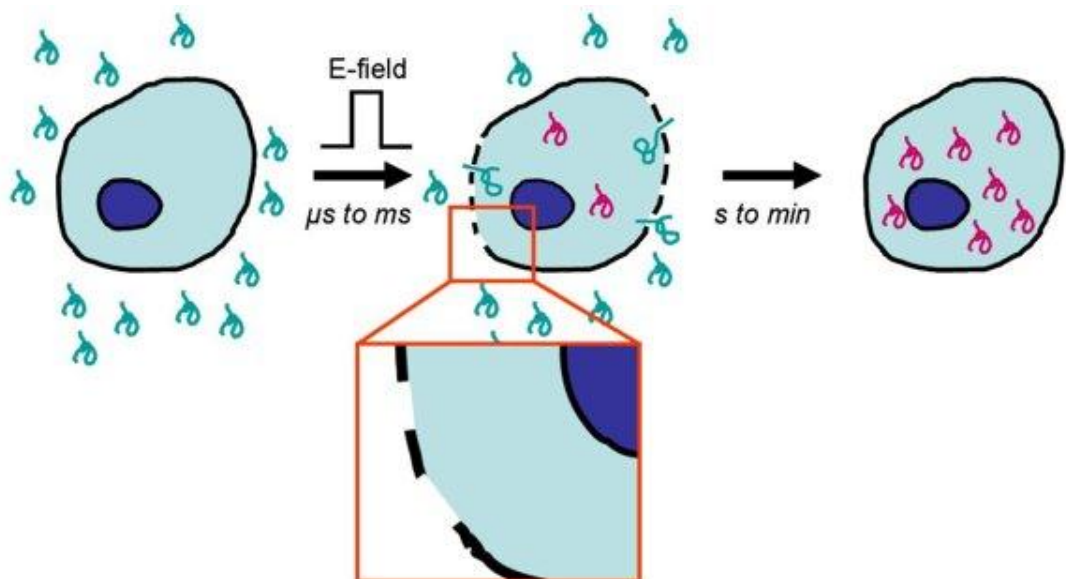


Figure 2.17 Schematic showing electroporation of a cell (taken from <http://www.utwente.nl/ewi/bios/research/Cellsonchips/cell%20electroporation.doc/>)

In this study transfection studies were performed using HeLa and A549 cells (at~85% confluent) and pDNA either co-spray dried with trehalose, raffinose and HPMC or not spray dried (used as a control) using the protocol described in *Appendix 2.3* and *2.4*. Results of this experiment are detailed in *Chapter 6*.

2.2.2.4 MTT (3-(4,5-Dimethylthiazol-2-yl)-2,5-diphenyltetrazolium bromide) assay

MTT is a yellow tetrazolium dye that is reduced by mitochondrial enzymes resulting in a colour change. This event only occurs in the presence of active mitochondrial reductase enzymes i.e. in viable mitochondria therefore, the colour intensity can directly be related to the number of viable cells. It is a useful technique to detect cytotoxic compounds. A549 cells were used as pDNA formulations generated were intended for pulmonary delivery therefore it is important to ensure the materials used did not cause any cell cytotoxicity.

MTT assay was conducted on A549 cells. Using a haemocytometer (*Appendix 2.2*) 5×10^3 cells were counted and loaded into each well of a 96-well plate. 10mL solutions of trehalose, raffinose and HPMC (in phosphate buffered saline solution (PBS)) were prepared for the MTT assay as detailed in *Table 2.6*. All solutions were filtered (0.22 μ m). 100 μ L of each solution was added to each well as detailed in *Figure 2.18*. For ease of referencing trehalose, raffinose and HPMC solutions are referenced according to %w/v where T represents trehalose, R raffinose and H HPMC. Control solutions were referenced according to media volume in starting solution (10mL) i.e. C6 represents control solution containing 6mL media and 4mL PBS.

Table 2.6 Concentrations of sugar and media solutions used in MTT assay

SAMPLE	%W/W	VOLUME OF SUGAR SOLUTION (ML)	VOLUME OF MEDIA (RPMI-1640) (ML)
TREHALOSE AND RAFFINOSE	10	4	6
	5	2	8
	3	1.2	8.8
	1	0.4	9.6
HPMC	2	4	6
	1	2	8
	0.6	1.2	8.8
	0.2	0.4	9.6

	1	2	3	4	5	6	7	8	9	10	11	12											
A																							
B													C	C6	C8.8	T10	T3	R10	R3	H2	H0.6		
C													C	C6	C8.8	T10	T3	R10	R3	H2	H0.6		
D													C	C6	C8.8	T10	T3	R10	R3	H2	H0.6		
E													MA	C8	C9.6	T5	T1	R5	R1	H1	H0.2		
F													MA	C8	C9.6	T5	T1	R5	R1	H1	H0.2		
G													MA	C8	C9.6	T5	T1	R5	R1	H1	H0.2		
H																							

Figure 2.18 Schematic illustration of a 96-well plate used in an MTT assay where C = cells with media only, MA = media (RPMI – 1640) alone, C = control solutions, T = trehalose solutions, R = raffinose solutions and H = HPMC solutions, ■ = phosphate buffered saline solution

The 96-well plate was incubated at 37°C for 24hours after which 10µL of MTT was added and plate was incubated at 37°C for a further 24hours. 96-well plate was analysed using a BMG labtech Polystar Optima microplate fluorimeter. Results of this experiment are detailed in *Appendix 2.3*.

2.2.3 SCANNING ELECTRON MICROSCOPY

Microscopy involves the study of objects that are too small to be examined by the unaided eye (Egerton, 2005). The first commercial electron microscope was manufactured by Cambridge Instruments in 1965 (Clarke, 2002). Scanning electron microscopy uses a focused beam of high-energy electrons to generate a variety of signals at the sample's surface. The signals derived from the electron-sample interactions reveals information which includes the sample morphology and texture. An SEM image is produced as a result of the detection and amplification of a number of secondary electrons emitted from the sample surface where they have been dislodged by a focused electron beam (from the instrument) moving across the sample surface

In this study the particle morphology was evaluated using a Scanning Electroscop JEOL JSM 5900LV. In order to improve conductivity, samples were coated with gold under vacuum SC7640 Gold Sputter Coater, 30 seconds 2.2kV 25mA on the rotating stage, Quorum technologies. All micrographs were taken at an acceleration voltage of 20kV.

2.2.4 PARTICLE SIZE ANALYSIS

2.2.4.1 *Laser particle sizing*

Laser diffraction is used as a method for particle size analysis of powders, suspensions, emulsions, and sprays. Laser light is diffracted as a result of its particle interaction. A spherical particle (i.e. that produced by spray drying) produces a ring shaped diffraction pattern. The particle diameter is dependent on the distance of the first minimum (i.e. between two rings) to the centre of the particle (Sympatec, 2012) with a small particle

having a larger diffraction pattern compared to that of a larger particle (*Figure 2.19*). As not all particles are spherical the particle sizer used in this study was able to analyse results independent of the orientation of the particles by integrating diffraction patterns irrespective of particle shape to 180°.

If particles form agglomerates, the laser measures the overall size of the agglomerate instead of the size of the primary particles. A complete dispersion of the sample is therefore of importance to ensure accurate particle size measurements

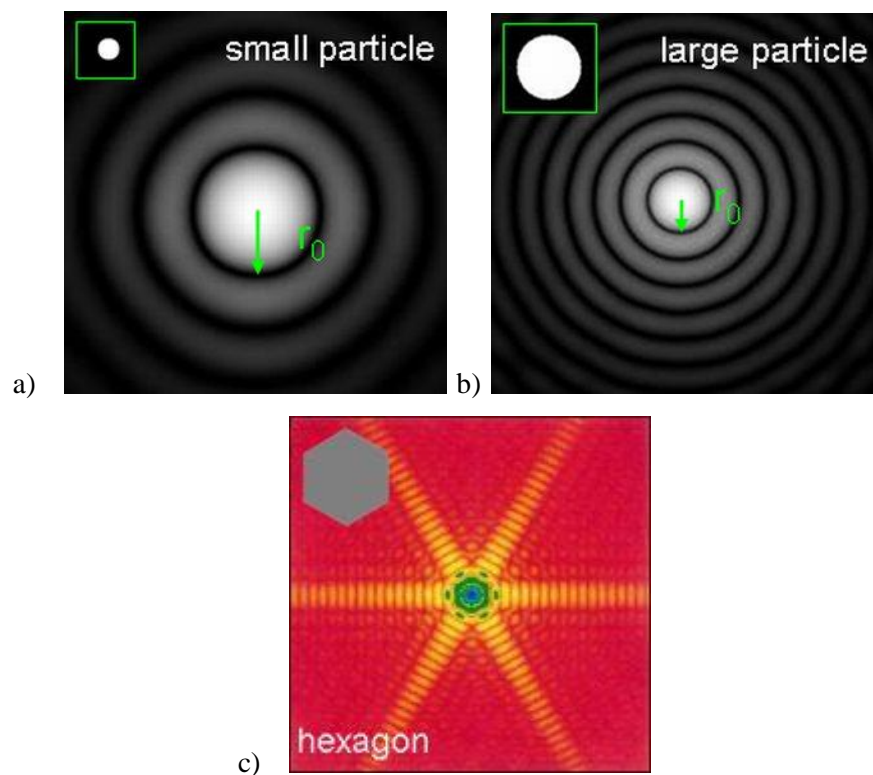


Figure 2.19 Diffraction patterns of a) small particle and b) large particle c) example of a calculated diffraction pattern for a non-spherical particle (taken from Sympatec (2012))

Particle size analysis was performed using a Sympatec laser particle sizer with a HELOS/Br detector. The liquid medium used was rapeseed oil. Two minute dispersion at

1000rpm was imposed at the start of each experiment and then three measurements were taken with each sample monitored for 10 seconds. A measuring range of 0.1-875 μ m was used. Data was exported and analysed using Microsoft Excel 2007.

2.2.4.2 Particle size analysis using the dry sieving method (mechanical agitation)

Analytical test sieves are made from a woven wire mesh attached to the base of an open cylindrical container (BritishPharmacopoeia, 2012). Mechanical sieving is most suitable where the majority of the particles are larger than about 75 μ m. For smaller particles, their light weight provides insufficient force during sieving to overcome surface forces of cohesion and adhesion that cause the particles to stick to each other and to the sieve (BritishPharmacopoeia, 2012). Dry sieving was used in this study as means of separating particles into size fractions for DSC analysis.

63, 125, 180, 250 and 355 μ m sieves were tarred, 25g of trehalose dihydrate was added on top (coarsest sieve) and the lid replaced. Sieves were agitated for 5 minutes and reweighed to determine the mass of material of each sieve including the collecting pan. Sieves were re-assembled and agitated for a further 5 minutes; this process was repeated until the mass on any of the sieves did not change by more than 5% or 0.1g. The analysis was repeated with a fresh samples using a single sieving time equal to that of the combined times as used above which was 40 minutes. These results are presented in *Chapter 3*.

2.2.5 X-RAY POWDER DIFFRACTION

X-rays were discovered by Wilhelm Röntgen in 1895. In X-Ray powder diffraction (XRPD) experiments, X-rays are generated by a cathode ray tube which is directed towards the sample. When certain geometrical conditions are satisfied (using the Bragg's Law equation, *Equation 2.2*), the interaction between the rays and sample produces a diffracted beam (Klug and Alexander, 1954). Bragg's Law (*Eq.2.2*) describes the relationship between the wavelength of the incident X-rays, angle of incidence and spacing between the crystal lattice planes of atoms.

$$n\lambda = 2d \sin\theta \quad \text{Eq. 2.2}$$

where X-rays of wavelength (λ) are incident of angle (θ) on a set of planes with spacing (d) (Sands, 1993). The intensity and position of the X-rays produces are recorded by a detector. A plot of the beam intensity against the angle of emergence produces a diffractogram with peaks seen corresponding to lattice spacing providing an insight into the orientation and molecular arrangement within a sample. Materials exhibiting long-range order (i.e. crystalline materials) produce XRPD diffractograms containing clearly defined sharp peaks of varying intensities which corresponds to the uniform lattice spacing, arrangements and orientation of molecules within a crystal lattice

XRPD measurements were used for the identification of crystalline samples as well as the confirmation of amorphous materials. Powder diffraction measurements were carried out on all amorphous samples using a Thermo-Arl- Xtra with a Cu-X-ray tube. The X-ray tube was operated at 45 kV and 40mA. Samples were slightly pressed on an aluminium sample tray using a glass slide and exposed to Cu K α radiation ($\lambda= 1.540562\text{nm}$). The XRPD patterns were recorded using diffraction angles (2θ) from 10° to 60° (step size,

0.01°; time per step, 0.5 seconds). Data was exported and analysed using Microsoft Excel 2007.

2.2.6 HOT STAGE MICROSCOPY

Hot stage microscopy experiments involve the controlled heating of a sample viewed through a microscope. Sample changes upon heating can be visually observed through the microscope which is attached to a computer where footage can be recorded as well as images captured. Hot stage microscopy when used in conjunction with other thermal techniques can provide useful insight into thermal events seen.

In this study a LeicaDML52 microscope with a 10X magnification lens was connected to a FP5/FP52, Mettler Toledo Instruments heating stage unit and a FP90 Mettler Toledo Instruments central processor unit. Samples were heated from 25°C to 250°C at a heating rate of 2°C/min. Studio86 Design capture software was used to record and capture thermal events in real time.

2.2.7 VARIABLE TEMPERATURE FOURIER TRANSFORM INFRARED SPECTROSCOPY

Infrared spectroscopy probes molecular vibrations, therefore functional groups can be associated with characteristic infrared absorption bands which correspond to the fundamental vibrations of the function groups. Vibrational spectroscopy is a form of infrared spectroscopy where molecules are excited by the absorption of infrared light. Fourier Transform Infrared spectroscopy (FTIR) is an effective tool for studying the molecular structures and abrupt changes in hydrogen bonding (i.e. glass transition) that can occur in amorphous sugars (Kacuráková and Mathlouthi, 1996). The mid infrared region

(4000cm^{-1} – 400cm^{-1}) possesses two types of vibrations: stretch vibrations which involve bond-length changes and the bending vibrations which involve changes in the bond angles (in-plane and out of plane) (Berthomieu and Hienerwadel, 2009). FTIR spectra of crystalline materials are characterized by sharp absorption bands throughout the mid infrared region from whilst broader absorption bands are visible for amorphous materials. The sharper and more intense peaks observed for crystalline materials is as a result of a higher degree of homogeneity of intermolecular interactions leading to less dispersion of vibrational levels and higher conformational selectivity (Wolkers et al., 2004).

A Fourier Transform Infrared (FITR) spectrometer consists of an infrared source, a detector, a Michelson interferometer consisting of a beam-splitter, a movable mirror (which continuously changes the optical path-length in one arm of the interferometer) and a Helium-Neon laser which is used as a reference to control the position and velocity of the movable mirror (BrukerOptics, 2008).

2.2.7.1 *The Michelson Interferometer*

A Michelson Interferometer (*Figure 2.20*) consists of a fixed mirror, a movable mirror and a semi-transparent mirror (beam-splitter). The infrared beam from the source is divided into two beams by the beam-splitter. One of the two beams reflects off the fixed mirror whilst the other beam reflects off the movable mirror. The two beams are then recombined so that they interfere with each other. The resulting intensity at the detector depends on the frequencies of the beam and the distance of the moveable mirror. The variation in intensity with mirror position is the interferogram and this is converted into a spectrum using a Fourier Transform (BrukerOptics, 2008).

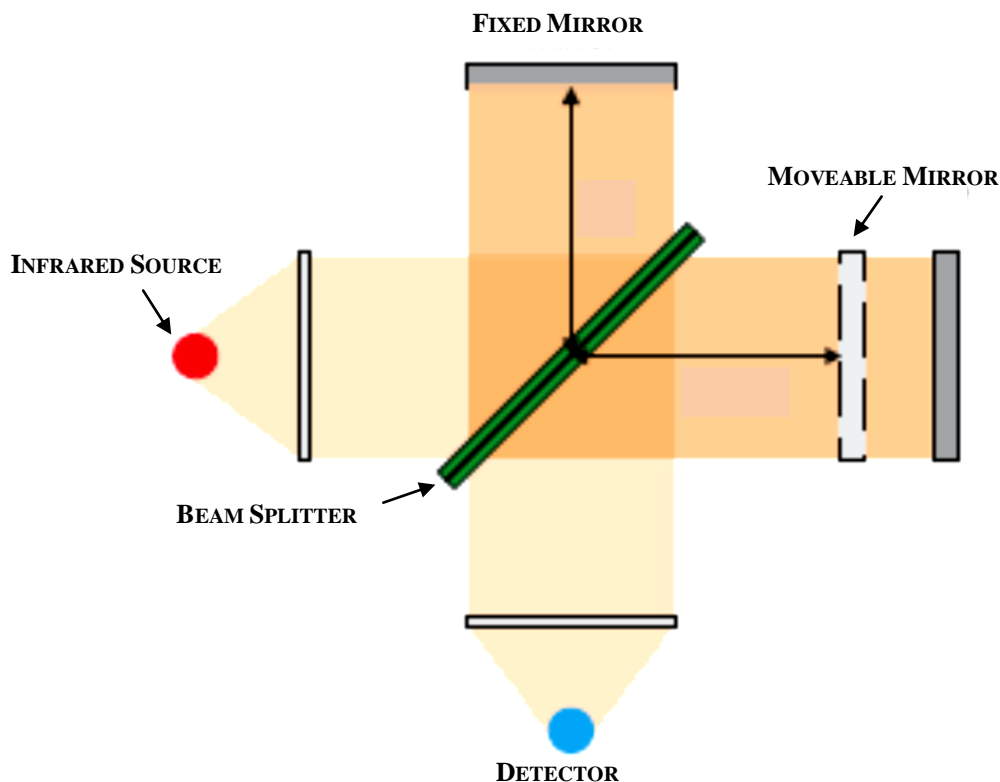


Figure 2.20 The Michelson Interferometer consisting of fixed mirror, movable mirror and a semi-transparent mirror (adapted from Bruker Optics, 2008)

The attenuated total reflection (ATR) accessory (*Figure 2.21*) when applied to FTIR can be used to probe information about the molecular structure of a sample in the solid state. A solid material is compressed onto the ATR crystal area to ensure good contact. The infrared beam penetrates (at nanometer depth) the ATR crystal at one end, reflects along the internal surfaces of the crystal and passes out the opposite end (PerkinElmer, 2005).

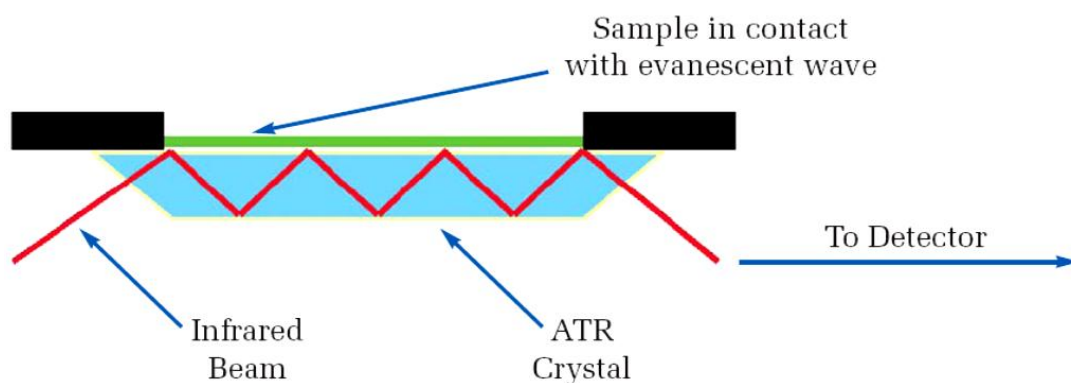


Figure 2.21 A multiple reflection ATR system (taken from the PerkinElmer Technical information (2005))

In this study ATR-FTIR absorption measurements were performed using a Bruker IFS66/SG spectrometer. Experiments were performed using the following parameters. Resolution 4cm^{-1} , scan time 16 scans (also for background) over 4000cm^{-1} - 500cm^{-1} . Spectra was analysed using Opus software version 6.0.

2.2.7.2 Exploratory Data Analysis

Exploratory data analysis of spectroscopic data obtained in variable temperature ATR-FTIR experiments were used to identify changes in spectra with increasing temperature which could be attributed to structural changes occurring in sample.

2.2.7.2.1 Hierarchical Cluster Analysis

Cluster analysis identifies groups of samples that behave in a similar manner or show similar characteristics. Hierarchical cluster analysis (HCA) calculates and compares distances between samples (or variables) in a data set. Small distances between samples implies similarities with respect to the measurements taken (Infometrix, 2008). Inter-

sample distances vary with type and number of measurements; therefore it is essential to transform them into a more standard scale of similarity (*Eq.2.3*).

$$\text{similarity}_{ab} = 1 - \frac{d_{ab}}{d_{max}} \quad \text{Eq. 2.3}$$

where d_{ab} is the multivariate distance between two samples a and b and d_{max} is the largest distance in the data set. Using this scale, a value of 1 is assigned to identical samples whilst a value of 0 to the most dissimilar samples.

A dendrogram (*Figure 2.22*) is a tree-shaped map constructed from a table of distances. The leaves (terminus of branches) represent single samples whilst the length of branches linking clusters is related to their similarity (plotted along the top of graph). This means that the longer the branch, the less the similarity the shorter the branch, and the greater the similarity. The dotted vertical line is used to identify clusters (Infometrix, 2008).

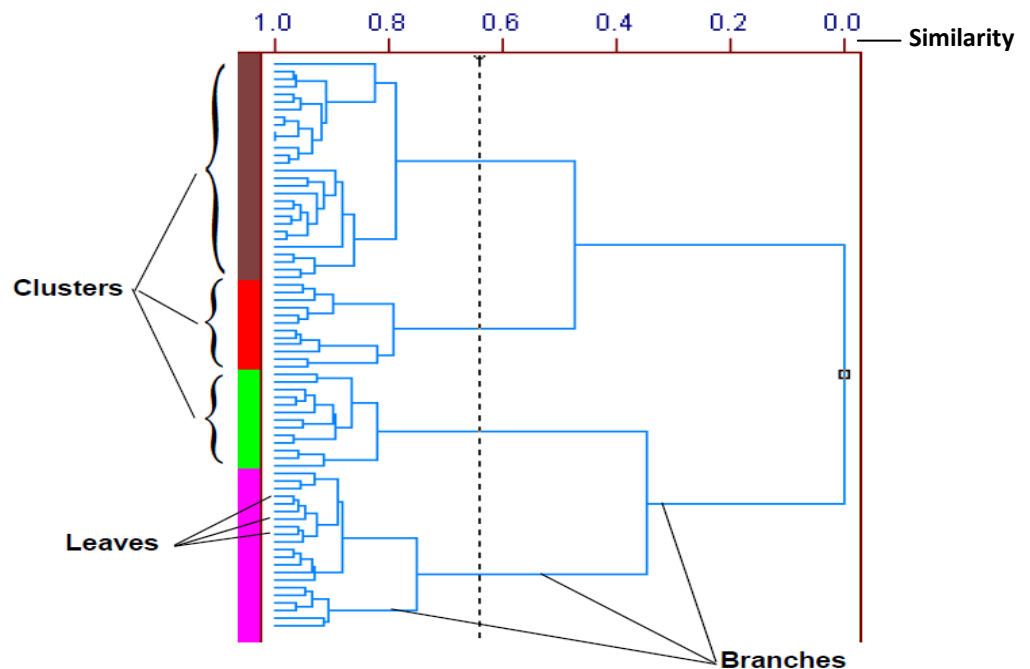


Figure 2.22 A dendrogram with 75 samples with four clusters at a similarity value of 0.5 (taken from Infometrix, 2008)

2.2.7.2.2 Principal Component Analysis

Principal component analysis (PCA) is a powerful visualization tool that finds linear combinations of original independent variables which account for maximal amounts of variation. PCA is designed to provide an insight into data variability in a multivariate data set. Consequently, allowing for the identification of natural clustering in a data set, as well as unusual samples. This information can be used to assign chemical meaning (or biological meaning or physical meaning) to the data patterns that emerge (Infometrix, 2008). The first principal component details the largest trend of the data whilst the second principal component details the second largest trend within the data set. Scores analysis can be used to illustrate inter-sample relationships. Data is plotted as a two dimensional (2D) scatter plot with a confidence ellipse is superimposed (*Figure 2.23*). This ellipse represents a 95% confidence level derived from the scores variance and is centered at the origin of the two score dimensions displayed

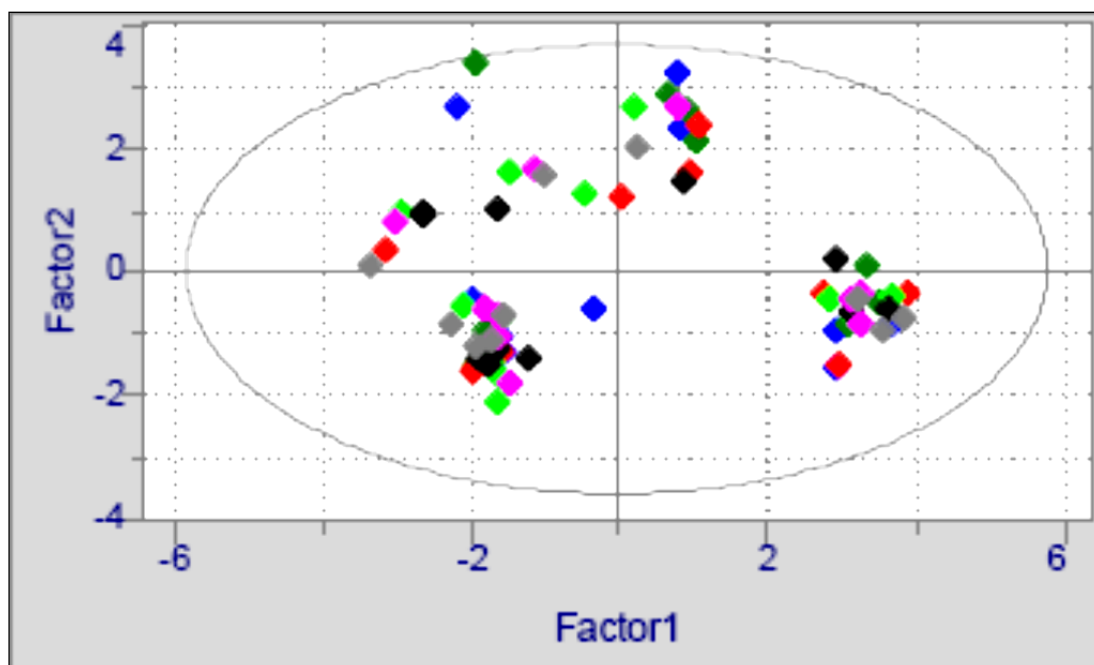


Figure 2.23 Example of a two dimensional PCA scores plot (taken from Infometrix, 2008)

Data obtained was analysed using Pirouette Multivariate Data Analysis Software (Version 4. Infometrix Inc).

2.2.8 DYNAMIC VAPOUR SORPTION

Sugars, like carbohydrates, are highly hygroscopic and will spontaneously sorb (adsorb and/or absorb) water vapour from their surroundings unless stored under completely dry conditions (Hancock and Shamblin, 1998). Sorbed water has the ability to change the physical and chemical properties of sugars. For example, sorbed water can facilitate isomerisation (Otsuka et al., 1993) and/or crystallisation processes (Yu et al., 2008) and have a plasticizing effect on the sample (Hancock and Zograf, 1996). Dynamic vapour sorption (DVS) is a valuable gravimetric technique used to investigate sample water uptake. Typically the sample is exposed to controlled conditions of temperature and humidity (between 0 and 90 %RH) as a function of time. The change in weight is measured as a function of time; in this way the kinetics of water uptake, glass transition and water induced crystallisation can be analysed. A typical DVS instrument consists of a balance (which constantly compares the weight of the sample and the reference pans throughout the experiment), humidity chamber with humidity sensors (which contains the specified humidity which is created by a water reservoir and tightly controlled nitrogen gas streams) (*Figure 2.24*).

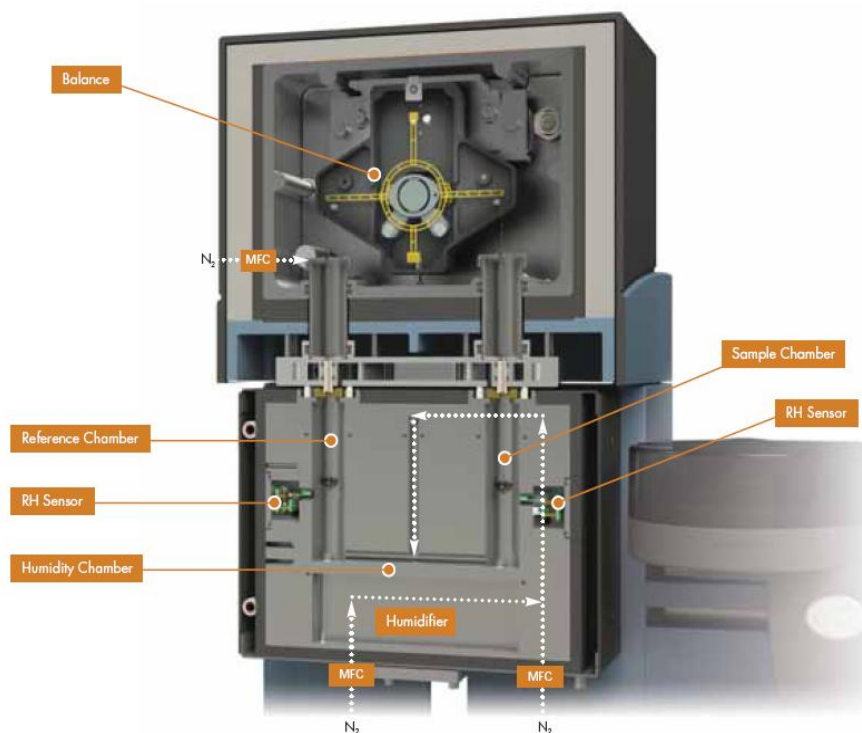


Figure 2.24 The internal organisation of a typical DVS instrument MFC = Mass Flow Controllers (taken from Q5000SA product literature from TA instruments 2010)

Sorption isotherm experiments involve a weighed sample exposed to a series of humidity step changes at constant temperature. The sample is held at each humidity level until no further weight change is detected or a set time has elapsed. The humidity is changed in controlled relative humidity steps and the process can be repeated in an increasing or decreasing procedure. Three stages of water vapour uptake occur for an amorphous solid. An initial uptake of water (surface adsorption) occurs before reaching the glass transition and prior to crystallisation, molecular mobility increases allowing bulk water absorption to occur (Hancock and Zograf, 1996). The resultant change in water adsorption rate creates an inflection in the adsorption profile which is attributed to the glass transition (Hassel and Hesse, 2007). A second transition occurs at some point on or after crystallisation which is due to increased humidity which prompts molecular re-arrangement to a more stable crystalline form (Hunter et al., 2010).

Crystallization can occur as a result of an increase in molecular mobility of the amorphous solid acquired by plasticization via water adsorption, promoting rapid nucleation and crystal growth. This is observed as a decrease in weight in the DVS profile as the crystalline form has a lower affinity for water than its corresponding amorphous form (Surana et al., 2004). Finally, a post-crystallisation period occurs whereby the crystalline material takes up additional water to complete crystallization. Crystallisation is a limiting factor determining the amount of water vapour that can be taken up by low molecular weight sugars for high molecular weight sugars that do not crystallise. The amount of water vapour taken up at very high humidities is almost unlimited (>50% w/v). Each amorphous sugar will sorb a different amount of water vapour under identical conditions as a result of its unique physical and chemical properties (Hancock and Shamblin, 1998).

DVS experiments were performed out on a Sorption Analyzer Q5000 (TA instruments) using quartz sample pans. The instrument was calibrated according to the deliquescence point of sodium bromide (57.60%RH). Samples of 1 to 2 mg were added to a tarred sample pan and the humidity chamber was sealed shut. An empty quartz pan was used as the reference and all experiments were run at 25°C to observe water kinetics without the influence of temperature changes. The experiments comprised of sequential humidity increments of 5%RH steps, from 10 to 90%. Each step was a maximum of 60 minutes. Data obtained was analysed using Universal Analysis 2000 software for Windows 2000/XP/Vista Version 4.7A.

2.2.9 THERMOGRAVIMETRIC ANALYSIS

Thermogravimetric analysis (TGA) measures weight changes in a material either as a function of increasing temperature or isothermally as a function of time under a controlled atmosphere. Weight changes can occur in any material and may be caused by decomposition, oxidation or dehydration. A typical TGA instrument consists of a balance (which is key to all TGA instruments), a heating system (or an infrared furnace) which controls the sample temperature, a heat exchange which dissipates heat from the furnace and mass flow controllers (MFC) which control the purge gas to the balance and furnace (*Figure 2.25*). The moisture content within a sample is an important quality control parameter as it can affect long-term stability and effectiveness as well as short-term processability. Free surface water (a source of problems) and bound water are present in most formulations. Free water refers to water that is absorbed from the environment and is not chemically attached to the material whilst bound water refers to water(s) of hydration that are chemically bound to the substance.

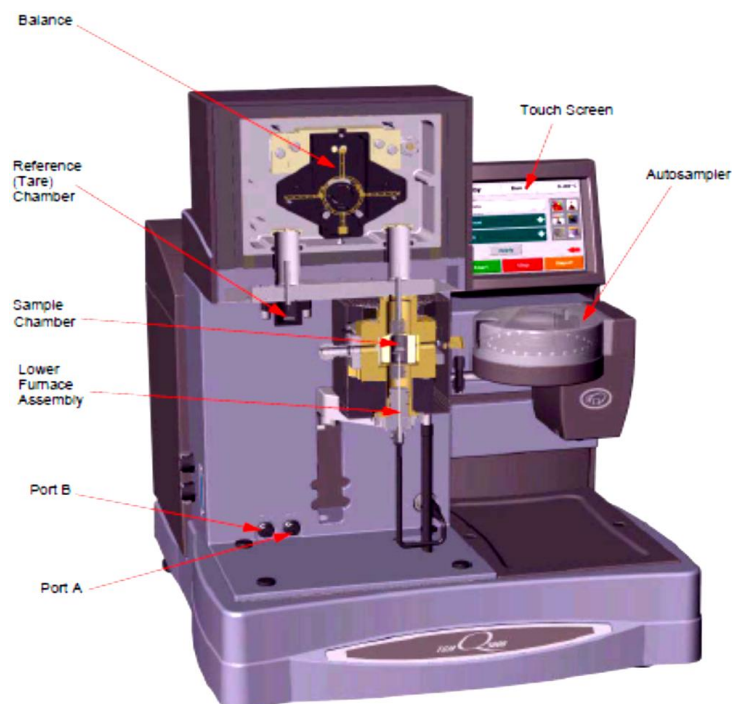


Figure 2.25 The internal organisation of a typical TGA instrument (taken from Q5000IR product literature from TA instruments 2007)

The disadvantage of this technique is that while weight changes can clearly be seen it is not always possible to determine what may have caused the change leading to possible misinterpretation of results.

TGA experiments were performed on a TA instruments Q5000IR TA instrument at a rate of 2°C/min from 30°C to 250°C using 10µL TA aluminium pans with corresponding lids. Data obtained was analysed using Universal Analysis 2000 software for Windows 2000/XP/Vista Version 4.7A.

Weight calibrations were performed once a month as recommended by the manufacturer's guidelines. The calibration involved using the automatic weight calibration function where the pan differential between two weight calibration pans was used to calibrate the weight. Temperature calibration was performed at the heating rate used for TGA experiments. The Curie Point of the paramagnetic magnet nickel was used. As the standard went through its Curie Point, its attraction to the instrument magnet changed which was observed as a weight change in TGA trace. The extrapolated endpoint of this weight change was adjusted to comply with nickel's known Curie Point Temperature (358°C).

2.2.10 CONVENTIONAL DIFFERENTIAL SCANNING CALORIMETRY

Differential scanning calorimetry (DSC) measurements provides both qualitative and quantitative information for both endothermic and exothermic transitions. Information such as crystallisation kinetics and identification of structural relaxations present can be obtained from the DSC experiments. *Figure 2.26* is a DSC thermograph of polyethyleneterephthalate (PET) showing typical thermal transitions like the glass

transition (endothermic), crystallisation (exothermic) and the melt (endothermic) that are easily detected by DSC. With relatively easy sample preparation, DSC can be used to analyse both solid and liquid materials. Experiments can be performed quickly and over a wide temperature range. There are two recognised forms of DSC, heat flux (the most common) and power compensation.

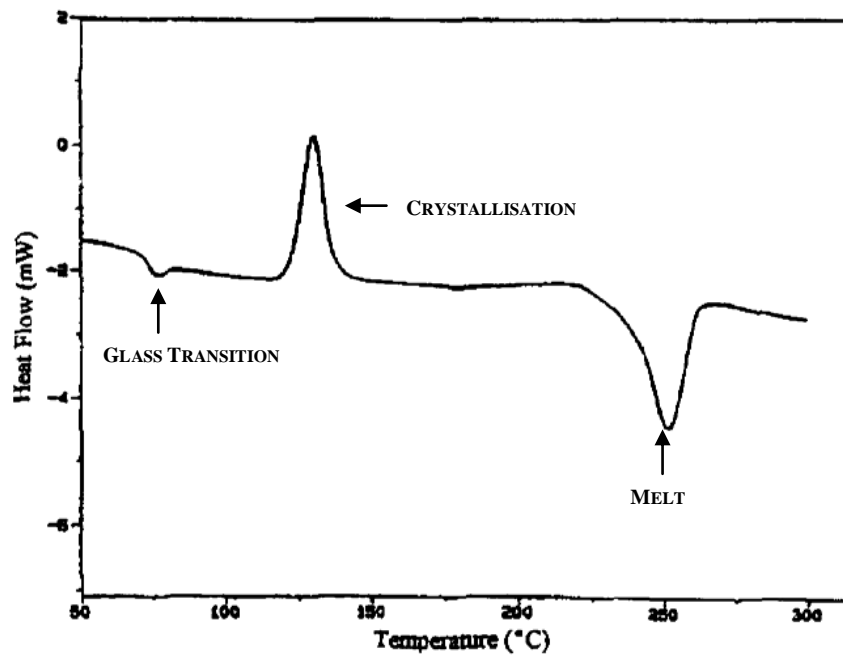


Figure 2.26 DSC Thermograph of PET showing a) a glass transition, b) a cold crystallisation exotherm and c) a melting endotherm taken from Coleman and Craig (1996)

2.2.10.1 Heat Flux DSC

Heat flux DSC consists of a sample and reference pan placed symmetrically in a furnace (*Figure 2.27*). When heated, the temperature difference between the two is measured and the resultant signal converted to heat flow. This is performed using a relationship derived from Newton's Law of Cooling and may be considered as a thermal analogue of Ohm's Law (*Equation 2.4*).

$$\Delta Q = \left(\frac{T_s - T_r}{R_T} \right) \quad \text{Eq. 2.4}$$

where ΔQ (J) is heat, R_T (KJ^{-1}), the thermal resistance of the cell, T_s (K), the temperature of the sample and T_r (K), the temperature of the reference. An assumption is made that the thermal gradients within the components of the cell (e.g. between the sample, reference and their holders) are negligible.

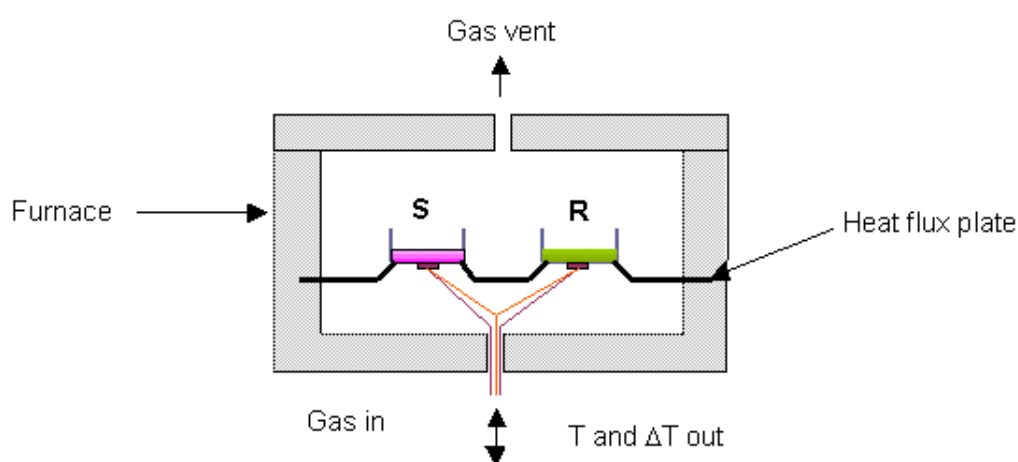


Figure 2.27 Heat Flux DSC Schematic showing sample (S) and reference (R) pan location within the same furnace (taken from <http://www.anasys.co.uk/library/dsc1.htm>)

2.2.10.2 Power Compensation DSC

Both the sample and reference pans are placed in separate furnaces in power compensation DSC (Figure 2.28). They are heated separately as opposed to both pans being heated from the sample source (as in heat flux DSC).

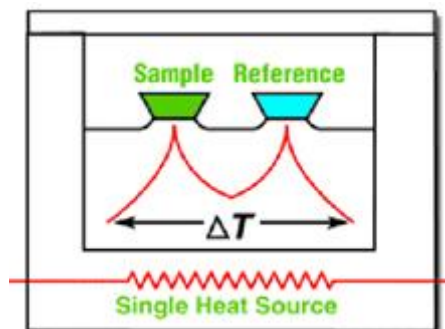


Figure 2.28 Power compensation schematic DSC Schematic showing sample and reference (R) pan location in separate furnace (taken from http://www.fchpt.stuba.sk/generate_page.php?page_id=2890)

Power compensation DSC works to maintain a zero temperature difference between the sample and reference. The power required to maintain this temperature difference is measured and is given by the following expression:

$$P = \frac{dQ}{dt} = I^2 R \quad \text{Eq. 2.5}$$

where P (W) is power, I (A) is the current supplied to the heater and R (Ω) is the resistance of the heater. (Coleman and Craig, 1996). Equation 2.6 is a simplified equation which describes the resultant heat flow at any point in a DSC or MTDSC experiment.

$$\frac{dQ}{dT} = C_p \beta + f(Tt) \quad \text{Eq. 2.6}$$

where $\frac{dQ}{dT}$ is the total heat flow, C_p is the thermodynamic heat capacity (i.e. that due to the energy stored within the sample, β the rate of temperature change and $f(Tt)$ is the heat flow from any kinetically controlled chemical or physical process (Reading et al., 1993).

Equation 2.7 shows that during a typical DSC experiment the heat flow is determined by the heat capacity. The heat capacity is defined as the amount of heat required to raise the

temperature of one gram of sample by one degree Celsius. The heat capacity at constant pressure (C_p) is give by the following equation

$$C_p = \frac{dQ}{dT} = \left(\frac{\partial H}{\partial T} \right)_{pn} \quad \text{Eq. 2.7}$$

Where Q is the heat exchanged or heat energy (J), H , the enthalpy and the subscripts ' p ' and ' n ' signify the conditions of constant pressure and composition. Finally, T (K) is the temperature. C_p can be expressed as $\text{JK}^{-1}\text{mol}^{-1}$ or as the specific $C_p \text{JK}^{-1}\text{g}^{-1}$.

C_p (at constant pressure) may also be expressed as described in equation 2.7

$$C_p = \frac{\partial Q}{\partial t_p} \times \frac{\partial t}{\partial T_p} \quad \text{Eq. 2.8}$$

where $\frac{\partial Q}{\partial t_p}$ is the heat flow and $\frac{\partial t}{\partial T_p}$ the heating rate.

DSC measurements were performed on a TA instruments DSC Q2000 with a refrigerated cooling system (RCS) attached. Dry nitrogen was used with the sample purge flow at 50mL/min. All DSC experiments and calibrations were performed using a Perkin Elmer 40 μL , 0.15mm aluminium pan (B014-3021) with an accompanying aluminium 0.05mm pin-holed lid (B700-1014) unless otherwise stated. Data obtained was analysed using Universal Analysis 2000 software for Windows 2000/XP/Vista Version 4.7A.

2.2.11 MODULATED TEMPERATURE DIFFERENTIAL SCANNING CALORIMETRY

Modulated Temperature DSC (MTDSC) was introduced in 1993 by Professor Mike Reading, under the name of Modulated DSC. It is an extension of DSC where a sine wave

modulation is applied to the standard (linear) temperature (*Figure 2.29*). As a result of the sine wave modulation, the heating rate is no longer constant but varies in a periodic (modulated) fashion (Reading et al., 1993). The period (i.e. time taken for one complete oscillation, i.e. reciprocal frequency) of temperature modulations is selected to allow for sufficient time for the heat flow to and from the sample during the temperature cycles.

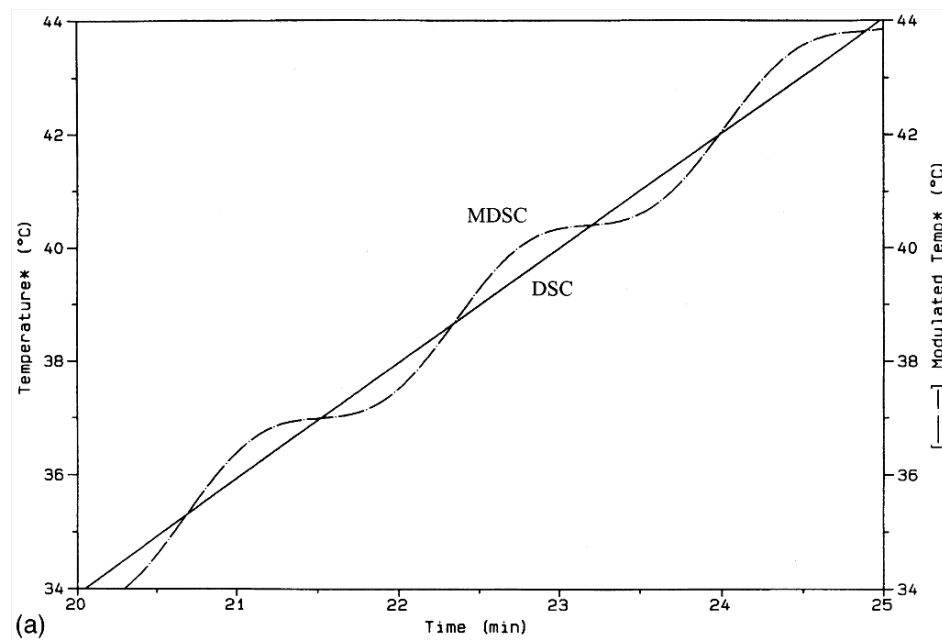


Figure 2.29 Temperature as a function of time for a typical DSC and MTDSC experiment (taken from Verdonck et al., (1999))

The total heat flow (only parameter observed in DSC experiments) is composed of two components, the kinetic component ($f(Tt)$, non-reversing) and the heat capacity ($C_p\beta$, reversing) component (Reading et al., 1993; Jones et al., 1997). MTDSC measures the total heat flow as well as the two individual components, the reversing and non-reversing components. *Figure 2.30* shows the de-convoluted signals i.e. the total heat flow, reversing heat flow and non-reversing heat flow which is calculated by subtracting the reversing heat flow from the total heat flow.

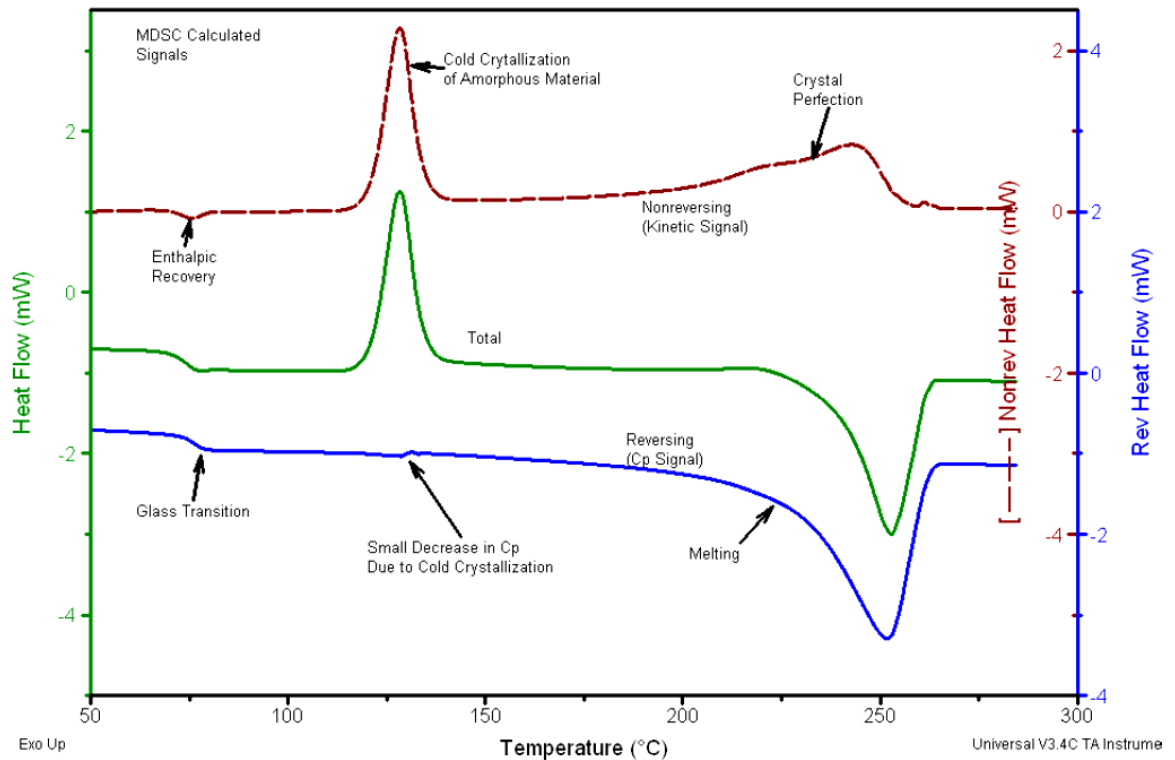


Figure 2.30 Deconvoluted signals (total heat flow, reversing heat flow and the non-reversing heat flow which is calculated by subtracting the reversing heat flow signal from the total heat flow signal) for MTDSC experiments of a quenched PET sample (taken from Thomas (2005))

In MTDSC experiments, Fourier Transform is used to separate the signals into the reversing and non-reversing components. As the reversing component is related to the sample's heat capacity, the glass transition event is accurately detected in the reversing heat flow. The T_g is shifted slightly in the reversing heat flow compared with the transition in the total heat flow, because the glass transition is a kinetic event and is affected by the applied frequency (Jones et al., 1997). The enthalpic relaxation and subsequent re-crystallisation are seen only in the non-reversing heat flow. MTDSC allows for the separation of overlapping transitions such as re-crystallisation and glass transition (Figure 2.30), which is of benefit when characterising complex materials. T_g in this thesis were calculated using the reversing signal for accuracy.

The general recommendations to select optimised MTDSC parameters for all thermal events (i.e. the underlying linear heating rate, R , temperature modulation amplitude, A , and temperature modulation period, P) are provided in *Table 2.6*.

Table 2.7 General recommendations to select optimised MTDSC parameters for all thermal events (Taken from Guinot and Leveiller (1999))

PARAMETER	RECOMMENDED RANGES OF EXPERIMENTAL VALUES
Modulation period (P)	40–100 s; a value of 60 s is generally recommended when using standard aluminum crimped pans and nitrogen purge gas
Underlying linear heating rate (R)	1–5°C:min; a value of 5°C:min should not be exceeded to allow for the specimen to follow the modulation; values below 1°C:min should be preferred whenever possible to ensure enough
Modulation amplitude (A)	$\pm 0.1^\circ\text{C}$ to $\pm 3^\circ\text{C}$ for a given linear heating rate, R , and period, P ; larger values: enhanced sensitivity; smaller values: enhanced resolution

To ensure optimal instrument performance routine calibrations i.e. baseline calibration, temperature and cell constant were performed on a monthly basis and also with any change of experimental parameters including pan type. Calibrations were performed using the TA instruments software “Advantage for Q series calibration wizard”. The DSC temperature was calibrated using *n*-octadecane ($T_m = 28.24^\circ\text{C}$), indium ($T_m = 256.66^\circ\text{C}$) and Tin ($T_m = 231.93^\circ\text{C}$) at 0.5, 1, 2, 10, 50 and $100^\circ\text{C}/\text{min}$. The heat capacity constant calibration was performed using aluminium oxide TA sapphire discs at 0.5, 1 and $2^\circ\text{C}/\text{min}$ with $\pm 0.212^\circ\text{C}$ modulation amplitude and 60 s period.

2.2.12 QUASI-ISOTHERMAL MODULATED TEMPERATURE DIFFERENTIAL SCANNING CALORIMETRY

MTDSC experiments are dependent not only on the underlying heating rate but also the modulation amplitude and period. As a result the modulated heating rate, the modulated heat flow and therefore heat capacity can have finite values even when the underlying heating rate is zero (i.e. under quasi-isothermal conditions). Quasi-isothermal MTDSC (Qi-MTDSC) is a variant of MTDSC where the temperature of the sample is modulated around a constant underlying temperature for a specified time. The temperature is then incrementally ramped up or down through a transition consisting of a series of quasi-isothermal data sets. This effectively means that the heating rate is negated (i.e. 0°C/min) by holding the sample at a range of selected temperatures about which the sample is modulated (Lai et al., 2010). This technique enables the analysis of energetic transitions in the absence of kinetic effects (i.e. removing the influence of time). In addition, the true temperature range over which an event occurs can be ascertained as thermal lags associated with the instrument and sample can be negated using this technique (Manduva et al., 2008; Hill et al., 1998).

As discussed in *Section 2.2.11*, in MTDSC experiments Fourier Transform is used to separate the total heat flow signal into the reversing and non-reversing components. The reversing heat capacity is obtained as a result of the ratio of the amplitudes of the modulated heat flow over the modulated temperature multiplied by the cell constant (Jones et al., 1997). The non-reversing component is determined by subtracting the reversing heat flow from the total heat flow. In order to convert from reversing heat capacity to reversing heat flow, the signal needs to be multiplied by the heating rate. In Qi-MTDSC experiments, the heating rate is zero therefore the non-reversing component cannot be

determined, as illustrated in *Figure 2.31*. As a result of this the reversing heat capacity was the signal used for analysis in Qi-MTDSC experiments in this study, as illustrated in *Figure 2.31* (taken from Judovits and Gupta (2011)).

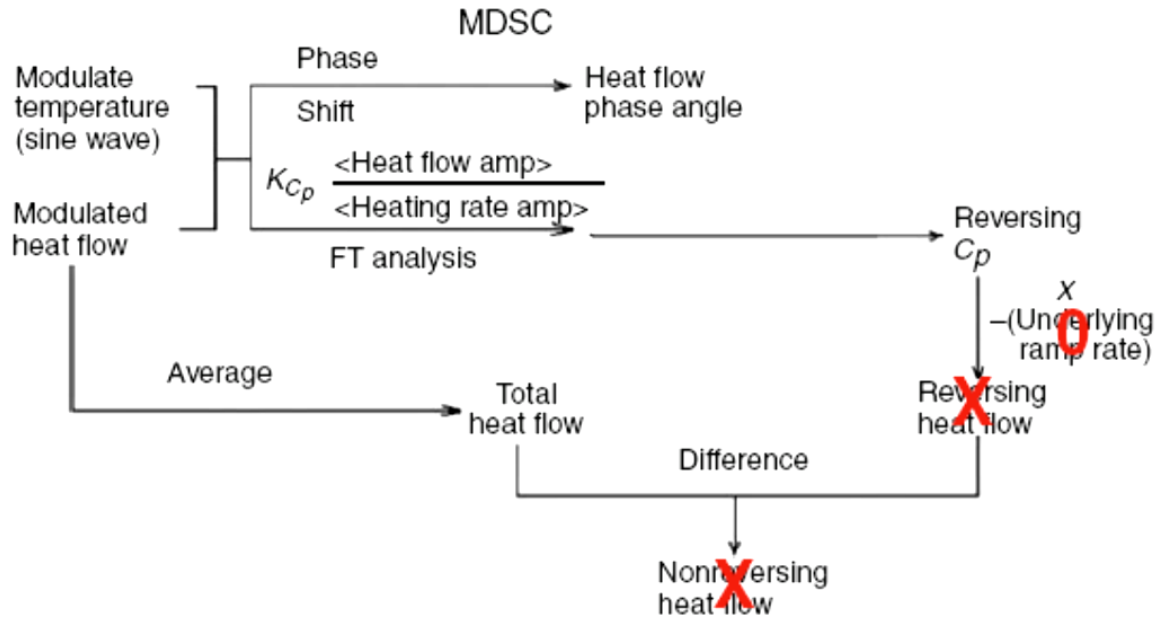


Figure 2.31 A schematic for Qi-MTDSC using a TA instruments 2920 DSC (taken from Judovits and Gupta (2011))

The measured glass transition temperature (in DSC experiments) is based on the change in the heat capacity. The magnitude of a glass transition and the ability to detect it varies with heating and/or cooling rate. The heating or cooling rate can reduce not only the sensitivity but the shape and temperature of the transition. Using Qi-MTDSC it is possible to achieve heat capacity trends that agree with theoretical predictions of the transitions (Manduva et al., 2008). Qi-MTDSC is a useful technique in identifying sample de-vitrification. In a study by Verdonck et al., (1999) PET was heated below its T_g and an increase in heat capacity was observed and corresponding to the de-vitrification of PET at T_g . A decrease in heat capacity was detected as the sample reached a temperature where cold crystallisation occurred (Verdonck et al., 1999) (*Figure 2.32*).

Qi-MTDSC methods were employed in this study as it not only allowed for the equilibrium (or at least close to equilibrium) state of a system as a function of temperature to be observed but also facilitated the observation of the process by which that equilibrium is reached.

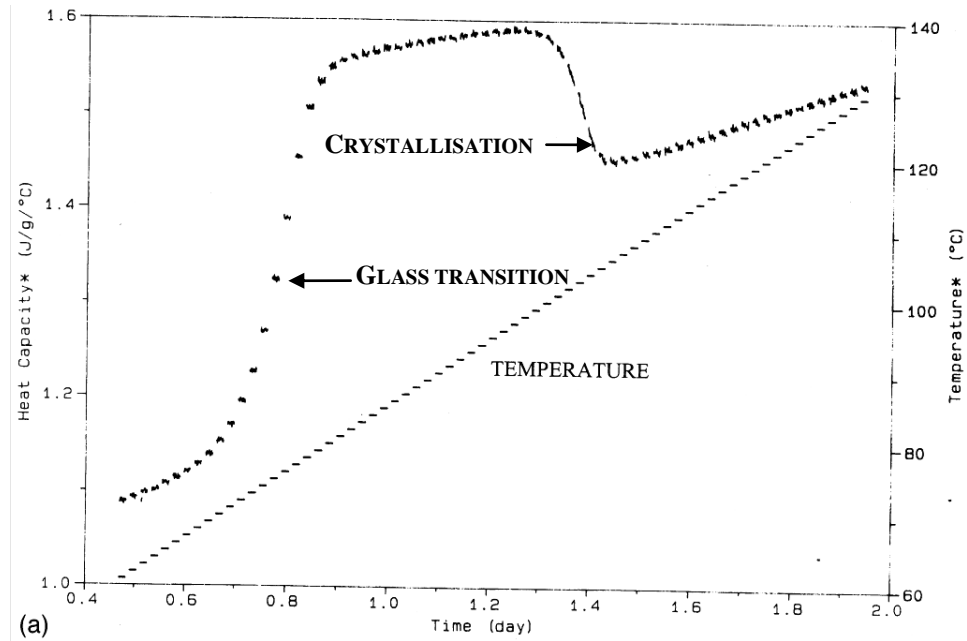


Figure 2.32 Heat capacity changes at a glass transition followed by crystallisation using Qi-MTDSC (taken from Verdonck et al 1999)

Qi-MTDSC methods were performed using a TA instruments DSC Q2000 with a temperature modulation of $\pm 1^\circ\text{C}$ and a period of 60 seconds with 2°C incremental increases over a set temperature range staying isothermal at each increase for 20 minutes. Data obtained was analysed using Universal Analysis 2000 software for Windows 2000/XP/Vista Version 4.7A.

2.2.12.1 Lissajous Figures

Lissajous figures are composed of two sinusoidally oscillating signals plotted against each other and are commonly used to investigate the response of a system to an applied modulated stimulus.

$$x = a \times \sin(2\pi ft) \quad \text{Eq. 2.9}$$

$$y = b \times \sin(2\pi ft + \sigma) \quad \text{Eq. 2.10}$$

where a and b are amplitudes, f the frequency, t is time and σ is the phase difference (Gough, 1995). If the amplitudes (a and b) are equal, this suggests that the stimulus or response are both sinusoidal with equal frequency and will therefore produce a curve that takes the form of a closed ellipse (Pockett, 2004). The shape of the figure produced depends on the frequency and phase of the two signals and can be altered when there are changes in frequency (y -axis) and phase difference (x -axis) which could result in a variety of curves (Gough, 1995). A Lissajous figure in Qi-MTDSC is a plot of the modulated heat flow as a function of time derivative of modulated temperature (*Figure 2.33*). An ellipse is generated when the modulated heat flow is out of phase with the sample temperature derivative and a phase lag has developed between the signals (Pockett, 2004).

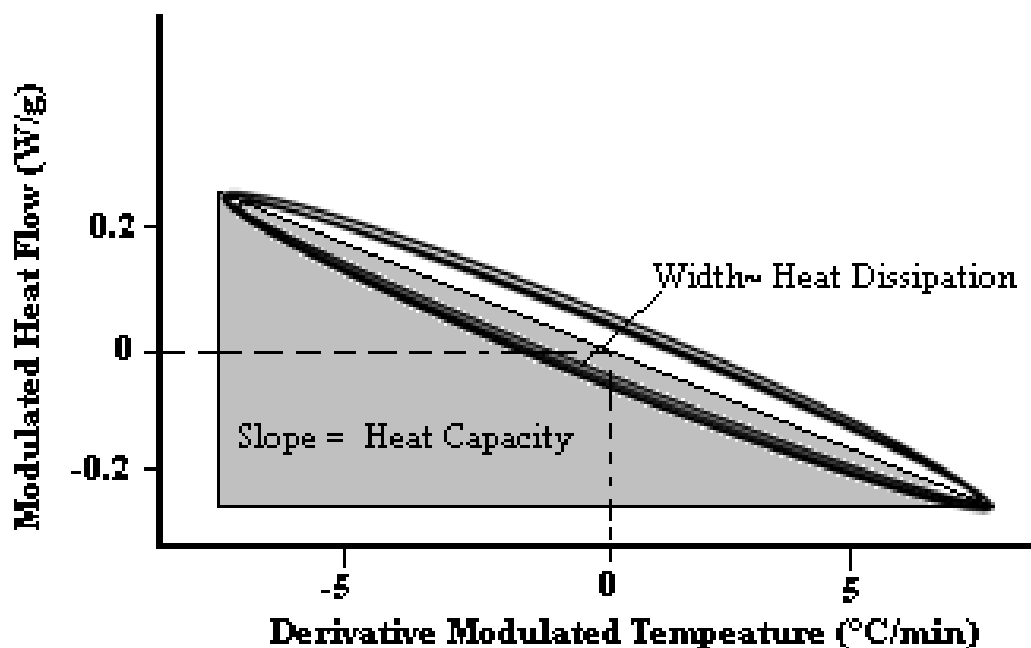


Figure 2.33 Example of Lissajous figures produced by plotting the Modulated Heat Flow (W/g) and Derivative Modulated Temperature (°C/min) of various ratios and phase differences (adapted from Kett, (2000))

The slope of the ellipse yields information about the heat capacity of the system whilst the width gives information about heat dissipation (Kett, 2000). A clear difference between the slope and width of ellipses above and below the transition should be visible. Lissajous figures may also be used in order to determine if a loss of steady state parameters has occurred as seen in previous studies (Hill et al., 1999).

2.2.13 HYPERDSC®

Slow heating rates can result in good resolution but poor sensitivity, whilst fast heating rates can result in poor resolution but good sensitivity (Gaisford, 2008). Fast heating rates have the same total heat flow as in a DSC or MTDSC experiment. However as

experiments occur over a shorter time period thermal event appears larger (Lappalainen et al., 2006). Using fast heating rates sample changes that may occur during slow heating (DSC or MTDSC) can be eliminated or reduced, allowing for the characterisation of samples in their "as received" state (Gabbott et al., 2003). This technique is also of particular advantage for materials possessing properties that may change upon prolonged exposure to increased temperatures like amorphous products or formulations of biological molecules (Gaisford, 2008). High speed or high performance conventional DSC operates at extremely fast heating rates from 200°C/min up to 750°C/min

High speed conventional DSC experiments were performed using a Perkin Elmer 8500 with 2nd generation HyperDSC® technology at heating rates of 500°C/min and 750°C/min over a temperature range of -90°C to 300°C. The instrument was calibrated using both indium and zinc standards. Perkin Elmer 40 µL pans were used with an accompanying pin-hole lid for all experiments. Data obtained was analysed using Pyris Manager software version 10.1.0.0411.



CHAPTER THREE

THE GENERATION AND CHARACTERISATION OF STANDARDISED FORMS OF TREHALOSE DIHYDRATE



3.1 BACKGROUND

The influences of batch variation of trehalose dihydrate have been briefly explored by Armstrong et al., (1996). This published abstract detailed work conducted on three different α,α -trehalose dihydrate batches by Armstrong et al., (1996). One batch exhibited a re-crystallisation exotherm at 170°C which was absent in the other two batches and two out of the three batches saw a melting endotherm at ~215°C (Armstrong et al., 1996). Differences were identified in DSC traces at 10°C/min and reducing the heating rate to 2°C/min did not eliminate these differences. Polymorphism was not identified using X-ray powder diffraction techniques. These results showed that whilst sample presentation and experimental conditions can influence the thermal response, the sample origin can also have affect on the crystal texture and consequently the observed thermal response which may persist after subsequent handling and processing.

At the time of the study presented here, further studies investigating the thermal transitions of α,α -trehalose dihydrate had not taken into account the possible contribution of inter-batch or intra-batch variations contributing to the thermal response. Preference in purchasing choice was only briefly addressed by Macdonald and Johari (2000), where they stated they preferred to purchase trehalose dihydrate from Aldrich chemicals over Sigma Chemicals Co. who at the time had a dihydrate sample of unstated purity which had previously been used elsewhere (Sussich et al., 1998; Ding et al., 1996). The objective of the work detailed in this section was to address the influence of inter-batch variation on the thermal response of trehalose dihydrate by performing a series of thermal, spectroscopic and X-ray diffraction techniques on three α,α -trehalose dihydrate batches obtained from two different manufacturers, Sigma-Aldrich and Acros Organics.

All materials are required to meet expectations of regulatory authorities though pharmacopoeia (e.g. British Pharmacopoeia) verification of materials is often only based on the identity, purity and chemical stability of the material, with only limited testing on particle and powder physical properties (Moreton, 2009). This results in materials like microcrystalline cellulose (Rowe et al., 1994) or lactose (Gamble et al., 2010) showing unexpected characteristics as certificate of analysis does not provide confidence of equivalency between batches. Several factors can result in batch to batch variation including (but are not limited to) variability in raw materials used, the manufacturing process as well as storage conditions (Moreton, 2009).

Trehalose exists in multiple crystalline anhydrous and hydrated forms and is thought to exist in two different amorphous forms, both with comparable T_g values. These properties were discussed in more detail in *Chapter 2*. The stable dihydrate undergoes a series of transformations giving rise to the generation of either dehydrated, partially hydrated or anhydrous crystalline forms or amorphous forms of trehalose. The interchange between these various forms is of considerable interest because of trehalose's ability to act as a protectant and/or stabilizing agent in pharmaceutical formulations. Reported thermal transitions of trehalose dihydrate vary with environmental conditions such as variations in humidity (Furuki et al., 2005), sample dehydration at low relative humidity at ambient temperature (Jones et al., 2006) and sample dehydration and analysis at varied heating rates (Willart et al., 2003; Rani et al., 2006).

Manufacturers' and suppliers' literature does not appear to acknowledge the existence of the various thermal transitions of trehalose dihydrate. Material Safety Data Sheets (MSDS) from Sigma-Aldrich, Acros and Fisher Bio-reagents all had listed melting points for trehalose dihydrate as 97-99°C. This melting point value appears to generally be

observed under high ambient vapour pressure and when moisture is retained within the system, suggesting dissolution of crystals as opposed to crystal melt. Investigations by Shafizad and Susott (1973) found observed dissolution of trehalose dihydrate crystals at 100°C in a tightly packed capillary tube, whilst in a capillary containing single crystals upon gentle heating dissolution of crystals was seen at 135°C. These early experiments shed light on the effect of environmental conditions on the thermal response of trehalose dihydrate as well as confusion which may arise from varied thermal responses.

Sample particle size appears to have a notable effect on the thermal response of trehalose dihydrate. Taylor and York (1998a) conducted DSC and dynamic TGA experiments at 10°C/min on different trehalose dihydrate particle size fractions (45, 75, 150, 250 and 425µm) (*Figure 3.1*). TGA data suggested water loss commenced at a lower temperature with decreasing particle size, to such an extent that the smallest particle fraction of <45µm had virtually completed dehydration by 110°C compared with large (>425µm) particles which at 110°C were just entering the temperature region of maximal weight loss. They concluded that two routes of crystallization existed for trehalose dihydrate and these routes were primarily dependent on the particle size of the crystals (*Figure 3.2*). More specifically, they suggested that larger particles crystallize directly to the stable crystalline anhydrate (T_{β}) via a solid-solid transition whilst smaller particles crystallize from an amorphous liquefied phase.

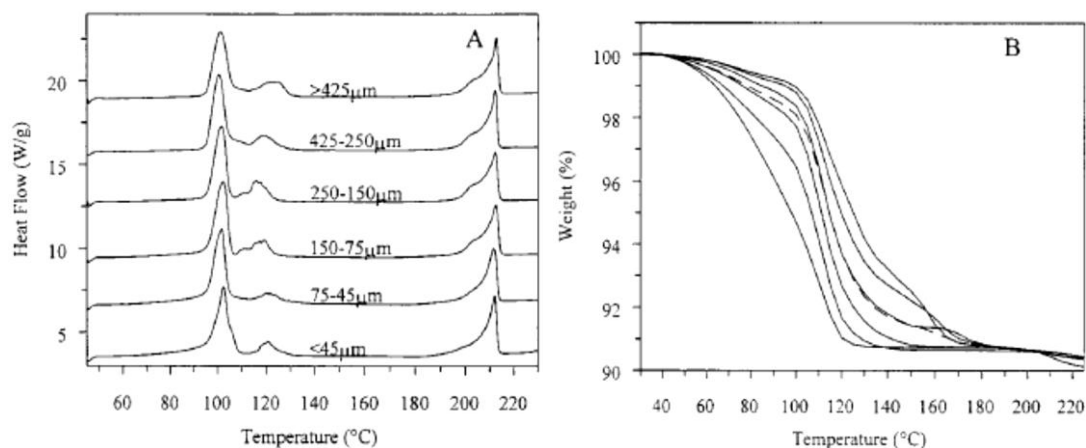


Figure 3.1 a) DSC traces of different particle size fractions of trehalose dihydrate heated at $10\text{ }^{\circ}\text{C min}^{-1}$. b) Dynamic TGA traces of different particle size fractions of trehalose dihydrate heated at $10\text{ }^{\circ}\text{C min}^{-1}$. From left to right: <45 , $45-75$, $75-150$, $150-250$, $250-425$, $>425\mu\text{m}$. The dashed line shows the material as supplied. (Taken from Taylor and York (1998a))

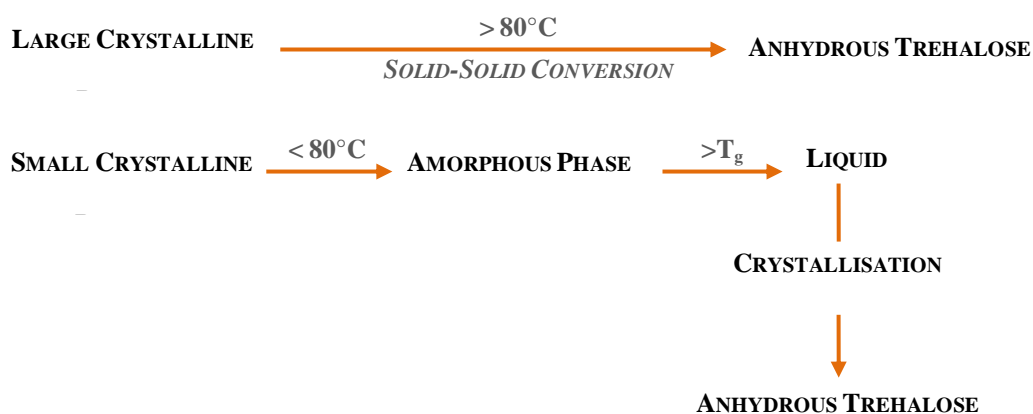


Figure 3.2 Route of crystallisation for large ($>425\mu\text{m}$) particles and small ($<45\mu\text{m}$) particles (Adapted from Horvat (2003) and Taylor and York, (1998a))

In order to fully understand the differences in the route of crystallisation for large ($>425\mu\text{m}$) and small ($<45\mu\text{m}$) particles factors which may influence the re-organisation of the dehydrate phase should be considered. It is well known that smaller particle size results in increased surface area. The larger surface area of smaller trehalose dihydrate particles would contribute to a faster dehydration rate however; the degree of disorder within the crystal lattice would also have a significant effect on the dehydration behaviour. Trehalose dihydrate obtained would have been subjected to milling during production;

smaller particles are a result of more extensive milling compared to larger particles. Therefore, smaller particles will be more disordered and likely to undergo more superficial dehydration. Dehydration would further accelerate the degree of disorder within the crystal lattice, as water plays an integral structural role within the crystal lattice of trehalose dihydrate.

3.2 PRELIMINARY WORK

3.2.1 STUDY OBJECTIVES

In this study, the effects of inter- batch variability of α,α -trehalose dihydrate were explored by performing a series of physico-chemical studies on three trehalose dihydrate batches obtained from two different manufacturers.

3.2.2 GENERAL METHODOLOGY

An array of techniques were used in this chapter to characterise three batches of α,α -trehalose dihydrate: two obtained from Sigma-Aldrich (product code T9531) Batch A (batch number 058K7357) and Batch B (batch number 020M7023) and the third from Acros Organics (product code 182550250) (batch number A0232606). For ease of referencing Sigma-Aldrich Batch A will be referred to as Sigma A and Sigma-Aldrich Batch B will be referred to as Sigma B. All samples had a stated purity of $\geq 99\%$ and were used “as received” from the manufacturers without any further purification. Particle morphology was determined using scanning electron microscopy (SEM), whilst particle size analysis was performed using laser diffraction. Sigma B particles were also subjected to separation into size fractions using the dry sieving method (mechanical agitation). X-

ray powder diffraction (XRPD) and ATR-FTIR were used as qualitative techniques to identify any differences in hydrogen bonding arrangement and crystal structure between batches. Thermal characterisation of batches was performed using differential scanning calorimetry (DSC) and thermogravimetric analysis (TGA) to determine sample water content. Hot stage microscopy (HSM) was used in conjunction with DSC to capture visual images of the samples to aid interpretation of observed thermal events. Full details of these techniques are outlined in *Chapter 2*, unless otherwise stated in the results and discussion section.

3.2.3 RESULTS AND DISCUSSION

3.2.3.1 *Particle size and morphology analysis*

Particle size analysis was performed using laser diffraction where the particle diameter is related to the light scattered through a variety of angles; further details of this technique are described in *Chapter 2*. Results are presented as the density distribution of particles (log of the volume size of the distribution) versus particle size. *Figure 3.3* (1.5 to 801 μm) shows the density distribution for all batches. Sigma B particles showed a bi-modal distribution with a mixture of large particles ranging between 360-660 μm and smaller particles 1.5-5 μm . Sigma A particles also displayed a bi-modal distribution between 160-460 μm and 33-140 μm . The Acros batch appeared to have a tri-modal distribution of particles, containing large particles ranging between 560-801 μm , 160-460 μm and finally smaller particles 1.5-33 μm . It is interesting to note the differences in distribution between all the batches, especially between Sigma-Aldrich batches. As mentioned earlier the particle size has an effect on the thermal behaviour of α,α -trehalose dihydrate with two

different routes of crystallisation identified for large ($>425\mu\text{m}$) and small ($<45\mu\text{m}$) particles.

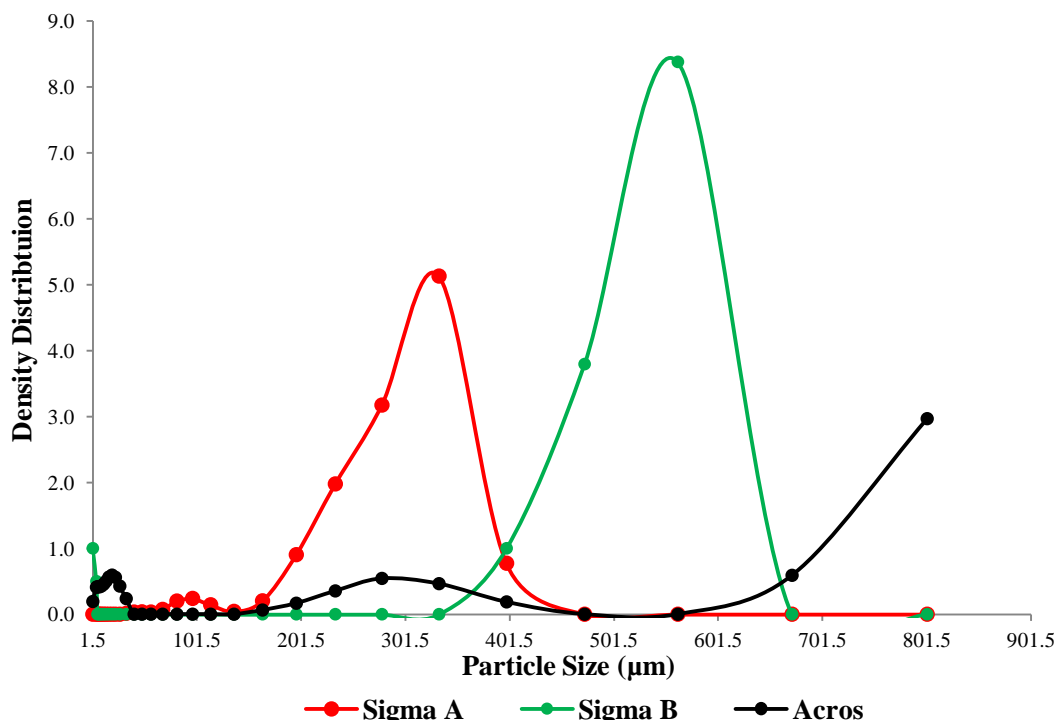


Figure 3.3 Plot showing particle size distributions for all batches (1.5 – 801.5 μm)

Particle morphology was studied using scanning electron microscopy (SEM). . *Figure 3.4* shows SEM images for all three batches. The SEM image for Sigma A illustrates large square shaped crystals with minimal aggregation, whilst Sigma B particles appeared to possess a high degree of aggregation where smaller particles had adhered to larger particles forming an agglomerate. This appears to have occurred at a greater extent with Sigma B compared to Sigma A and the Acros batch. Acros particles were rectangular in shape with evidence of some aggregation.

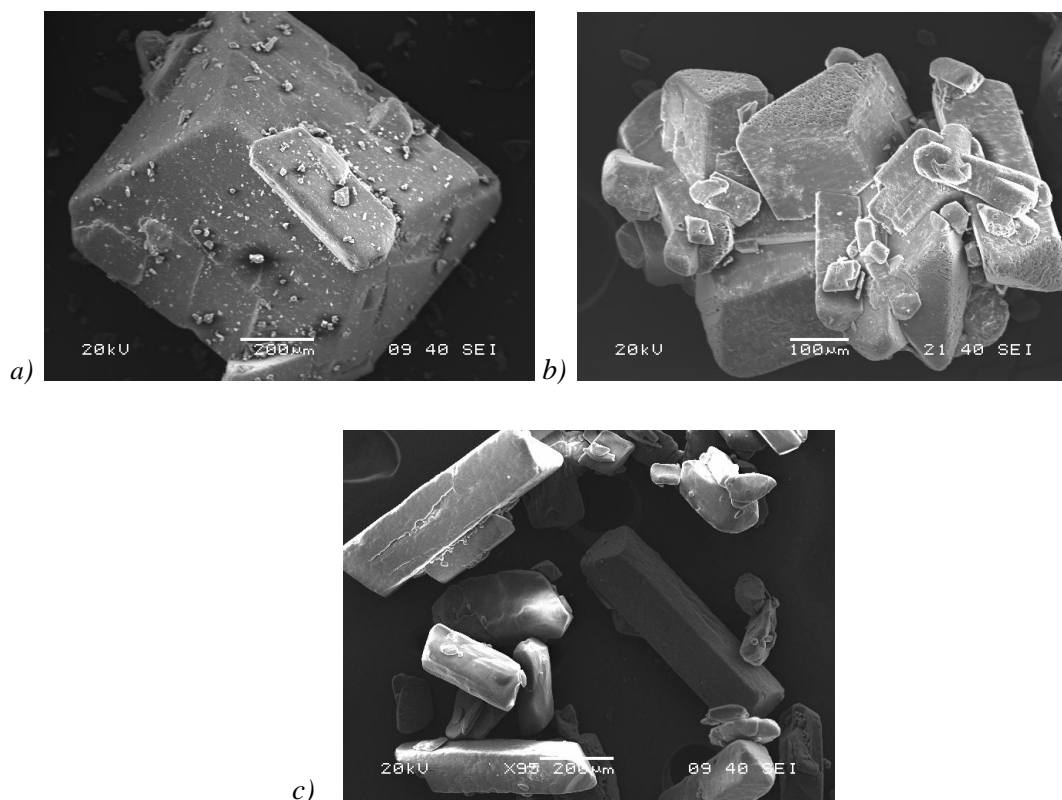


Figure 3.4 SEM images of un-fractionated a) Sigma A b) Sigma B c) Acros particles. Scale bar corresponds to a) 100 μ m b) 200 μ m and c) 200 μ m

3.2.3.2 XRPD analysis

XRPD diffractograms for all batches (*Figure 3.6, 3.7, 3.8*) were compared with calculated XRPD diffractogram obtained from crystal structures of trehalose dihydrate (Brown et al., 1972) deposited in the Cambridge Structural Database (CSD) (*Figure 3.5*). The XRPD diffractogram obtained from CSD was used as a reference.

XRPD profile of all batches (*Figure 3.6, 3.7, 3.8*) showed characteristic XRPD and expected diffractograms for α,α -trehalose dihydrate with intense peaks of ca. 2θ 23.8° and 15.2° and a small peak of ca. 2θ 8.8° observed. Though characteristic and expected peaks were identified in all samples, XRPD profile of all batches differed from the XRPD

diffractogram obtained from CSD. The reduced intensity in peaks seen in the Acros batch diffractogram at 30 to 60° was due to scaling. However, differences in the XRPD profile of all batches relative to the reference profile suggested structural variations between the batches indicating that the crystalline structure of the batches were not entirely similar.

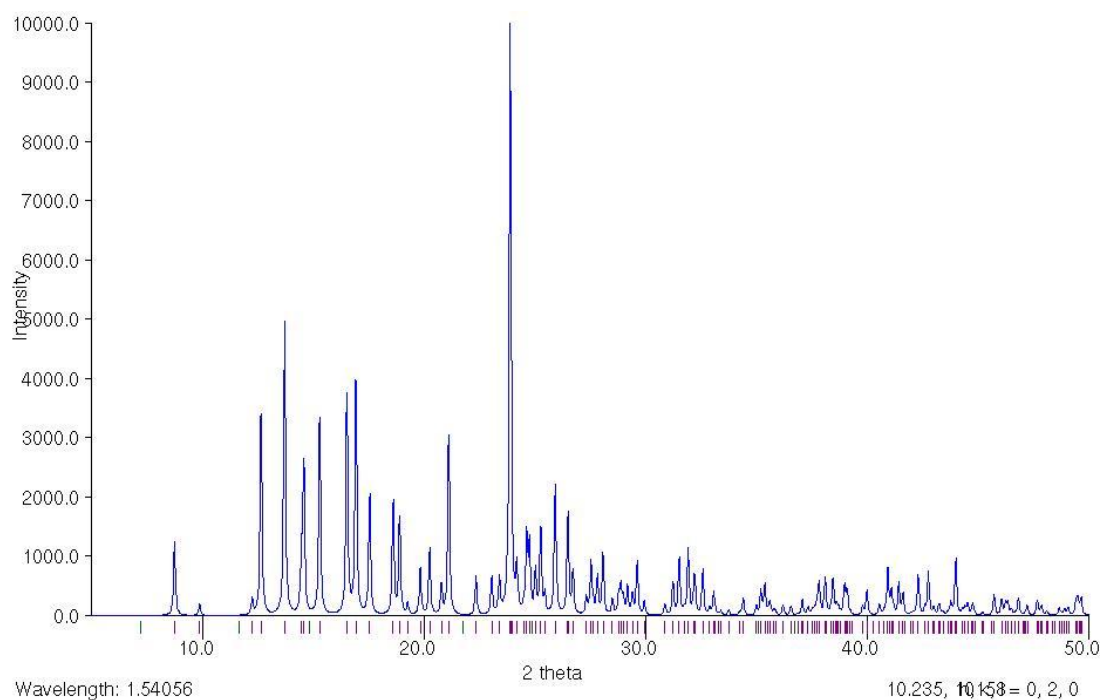


Figure 3.5 XRPD diffractogram of Trehalose dihydrate obtained from the Cambridge Structural Database (CSD) (Brown *et al.*, 1972)

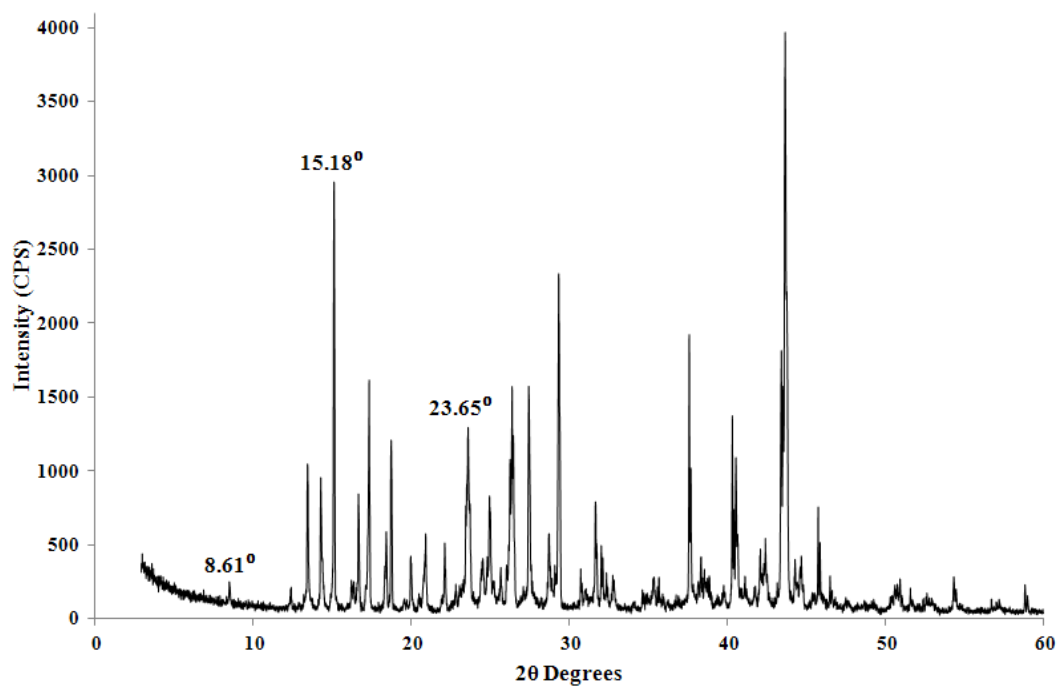


Figure 3.6 XRPD diffractogram of Sigma A

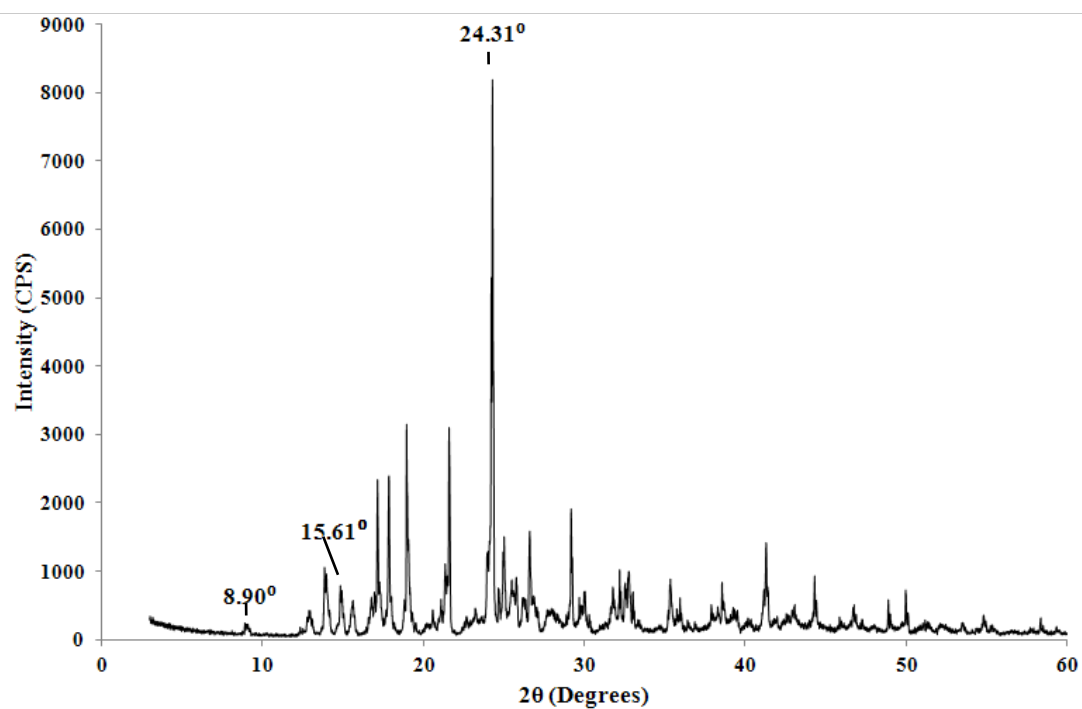


Figure 3.7 XRPD diffractogram of Sigma B

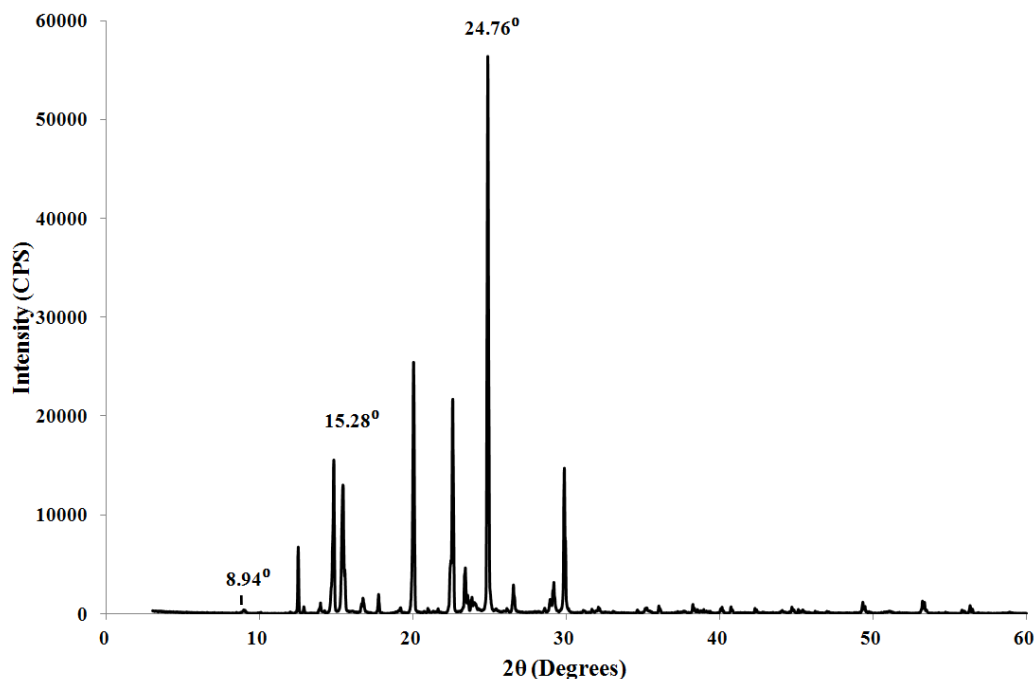


Figure 3.8 XRPD diffractogram of Acros Batch

3.2.3.3 Spectroscopic analysis

Figure 3.9 shows ATR-FTIR spectra of all three batches, which are in agreement with literature reports for α,α -trehalose dihydrate (Gil et al., 1996; Kacuráková and Mathlouthi, 1996) and showed characteristic peaks at 3500cm^{-1} , 1650cm^{-1} , 994cm^{-1} and 954cm^{-1} . A sharp band at $\sim 3500\text{cm}^{-1}$ corresponds to the OH stretch vibration of water with hydrogen bonding to other molecules. The peak observed at $\sim 3500\text{cm}^{-1}$ corresponds to the stretch vibrations of two crystal water molecules in trehalose dihydrate. This peak was observed in all samples along with a few shoulder peaks between 3600 and 3000cm^{-1} . A peak observed at $\sim 1650\text{cm}^{-1}$ is referred to as the H_2O scissoring mode of crystal water, identification of this peak confirms the presence of crystal water within a sample. Peaks observed at $\sim 994\text{cm}^{-1}$ and $\sim 954\text{cm}^{-1}$ correspond to the α -(1 \rightarrow 1) glycosidic bond. Though batches showed differences in particle size distributions and XRPD profile, ATR-FTIR spectra of all batches were identical.

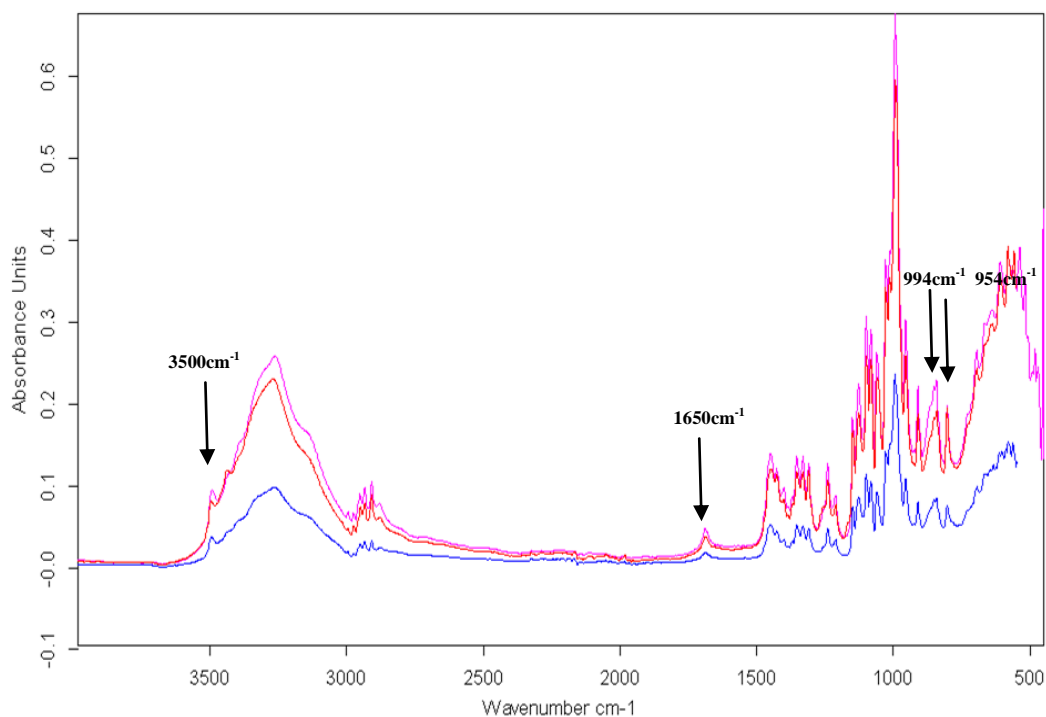


Figure 3.9 ATR-FTIR spectra of Sigma A (pink), Sigma B (red), Acros (blue)

3.2.3.4 Thermal analysis

The objective of the work described in this section was to characterise the thermal properties of Sigma A, B and the Acros batch using conventional DSC (DSC), thermogravimetric analysis (TGA) and hot stage microscopy (HSM). DSC experiments were performed using pin-holed pans at 2°C/min from 30°C to 250°C to study sample thermal transitions. Noise was observed in the baseline of Sigma B and Acros particles during DSC experiments. Therefore, hot stage microscopy (HSM) studies were used in conjunction with DSC (using the same heating parameters) to capture visual images of the samples to aid interpretation of observed thermal events. Details of these techniques are fully discussed in *Chapter 2*.

Figures 3.10, 3.11 and 3.12 show the DSC traces for all batches. Noise in the baseline was not observed in any sample before the first transition occurring ~95°C. The DSC heat flow

signal for Sigma A (*Figure.3.10*) showed a sharp low temperature endotherm at onset 95.4°C with no presence of noise in the baseline. A broad degradation endotherm was observed at onset 222.8°C. Two low temperature endotherms were observed in DSC experiments conducted on Sigma B (*Figure 3.11*) at onsets 94.6°C and 99.6°C whilst a single low temperature endotherm was observed at onset 96°C for the Acros (*Figure 3.12*) batch. For both samples, this was followed by noise in their baselines with a series of endotherms observed at higher temperatures and an irregularly-shaped endotherm at onset ~201°C and peak 208°C.

Measured water contents (TGA) for Sigma A, B and Acros batches were 9.02%, 9.20% and 9.14% respectively. These values were within the expected water content values of trehalose dihydrate of 9.5%.

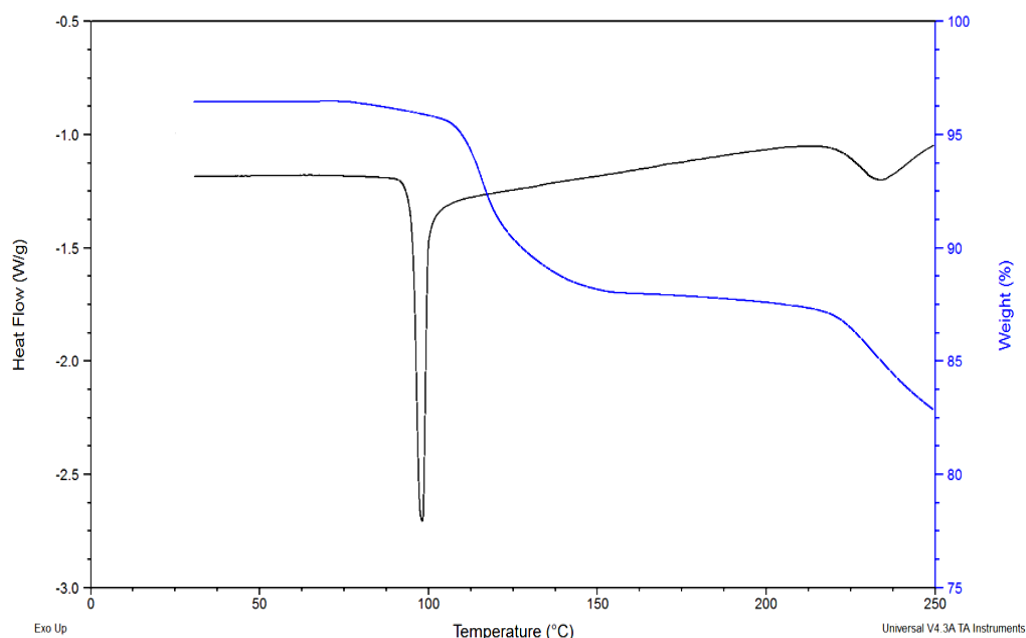


Figure 3.10 Typical TGA (*blue line*) and DSC (*black line*) heat flow signal for un-fractionated Sigma A at 2°C/min using a pin-holed pan

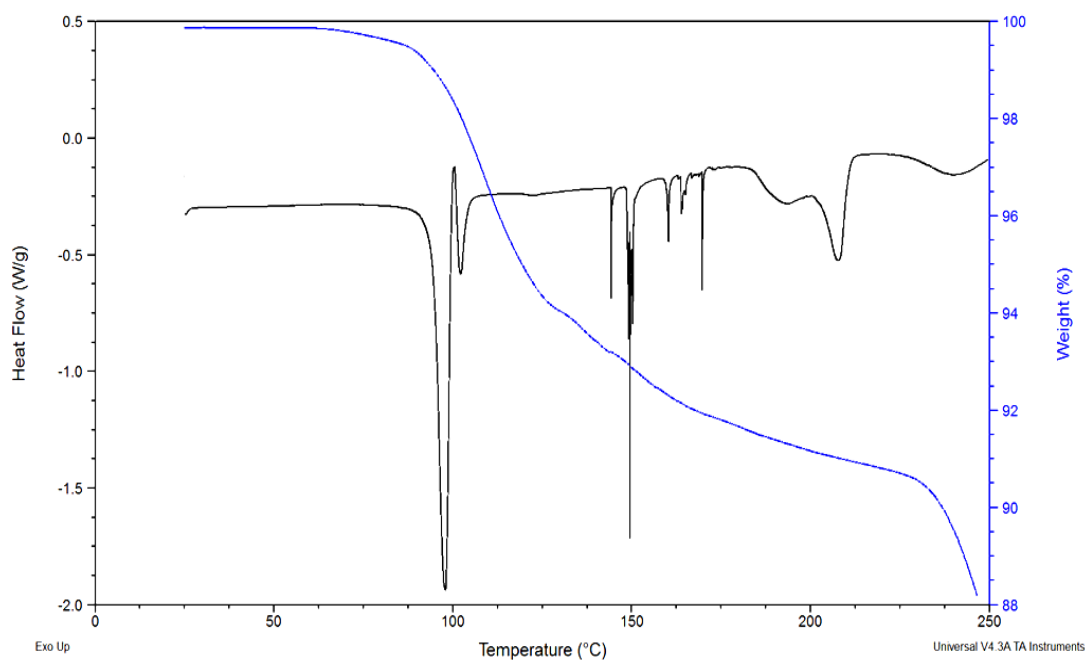


Figure 3.11 Typical TGA (**blue line**) and DSC (**black line**) heat flow signal for un-fractionated Sigma B at 2°C/min using a pin-holed pan

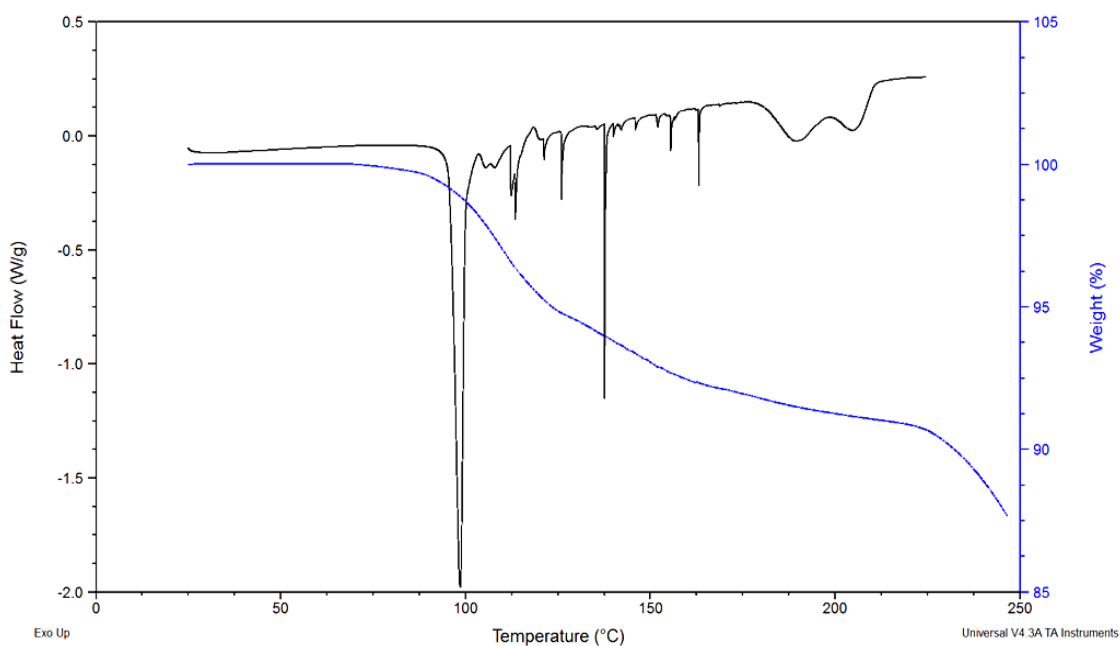


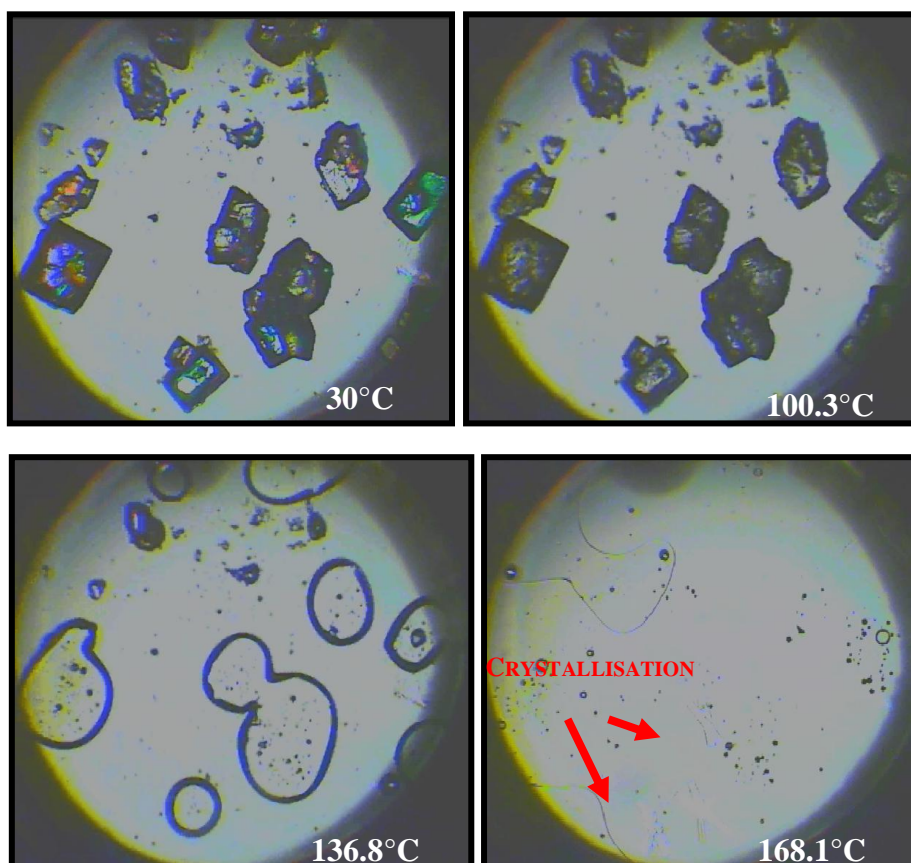
Figure 3.12 Typical TGA (**blue line**) and DSC (**black line**) heat flow signal for un-fractionated Acros at 2°C/min using a pin-holed pan.

Similar events i.e. noise in baseline at higher temperatures for un-fractionated α,α -trehalose dihydrate have been observed (Horvat, 2003) and were thought to be attributed to

a difference in the rate of dehydration of smaller particles (<45 μm) compared with the larger particles (>425 μm). All batches had varied particle size distribution which could be attributed to the observed thermal response. Noise was observed in all repeats of Sigma B and Acros batches. The results obtained identified notable differences in thermal response between batches. To shed light on these events HSM studies were conducted to capture visual images of the samples to aid interpretation of the thermal events.

HSM studies were conducted on all three batches: all were cohesive, agglomerated, coloured and showed birefringence at 30°C (*Figure 3.13, 3.14 and 3.15*). Birefringence results from the refractive index of a sample, which is derived from a ratio between the speed of light within a vacuum and the speed of light within the sample. It refers to colour produced when polarised light passes through a crystal. A sample is deemed birefringent when a light ray splits into two beams when passing through it having the effect of birefringence (or double refraction). *Figure 3.13* shows HSM images captured at specific temperatures for Sigma A samples on heating at 2°C/min. On heating a change in birefringence was observed starting at 100.3°C continuing to 119.5°C with crystals appearing darker and becoming more opaque. Further heating resulted in dissolution of crystals starting at 121.8°C in some crystals with complete dissolution of all crystals at 136.8°C. Crystallisation started at 168.1°C resulting in fully formed crystals at 188.1°C with their consequent melt at 214.6°C. *Figure 3.14* display HSM images captured at specific temperatures for Sigma B samples on heating at 2°C/min. On heating a change in birefringence was observed starting at 99°C continuing to 125°C with crystals appearing darker and becoming more opaque. Further heating resulted in the dissolution of crystals starting at 137.5°C in crystal (marked X) with complete dissolution of all crystals at 143.2°C. Crystallisation started in the crystal marked X 143.2°C. Full crystallisation in all

crystals was observed at 172.1°C with their consequent melt at 210.2°C and 213.4°C respectively. *Figure 3.15* shows HSM images captured at specific temperatures for Acros samples on heating at 2°C/min. On heating a change in birefringence was observed starting at 97.3°C continuing to 149.3°C with crystals appearing darker and becoming more opaque. Further heating resulted in the dissolution of crystals starting at 149.3°C in crystal (marked X) and followed by almost immediate crystallisation growth. Complete dissolution of all crystals occurred at 159.9°C with their melt observed at 211.8°C.



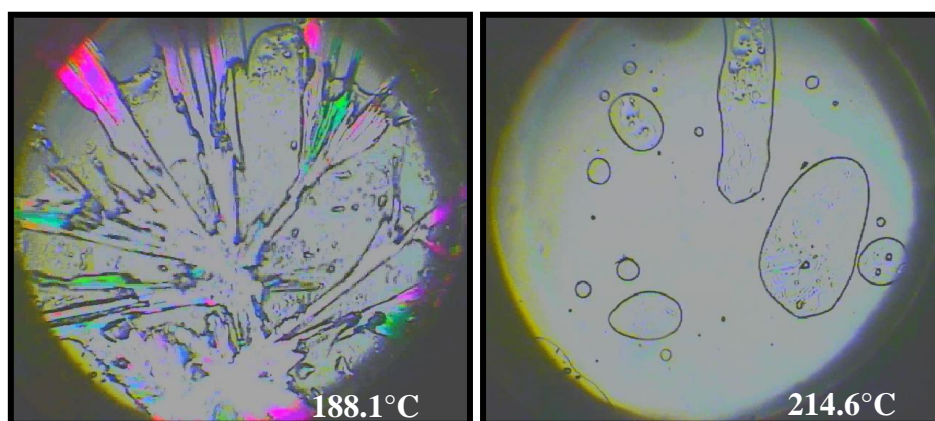
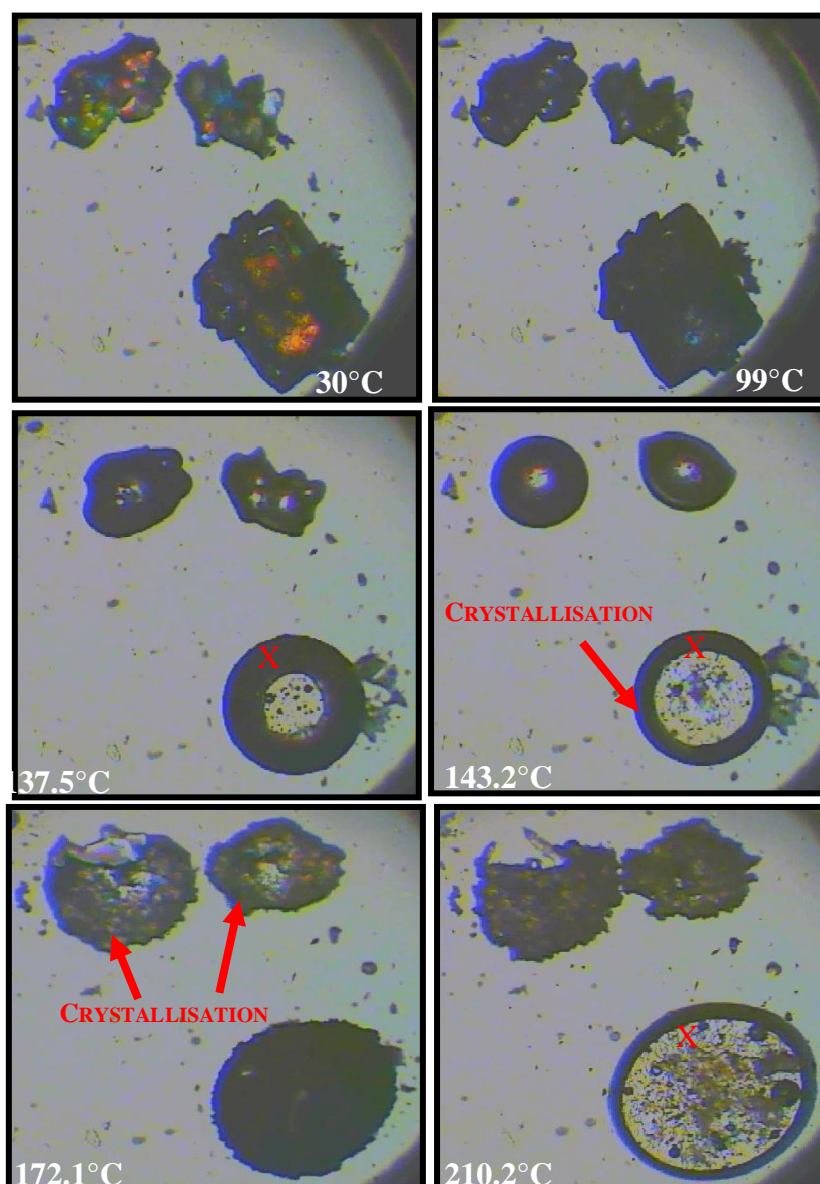


Figure 3.13 Hot stage microscopy images captured at specific temperatures for Sigma A sample heated at 2°C/min



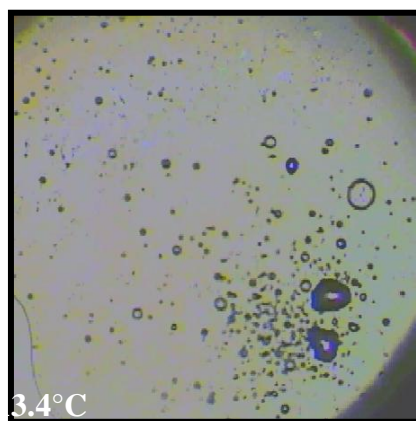
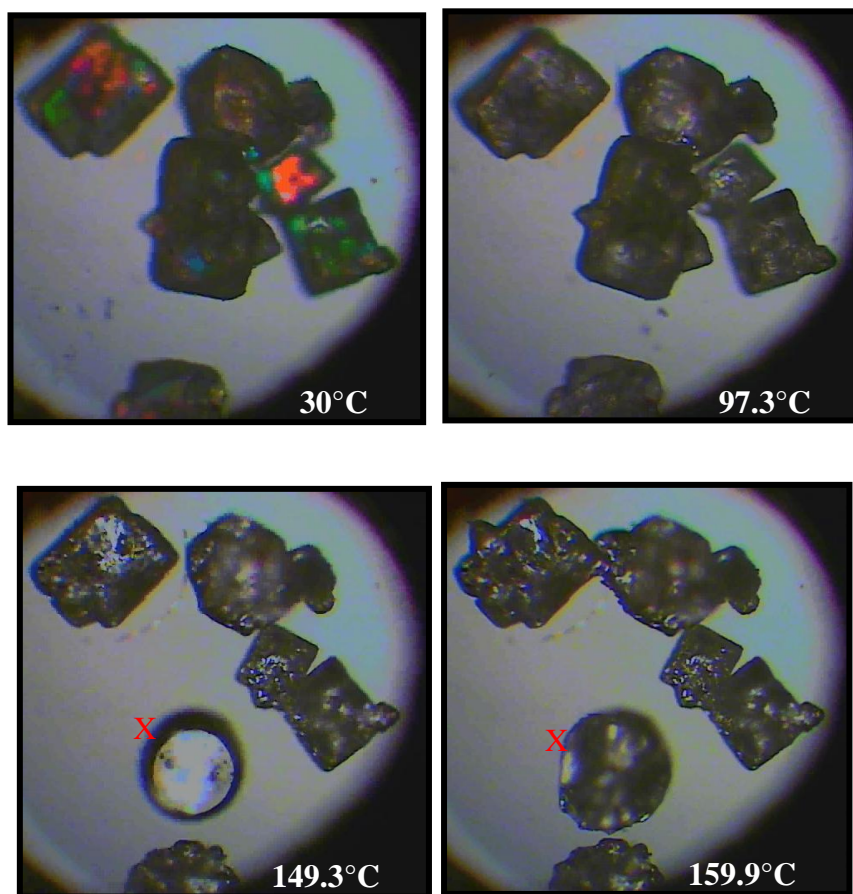


Figure 3.14 Hot stage microscopy images captured at specific temperatures for Sigma B sample heated at 2°C/min



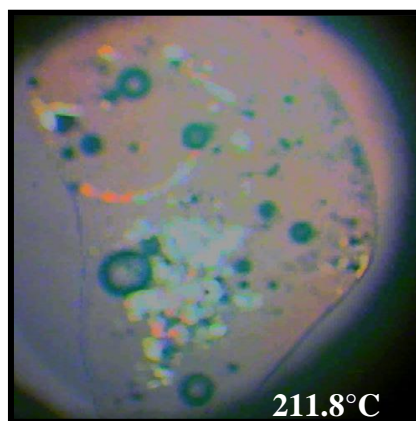


Figure 3.15 Hot stage microscopy images captured at specific temperatures for Acros sample heated at 2°C/min

Overall the results obtained from HSM studies on all batches suggested the change in birefringence observed at ~97°C could be as a result of dehydration of the stable dihydrate (T_h) possibly producing the isomorph desolvate of the dihydrate (T_a), which possess the same crystal structure of the parent crystal (in this instance T_h) with reduced hydration. Further heating resulted in the dissolution of crystals and generation of a liquid. Crystallization was observed from the liquid with the growth of needle-shaped crystals from nucleation points. It could be assumed that the generated crystals were that of the anhydrate T_β as they melted at approximately ~210°C (the documented melting point of T_β). Whilst these results were insightful they were contrary to results obtained in DSC experiments conducted at 2°C/min. In particular, the identification of a crystallisation event in HSM studies occurring at ~160°C in all batches. Evidence of cold crystallisation was not observed in DSC studies.

Reasons for difference between DSC and HSM studies could be because HSM studies are conducted in an open air environment. Relating this in DSC terms, HSM studies could

reflect events occurring in an open pan experiment. This would have an influence on results especially with trehalose dihydrate whose thermal response has been shown to be greatly influenced by pan type. Unfortunately, to date advances in the HSM technique has not taken this into account. Open pan studies were not conducted due to risk of cell contamination.

3.2.3.4.1 Using the dry sieving method to separate Sigma B particles

As both Sigma B particles and Acros particles displayed noise in the baseline in DSC experiments, the dry sieving method was adopted to separate particles into size fractions for further DSC analysis. This was to ascertain whether the observed effects were particle dependent as suggested by Horvat, (2003). Dry sieving methods involve the stacking of analytical sieves on top of each other in order of coarseness and then placing the test powder on the top sieve. Sieves are subjected to a period of mechanical agitation resulting in the separation of particles into size fractions. To allow for sufficient fraction collection a minimum initial sample mass of 25g was required. As this amount was not available with the Acros batch only Sigma B particles were analysed in this manner.

Sigma B contained a varied distribution of particles. In order to identify the cause of the noise observed in the baseline of DSC profiles the dry sieving method was used as a means of separating the particles into the following particle fractions <63 μm , 63 to 125 μm , 125 to 180 μm , 180 to 250 μm , 250 to 355 μm for DSC analysis. The majority of particles (~52%) in this batch were sized at 355 μm and above (*Table 3.1*).

Table 3.1 Particle size distribution of Sigma B obtained by the dry sieving method

Particle size (μm)	%
250 to 355	51.99
180 to 250	5.31
125 to 180	8.93
63 to 125	4.15
<63	3.53

Figure 3.16 shows a DSC trace of fractionated batch B particles. The first low temperature endotherm was observed at (onset) 94.78°C (<63 μm), 94.86°C (63 to 125 μm), 94.58°C (125 to 180 μm), 94.64°C (180 to 250 μm) and 94.41°C (250 to 355 μm), i.e. no real difference. Interestingly an exotherm was observed immediately at 99.80°C (180 to 250 μm) and 101.63°C (250 to 355 μm) but not in all size fractions. Noise was observed at higher temperatures from 143°C to 175.98°C (62 μm), 115.06°C to 171.69°C (125 μm), 160.45°C to 177.28°C (180 μm), 149.30°C to 174.75°C (250 μm) and 141.31°C to 172.98°C (355 μm). An irregular shaped melting endotherm was observed in all particle size fractions at 208°C (63 μm), 208.15°C (125 μm), 208.09°C (180 μm), 207.57°C (250 μm) and 207.16°C (355 μm).

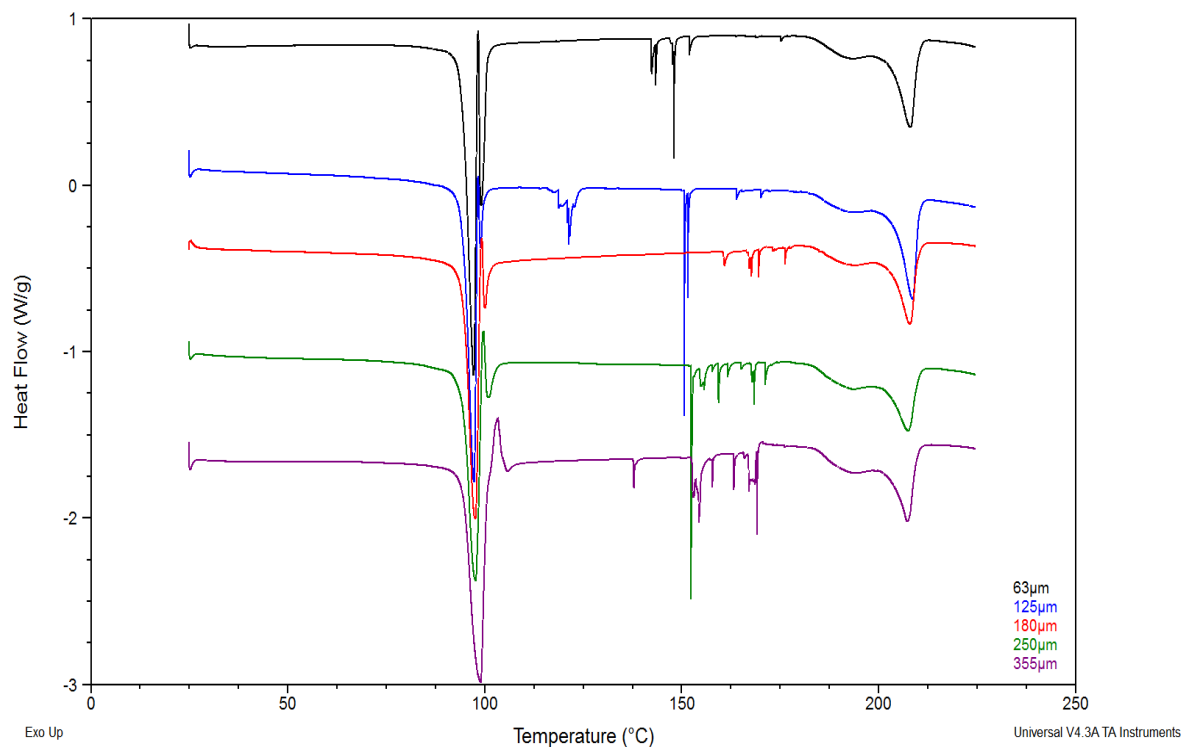


Figure 3.16 Typical DSC heat flow signal for fractionated Sigma B <math><63\mu\text{m}</math>, 63 to 125 $\mu\text{m}</math>, 125 to 180 $\mu\text{m}</math>, 180 to 250 $\mu\text{m}</math> and 250 to 355 $\mu\text{m}</math> at 2°C/min using a pin-holed pan$$$$

The results detailed in this study showed that samples with reduced particle size still exhibited noise in the DSC baseline at higher temperatures (i.e. greater than 160°C). This is contrary to previous studies where α,α -trehalose dihydrate particles (obtained from Pfanstiehl Laboratories Inc. Waukegan, IL USA) of size >180 μm showed noise in their baselines at high temperatures, whilst particles below this range did not have a noisy baseline (Horvat, 2003). These results did not confirm the influence of particle size on the thermal response. Therefore, reasons for differences between Sigma B response and the other samples could not be attributed to differences in particle size but differences in intrinsic properties of each batch which have not identified using thermal analysis techniques.

3.2.4 CONCLUSION

In this study, the effects of inter-batch variability of α,α -trehalose dihydrate were explored by performing a series of physico-chemical studies on three trehalose dihydrate batches obtained from two different manufacturers. Results are summarized in *Table 3.2*. The results in this study showed a high level of inter-batch variability between trehalose dihydrate batches. Results obtained suggested that Sigma B and Acros batches differed from Sigma A particles. Interestingly, XRPD data suggested structural variations between the batches indicating that the crystalline structure of the batches were not entirely similar. Thermal analysis characterisation of batches did not confirm the influence of particle size on the thermal response.

This phenomenon has previously been investigated elsewhere with microcrystalline cellulose (polymer) and anhydrous lactose (low molecular weighted sugar). The effect of batch variation (Landin et al., 1993a) and country of origin (Landin et al., 1993b; Rowe et al., 1994) on the properties of microcrystalline cellulose were explored.

Chemical composition and physical structure of microcrystalline cellulose was significantly dependent on both the raw materials, country of origin as well as manufacturing conditions. A study by Gamble et al.,(2010) demonstrated difference in the solid state properties of batches of anhydrous lactose obtained from three different manufactures. Whilst the variability between the samples was low there was some evidence of batch to batch variability. None of the differences observed appeared to have a significant impact on the compression or compaction properties of the batches.

Table 3.2 Summary of Sigma A, B and Acros batches results

	SIGMA A	SIGMA B	ACROS
PARTICLE SIZE	Bi-modal distribution 160-460 μm and 33-140 μm	Bi-modal distribution 360-660 μm and 1.5-5 μm	Tri-modal distribution 560-801 μm , 160-460 μm and 1.5-33 μm
SEM	large square shaped crystals with minimal aggregation	high degree of aggregation, agglomerate	rectangular in shape with some aggregation
XRPD	Expected peaks for α,α -trehalose dihydrate ca. 2θ 23.8° and 15.2° and a small peak of ca. 2θ 8.8° observed however differences in the XRPD profile of all batches relative to the reference profile		
ATR-FTIR	Characteristic ATR-FTIR spectra showing peaks at 3500 cm^{-1} , 1650 cm^{-1} , 994 cm^{-1} and 954 cm^{-1}		
DSC	Endotherms observed at 95.4°C and 222.8°C	Endotherms observed at 94.6°C, 99.6C and 201°C noise in baseline	Endotherms observed at 96°C and 208°C noise in baseline
WATER CONTENT	9.02%	9.20%	9.14%
HOTSTAGE MICROSCOPY	Change in birefringence observed at ~97°C, Further heating resulted in the dissolution of crystals and generation of a liquid. Crystallization was observed from the liquid with the growth of needle-shaped crystals from nucleation points generated crystals melted at approximately ~210°C		

Inter-batch variability can occur with all materials however, an issue arises if the variability has a significant impact on data interpretation or (if used as part of a formulation) if these difference would have a significant impact on formulation performance. Whilst the latter is outside the objectives of this study, the results detailed in this section have shown that inter-batch variability had an impact on data interpretation of the properties of trehalose dihydrate. Physico-chemical characterisation of batches did not shed light on reason for batch variability. Leading to the conclusion that differences observed here could have been due to the raw materials used or manufacturing process as

previously identified with other materials. These results highlighted a need for “standardised forms” of α,α -trehalose dihydrate to “erase” any processing history in order to achieve a clear understanding of the thermal transitions of α,α -trehalose dihydrate and ensure thermal transitions observed and forms identified are not only reproducible but are not due to inter- batch variations.

3.3 GENERATION AND CHARACTERISATION OF STANDARDISED SAMPLES OF α,α -TREHALOSE DIHYDRATE

3.3.1 STUDY OBJECTIVE

Previous work in the literature identifying and characterising the thermal transitions of α,α -trehalose dihydrate failed to take into account the possible effects of inter- and intra-batch variability on the observed response. Preliminary work detailed in *Section 3.2* performed a series of thermal, spectroscopic and X-ray diffraction techniques on α,α -trehalose dihydrate obtained from two different manufacturers. Results obtained highlighted the need for standardised forms of α,α -trehalose dihydrate to, in effect, “erase” the processing history of manufactured trehalose dihydrate, and to achieve a clearer understanding of the thermal transitions which cannot be attributed to inter- batch variations.

The main objective of this study was to generate standardised forms of α,α -trehalose dihydrate. By performing a series of physico-chemical experiments, characterise forms with a view to gain a further and clearer understanding of the thermal transitions of α,α -trehalose dihydrate with a focus on transitions occurring between 30°C and 160°C.

3.3.2 SAMPLE PREPARATION

Two methods were employed to produce two different forms of trehalose dihydrate. Method I was based on work by Dupray et al. (2009), whilst method II was based on water sorption studies (detailed in *Chapter 4*).

3.3.2.1 Method I, α,α -trehalose dihydrate crystals generated by slow evaporation of a 46.6%w/w saturated solution

Crystals were generated by preparing a saturated trehalose solution (46.6% w/w) (solubility of trehalose dihydrate at 20°C (Lammert et al., 1998)). 46.6g of trehalose (dihydrate calculated as anhydrous was dissolved in 100g of distilled (filtered 0.45 μ m) water. The solution was left to re-crystallise by slow evaporation at room temperature. For ease of referencing, these samples will now be referred to as T_{h1}. This method was originally used by Dupray et al., (2009) to generate large dihydrate crystals, though full details of crystal size were not provided by the author crystals used in their study were 2-4mm in length and 4-10mg in weight. Whilst it was not their intention to generate a standardized form of T_h, by dissolving trehalose dihydrate and allowing the formation of new crystals this in effect eliminated any manufacturer processing effects that may contribute to thermal response.

3.3.2.2 Method II, α,α -trehalose dihydrate crystals generated by exposure of amorphous trehalose to 75%RH at room temperature

Preliminary water sorption studies on amorphous trehalose used the preset sorption isotherm method of the Dynamic Vapour Sorption (DVS) (details of this method are outlined in *Chapter 2* and results are detailed in *Chapter 4*), which measures the amount of

water adsorbed over a range of RH% at a constant temperature. Based on these results freshly prepared amorphous trehalose samples (generated by spray drying) were exposed to 75%RH (using a sodium chloride saturated solution stored at room temperature) for twelve hours to ensure full crystallisation. For ease of referencing, these samples will now be referred as T_{h2}.

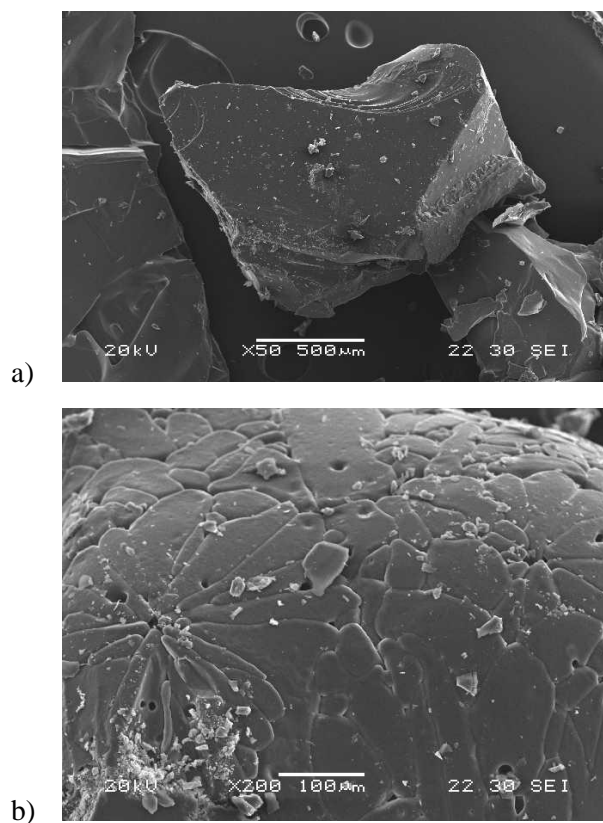
3.3.3 METHODOLOGY

An array of techniques were employed in this chapter to characterise the generated standardised forms. Particle morphology was determined using scanning electron microscopy (SEM) and particle size analysis using laser diffraction. Powder X-ray Diffraction (XRPD) and ATR-FTIR were used as qualitative techniques to confirm crystallinity as well as compare hydrogen bonding arrangement between samples. Thermal characterisation of samples was performed using thermogravimetric Analysis (TGA), conventional DSC (DSC) (at fast heating rates), modulated temperature DSC (MTDSC), quasi-isothermal MTDSC (Qi-MTDSC) and variable temperature ATR-FTIR to study thermal events. Hot stage microscopy (HSM) was used in conjunction with DSC techniques to capture visual images of the samples to aid interpretation of the thermal events observed in MTDSC and Qi-MTDSC. Full details of these techniques are outlined in *Chapter 2* unless otherwise stated in the results and discussion section.

3.3.4 RESULTS AND DISCUSSION

3.3.4.1. Particle morphology and size analysis of standardised trehalose dihydrate batches

SEM images of T_{h1} (Figure 3.17a and b) saw particles were irregularly shaped with little aggregation. T_{h2} particles (Figure 3.17c and d) were also irregular in shape and little particle aggregation. The particles however, had different surface textures with T_{h1} particles possessing more angular, defined edges whilst T_{h2} particles possessed smooth edges.



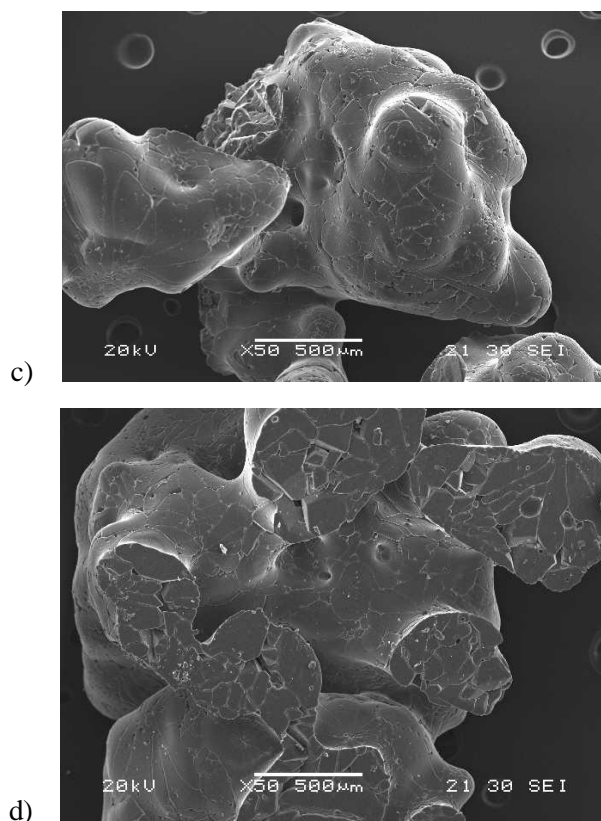


Figure 3.17 SEM image of a) T_{h1} b) T_{h1} Cross section showing grain boundaries c) T_{h2} d) T_{h2} Cross section showing grain boundaries. Scale bar corresponds to 500 μm (a, c and d) and 100 μm (b)

Particle size analysis was performed using laser particle diffraction. T_{h1} particles showed a bi-modal distribution with particle size ranging between 68 μm and 196 μm and a small portion of samples were 1.5 μm in size (Figure 3.18). T_{h2} particles (Figure 3.19), showed a normal distribution with particles ranging from 1.5 μm to 280 μm . Overall T_{h1} and T_{h2} particles were similar in size range therefore any differences observed in thermal response of these samples could be assumed not to be due to differences in particle size.

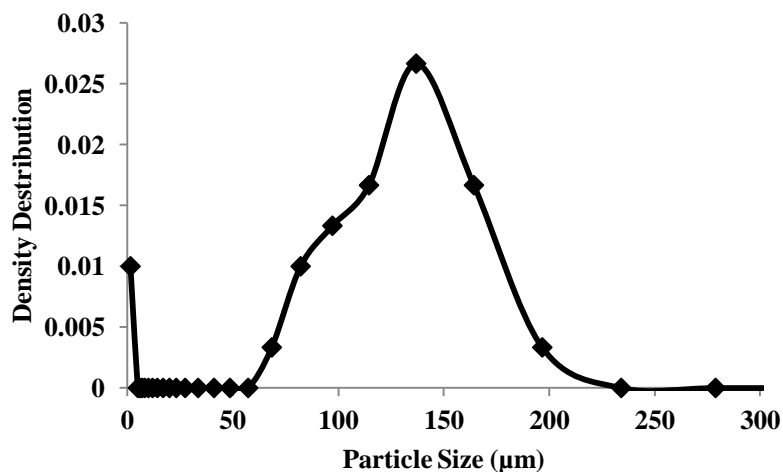


Figure 3.18 Plot showing particle size distribution from T_{h1}

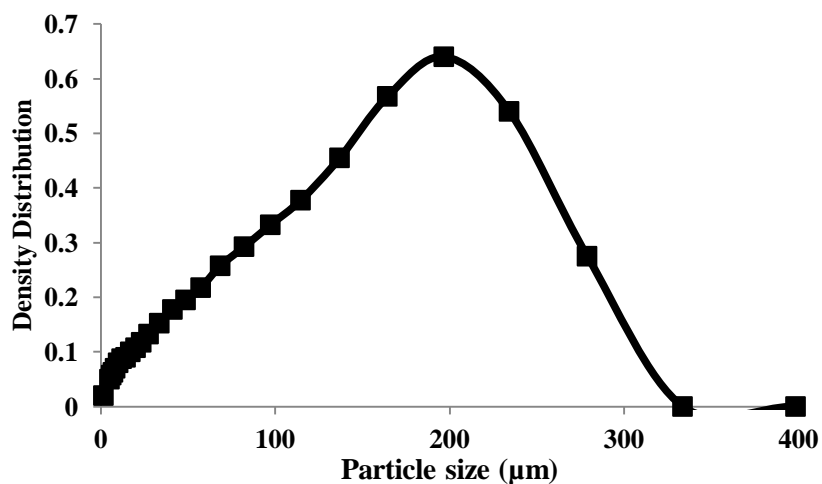


Figure 3.19 Plot showing particle size distribution from T_{h2}

3.3.4.2 X-Ray Diffraction Analysis

XRPD diffractogram obtained from crystal structures of trehalose dihydrate (Brown et al., 1972) deposited in the Cambridge Structural Database (CSD) (Figure 3.5). The XRPD diffractogram obtained from CSD was used as a reference.

XRPD diffractograms for T_{h1} (Figure 3.20) and T_{h2} (Figure 3.21) confirmed both samples were crystalline. Both forms possessed characteristic XRPD pattern for trehalose

dihydrate where peaks of ca. 2θ 23.81° (T_{h1}), 23.96° (T_{h2}) and 15.08° (T_{h1}), 15.50° (T_{h2}) and a smaller peak of ca. 2θ 8.69° (T_{h1}), 8.92° (T_{h2}).

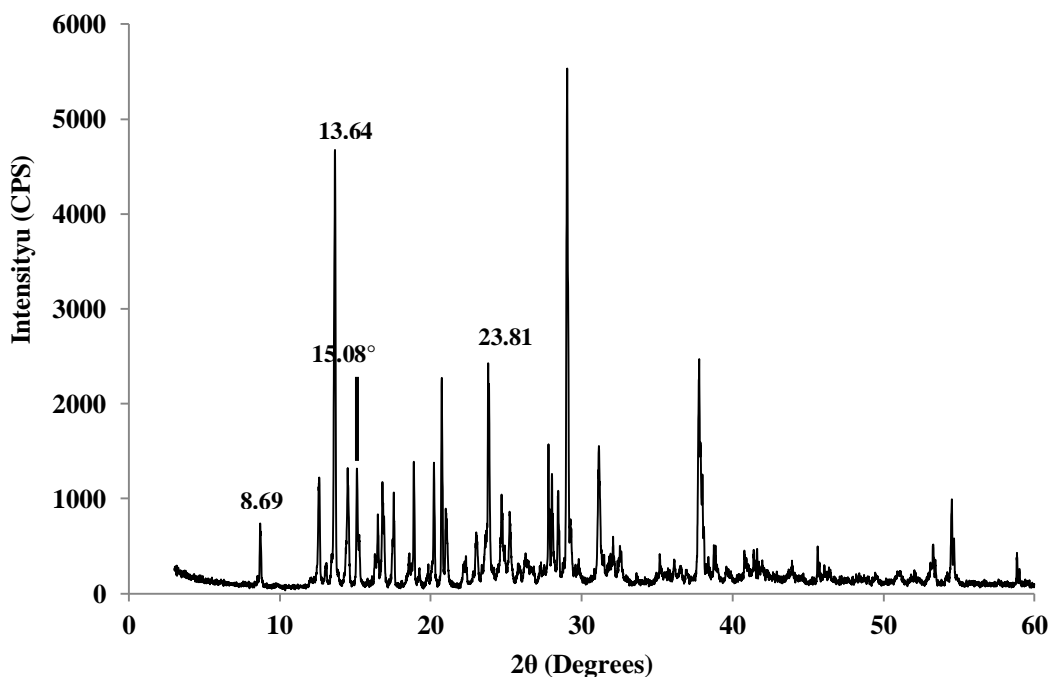


Figure 3.20 XRPD diffractogram of T_{h1} standardised form generated by slow evaporation (method I)

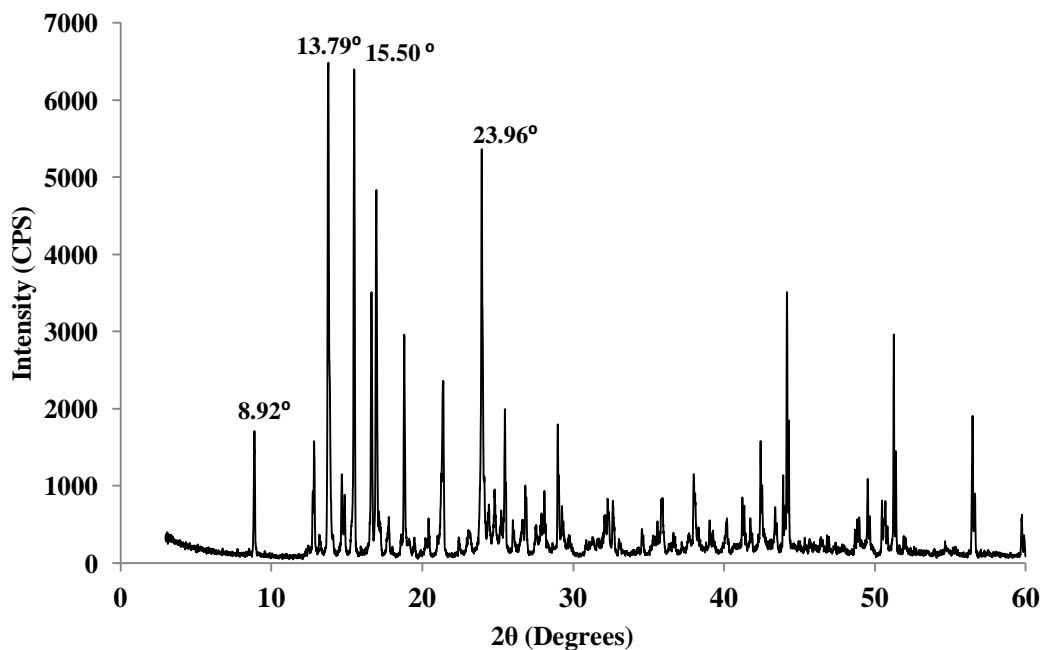


Figure 3.21 XRPD diffractogram of T_{h2} standardised form generated by exposure of amorphous trehalose to 75%RH at room temperature (Method II)

XRPD diffractograms of both T_{h1} and T_{h2} showed slight variations in peak intensities. This is related to variation in the scattering intensity of molecules within the crystal structures and arrangement within their crystal lattice

3.3.4.3 Spectroscopic analysis

Figure 3.22 shows ATR-FTIR spectra of T_{h1} and T_{h2} , which are in agreement with literature reports for α,α -trehalose dihydrate (Gil et al., 1996; Kacuráková and Mathlouthi, 1996) and showed characteristic peaks at 3500cm^{-1} , 1650cm^{-1} , 994cm^{-1} and 954cm^{-1} . These results show that although samples were generated via different methods, the resulting spectra are identical.

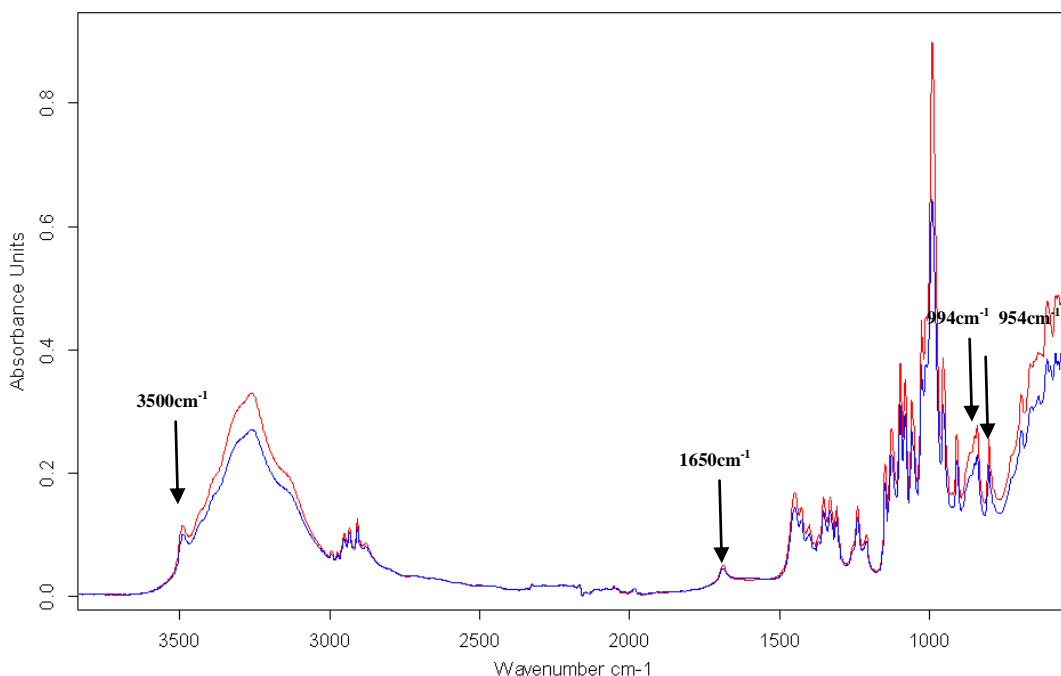


Figure 3.22 ATR-FTIR spectra of T_{h1} (blue) and T_{h2} (red)

3.3.4.4 Thermal analysis

The objective of the work detailed in this section was to thoroughly characterise the thermal properties of T_{h1} and T_{h2} using thermal analysis techniques. Thermogravimetric Analysis (TGA) was used to determine the water content whilst conventional DSC (DSC) (at fast heating rates), modulated temperature DSC (MTDSC) and quasi-isothermal MTDSC (Qi-MDSC) were used to study the thermal transitions. Hot stage microscopy (HSM) was used in conjunction with both DSC studies to capture visual images of the samples to aid interpretation of observed thermal events. Variable temperature ATR-FTIR was also used as a means of studying molecular changes as a function of temperature.

3.3.4.4.1 Effect of pan type on thermal response: pin holed pans

Previous studies observing the influence of pan-type on thermal response of α,α -trehalose dihydrate concluded that pan-type had a profound effect on the resultant thermal response. In this section the influence of pan type on thermal behaviour of both T_{h1} and T_{h2} was explored using a pin-holed and a closed pan system. Open pan system experiments were not conducted due to risk of cell contamination.

Figure 3.23 is a typical MTDSC total, non-reversing and reversing heat flow signals for T_{h1} at $2^\circ\text{C}/\text{min} \pm 0.212^\circ\text{C}$ modulation over a 60 second period using a pin-holed pan. The baseline was clear and two endotherms were observed in MTDSC experiments. The first at onset 96.3°C whilst the second broad endotherm observed at 224.3°C most likely corresponded to the degradation temperature. *Figure 2.24* is a typical TGA weight loss profile of T_{h1} heated at $2^\circ\text{C}/\text{min}$ to 250°C . T_{h1} crystals had a water content of 8.99% (expected 9.5%). TGA profile saw an initial decrease in weight loss at 72°C (2%),

followed by a second decrease at 109°C (5%) after which steady weight loss continued until 220°C, where a dramatic decrease in weight was observed, characteristic of sample decomposition.

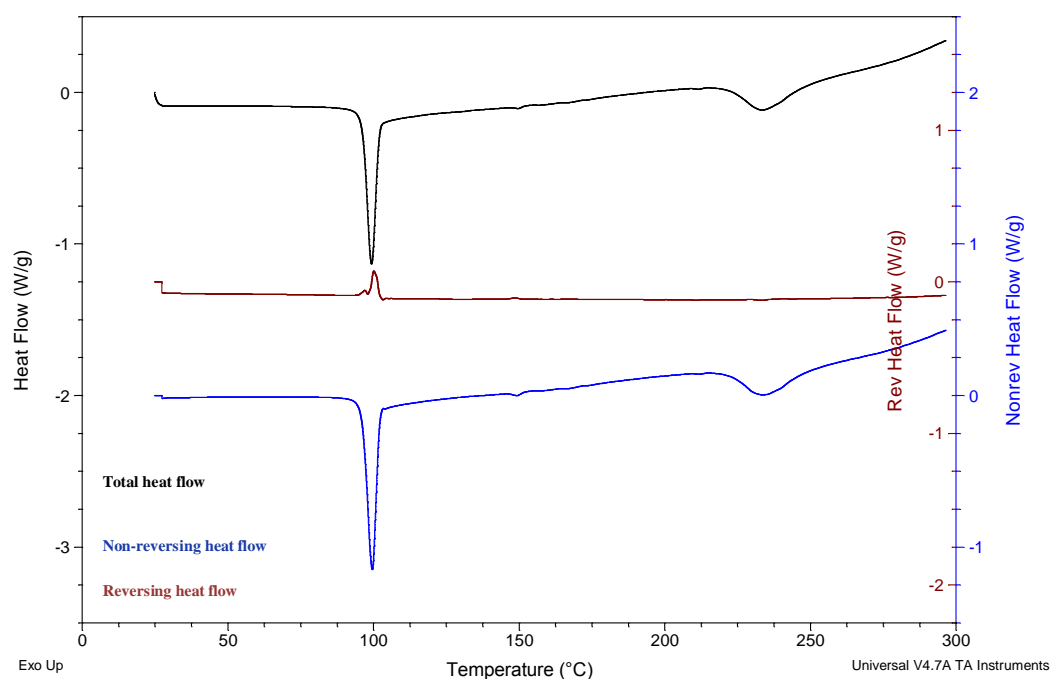


Figure 3.23 Typical MTDSC total, non-reversing and reversing heat flow signals for T_{h1} at $2^{\circ}\text{C}/\text{min} \pm 0.212^{\circ}\text{C}$ modulation over a 60 second period using a pin-holed pan

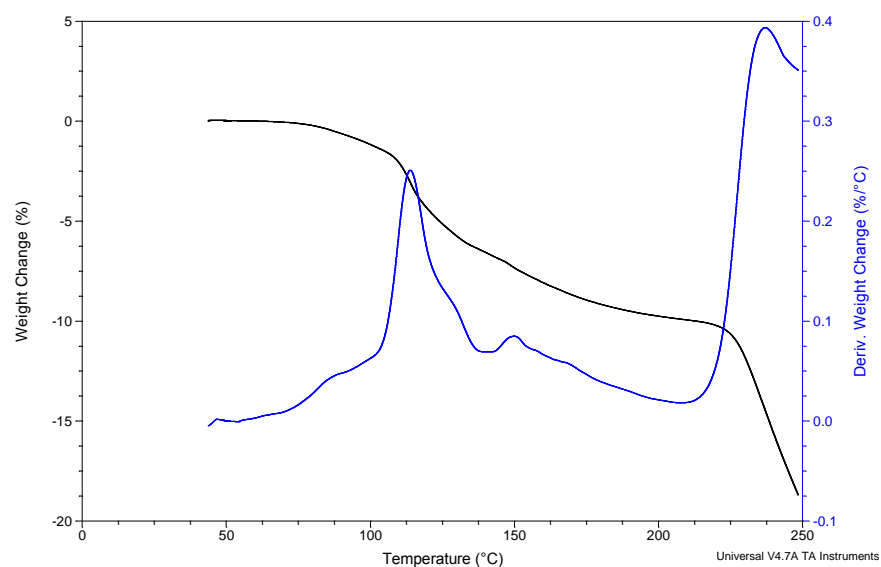


Figure 3.24 Typical TGA weight loss profile of T_{h1} heated at $2^{\circ}\text{C}/\text{min}$ to 250°C

Figure 3.25 is a typical MTDSC total, non-reversing and reversing heat flow signals for T_{h2} at $2^{\circ}\text{C}/\text{min} \pm 0.212^{\circ}\text{C}$ modulation over a 60 second period using a pin-holed pan. Three endotherms were observed at (onset) 91.6°C , 106.1°C and 209.9°C . T_{h2} crystals had a water content of 9.66%. Figure 3.26 illustrates a typical TGA weight loss profile of T_{h2} heated at $2^{\circ}\text{C}/\text{min}$ to 250°C . TGA profile saw an initial decrease in weight at 72°C (3%) followed by another weight loss event at 107°C (6%). Further weight loss was observed until 220°C , when a large decrease in weight was observed characteristic sample decomposition.

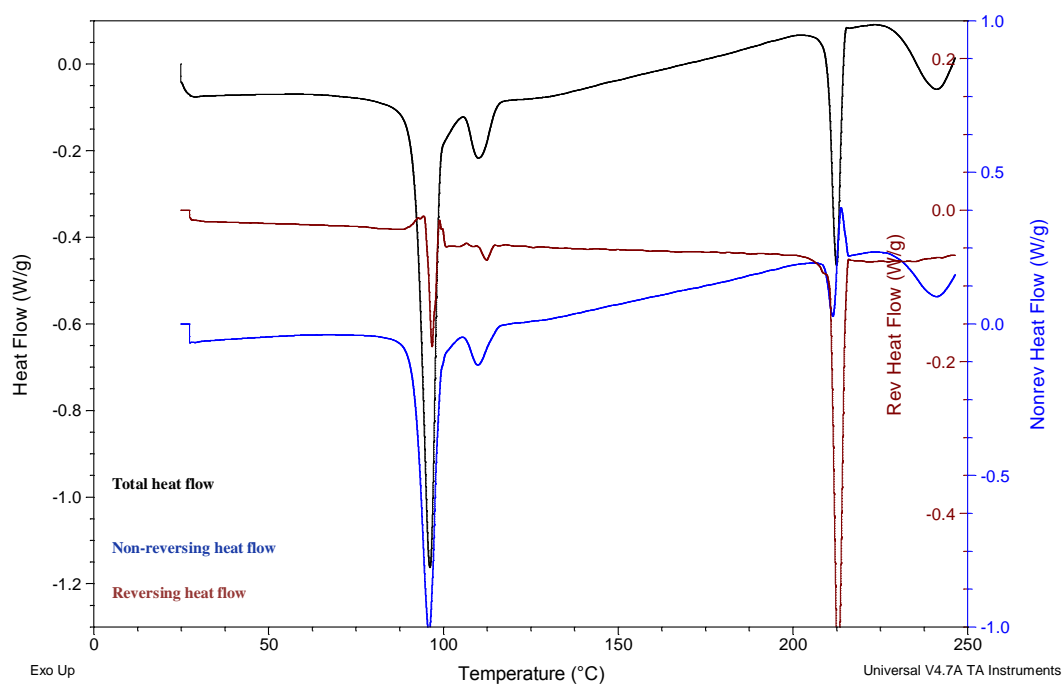


Figure 3.25 Typical MTDSC total, non-reversing and reversing heat flow signals for T_{h2} at $2^{\circ}\text{C}/\text{min} \pm 0.212^{\circ}\text{C}$ modulation over a 60 second period using a pin-holed pan

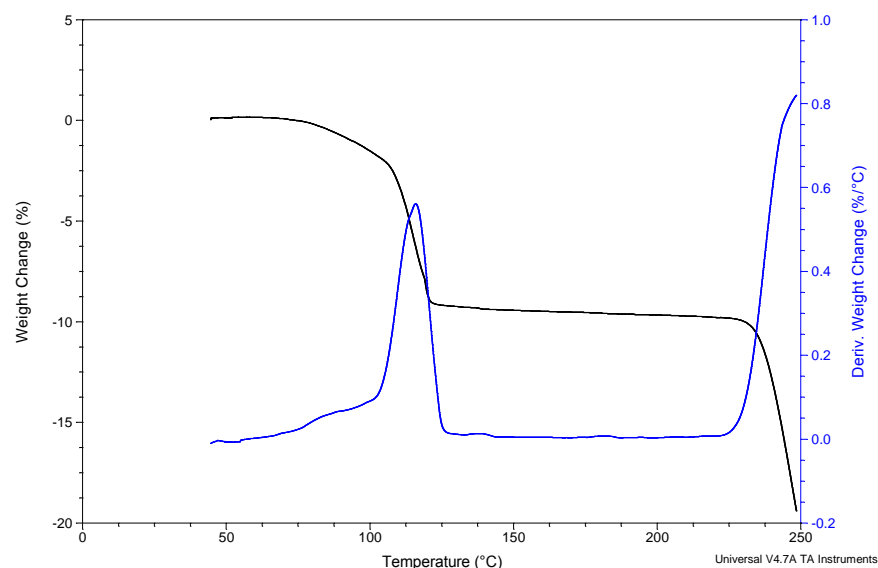


Figure 3.26 Typical TGA weight loss profile of T_{h2} heated at $2^{\circ}\text{C}/\text{min}$ to 250°C using pin-holed pan

The TGA responses for T_{h1} and T_{h2} differed. T_{h2} contained slightly more water in its crystal structure compared to T_{h1} however, both were within expected values. MTDSC studies saw a different response for T_{h1} and T_{h2} samples. On heating, a single low temperature endotherm was identified in T_{h1} samples compared to low temperature endotherms in T_{h2} samples. Both observed a single endothermic peak at 224.3°C (T_{h1}) and 209.9°C (T_{h2}).

3.3.4.4.2 Effect of pan type on thermal response: closed pan

MTDSC and TGA experiments were conducted using a Perkin Elmer $40\ \mu\text{L}$, 0.15mm aluminium pan (B014-3021) with an accompanying aluminium lid without a hole (from the “Al-Pans-Set” obtained from Perkin Elmer (B0510800)). *Figure 3.27* shows a typical MTDSC total, non-reversing and reversing heat flow signals for T_{h1} at $2^{\circ}\text{C}/\text{min} \pm 0.212^{\circ}\text{C}$ modulation over a 60 second period using a closed pan system. Two sharp endotherms

were observed. The first endotherm was observed at (onset) 95.4°C whilst the second endotherm at (onset) 119.6°C. TGA experiments (*Figure 3.28*) indicated a water content of 8.98% and weight loss profile similar to that observed in pin-holed experiments.

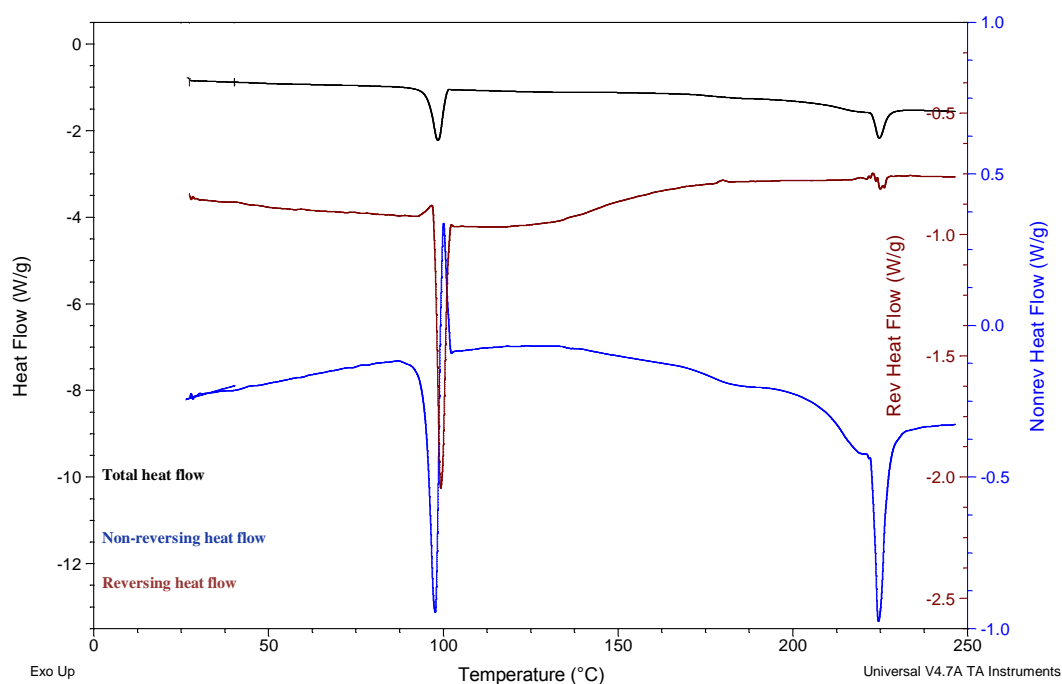


Figure 3.27 Typical MTDSC total, non-reversing and reversing heat flow signals for T_{h1} at $2^{\circ}\text{C}/\text{min} \pm 0.212^{\circ}\text{C}$ modulation over a 60 second period using a closed pan system

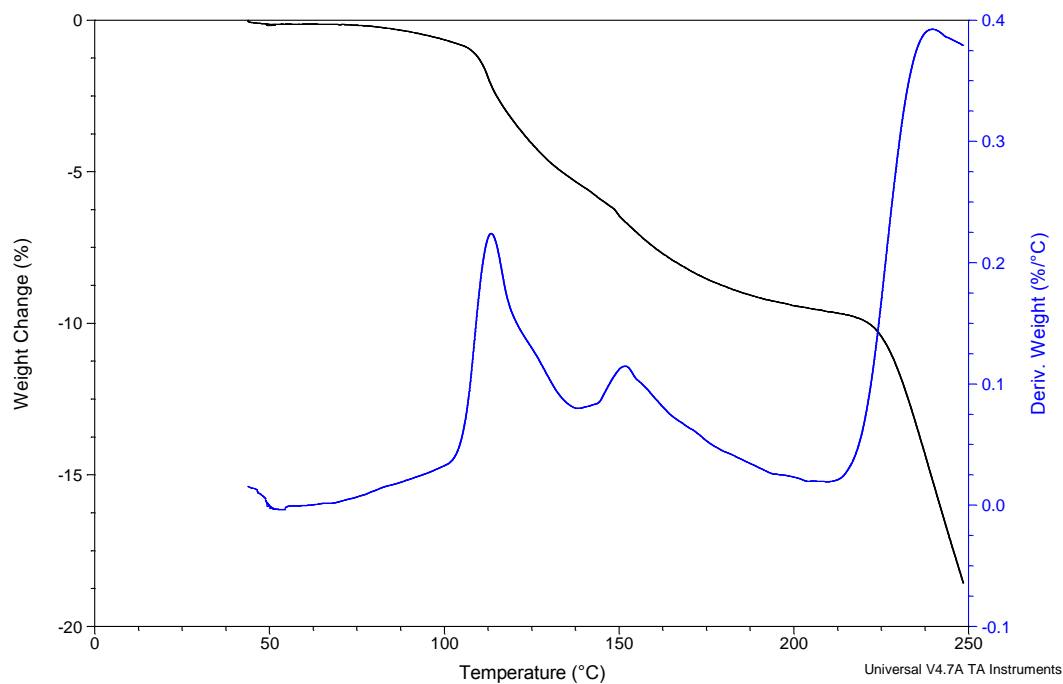


Figure 3.28 Typical TGA weight loss profile of T_{h1} heated at $2^{\circ}\text{C}/\text{min}$ to 250°C using a closed pan system

Two endotherms were observed in MTDSC experiments performed on T_{h2} using a closed pan system (*Figure 3.29a*). The first endotherm occurred at (onset) 93.9°C , whilst a crystallisation exotherm was identified immediately after in the total and non-reversing heat flow but not in the reversing heat flow (*Figure 3.29b*). This was followed by a second endotherm at (onset) 220.8°C . TGA studies indicated a water content of water content 9.56%. A second endotherm previously observed in pin-holed pan experiments at $\sim 106^{\circ}\text{C}$ was not observed in closed pan experiments. The second endotherm observed in pin-holed studies could be ascribed to water loss from the crystal lattice. TGA results (*Figure 3.30*) provided evidence to suggest that water had not completely escaped the crystal lattice at the observed exotherm temperature. Therefore, this could facilitate the generation of a hydrated or partially hydrated form of trehalose. Previous studies (Furuki et al., 2005) have speculated that an exotherm (said to occur between 100 and 160°C) observed after

the first low temperature endotherm correlates to the crystallisation of the stable anhydrate T_{β} . However, at low temperatures it would be more accurate to assume the form generated is the isomorph desolvate of the stable dihydrate, T_{α} . This form is generated by evaporation of the dihydrate (T_h). The stable dihydrate and T_{α} share a reversible relationship: when T_{α} is exposed to moisture it is reverted back to the dihydrate at low temperatures when water is still present in the system.

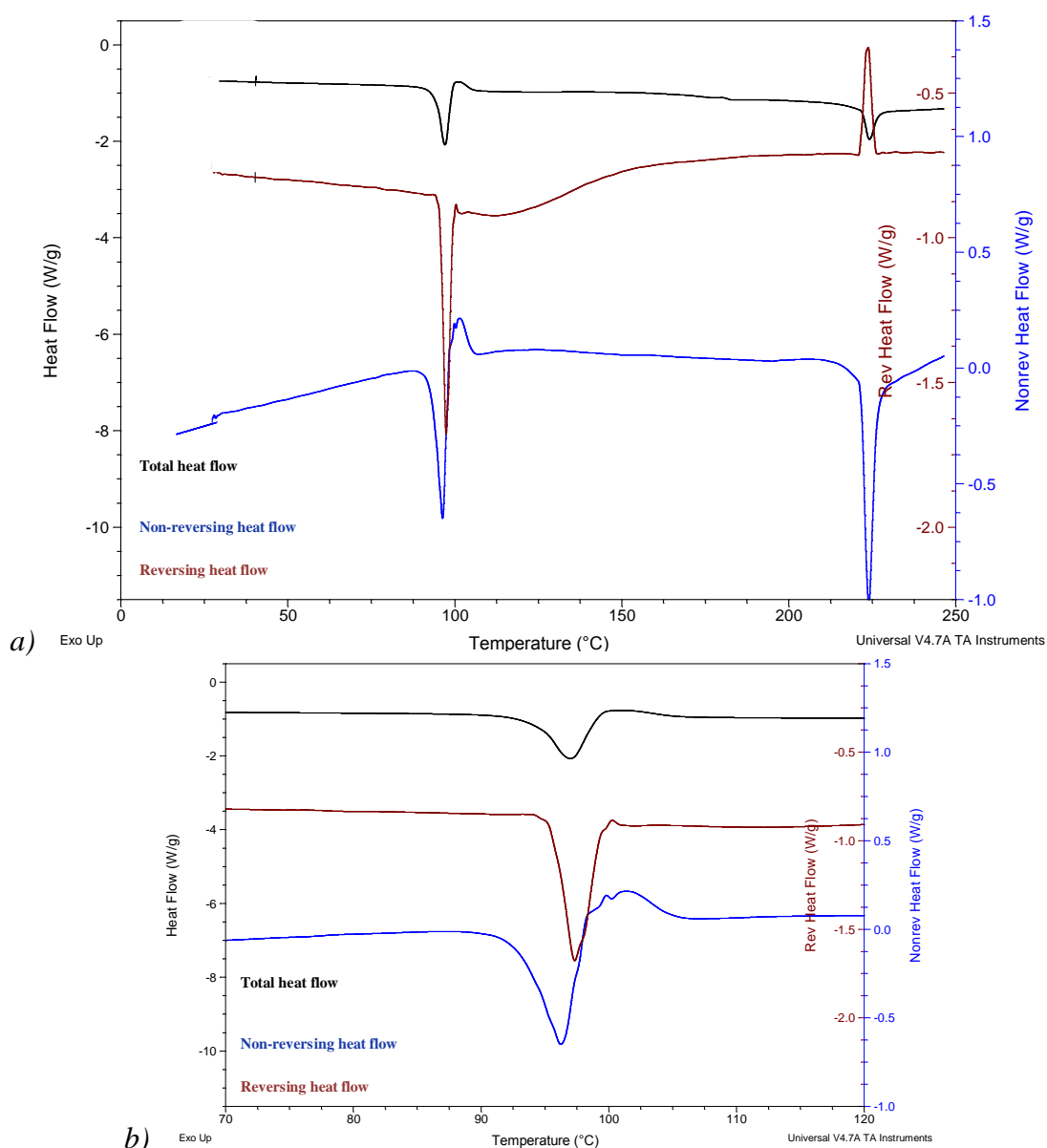


Figure 3.29 a) Typical MTDSC total, non-reversing and reversing heat flow signals for T_{h2} at $2^{\circ}\text{C}/\text{min} \pm 0.212^{\circ}\text{C}$ modulation over a 60 second period using a closed pan system b) a close up of possible crystallisation seen after low temperature endotherm.

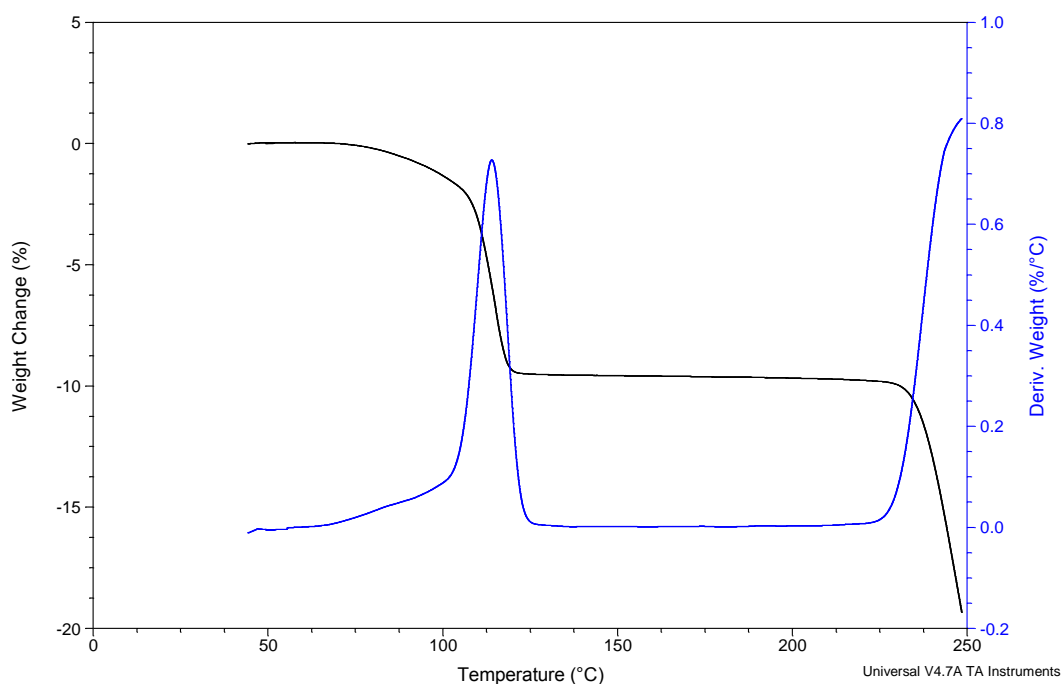


Figure 3.30 Typical TGA weight loss profile of T_{h2} heated at $2^{\circ}\text{C}/\text{min}$ to 250°C using a closed pan system

MTDSC and TGA results for T_{h1} and T_{h2} samples are summarised in *Table 3.3*. Both MTDSC and TGA results indicated that when both samples are heated in a closed pan system, water loss is impeded which in turn alters the temperature for phase transitions. The loss of two water molecules occurred over the same temperature range in both T_{h1} and T_{h2} using both pin hole and closed pans. As discussed in *Chapter 2*, water molecules within a trehalose dihydrate crystal play an integral role in its structure. The observed differences in thermal response may be explained with reference to the crystal structure, molecular arrangement and location of water molecules within T_{h1} and T_{h2} .

Table 3.3 Summary of endotherm values ($^{\circ}\text{C}$) for T_{h1} and T_{h2} MTDSC heat flow experiments at $2^{\circ}\text{C}/\text{min} \pm 0.212^{\circ}\text{C}$ modulation over a 60 second period and TGA weight loss data of T_{h1} and T_{h2} heated at 2°C to 250°C

	T_{h1}			T_{h2}		
	ENDOTHERM 1 ($^{\circ}\text{C}$)	ENDOTHERM 2 ($^{\circ}\text{C}$)	ENDOTHERM 3 ($^{\circ}\text{C}$)	ENDOTHERM 1 ($^{\circ}\text{C}$)	ENDOTHERM 2 ($^{\circ}\text{C}$)	ENDOTHERM 3 ($^{\circ}\text{C}$)
Pin holed pan	96.3 (± 0.15)	224.3 (± 1.9)	-	91.6 (± 0.24)	106.1 (± 0.57)	209.9(± 0.07)
Closed pan	95.4 (± 0.0)	227.8 (± 3.0)	-	93.9 (± 0.33)	220.8 (± 1.3)	
WATER CONTENT (%)						
	T_{h1}			T_{h2}		
Pin holed pan	8.99 (± 0.01)			9.66 (± 0.13)		
Closed pan	8.98 (± 0.01)			9.56 (± 0.08)		

3.3.4.4.3 Effect of heating rate on thermal response of standardized forms of α,α -trehalose dihydrate

Slow heating rates result in good resolution of thermal events, but unfortunately with poor sensitivity, whilst fast heating rates results in poor resolution but good sensitivity of thermal events (Gaisford, 2008). Previous studies have identified the dehydration process of trehalose dihydrate to be dependent on the heating rate (Sussich et al., 2002; Sussich and Cesaro, 2008). In this section the effect of heating rate on the thermal response of T_{h1} and T_{h2} was explored. T_{h1} and T_{h2} were subjected to increasing heating rates from 2 to $100^{\circ}\text{C}/\text{min}$. Higher heating rates were used to further eliminate possible kinetic effects on the observed thermal transitions. Slow heat/cool experiments were conducted using MTDSC with a focus on characterising thermal events occurring from 30°C to 160°C . Finally, Qi-MTDSC experiments were conducted to allow for the thermal characterisation

of both standardised samples without the influence of heating rate. All experiments in this section were conducted using a Perkin Elmer 40 μL , 0.15mm aluminium pan (B014-3021) with an accompanying aluminium 0.05mm pin-holed lid (B700-1014).

Conventional 2, 20, 50 and 100°C/min using a TA Instruments Q2000

DSC experiments were conducted at 2, 20, 50 and 100°C/min using a TA Instruments Q2000. *Figure 3.31* shows a typical DSC heat flow signal for T_{h1} at 2, 20, 50 and 100°C/min using a pin-holed pan. A single endotherm was observed at 96.3°C for T_{h1} in DSC experiments conducted at 2°C/min. At 20°C/min however, three endotherms were observed at 99.6°C, 125.0°C and 208.4°C. Two endotherms were observed at 100°C/min and 50°C/min at 106.8°C, 134.4°C and 101.3°C, 132.5°C respectively. At high heating rates (i.e. 100 and 50°C/min) experiments were not performed over 250°C due to instrument limitations and cell contamination risks. Three endotherms were observed in all DSC experiments (at 2, 20, 50 and 100°C/min) for T_{h2} (*Figure 3.32*). The onset temperatures appeared to shift with increasing heating rate for the first two endotherms, but not for the third endotherm which remained relatively constant at ~210°C. The results for both T_{h1} and T_{h2} are summarised in *Table 3.4*.

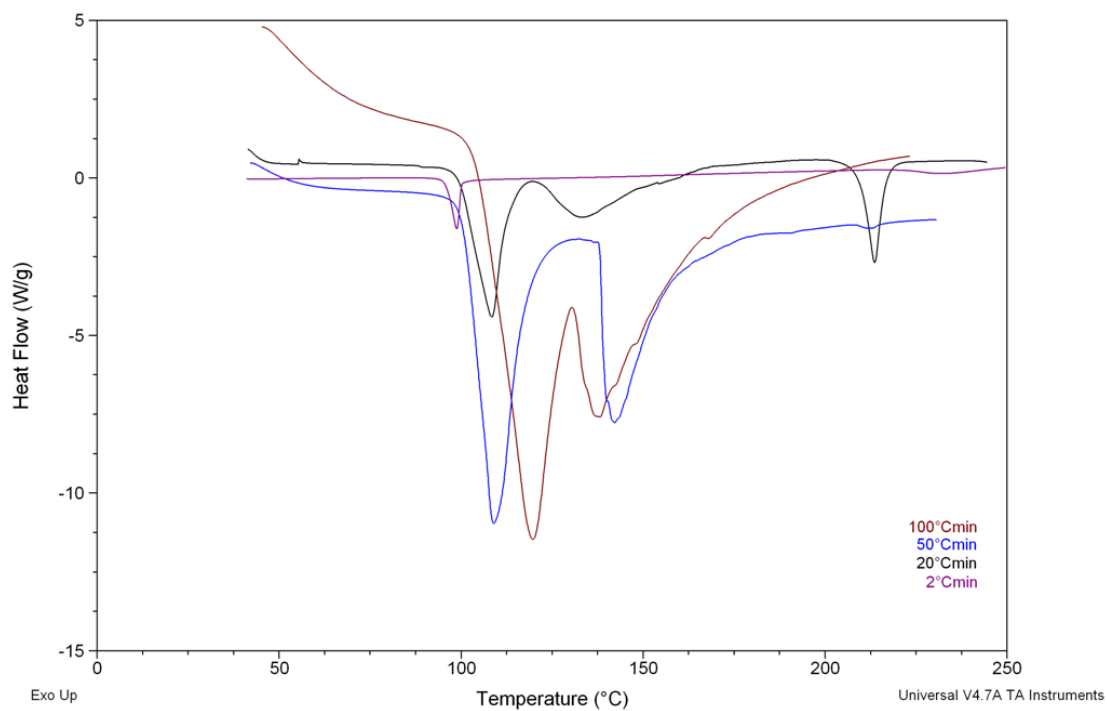


Figure 3.31 Typical DSC heat flow signal for T_{h1} at 2, 20, 50 and 100°C/min using a pin-holed pan

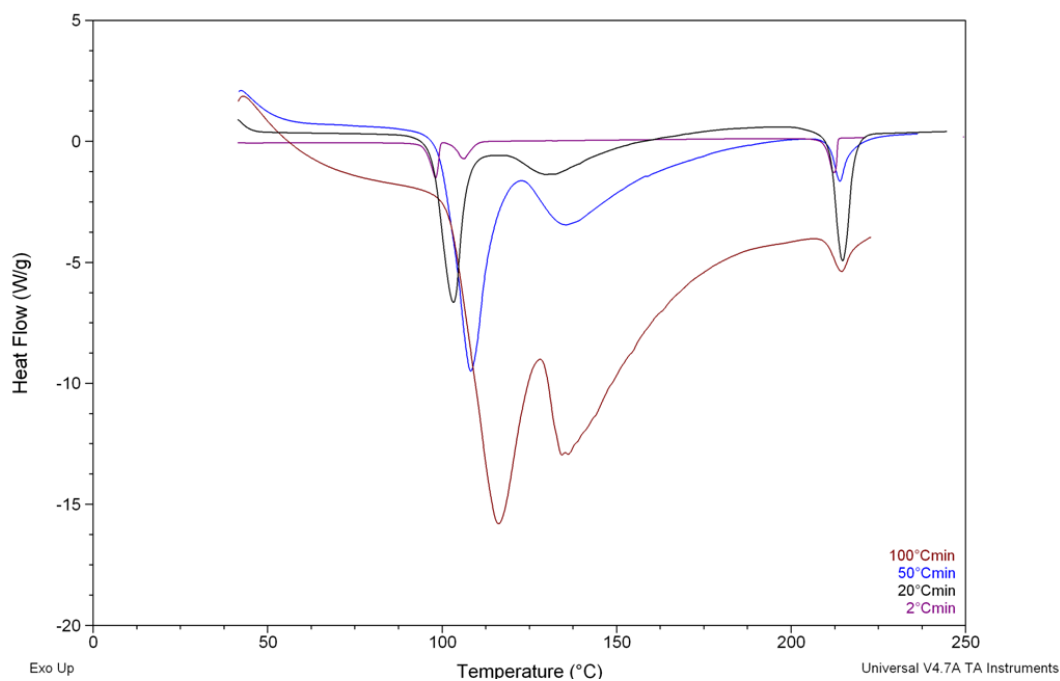


Figure 3.32 Typical DSC heat flow signal for T_{h2} at 2, 20, 50 and 100°C/min using a pin-holed pan

Table 3.4 Endotherm values ($^{\circ}\text{C}$) for T_{h1} and T_{h2} DSC heat flow experiments at heating rates of experiments at 2, 20, 50 and $100^{\circ}\text{C}/\text{min} \pm 0.212^{\circ}\text{C}$ modulation over a 60 second period using a pin-holed pan

	T_{h1}			T_{h2}		
	ENDOTHERM	ENDOTHERM	ENDOTHERM	ENDOTHERM	ENDOTHERM	ENDOTHERM
	1	2	3	1	2	3
2$^{\circ}\text{C}/\text{min}$	96.3 $^{\circ}\text{C}$ (± 0.50)	-	-	95.5 $^{\circ}\text{C}$ (± 0.80)	105.8 $^{\circ}\text{C}$ (± 2.17)	210.1 $^{\circ}\text{C}$ (± 2.02)
20$^{\circ}\text{C}/\text{min}$	99.6 $^{\circ}\text{C}$ (± 0.00)	125.0 $^{\circ}\text{C}$ (± 0.45)	208.4 $^{\circ}\text{C}$ (± 2.14)	96.8 $^{\circ}\text{C}$ (± 0.02)	120.9 $^{\circ}\text{C}$ (± 0.30)	210.9 $^{\circ}\text{C}$ (± 0.17)
50$^{\circ}\text{C}/\text{min}$	101.3 $^{\circ}\text{C}$ (± 0.26)	132.5 $^{\circ}\text{C}$ (± 0.86)	-	101.7 $^{\circ}\text{C}$ (± 0.78)	127.0 $^{\circ}\text{C}$ (± 1.22)	211.2 $^{\circ}\text{C}$ (± 0.04)
100$^{\circ}\text{C}/\text{min}$	106.8 $^{\circ}\text{C}$ (± 1.9)	134.4 $^{\circ}\text{C}$ (± 0.34)	-	103.3 $^{\circ}\text{C}$ (± 1.0)	130.8 $^{\circ}\text{C}$ (± 2.18)	209.9 $^{\circ}\text{C}$ (± 0.44)

T_{h1} appeared sensitive to increasing heating rate with a different thermal response observed at $2^{\circ}\text{C}/\text{min}$ compared to the thermal response observed at $20^{\circ}\text{C}/\text{min}$, $50^{\circ}\text{C}/\text{min}$ and $100^{\circ}\text{C}/\text{min}$, whilst increasing the heating rate did not have an effect on the thermal response of T_{h2} . The reason for the differences observed could be related to the influence of water residence time on each sample; however, further experiments are required to confirm this theory.

HyperDSC[®] at 500 $^{\circ}\text{C}/\text{min}$ and 750 $^{\circ}\text{C}/\text{min}$

Figure 3.33 and *Figure 3.34* show HyperDSC[®] heat flow responses for T_{h1} and T_{h2} at heating rates of 500 and $750^{\circ}\text{C}/\text{min}$. In both cases, an endotherm was observed at 106°C

(T_{h1}) and 102°C (T_{h2}) at 500°C/min and 125°C (T_{h1}) and 104°C (T_{h2}) summarised in *Table 3.3*. At 750°C/min (*Figure 3.33* and *Figure 3.34*) an additional exotherm was seen at 150°C (in both samples).

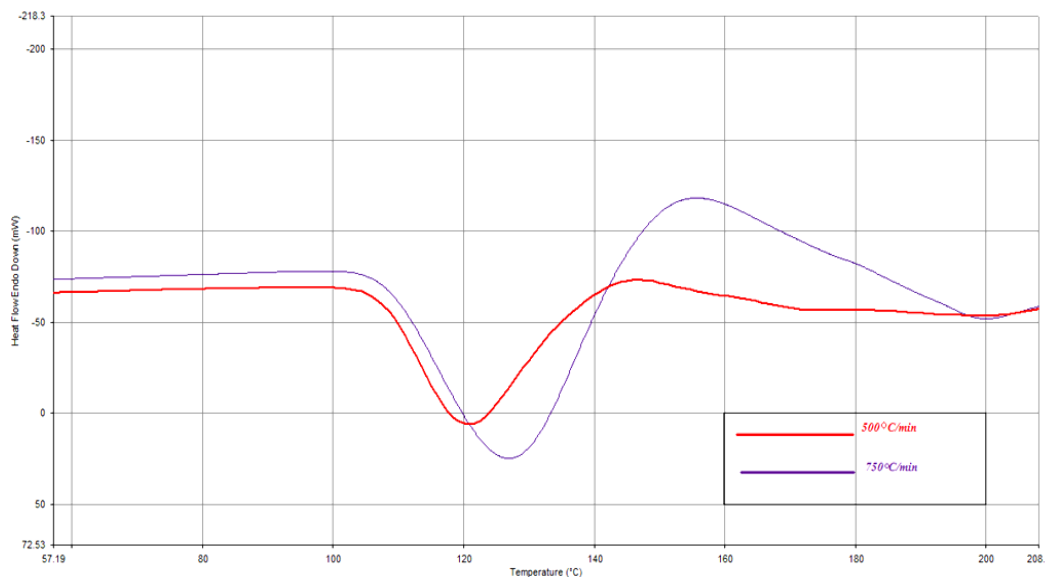


Figure 3.33 Typical HyperDSC[®] heat flow signal for T_{h1} at 500 and 750°C/min using a pin-holed pan

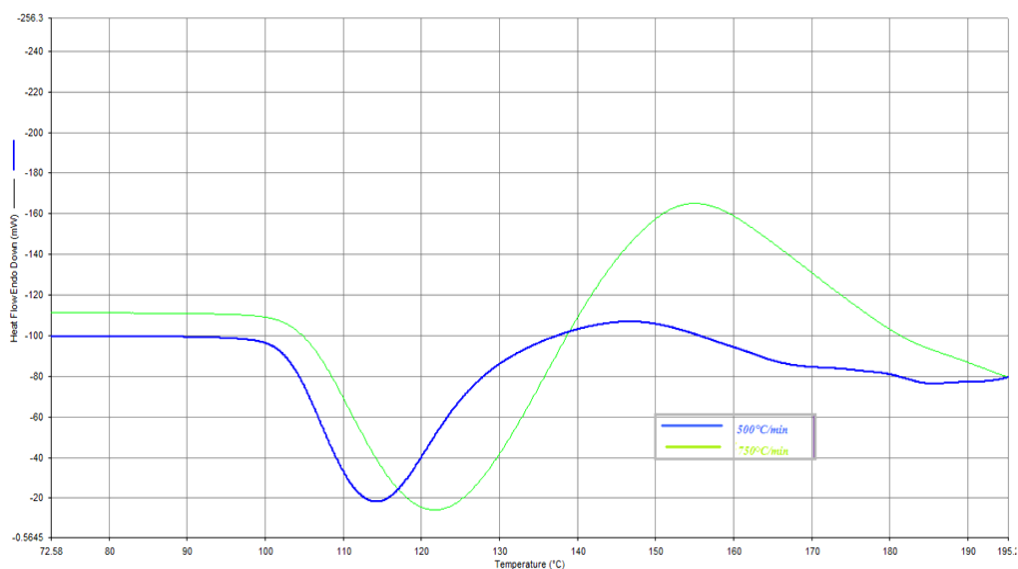


Figure 3.34 Typical HyperDSC[®] heat flow signal for T_{h2} at 500 and 750°C/min using a pin-holed pan

A single endotherm was observed for T_{h2} at 500 and 750°C/min which differed significantly from data obtained in MTDSC pin-holed experiments. A reason for this change is likely to be because the heating rate used in HyperDSC[®] experiments is too fast to allow the second thermal event seen at lower rates to occur. The exotherm observed at 750C/min in both samples was attributed to baseline re-equilibrium effects. Given that at high heating rates, the time to cross the same temperature window (as in MTDSC and DSC experiments) is reduced, any amorphous states achieved by dehydration at high heating rates would not be able to re-crystallise

Table 3.5 Endo- and exotherm values (°C) for T_{h1} and T_{h2} DSC heating rate experiments at 500 and 750°C/min using a pin-holed pan ($n = 3$)

	T_{h1}		T_{h2}	
	ENDOTHERM	EXOTHERM	ENDOTHERM	EXOTHERM
500°C/min	106°C (±0.2)	—	102°C (±1.2)	—
750°C/min	125°C (±0.5)	150°C (±0.3)	104°C (±0.6)	150°C (±0.80)

Use of slow heating and cooling rates (2, 1 and 0.5°C/min)

The dehydration process of trehalose dihydrate and the products formed are dependent on the heating rate, which in turn relates to the residence time and interaction between crystal water and trehalose. Slow heating/cooling MTDSC experiments were conducted to observe these effects with a focus on identifying products formed if any after the low

temperature endotherms observed in *Section 3.3.4.4.1*. Slow heating and cooling MTDSC experiments were performed on T_{h1} at 0.5, 1 and 2°C/min using a $\pm 0.212^\circ\text{C}$ modulation over a 60 second period. The first heat saw a single endothermic peak (*Figure 3.35*) invariant with heating rate in the total heat flow at 96.3°C (0.5°C/min), 96.2°C (1°C/min) and 96.0°C (2°C/min).

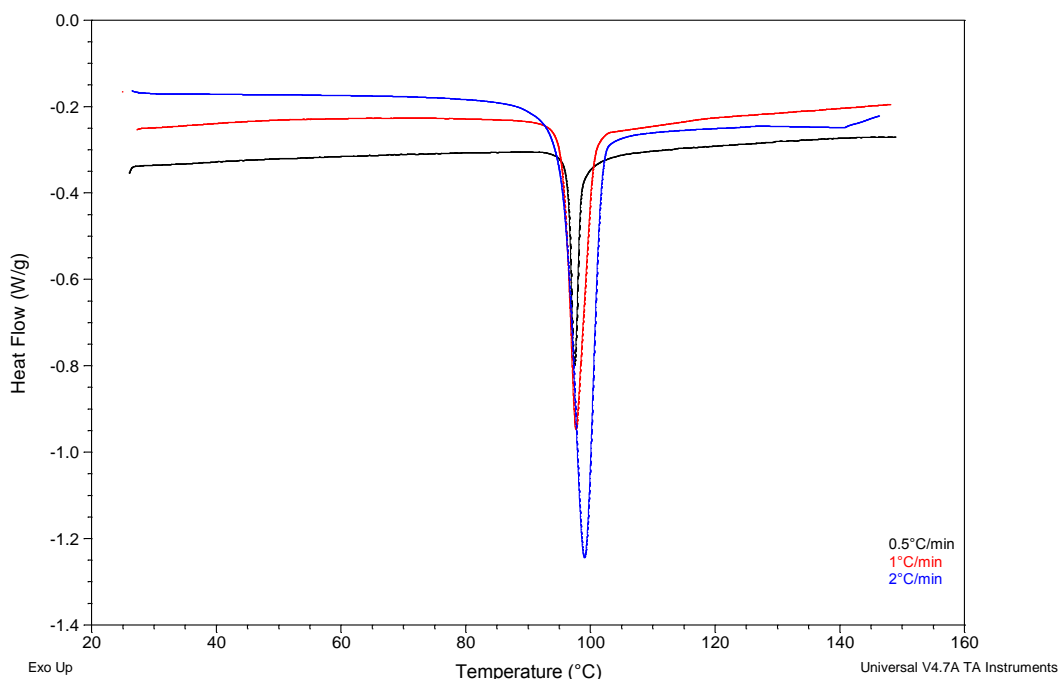


Figure 3.35 Typical MTDSC total heat flow signal (1st heat) for T_{h1} at 0.5, 1 and 2°C/min $\pm 0.212^\circ\text{C}$ modulation over a 60 second period using a pin-holed pan

The in-situ generation of an amorphous form of T_{h1} was observed at all heating rates indicated by a step change in the reversing heat flow signal on the cooling cycle characteristic of a T_g at 106.2°C at 0.5°C/min, 108.2°C at 1°C/min and 92.8°C at 2°C/min (*Figure 3.36*). The presence of water in the glassy forms generated was confirmed by T_g values being lower than reported in the literature (expected $T_g = 117^\circ\text{C}$ (Jain and Roy, 2009)). The T_g of amorphous trehalose is expected to decrease by approximately 10°C for each 1% of water, compared to the anhydrous value (Crowe et al., 1996).

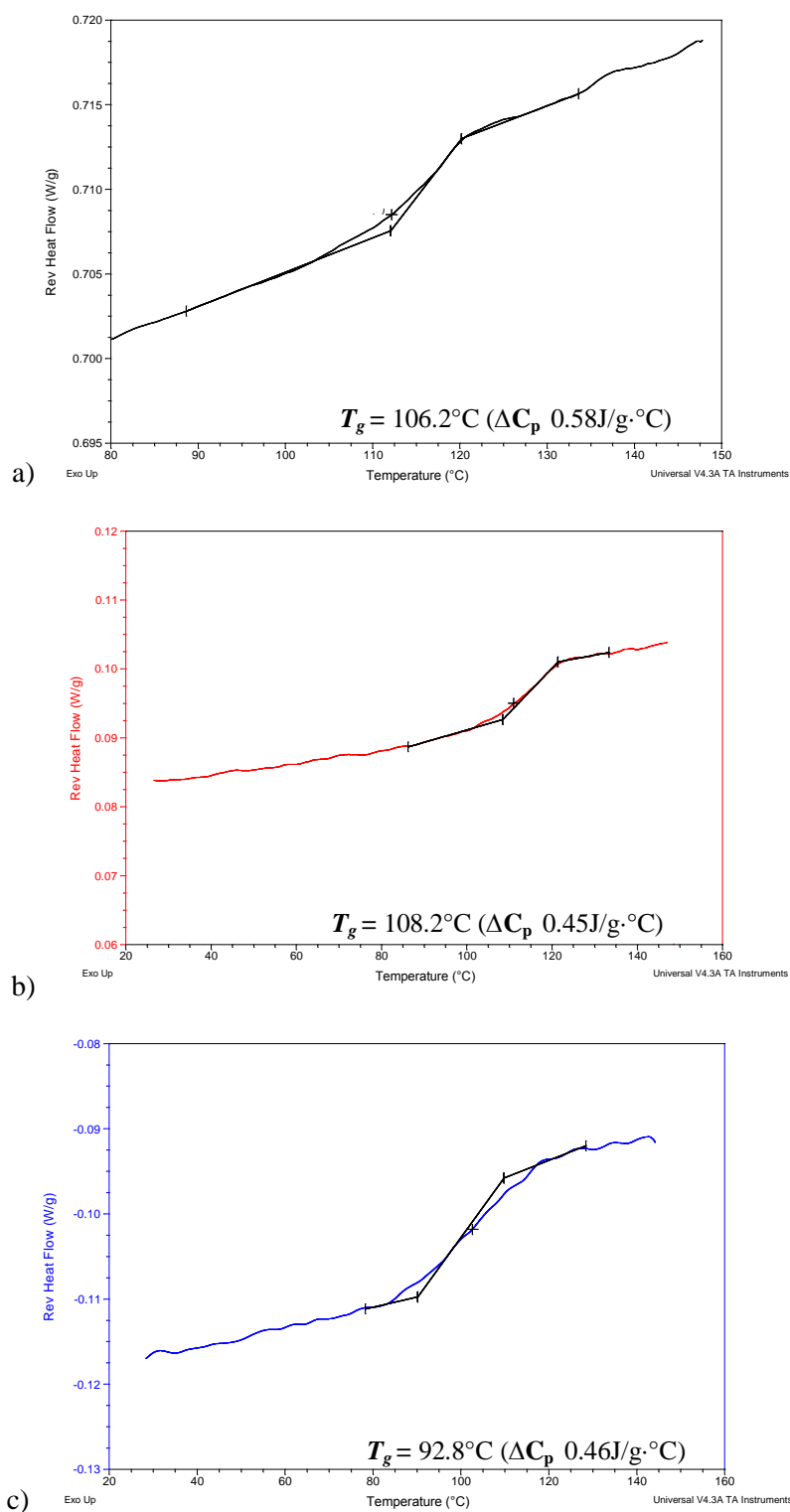
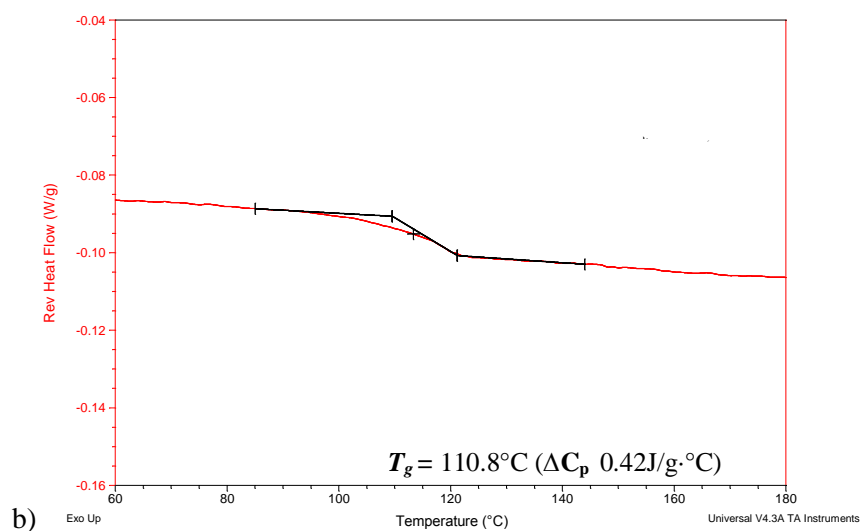
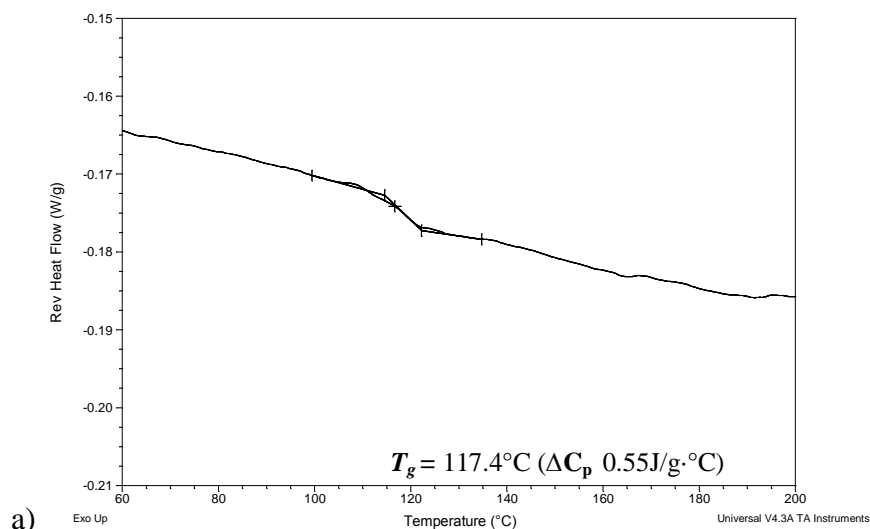


Figure 3.36 Typical MTDS (cooling) reversing heat flow signal for T_{h1} at a) 0.5°C/min b) 1°C/min c) 2°C/min $\pm 0.212^\circ\text{C}$ modulation over a 60 second period using a pin-holed pan

The second heating period showed a classic T_g response in the reversing heat flow at 117.37°C (0.5°C/min), 110.77°C (1°C/min) and 95.99°C (2°C/min) (Figure 3.37). The

glass transition observed was considered to be the “true” non-plasticized T_g of the amorphous form generated, as the residual moisture content of the samples was expected to be very low. It is expected that water was driven off in the first heat and then on the second heat therefore T_g values obtained during the second heat would be influenced by less residual moisture compared to T_g values obtained during the cooling cycle.



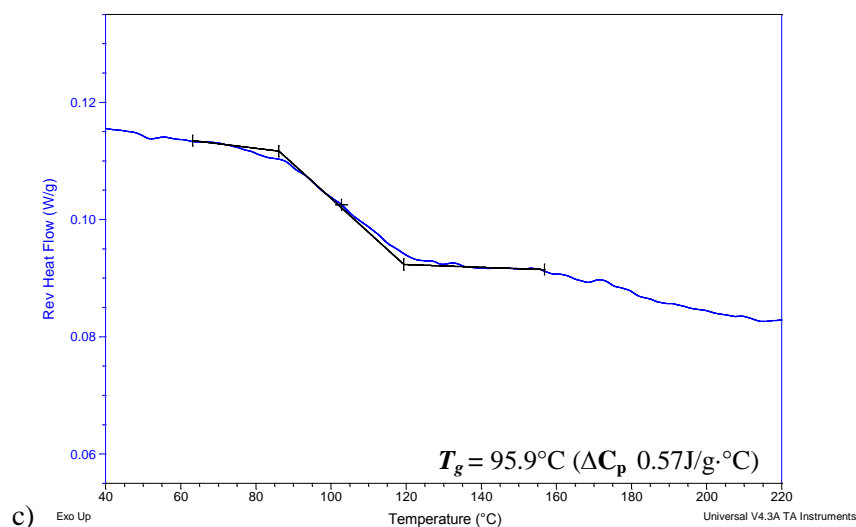
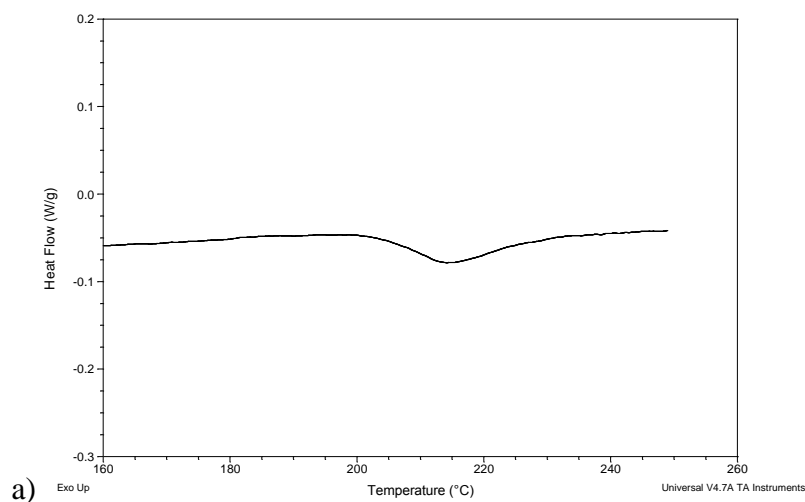


Figure 3.37 Typical MTDSC (2^{nd} heat) reversing heat flow signal for T_{h1} at a) $0.5^\circ\text{C}/\text{min}$ b) $1^\circ\text{C}/\text{min}$ c) $2^\circ\text{C}/\text{min} \pm 0.212^\circ\text{C}$ modulation over a 60 second period using a pin-holed pan

A broad endotherm (*Figure 3.38*) was observed in the total heat flow (second heat) invariant of heating rate at $\sim 206^\circ\text{C}$. Interestingly, an exotherm was observed during $1^\circ\text{C}/\text{min}$ MTDSC experiments at 179.6°C seen in the total heat flow and the non-reversing heat flow but was not present in the reversing heat flow (*Figure 3.40b*).



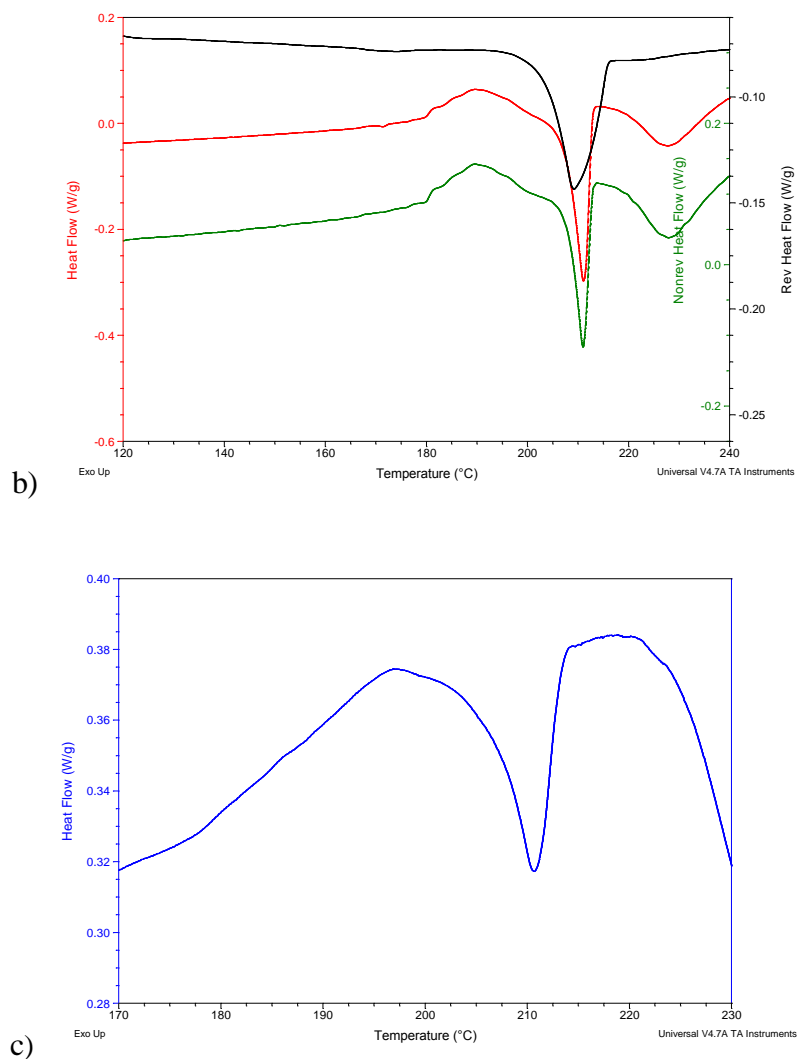


Figure 3.38 Typical MTDSC (2^{nd} heat) Total heat flow signal for T_{h1} at a) $0.5^\circ\text{C}/\text{min}$ b) (in total, reversing and non-reversing heat flow) $1^\circ\text{C}/\text{min}$ c) $2^\circ\text{C}/\text{min} \pm 0.212^\circ\text{C}$ modulation over a 60 second period using a pin-holed pan

Slow heating and cooling MTDSC experiments were conducted on T_{h2} at 0.5, 1 and $2^\circ\text{C}/\text{min} \pm 0.212^\circ\text{C}$ modulation over a 60 second period using pin holed pans. The first heating cycle saw two broad low temperature endothermic peaks invariant with heating rate in the total heat flow as depicted in *Figure 3.39*. The first was observed at 92.8°C ($0.5^\circ\text{C}/\text{min}$), 93.2°C ($1^\circ\text{C}/\text{min}$) and 95.1°C ($2^\circ\text{C}/\text{min}$). The second endotherm was seen at 101.9°C ($0.5^\circ\text{C}/\text{min}$), 102.3°C ($1^\circ\text{C}/\text{min}$) and 102.4°C ($2^\circ\text{C}/\text{min}$).

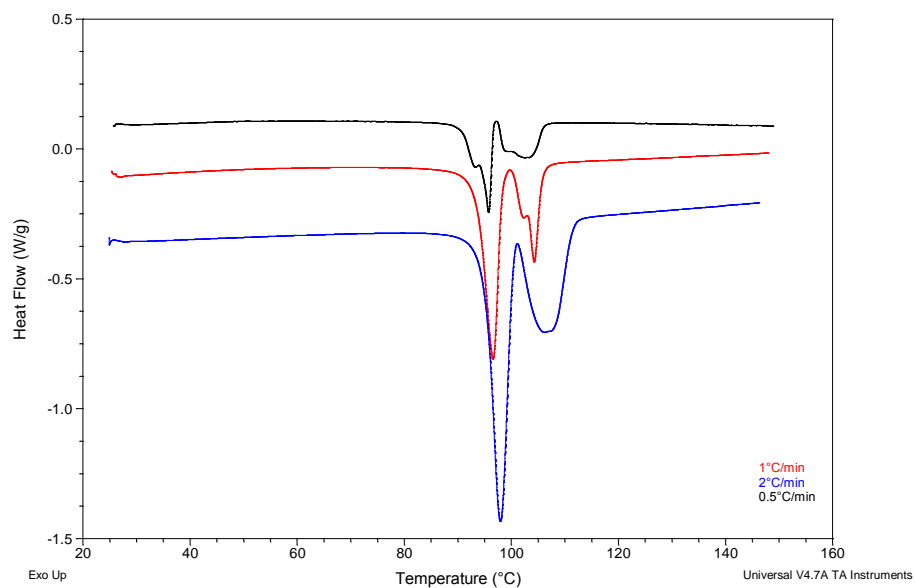


Figure 3.39 Typical MTDSC (1^{st} heat) total heat flow signal for T_{h2} at 0.5, 1 and 2°C/min $\pm 0.212^{\circ}\text{C}$ modulation over a 60 second period using a pin-holed pan

On cooling and on the second heating a glass transition was not detected in the reversing heat flow (insert *Figure 3.40*).

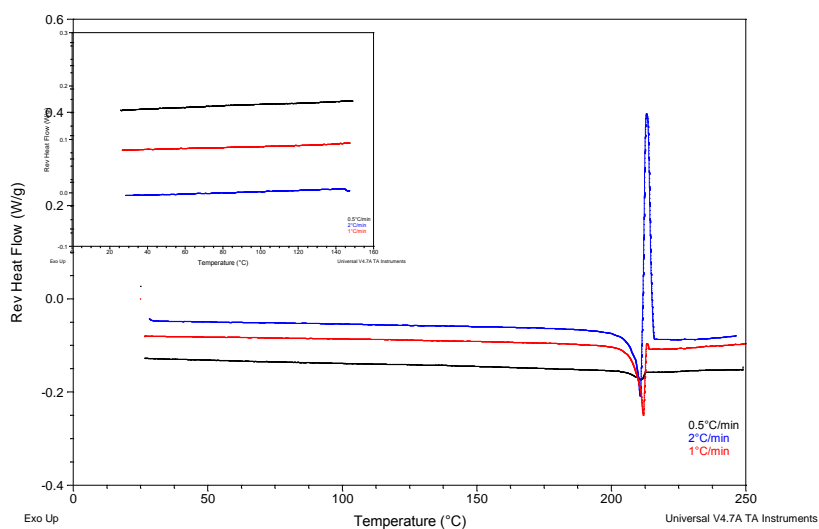


Figure 3.40 Typical MTDSC (2^{nd} heat) total heat flow and cooling (insert) in reversing heat flow signal for T_{h2} at 0.5, 1 and 2°C/min $\pm 0.212^{\circ}\text{C}$ modulation over a 60 second period using a pin-holed pan

An endotherm was observed (*Figure 3.41*) in the second heat (in the total heat flow) at 206.7°C (0.5°C/min), 209.3°C (1°C/min) and 209.6°C (2°C/min). Though a T_g was not identified but an endotherm observed at ~212°C (in the total heat flow) in variant of heating rate.

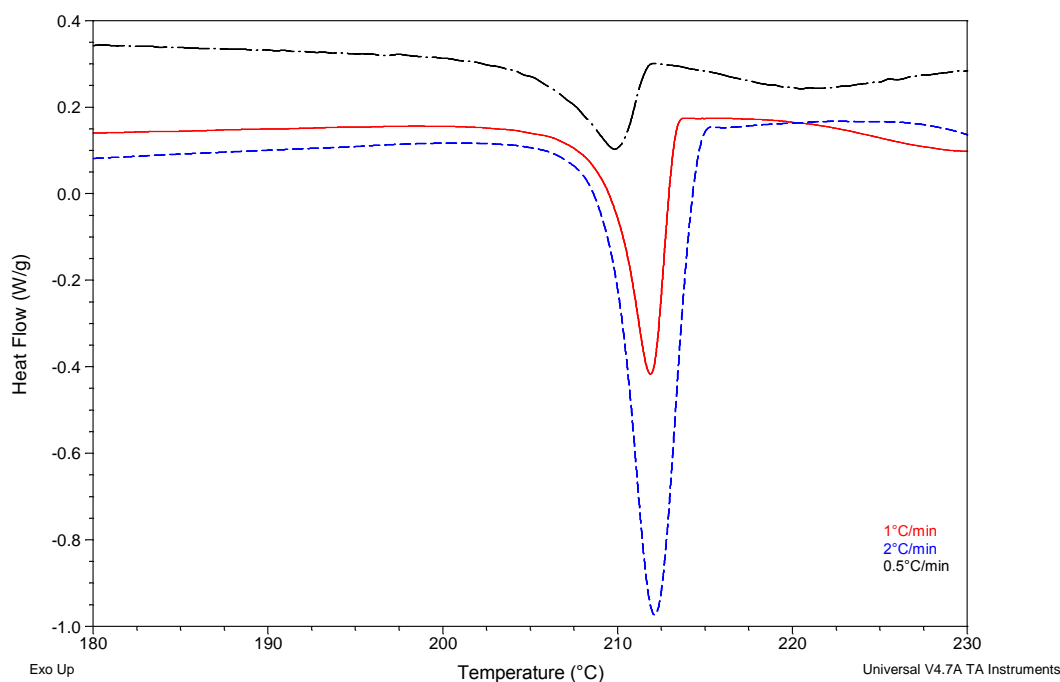


Figure 3.41 Typical MTDSC (2nd heat) Total heat flow signal for T_{h2} at 0.5, 1, 2 °C/min $\pm 0.212^\circ\text{C}$ modulation over a 60 second period using a pin-holed pan

Table 3.6 provides a summary of all values obtained during MTDSC slow heating experiments conducted at 0.5, 1, and 2°C/min for T_{h1} and T_{h2} samples. In general, T_{h1} samples did show a difference in thermal response with decreasing heating rate. The in-situ generation of an amorphous phase was observed in all heating rates. During the second heat invariant of heating rate, an endotherm was observed at ~206°C. An exotherm was also observed prior to the final endotherm in the total and non-reversing heat flow during 1°C/min experiments (at ~179°C). This was not observed at other heating rates and suggests that conditions in the 1°C/min experiments were favourable for sufficient nuclei

formation and growth within the amorphous phase when heated above T_g to a detectable limit. This phenomenon has been documented elsewhere (Sussich and Cesaro, 2008) in a study observing the effects of heating rate on the thermal response of α,α -trehalose dihydrate at a heating rate of $1^\circ\text{C}/\text{min}$ and $30^\circ\text{C}/\text{min}$ using an open pan DSC system. It was speculated that conditions at a slow heating rate of $1^\circ\text{C}/\text{min}$ compared to studies at a higher heating rate of $30^\circ\text{C}/\text{min}$, provided enough time to “cross the $T_g - T_m$ window” and allow the amorphous form generated from the melt of the anhydrous form, T_α at 130°C to undergo cold crystallisation. Should this theory be accurate, an exotherm would be expected at an even slower heating rate of $0.5^\circ\text{C}/\text{min}$; however this was not observed.

In comparison, MTDSC slow heating experiments conducted on T_{h2} saw the same thermal response invariant of heating rate. Two low temperature endotherms were observed in the first heat. It was concluded that a T_g was not detected in T_{h2} experiment as it had a weaker glass transition signal compared to the T_g observed in the cooling cycle in T_{h1} experiments. To gain better resolution of weak glass transitions, a large modulation amplitude should be used typically around ± 1.5 to 2°C (Guinot and Leveiller, 1999). This was taken into consideration when choosing experimental parameters for quasi-isothermal MTDSC experiments. Modulation amplitude of $\pm 1^\circ\text{C}$ was chosen to improve resolution of the weaker glass transition, a larger value was not used so as to prevent the modulation from over-spanning the transition width (Guinot and Leveiller, 1999). An endotherm was observed at $\sim 209^\circ\text{C}$ in the total heat flow in all heating rates.

Table 3.6 Summary of endotherm and T_g values for T_{h1} and T_{h2} MTDSC slow heating and cooling experiments conducted at a heating rate of 0.5, 1, and 2°C/min $\pm 0.212^\circ\text{C}$ modulation over a 60 second period using a pin-holed pan ($n=3$)

	T_{h1}			
	FIRST HEAT (TOTAL HEAT FLOW) ENDOTHERM	COOLING CYCLE (REVERSING HEAT FLOW) T_g	2 ND HEAT (REVERSING HEAT FLOW) T_g	2 ND HEAT (TOTAL HEAT FLOW) ENDOTHERM
	0.5°C/min	96.3°C (± 0.72)	106.2°C (± 0.63) ΔC_p 0.58J/g $\cdot^\circ\text{C}$	117.4°C (± 0.56) ΔC_p 0.55J/g $\cdot^\circ\text{C}$
1°C/min	96.2°C (± 0.13)	108.2°C (± 0.56) ΔC_p 0.45J/g $\cdot^\circ\text{C}$	110.8°C (± 0.34) ΔC_p 0.42J/g $\cdot^\circ\text{C}$	(179.6°C (± 0.70)Exotherm) 206.97°C (± 2.13)
2°C/min	96.0°C (± 0.75)	92.8°C (± 0.21) ΔC_p 0.46J/g $\cdot^\circ\text{C}$	95.9°C (± 1.45) ΔC_p 0.57J/g $\cdot^\circ\text{C}$	206.3°C (± 1.56)
T_{h2}				
	FIRST HEAT (TOTAL HEAT FLOW)		COOLING CYCLE AND 2 ND HEAT (REVERSING HEAT FLOW) T_g	2 ND HEAT (TOTAL HEAT FLOW) ENDOTHERM
	ENDOTHERM 1	ENDOTHERM 2		
0.5°C/min	92.8°C (± 0.08)	101.9°C (± 1.29)	-	206.7°C (± 1.78)
1°C/min	93.2°C (± 2.04)	102.3°C (± 1.75)	-	209.3°C (± 0.06)
2°C/min	95.1°C (± 0.05)	102.4°C (± 2.75)	-	209.6°C (± 0.63)

Use of Quasi Isothermal MTDSC

Qi-MTDSC is a variant of MTDSC where the experimental temperature is modulated around a constant underlying temperature for a specified time, after which the temperature is incrementally ramped up or down so as to obtain a profile through a transition (Manduva et al., 2008). The heating rate is negated by holding the sample at a range of selected temperatures about which the sample is modulated. The reversing heat capacity is signal

used in Qi-MTDSC experiments, reasons for this and further details of this technique were discussed in full detail in *Chapter 2*. Qi-MTDSC experiments were conducted from 80°C to 160°C to characterise the transitions occurring within this temperature range and shed light on thermal response observed in slow heating MTDSC experiments. Parameters used were chosen to improve the resolution of the weaker glass transition of the glass produced from the structural collapse of T_{h2} .

A typical Qi-MTDSC trace showing the reversing heat capacity signal as a function of time (temperature modulation of $\pm 1^\circ\text{C}$, 20 minute isothermal periods with 2°C increments) from 80°C to 160°C for T_{h1} is shown in *Figures 3.42*. The temperature range through which the heat capacity alters as the sample undergoes a series of thermal transitions is clearly seen. The sudden change in heat capacity observed at 96°C in the Qi-MTDSC trace (*Figure 3.42*) correlated to the single endotherm seen in MTDSC experiments. The heat capacity did not level off immediately, instead increased from 110°C to 128°C after which it reached a plateau.

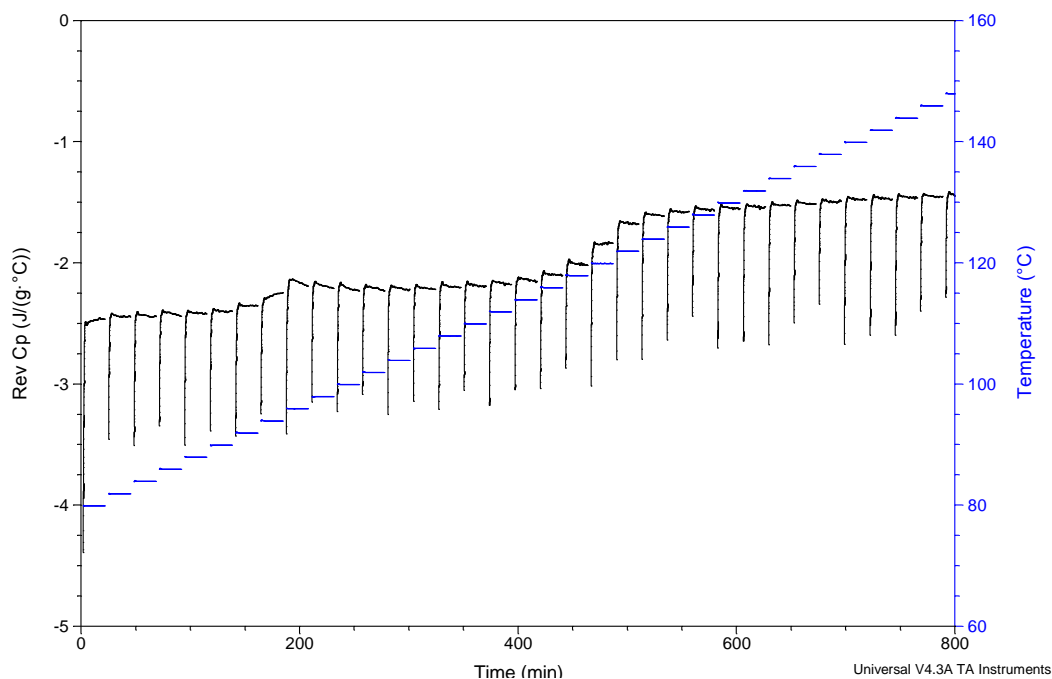


Figure 3.42 Typical Q_i -MTDSC reversing heat capacity (as a function of time) signal of T_{h1} at a temperature modulation of $\pm 1^\circ\text{C}$, 20 minute isothermal periods with 2°C increments using a pin-holed pan

Q_i -MTDSC trace for T_{h2} is shown in *Figure 3.43*. An incremental increase in heat capacity was observed from 80°C to 86°C followed by an abrupt decrease seen at 88°C which was then followed by a dramatic and sudden increase in heat capacity at 90°C . A decrease in heat capacity was observed from 92 to 110°C followed by a steep, but gradual increase from 112°C to 128°C . After this event, a plateau in heat capacity followed by a decrease in heat capacity from 142°C to 154°C was observed.

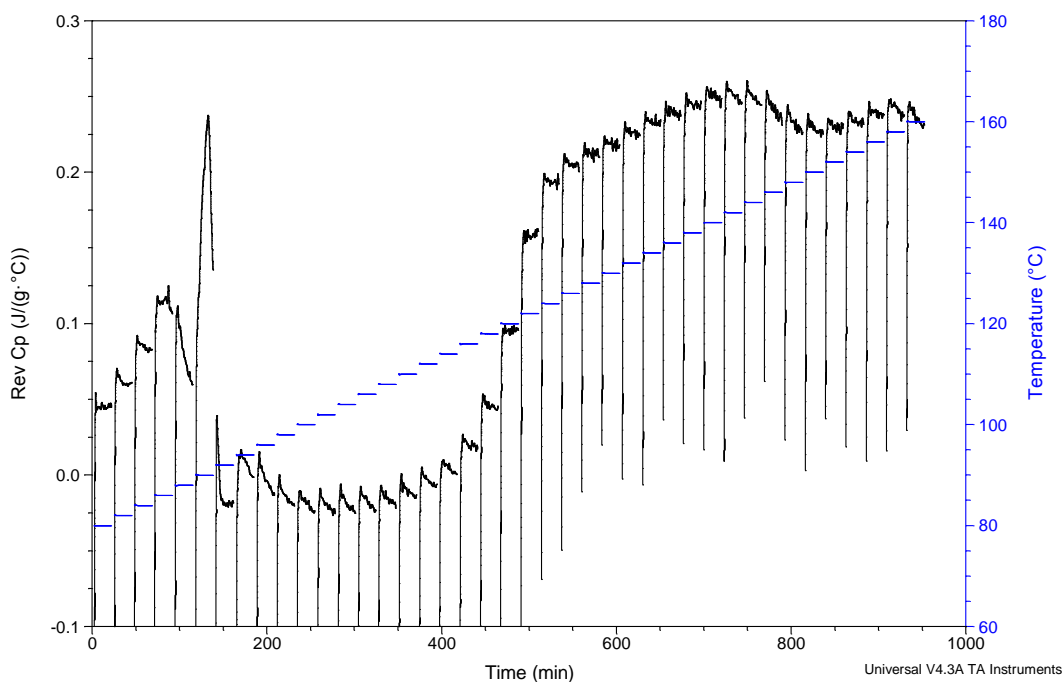


Figure 3.43 Typical Qi-MTDSC reversing heat capacity (as a function of time) signal of T_{h2} at a temperature modulation of $\pm 1^\circ\text{C}$, 20 minute isothermal periods with 2°C increments using a pin-holed pan

As discussed in *Chapter 2*, Qi-MTDSC is a useful technique in identifying sample de-vitrification. In a study by Verdonck et al., (1999) PET was heated below its T_g an increase in heat capacity was observed and corresponding to the de-vitrification of PET at T_g . A decrease in heat capacity was detected as the sample reached a temperature where cold crystallisation occurred (Verdonck et al., 1999). The results obtained in this section suggest on heating both T_{h1} and T_{h2} are dehydrated resulting in structural collapse and the in-situ generation of a glassy state. This was observed for T_{h1} in slow heating MTDSC experiments were a glass transition was observed in cooling cycle and second heat cycle in the reversing heat flow. A glass transition was not observed in the cooling cycle or second heat cycle in slow heating MTDSC experiments for T_{h2} . It was concluded that a T_g was not detected in T_{h2} slow MTDSC experiments as it had a weaker glass transition signal compared to the T_g observed in the cooling cycle in T_{h1} experiments. This was taken into

consideration when choosing Qi-MTDSC parameters. Qi-MTDSC experiments did not detect a cold crystallisation event between 80°C and 160°C from the glass produced from the structural collapse of T_{h1} , however a cold crystallisation event was detected from the glass produced by T_{h2} (onset 142°C).

A Lissajous figure in Qi-MTDSC is a plot of the modulated heat flow as a function of time derivative of modulated temperature. Lissajous figures can be used to aid further interpretation of energetic transitions identified in Qi-MTDSC experiments. *Figure 3.44* displayed a change in heat capacity at 96°C which correlated to the endotherm observed earlier in the study. Lissajous figures were plotted for T_{h1} at 80°C and 96°C (*Figure 3.44*) in order to analyse and draw conclusion from any changes observed. 80°C was chosen as it was assumed based on previous results that at this temperature no thermal events occurred. Both the slope and width of the Lissajous figures changed from 80°C to 96°C. A change in slope is suggestive of a change in heat capacity within the sample, whilst a change in width relates to the heat dissipation of the system. The change in heat dissipation observed in this experiment could be related to the evaporation of crystal water from T_{h1} , HSM studies were conducted to confirm this and are discussed in the following section. Ellipses at 96°C were not as superimposed as they were at 80°C suggestive of an underlying change taking place as a function of time. A change in ellipse shape is usually suggestive of an additional energetic process taking place e.g. melting or crystallisation, however, this was not observed here

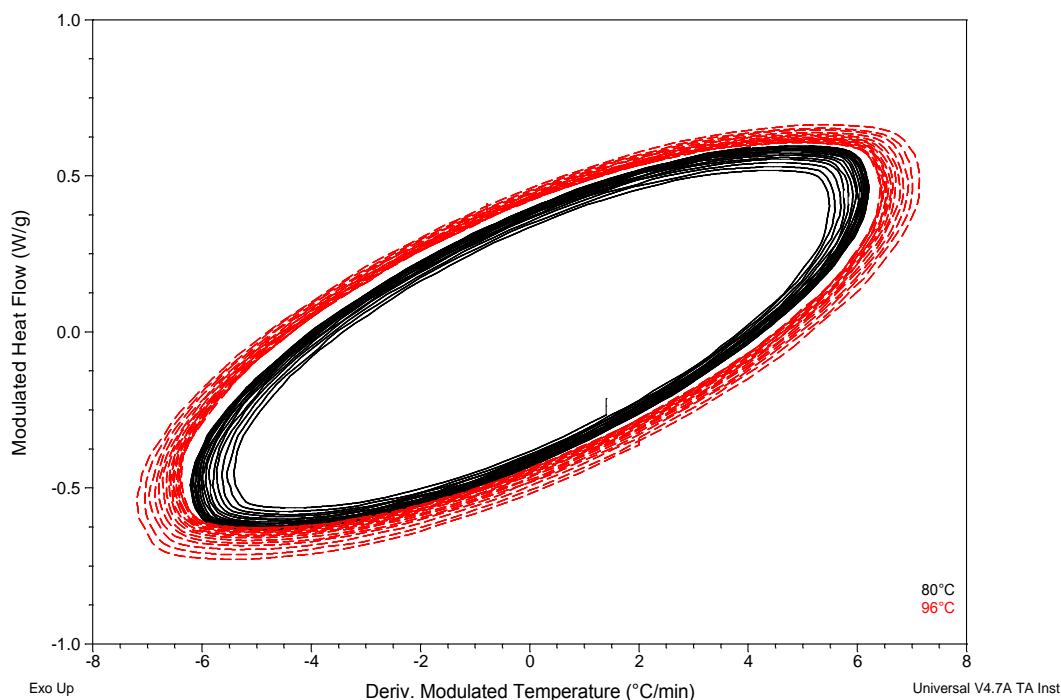


Figure 3.44 Typical Lissajous figure in *Qi*-MTDSC as modulated heat flow (as a function of time derivative of modulated temperature) signal for T_{h1} at 80°C (**black**) and 96°C (**red**) using pin-holed pans

A typical Lissajous figure for T_{h2} (plotted as modulated heat flow as a function of time derivative of modulated temperature) at 80°C and 86°C is shown in *Figure 3.45*. Lissajous plots identified a change in width which as discussed earlier relates to the heat dissipation of the system, as well as a change in slope which correlates to the heat capacity of the system. These results suggest that at 86°C an event occurs similar to that identified at 96°C in T_{h1}

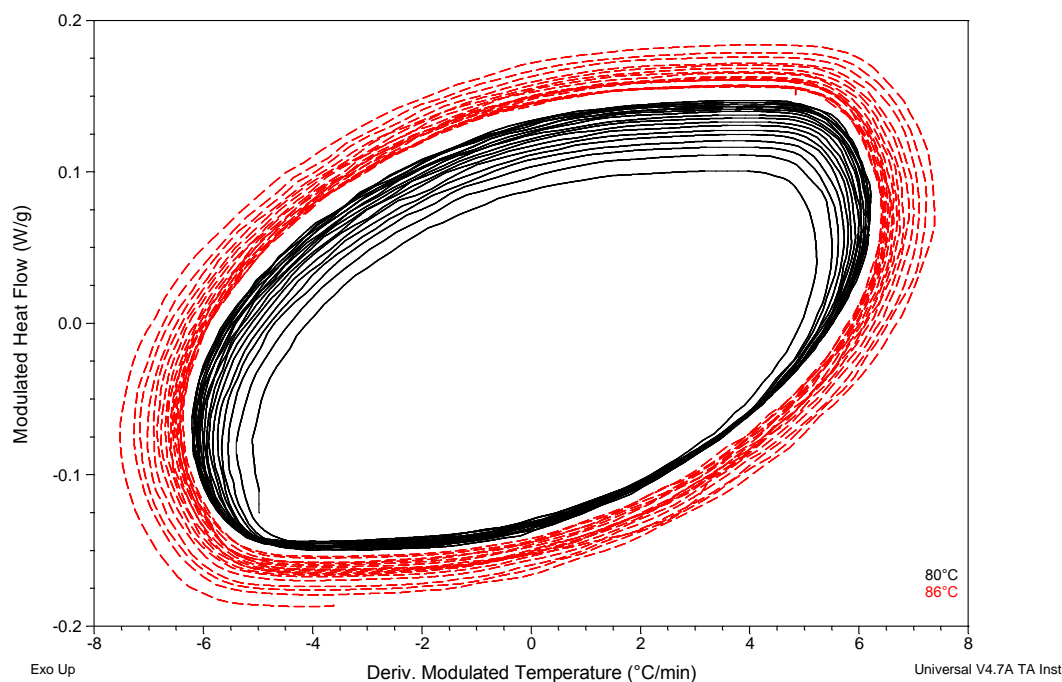


Figure 3.45 Typical Lissajous figure in Qi-MTDSC as modulated heat flow (as a function of time derivative of modulated temperature) signal for T_{h2} at 80°C (**black**) and 86°C (**red**) using a pin-holed pan

Qi-MTDSC experiments conducted on T_{h2} at 90°C shown in *Figure 3.40* (also shown in *Figure 3.46a*) showed an increase in the heat capacity in four stages depicted as 90-1, 90-2, 90-3 and 90-4 on the trace. 90-1 corresponded to the first 2 minutes of the isothermal period (sample held at 90°C isothermally for 20 minutes). Whilst 90-2, 90-3 and 90-4 corresponded to data obtained from 2 to 8 minutes, 8 to 13 minutes and 13 to 20 minutes of the isothermal period respectively. In order to gain further insight into these changes, the modulated heat flow as a function of time derivative of modulated temperature was plotted generating a Lissajous figure (*Figure 3.46b*). The plotted Lissajous figures did not appear to change drastically in slope however they did appear to increase drastically in width (heat dissipation) and a distortion of shape with increasing time at 90°C. Ellipse distortion was suggestive of an additional energetic process occurring like a melting event at 90°C.

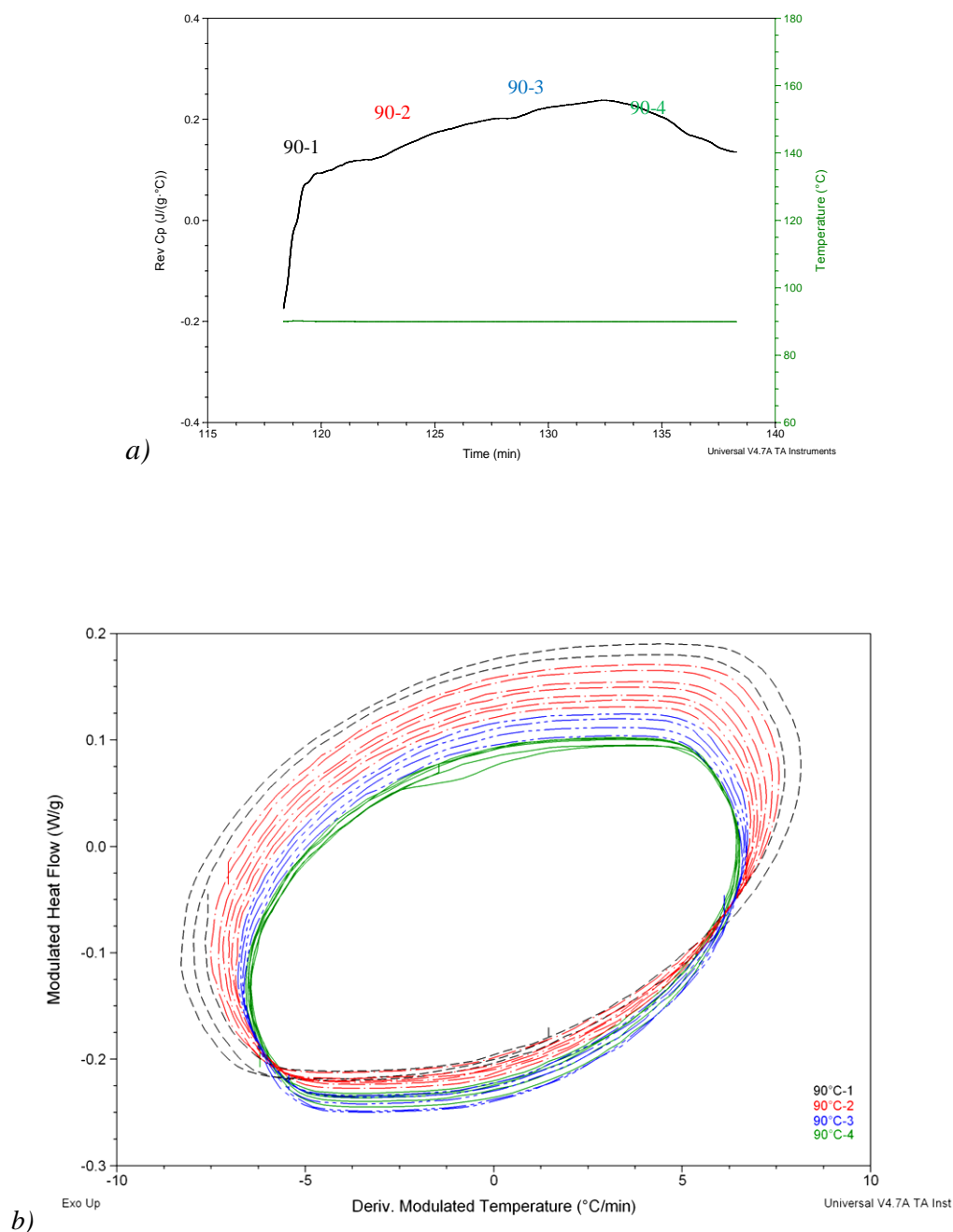
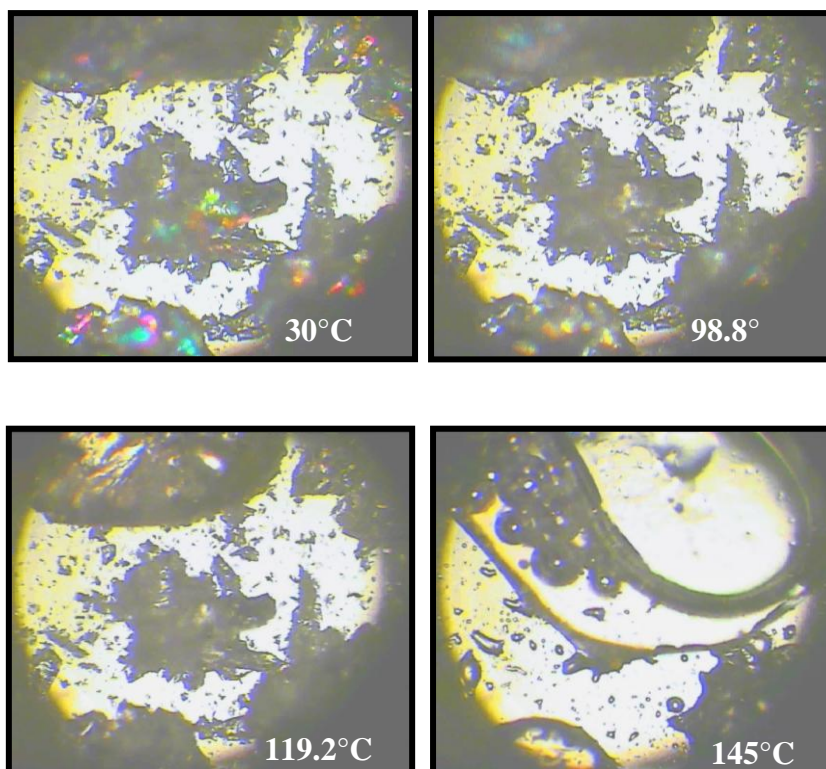


Figure 3.46 a) Typical Q_i -MTDSC Reversing heat capacity (as a function of time) signal for unfractionated T_{h2} at 90°C b) Typical Lissajous figure in Q_i -MTDSC as modulated heat flow (as a function of time derivative of modulated temperature) signal for unfractionated T_{h2} at 90°C showing different changes in heat capacity when held isothermal for 20 minutes

To shed light on the results obtained in this section HSM studies were conducted on both T_{h1} and T_{h2} from 30°C to 250°C .

3.3.4.4.4 Visualisation of thermal events using hot stage microscopy

During HSM experiments, T_{h1} and T_{h2} were subjected to a controlled heating programme from 30°C to 250°C at 2°/min. Transitions were visualised via a video capture microscope. Both particles were coloured and showed birefringence at 30°C (Figure 3.47 and 3.48). Figure 3.47 shows HSM images captured at specific temperatures for T_{h1} samples on heating at 2°C/min. A change in birefringence was observed on heating, commencing at 84°C and continuing to 98.8°C with crystals appearing darker and becoming more opaque. Further heating resulted in the dissolution of some crystals at 118°C, with complete dissolution of all crystals at 145°C. Crystallisation commenced at 166°C resulting in fully formed crystals at 205.7°C with their subsequent melt at 209°C.



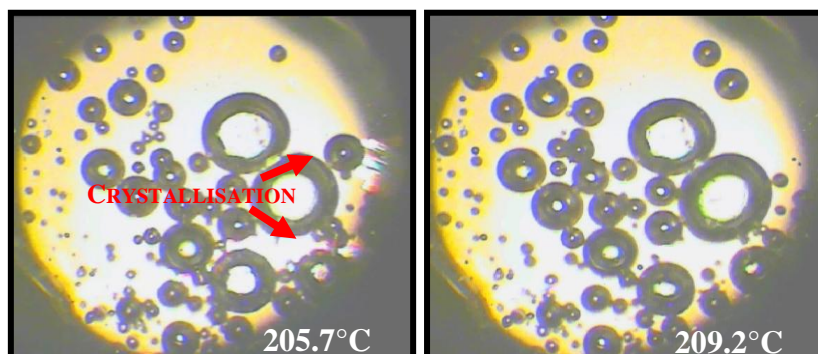
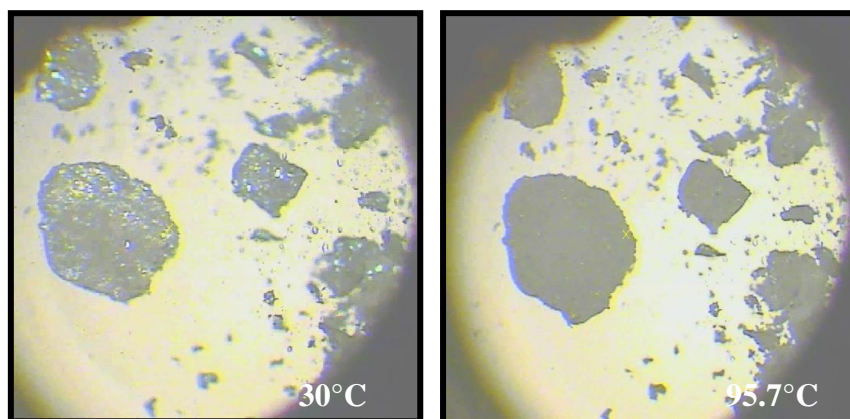


Figure 3.47 Hot stage microscopy images captured at specific temperatures for T_{h1} sample heated at 2°C/min

T_{h2} samples (Figure 3.48) on heating showed a change in birefringence at 89.9°C continuing to 95.7°C with crystals appearing darker and becoming more opaque. Further heating resulted in the dissolution of all crystals, starting at 135°C in some crystals with complete dissolution of all crystals at 190°C. Crystallisation was not observed in this experiment.



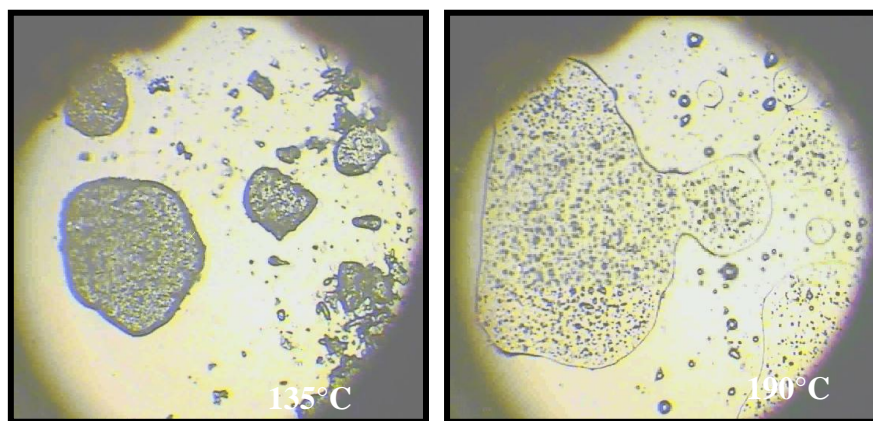


Figure 3.48 Hot stage microscopy images captured at T_{h2} sample which at $2^{\circ}\text{C}/\text{min}$

HSM studies for T_{h1} showed evaporation from the crystal lattice started at 84°C (identified by a change in birefringence). This event was identified in Qi-MTDSC studies as a change in width of the Lissajous figure at 96°C and in MTDSC experiments (at $\sim 96^{\circ}\text{C}$) where an endotherm was observed. Further heating in HSM studies resulted in dissolution of crystals which lead to crystal formation (from the liquid) at $\sim 205^{\circ}\text{C}$. This was identified in slow heat/cool MTDSC experiments conducted at $1^{\circ}\text{C}/\text{min}$ at $\sim 179^{\circ}\text{C}$ however due to experimental limitations such events were not observed in Qi-MTDSC studies.

HSM studies for T_{h2} showed evaporation from the crystal lattice at $\sim 95^{\circ}\text{C}$ which was identified in Qi-MTDSC studies at a lower temperature (86°C) as a change in width of the Lissajous figures (similar to T_{h1}). After dissolution of T_{h2} crystals crystallisation was not observed in HSM studies which was contrary to Qi-MTDSC and MTDSC (closed pan at $2^{\circ}\text{C}/\text{min}$) studies.

As previously discussed, reasons for difference between Qi-MTDSC, MTDSC and HSM studies could be because HSM studies are conducted in an open air environment. Relating this in DSC terms, HSM studies could reflect events occurring in an open pan experiment. Open pan studies were not conducted due to risk of cell contamination.

3.3.4.5 Variable temperature ATR-FTIR at 2°C/min

The heating and cooling of a sample results in phase changes which leads to a change in the physical property of the sample. As discussed earlier in *Chapter 2*, ATR-FTIR is a form of vibrational infrared spectroscopy where molecules are excited by the absorption of infrared light. During variable temperature ATR-FTIR experiments a sample is subjected to controlled heating over a set temperature range, spectra is taken at controlled intervals (e.g. every minute). As the spectra is sensitive to both inter- and intra- molecular changes that occur as a result of heat changes, it is an effective technique for the studying of molecular structures and abrupt changes in hydrogen bonding as a function of temperature.

In this study variable temperature ATR-FTIR was used as a complementary qualitative technique in conjunction with DSC, MTDSC and Qi-MTDSC studies to observe changes in molecular characteristics due to increased temperature which could be attributed to structural changes leading to the formation of anhydrous crystalline or amorphous forms of trehalose. Variable temperature ATR-FTIR experiments conducted on T_{h2} confirmed the presence of a crystalline material identified in Qi-MTDSC studies. A crystalline sample was not identified in variable temperature ATR-FTIR studies conducted on T_{h1} . Unfortunately, due to experimental limitations heating higher than 200°C was not possible with the heating plate used in this experiment. Therefore, the identification of the

crystalline material identified in HSM studies at 205.7°C was not possible. Exploratory data analysis of spectroscopic data (i.e. hierarchical cluster analysis (HCA) and principle component analysis (PCA)) was used to identify changes in spectra with increasing temperature which could be attributed to structural changes occurring in sample.

Variable temperature ATR-FTIR experiments were conducted as described in *Chapter 2* with an applied heating rate of 2°C/min from 30°C to 198°C spectra were obtained at 1 minute intervals. Exploratory data analysis of spectroscopic data HCA and PCA was conducted on data obtained. As discussed in *Chapter 2*, HCA calculates and compares distances between samples (or variables) in a data set. A similarity value of 1 is assigned to identical samples whilst a value of 0 to the most dissimilar samples. PCA is a powerful visualization tool that finds linear combinations of original independent variables which account for maximal amounts of variation. Scores analysis can be used to illustrate inter-sample relationships. Data is plotted as a two dimensional (2D) scatter plot with a confidence ellipse is superimposed. This ellipse represents a 95% confidence level derived from the scores variance and is centered at the origin of the two score dimensions displayed. Further details of both these techniques are discussed in *Chapter 2*.

As previously discussed ATR-FTIR spectra of α,α -trehalose dihydrate shows characteristic peaks at 3500 cm^{-1} , 1650 cm^{-1} , 994 cm^{-1} and 954 cm^{-1} . A sharp band at ~3500 cm^{-1} corresponds to the OH stretch vibration of water with hydrogen bonding to other molecules. The peak observed at ~3500 cm^{-1} corresponds to the stretch vibrations of two crystal water molecules in trehalose dihydrate. A peak observed at ~1650 cm^{-1} is referred to as the H₂O scissoring mode of crystal water, identification of this peak confirms the presence of

crystal water. Peaks observed at $\sim 994\text{cm}^{-1}$ and $\sim 954\text{cm}^{-1}$ correspond to the α -(1 \rightarrow 1) glycosidic bond.

Figure 3.50 illustrates variable temperature ATR-FTIR spectra of T_{hl} showing two clusters as identified in HCA data. *Figure 3.49* shows the results of the HCA dendrogram of T_{hl} for variable temperature ATR-FTIR spectra obtained from 30°C to 198°C at a heating rate of $2^\circ\text{C}/\text{min}$ spectra at 1 minute intervals. HCA dendrogram identified two clusters with a relatively low similarity value of approximately 0.3 indicating that samples identified within these clusters were relatively dissimilar. The first cluster correlated to spectra obtained at 30°C to 116°C , whilst the second cluster correlated to spectra obtained at 118°C to 198°C (*Figure 3.50*). Analysis of ATR-FTIR spectra showed that from 30°C to 116°C (depicted in red *Figure 3.50*) T_{hl} was crystalline as characterised by sharp absorption bands at 3500cm^{-1} , 1650cm^{-1} , 994cm^{-1} and 954cm^{-1} . At 118°C spectra changed and exhibited broad features which are an indication of a wide range of hydrogen bond lengths and orientations within a sample characteristic of an amorphous form. The peak observed at 3500cm^{-1} corresponds to the stretch vibrations of two crystal water molecules in trehalose dihydrate disappeared. A shift in the peak observed $\sim 1650\text{cm}^{-1}$ which correlates to residual water shifted in the amorphous form which indicated that water molecules in the crystalline form are more strongly hydrogen bonded to trehalose molecules compare to water molecules bound in the amorphous form. This phenomenon has been observed elsewhere (Wolkers et al., 2004). No further changes in the spectra were observed between 188°C to 198°C as expected.

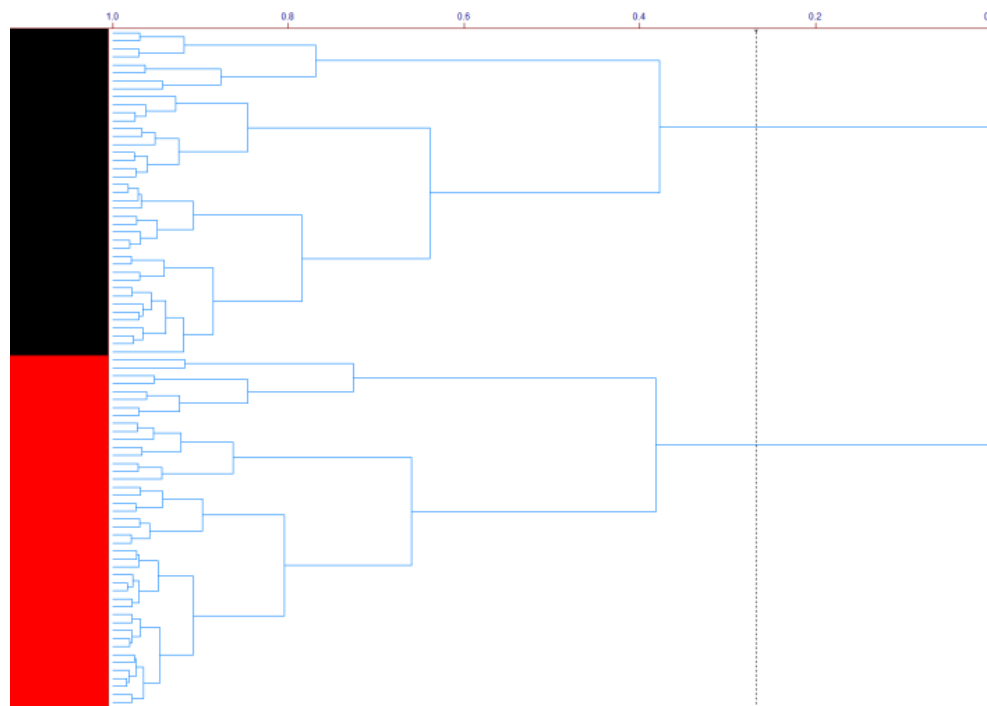


Figure 3.49 A hierarchical cluster analysis dendrogram of T_{h1} for variable temperature ATR-FTIR spectra obtained from 30°C to 198°C at a heating rate of 2°C/min spectra at 1 minute intervals

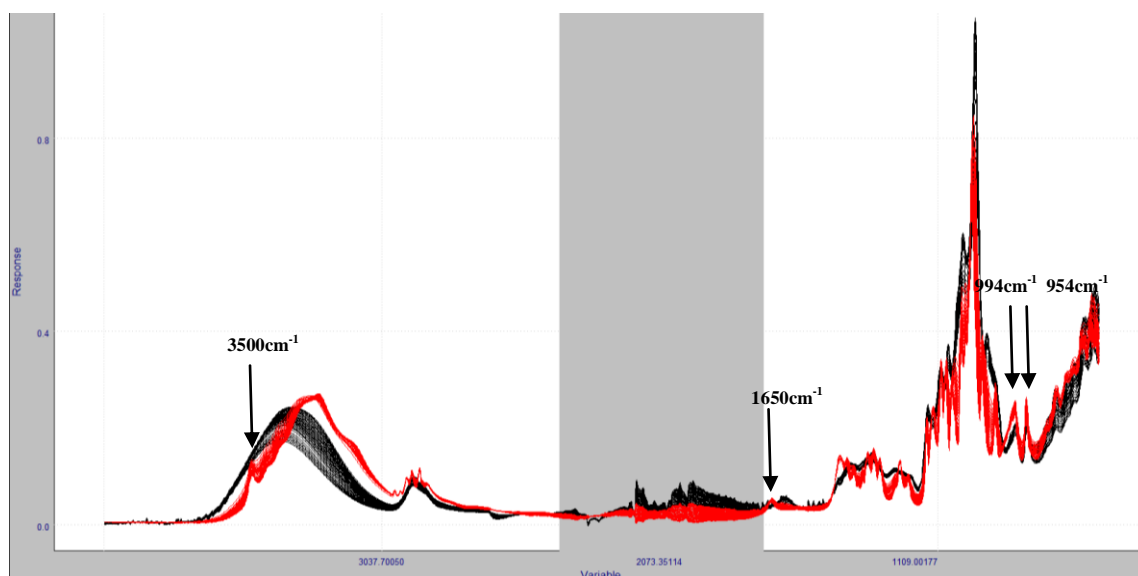


Figure 3.50 Variable temperature ATR-FTIR spectra of T_{h1} showing two clusters as identified in HCA data (**black**) correlates to spectra at 30°C to 116°C, (**red**) correlates to spectra at 118°C to 198°C

Figure 3.51 shows the results of the hierarchical cluster analysis dendrogram of T_{h2} for variable temperature ATR-FTIR spectra obtained from 30°C to 198°C at a heating rate of

2°C/min spectra at 1 minute intervals. *Figure 3.52* illustrates Variable temperature ATR-FTIR spectra of T_{h2} showing three clusters as identified in HCA data. HCA dendrogram identified three clusters with a relatively low similarity value of approximately 0.22 indicating the samples identified within these clusters were comparatively dissimilar. The first cluster correlated to a spectra obtained at 30°C to 116°C, the second to a spectra obtained at 118°C to 134°C and the third cluster to a spectra obtained at 136°C to 198°C (*Figure 3.52*). Analysis of the spectra showed that from 30°C to 116°C (depicted in green in *Figure 3.52*) T_{h2} was crystalline as characterised by sharp absorption bands at 3500 cm^{-1} , 1650 cm^{-1} , 994 cm^{-1} and 954 cm^{-1} in a similar trend to T_{h1} samples. Spectra changed at 118°C, the peaks observed at 3500 cm^{-1} and 1650 cm^{-1} disappeared and a peak at 3300 cm^{-1} was observed along with peaks at 994 cm^{-1} and 954 cm^{-1} . Spectra changed at 136°C changed and exhibited broad features indicative of a wide range of hydrogen bond lengths and orientations within a sample characteristic of an amorphous form.

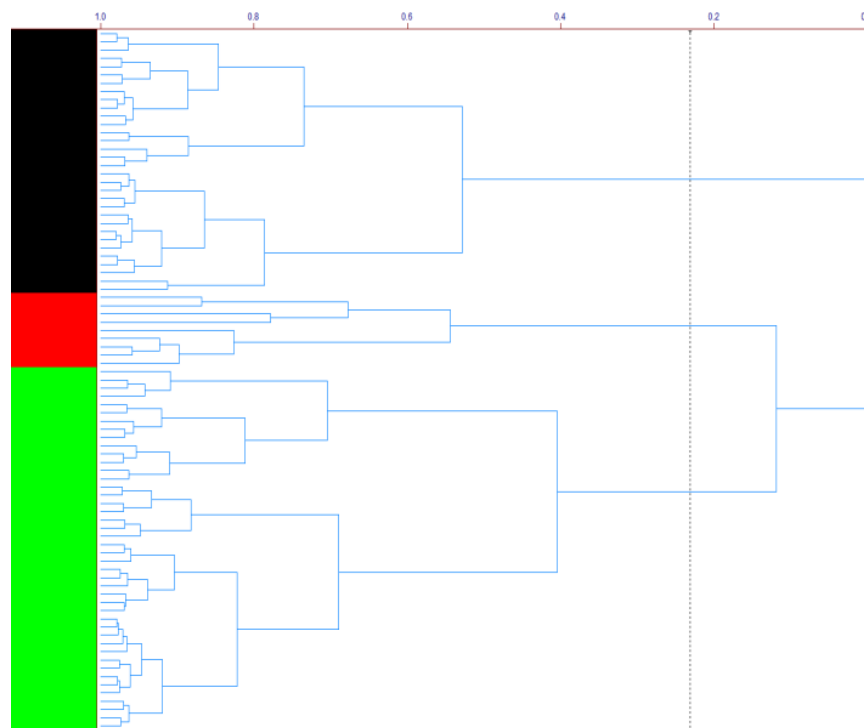


Figure 3.51 A hierarchical cluster analysis dendrogram of T_{h2} for variable temperature ATR-FTIR spectra obtained from 30°C to 198°C at a heating rate of 2°C/min spectra at 1 minute intervals

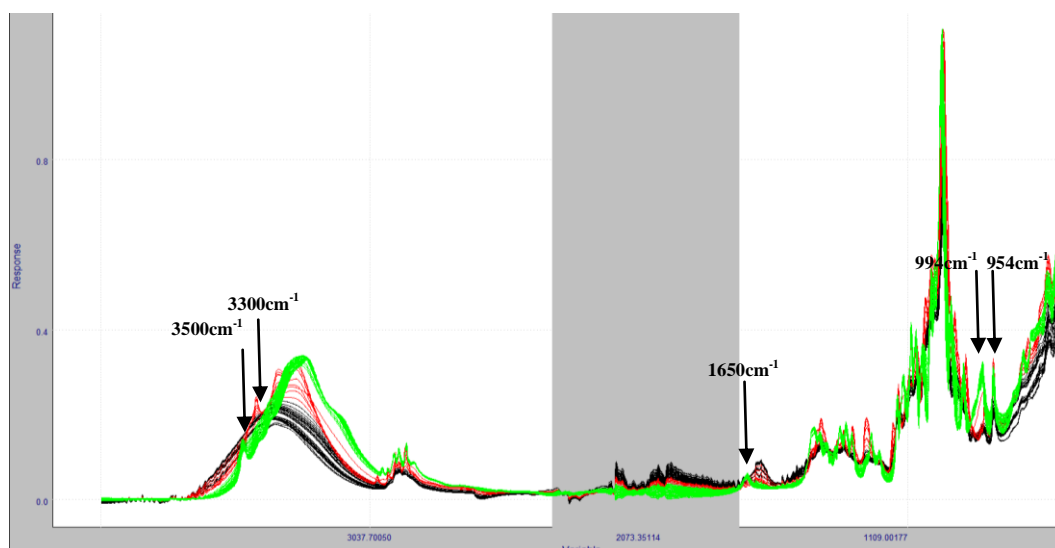


Figure 3.52 ATR-FTIR spectra of T_{h2} showing three clusters as identified in HCA data (**green**) correlates to spectra at 30°C to 116°C, (**red**) correlates to spectra at 118°C to 134°C (**black**) correlates to spectra at 136°C to 198°C

HCA identified an intermediate crystalline entity (which will now be referred to as T_{hx}) that started forming at 118°C. Further analysis of HCA dendrogram coupled with two dimensional PCA scores data (*Figure 3.53*) and ATR-FTIR spectra showed that an intermediate crystalline entity was fully formed at 118°C. As discussed previously, spectra changed at 136°C to features characteristic of an amorphous form. These results implied that an amorphous form was generated by the melt of the intermediary crystalline entity, T_{hx} . Two dimensional PCA scores data for both T_{h1} and T_{h2} (*Figure 2.50* and *Figure 2.51*) showed the variable temperature ATR-FTIR spectra was divided into two groups and three groups respectively.

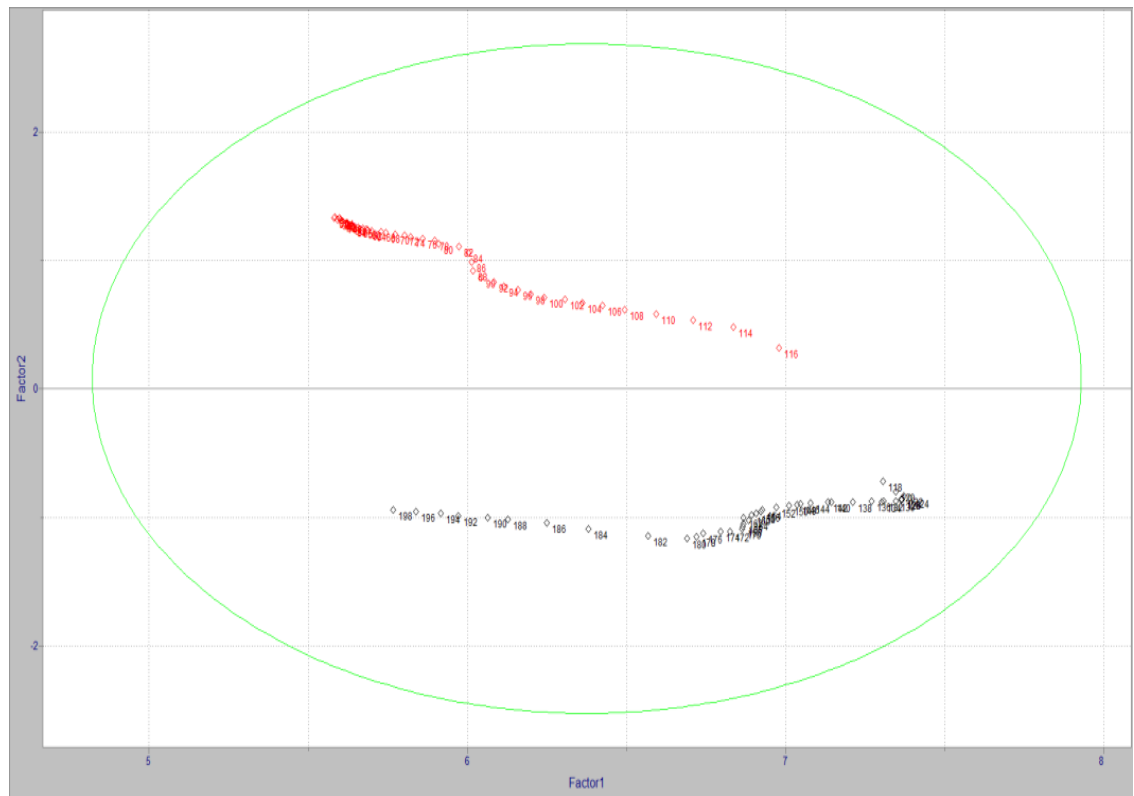


Figure 3.53 Two dimensional PCA scores plot of T_{h1}

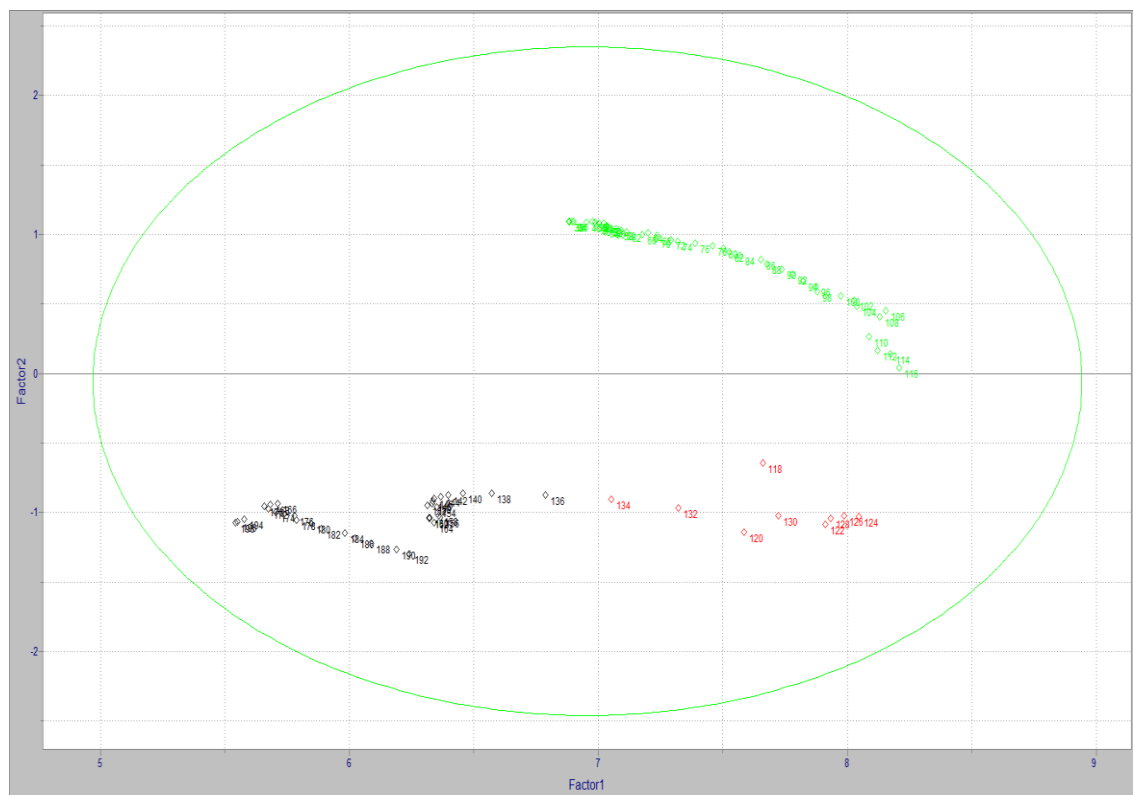


Figure 3.54 Two dimensional PCA scores plot of T_{h2}

PCA data and HCA data were in agreement for all the points as can be seen from the colour coding. PCA data was however, able to identify difference in molecular arrangement between both samples from 30°C to 116°C.

3.3.4.6 Generation and basic characterisation of T_{hx} form

Variable temperature ATR-FTIR studies showed that T_{h1} and T_{h2} experienced similar transitions from 30°C to 116°C after which their transitions differed. An intermediary crystalline structure was identified after heating T_{h2} at 118°C. Further investigations into this intermediary state were performed using variable temperature ATR-FTIR by heating T_{h2} at 2°C/min from 116°C to 120°C and holding isothermally for 12 hours to ensure full formation (*Figure 3.55*). This procedure was carried to test out the reproducibility of the crystalline form generated. After this, T_{hx} samples were generated by heating T_{h2} in an oven pre-heated at 120°C with no vacuum. Upon generation of this sample, it was characterised using SEM, XRPD, TGA and MTDSC techniques.

ATR-FTIR results showed that the crystalline form generated after T_{h2} was held isothermally at 120°C for 12 hours was similar to that generated in previous ATR-FTIR studies characterised by the presence of peaks at 3300 cm^{-1} , 994 cm^{-1} and 954 cm^{-1} . This crystalline form was then generated in an oven pre-heated to 120°C with no vacuum and was again tested to confirm it was the same as that observed in variable temperature ATR-FTIR studies of T_{h2} (*Figure 3.56*).

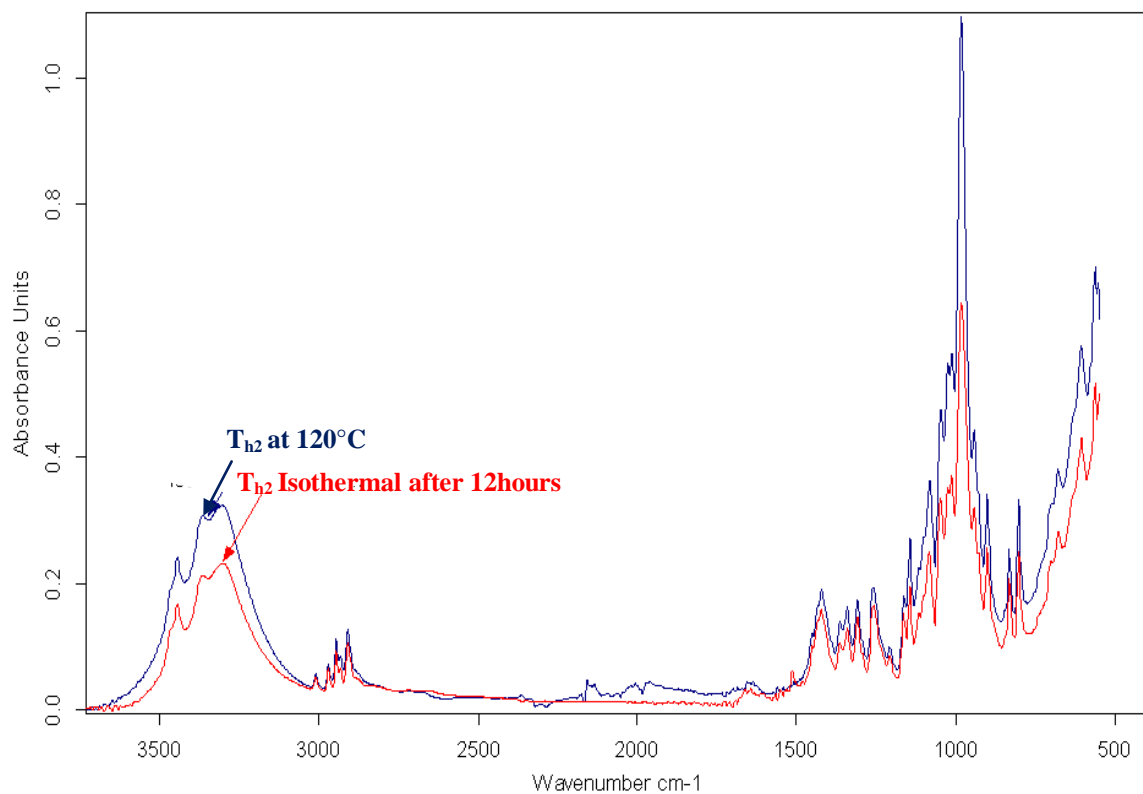


Figure 3.55 ATR- FTIR Spectra of T_{h2} at 120°C (**blue**), T_{h2} held isothermal for 12hours (**red**)

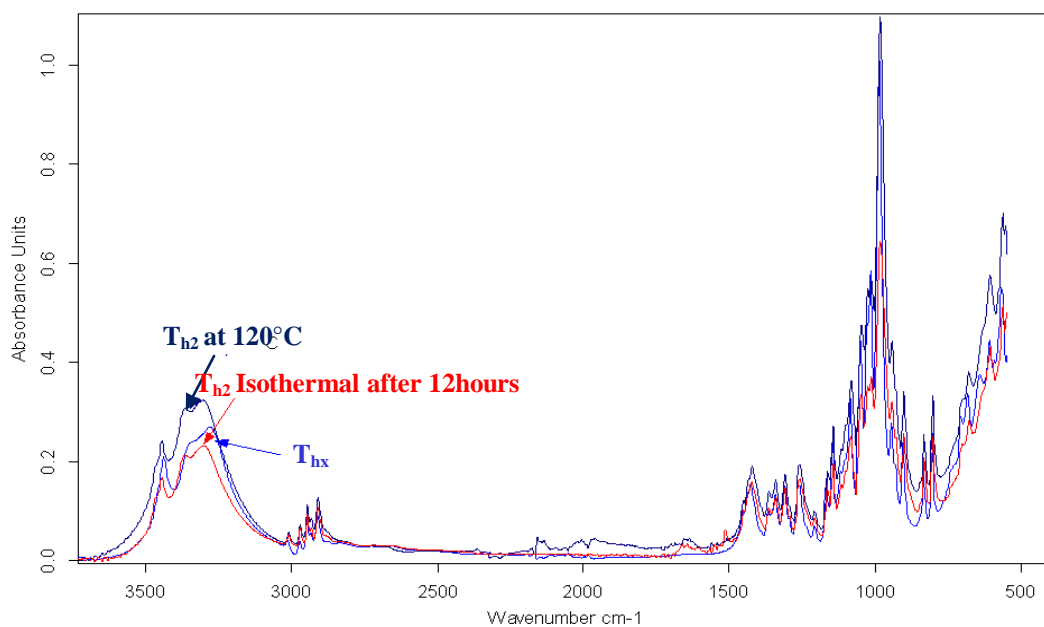


Figure 3.56 ATR- FTIR Spectra of T_{h2} at 120°C (**blue**), T_{h2} held isothermal for 12hours (**red**), T_{hx} generated at 120°C in an oven (**blue**)

Particle morphology of T_{hx} was determined using SEM techniques. SEM images of T_{hx} are illustrated in *Figure 3.57*. T_{hx} samples were irregular in shape and had a different texture and morphology to T_{h2} . Particles were agglomerated together and appeared chalky in character.

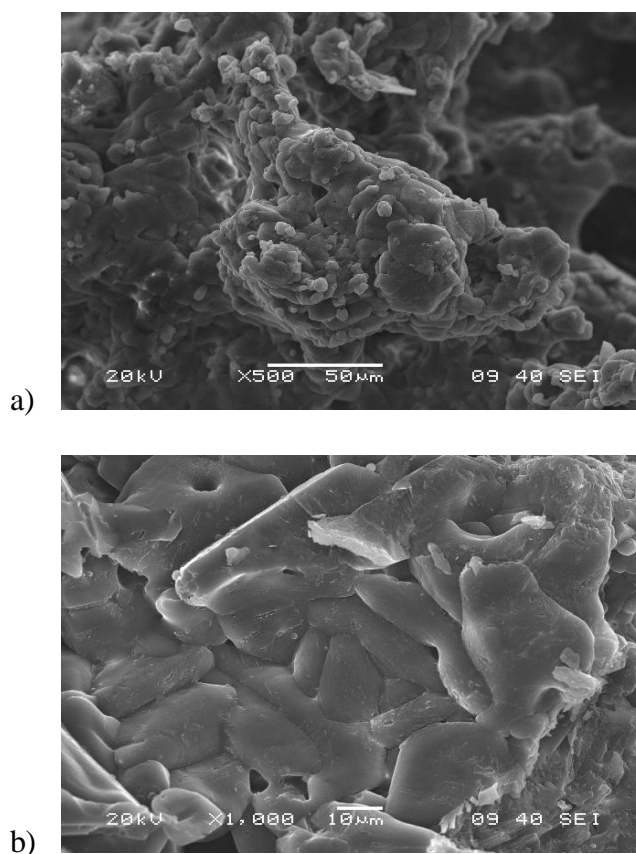


Figure 3.57 a) SEM image of T_{hx} b) Cross section showing grain boundaries. Scale bar corresponds to a) $50\mu\text{m}$ b) $10\mu\text{m}$

XRPD studies were performed on T_{hx} to confirm its solid state. XRPD diffractogram of T_{hx} (*Figure 3.58*) exhibited clearly defined sharp peaks of varied intensities. These peaks correspond to the uniform lattice spacing and arrangements and orientation of molecules in the crystal lattice. Peaks at 2θ 6.94° , 2θ 17.70° , 2θ 20.78° and 2θ 22.72° were identified. In previous studies the anhydrous form T_a has been identified by a peak existing at ca. 2θ

16° which does not appear in the XRPD diffractogram of the dihydrate or the stable anhydrous form T_β (Furuki et al., 2005). T_β is defined by peaks at *ca.* 2θ 6.7° , *ca.* 2θ 20.5° and *ca.* 2θ 22.5° . Interestingly, XRPD diffractogram appeared to have an amorphous halo which was not evident in XRPD diffractograms of T_{h1} or T_{h2}

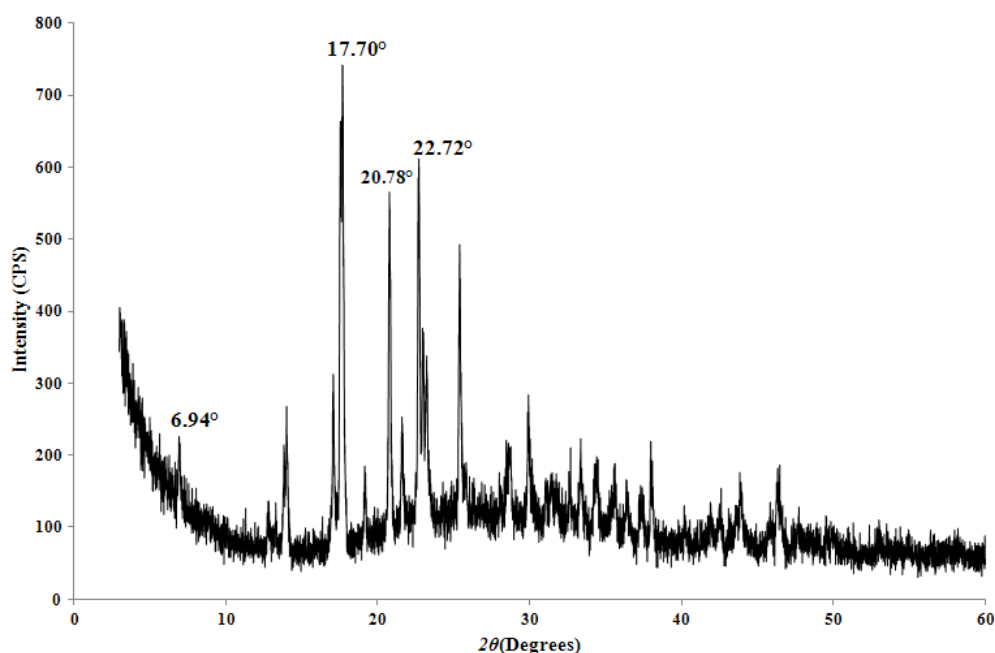


Figure 3.58 XRPD diffractogram of T_{hx}

In this study, MTDSC experiments were performed on T_{hx} at $2^\circ\text{C}/\text{min}$ with a $\pm 0.212^\circ\text{C}$ modulation over a 60 second period. A typical MTDSC total and reversing heat flow signal of T_{hx} is shown in *Figure 3.59*. The results obtained here proved very interesting. In the reversing heat flow signal (amplified image provided in *Figure 3.60*), a step change characteristic of a glass transition event (with associated enthalpic recovery) was observed at 121.77°C with a heat capacity change (ΔC_p) of $0.5206\text{J}/\text{g}\cdot^\circ\text{C}$. In the total heat flow, a single endotherm was observed at 210.27°C .

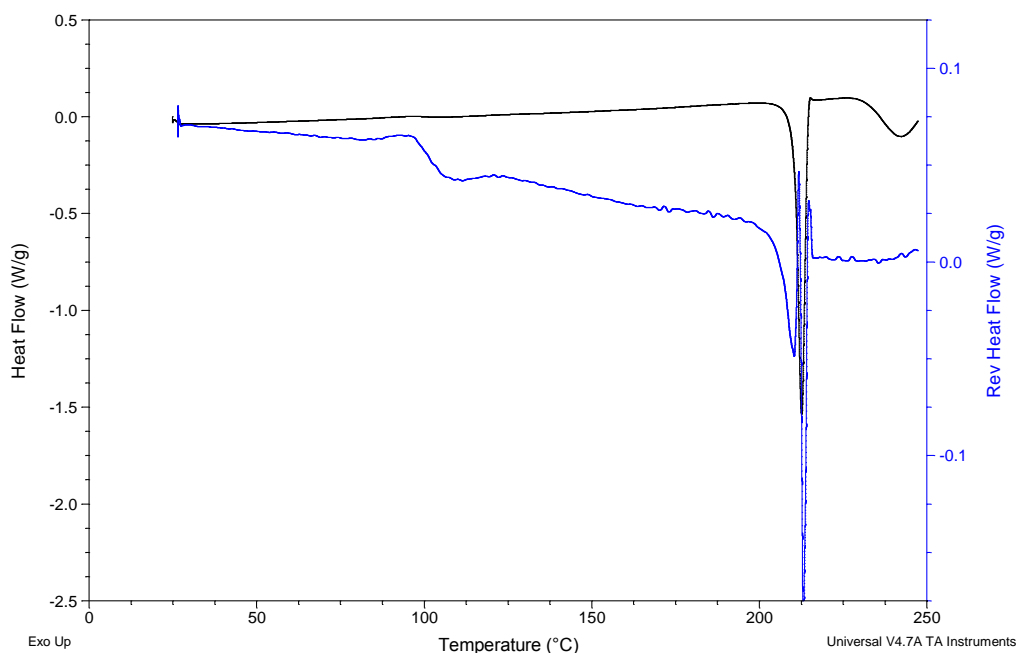


Figure 3.59 Typical MTDSC total and reversing heat flow signals for T_{hx} at $2^{\circ}\text{C}/\text{min} \pm 0.212^{\circ}\text{C}$ modulation over a 60 second period using a pin-holed pan

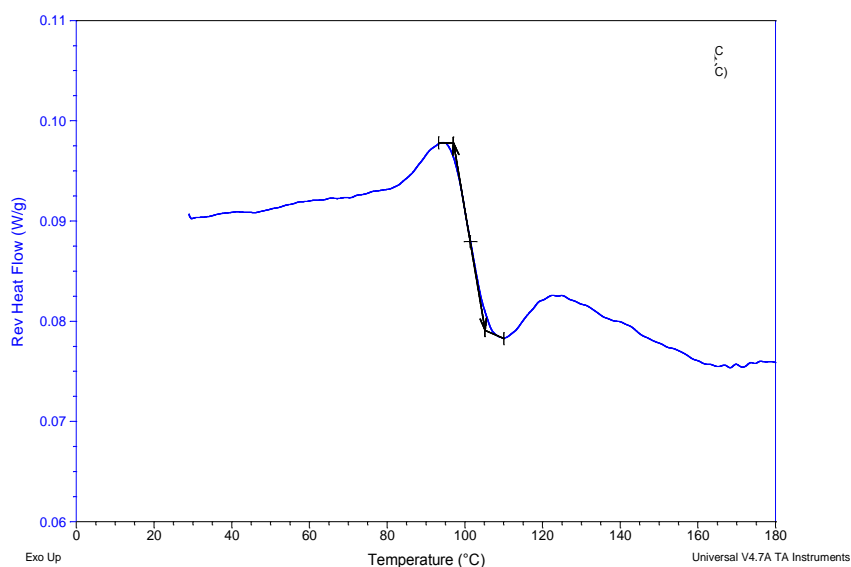


Figure 3.60 Typical MTDSC reversing heat flow signals for T_{hx} at $2^{\circ}\text{C}/\text{min} \pm 0.212^{\circ}\text{C}$ modulation over a 60 second period using a pin-holed pan

A typical TGA profile for T_{hx} conducted at $2^{\circ}\text{C}/\text{min}$ (Figure 3.61) showed very interesting results. Sample appeared to gain weight (1.4%) and then lost weight at 133°C (1.0%).

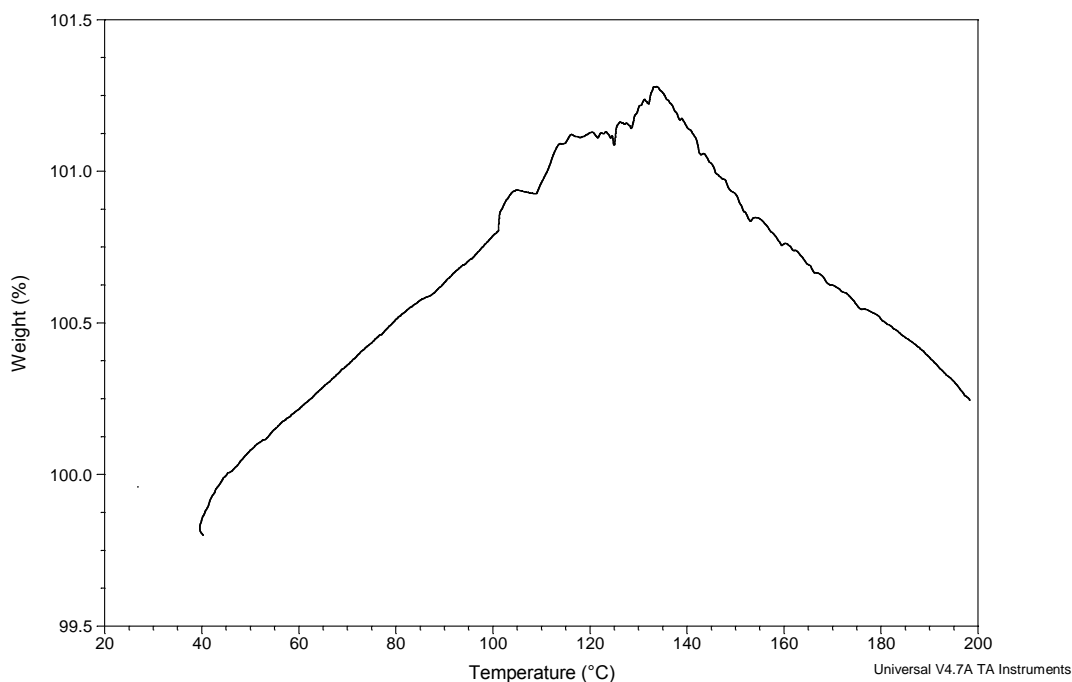


Figure 3.61 Typical TGA profile for T_{hx}

These preliminary TGA, MTDSC and XRPD data suggested that T_{hx} is a form of trehalose with XRPD characteristics similar to T_{α} and T_{β} though also displaying an amorphous halo suggesting an amorphous element. MTDSC results suggested T_{hx} was amorphous by the presence of a glass transition seen before the melt at $\sim 210^{\circ}\text{C}$ and no other endotherms observed prior to the glass transition event. No crystallisation was observed after the glass transition. TGA data showed some very interesting results, showing weight gain and not expected weight loss with increasing temperature followed by a dramatic decrease in weight at 133°C .

Previous studies (Sussich and Cesaro, 2008; De Giacomo, 2008) have suggested the existence of a non-crystallisable amorphous form of trehalose (T_{am2}) generated from the melt of an anhydrous trehalose form (in the literature this is reported as T_{β} which melts at

210°C). Final MTDSC experiments conducted on T_{hx} were performed to identify if any transitions were observed on gentle heating T_{hx} past its melt and cooling at the same heating temperature.

Experiments involved heating T_{hx} from 100°C to 215°C at 2°C/min. The sample was held isothermally at 215°C for 5 minutes to ensure full melting of T_{hx} and melting of any possible nuclei present. Sample was then cooled at 2°C/min to 25°C and finally reheated to 250°C. A typical MTDSC reversing heat flow signal for T_{hx} in the cooling cycle is shown in *Figure 3.62*. A T_g was observed at 116.89°C (ΔC_p , 0.32J/g·°C). In the heating cycle shown in *Figure 3.63* a T_g was observed at a slightly higher temperature of 117.53°C (ΔC_p , 0.72J/g·°C). A total heat flow signal for the amorphous form generated by the melt of T_{hx} is also depicted in *Figure 3.63*. Further heating past the T_g showed identified a broad endotherm observed at 227°C.

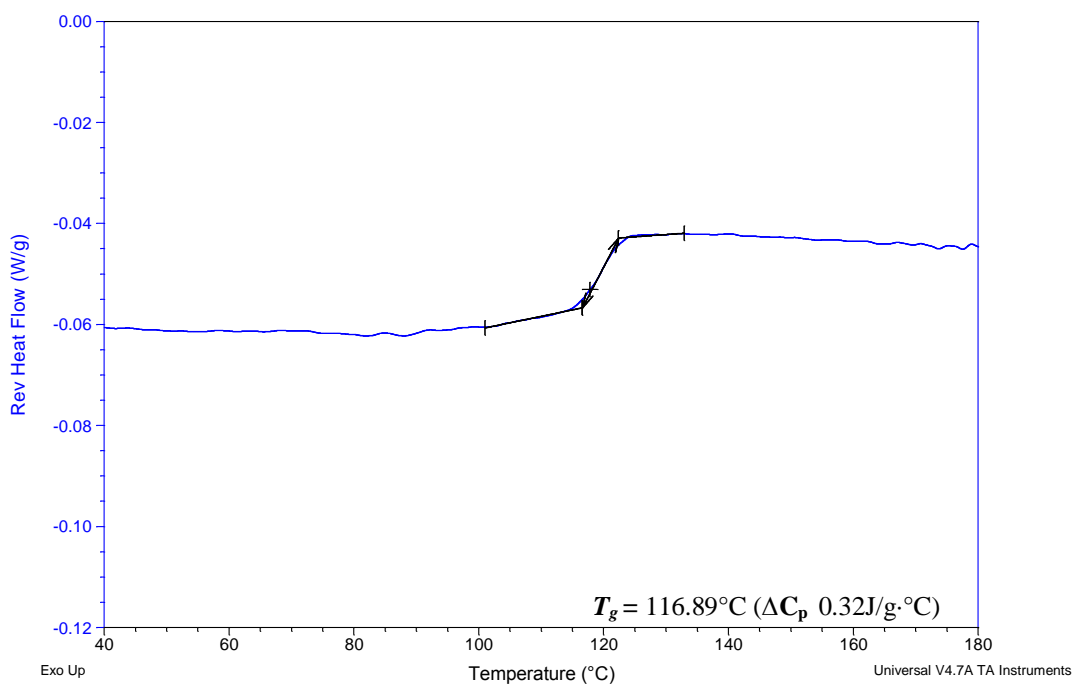


Figure 3.62 Typical MTDSC (cooling cycle) reversing heat flow signals for T_{hx} at 2°C/min $\pm 0.212^\circ\text{C}$ modulation over a 60 second period using a pin-holed pan

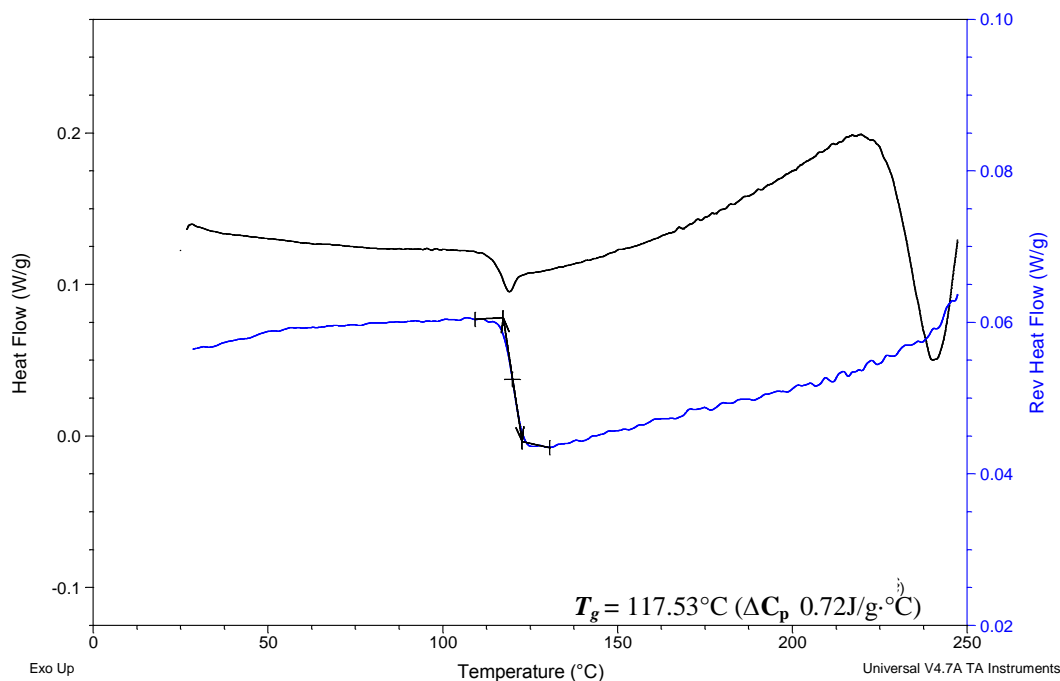


Figure 3.63 Typical MTDSC (heating cycle) reversing heat flow signals for T_{hx} at $2^{\circ}\text{C}/\text{min}$ $\pm 0.212^{\circ}\text{C}$ modulation over a 60 second period using a pin-holed pan

These results showed that an amorphous form was generated from the melt of T_{hx} . De Giacomo, (2008) has proposed the existence of two amorphous phases referred to as T_{am1} and T_{am2} . T_{am2} (T_g 117.9°C) is a non-crystallisable amorphous phase said to be the liquid obtained from the melt of T_{β} which occurs at $\sim 210^{\circ}\text{C}$. By these methods the liquid is unable to crystallise. Whilst a crystallisable amorphous phase, T_{am1} (T_g 117.3°C) is generated from the melt of the isomorph desolvate of the dihydrate T_{α} which occurs at $\sim 135^{\circ}\text{C}$. The results detailed in this section confirmed the generation of an amorphous form from the melt of T_{hx} however, T_{hx} has been preliminarily identified as a mixture of T_{α} , T_{β} possessing an amorphous element to its form. Further characterisation of this form is required to fully determine the correlation of these finds to findings in the literature. Further experiments were not conducted on T_{hx} as this was outside of the objectives of this thesis.

3.4 SECTION SUMMARY

In this section the properties of T_{h1} , T_{h2} and T_{hx} are summarised in this section before a conclusion is reached on the results.

The main objective of this study was to generate standardised forms of trehalose dihydrate and characterise samples with an aim to gain a further and clearer understanding of the thermal transitions of trehalose dihydrate with a focus on the transitions that occur between 30°C to 160°C. Two methods were employed to generate two different standardised forms of trehalose dihydrate. Method I was based on a method by Dupray et al., (2009). T_{h1} samples were generated by slow evaporation of a 46.6%w/w (solubility of trehalose dihydrate at 20°C (Lammert et al., 1998)) saturated trehalose solution, whilst method II was based on water sorption studies (further discussed in *Chapter 4*) where amorphous trehalose was exposed to 75%RH (using a sodium chloride saturated solution stored at room temperature) generating T_{h2} samples. T_{hx} was generated by heating T_{h2} in an oven pre-heated at 120°C with no vacuum.

T_{h1}

T_{h1} was confirmed to be trehalose dihydrate using XRPD and ATR-FTIR techniques were characteristic XRPD peaks and FTIR peaks were observed.

Thermal characterisation of T_{h1} showed that transitions were greatly influenced by pan type and heating rate. In both pin hole and closed pan systems a single low temperature endotherm was observed, the higher temperature endotherm observed at 224.3°C in pin-

holed pan studies shifted to 119.6°C in closed pan experiments. At 20°C/min fast heating DSC experiments three endotherms were observed (two low temperature endotherms and one higher temperature endotherm) were observed in contrast to two endotherms and a single endotherm observed at 50, 100, 500 and 750°C/min.

Slow heat/cool MTDSC experiments were conducted to observe the effects of heating rate on the products formed after the low temperature endotherm was observed. Results suggested that on heating; T_{h1} was dehydrated resulting in structural collapse and the in-situ generation of a glassy liquid. This phenomenon was confirmed in Qi-MTDSC and variable temperature ATR-FTIR studies. HSM studies identified crystallisation from this liquid at ~202°C unfortunately due to experimental limitations these effects were not reproduced in Qi-MTDSC or variable temperature ATR-FTIR studies. However a crystallisation exotherm was observed in slow heat/cool MTDSC experiments in the second heat at 1°C/min at ~179°C/min.

Dupray et al., (2009) conducted open pan DSC and TGA experiments on T_{h1} at 1°C/min (*Figure 3.64*). The first endotherm (1) was assigned to dehydration associated with a transition from trehalose dihydrate to an amorphous form. An exotherm (2) was observed linked to a cold crystallisation event corresponding to the re-crystallisation of the stable anhydrate T_{β} . Dupray et al., (2009) suggest that the second low temperature endotherm was caused by a migration of a fluid phase beneath the crystallized surface which leaves the crystal at ~124°C (3). This was then followed by the melt of T_{β} (4).

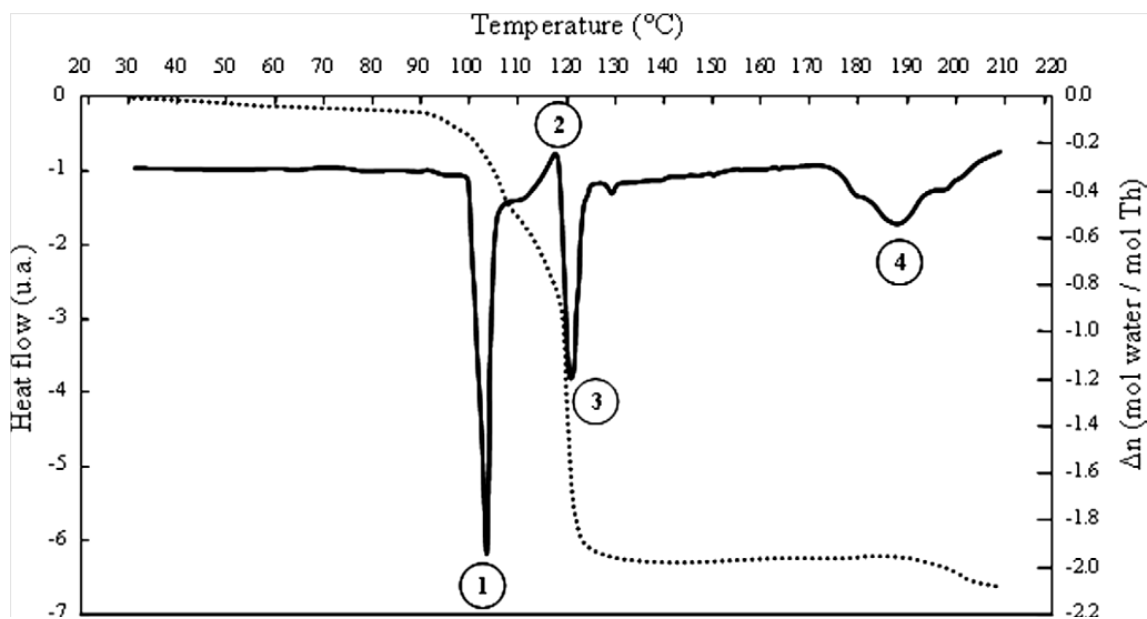


Figure 3.64 DSC (solid line) and TGA (dotted line) curves for T_{h1} taken from Dupray *et al.*, (2009) at a heating rate of $1^{\circ}\text{C}/\text{min}$

T_{h2}

T_{h2} was confirmed to be trehalose dihydrate using XRPD and ATR-FTIR techniques were characteristic XRPD peaks and FTIR peaks were observed.

Thermal characterisation of T_{h2} showed that transitions were influenced by pan type and to a lesser extent heating rate. Three endotherms were observed in pin-holed experiments in contrast to two endotherms observed in closed pan studies. The second endotherm observed in pin-holed studies was attributed to water loss. MTDSC and TGA results indicated that when both samples are heated in a closed pan system, water loss is impeded which in turn alters the temperature for phase transitions.

In slow/cool MTDSC experiments, T_g was not detected in the cooling cycle or in the second heat. This could have been due to a weaker glass transition signal compared to the T_g observed in the cooling cycle and second heat in T_{h1} experiments. Modulation amplitude of $\pm 1^\circ\text{C}$ was chosen to improve resolution of the weaker glass transition in Qi-MTDSC experiments. An endotherm was observed at $\sim 209^\circ\text{C}$ in the total heat flow in all heating rates in slow MTDSC experiments. These results were not supported by HSM studies.

Qi-MTDSC suggested that on dehydration of T_{h2} resulted in structural collapse and the in-situ generation of a glassy liquid. However, variable temperature ATR-FTIR showed that upon heating T_{h2} , T_{hx} was formed at 118°C .

T_{hx} samples were generated by heating T_{h2} in an oven pre-heated at 120°C with no vacuum. These preliminary TGA, MTDSC and XRPD data suggested that T_{hx} is a form of trehalose with XRPD characteristics similar to T_α and T_β though also displaying an amorphous halo suggesting an amorphous element. Further MTDSC experiments confirmed the generation of an amorphous form from the melt of T_{hx} . Further characterisation of this form is required to fully determine the correlation of these finds to findings in the literature.

Figure 3.65 is a schematic illustrating the thermal transitions of T_{h1} , T_{h2} and T_{hx} identified from experiments conducted in this study. This shows that dehydration of T_{h1} resulted in structural collapse leading to the generation of an amorphous form. Further heating lead to

the re-crystallisation of T_{β} confirmed by the subsequent melt at $\sim 210^{\circ}\text{C}$. In contrast, dehydration of T_{h2} resulted in the structural collapse and molecular re-arrangement to T_{hx} further heating resulted in generation of an amorphous liquid.

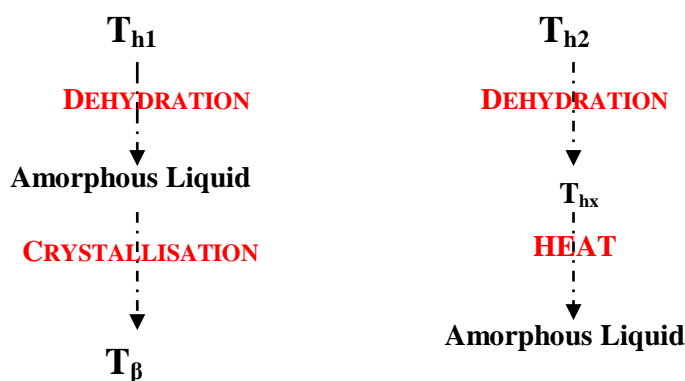


Figure 3.65 schematic illustrating the thermal transitions of T_{h1} , T_{h2} and T_{hx}

3.5 CONCLUSION

Preliminary work detailed in *Section 3.2* aimed to determine the influence of inter- and intra-batch variations on the thermal response of trehalose dihydrate by performing a series of thermal, spectroscopic and X-ray diffraction techniques on trehalose dihydrate obtained from two different manufacturers. Results obtained confirmed the need for standardised forms of trehalose dihydrate to “erase” the processing history of in order to achieve a clear understanding of the thermal transitions of trehalose dihydrate.

The main objective of the work detailed in this section was to generate standardised forms of trehalose dihydrate and characterise samples with an aim to gain a further and clearer understanding of the thermal transitions of trehalose dihydrate with a focus on the transitions that occur between 30°C to 160°C . Two methods were employed to generate two different standardised forms of trehalose dihydrate. Method I was based on a method

by Dupray et al., (2009). T_{h1} samples were generated by slow evaporation of a 46.6% w/w (solubility of trehalose dihydrate at 20°C (Lammert et al., 1998)) saturated trehalose solution, whilst method II was based on water sorption studies (further discussed in *Chapter 4*) where amorphous trehalose was exposed to 75%RH (using a sodium chloride saturated solution stored at room temperature) generating T_{h2} samples.

In contrast to trehalose dihydrate batches Sigma B and Acros batch a clearer baseline was observed in MTDSC studies conducted on standardised forms T_{h1} and T_{h2} . Using standardised forms of trehalose dihydrate, physico-chemical properties identified could be attributed to the intrinsic properties of the sample and preparation method and not due to sample variability. Using standardised forms, a clearer understanding of the thermal transitions and thermal behaviour of trehalose dihydrate on heating were able to be made.

CHAPTER FOUR

CHARACTERISATION OF AMORPHOUS AND

CRYSTALLINE SUGARS

4.1 BACKGROUND

In order to proceed with further experiments, it was important to have an understanding of the basic physico-chemical properties of the amorphous samples generated.

4.2 STUDY OBJECTIVE

The objective of the work detailed in this chapter was to generate pure amorphous sugars (via spray drying) and characterise their physico-chemical properties using a range of diffraction, spectroscopic and thermal techniques with reference to their crystalline counterparts. Standardised forms of trehalose dihydrate (T_{h1} and T_{h2}) were extensively characterised in the previous Chapter full details of these results are presented in *Chapter 3*.

4.3 GENERAL METHODOLOGY

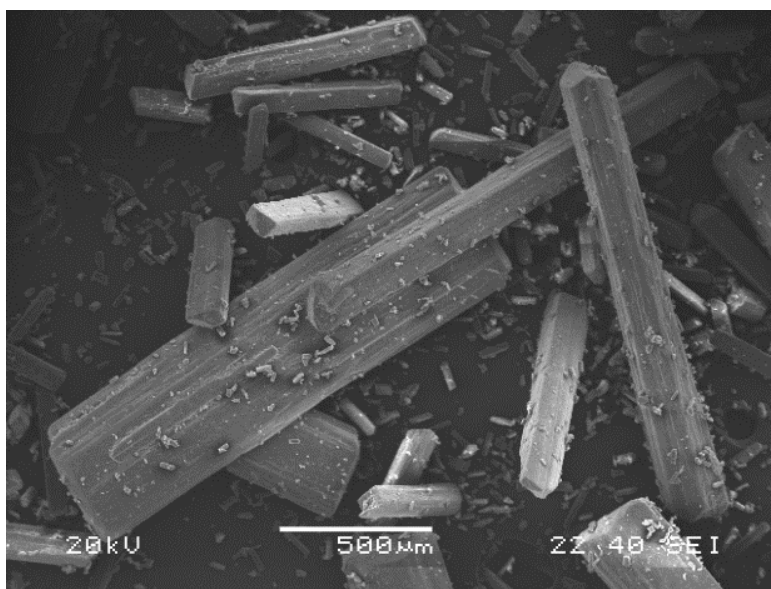
Amorphous sugar samples (trehalose, raffinose and sucrose) were generated via spray drying. Full details of the method and spray drying parameters used are detailed in *Chapter 2*. Particle morphology and size distribution were determined using scanning electron microscopy (SEM) and particle size analysis using laser diffraction. X-ray powder diffraction (XRPD) and ATR-FTIR were used as techniques to distinguish between the natures of the amorphous and crystalline samples. Modulated temperature DSC (MTDSC) was used to thermally characterise samples. Thermogravimetric analysis (TGA) was used to determine sample water content. Kinetics of water uptake was investigated in amorphous samples using dynamic vapour sorption (DVS). Full details of these

techniques are outlined in *Chapter 2* unless otherwise stated in the results and discussion section.

4.4 RESULTS AND DISCUSSION

4.3.1 PARTICLE SIZE AND MORPHOLOGY ANALYSIS OF CRYSTALLINE AND AMORPHOUS SAMPLES

Figure 4.1 and *Figure 4.2* show SEM images for raffinose pentahydrate and crystalline sucrose respectively. SEM images of raffinose pentahydrate (*Figure 4.1*) showed obviously large crystals as well as smaller crystals that appeared needle-shaped in character. At a higher magnification (*Figure 4.1b*), smaller crystals identified in *Figure 4.1* are confirmed to be needle-like crystals and were also accompanied by smaller irregular shaped crystals.



a)

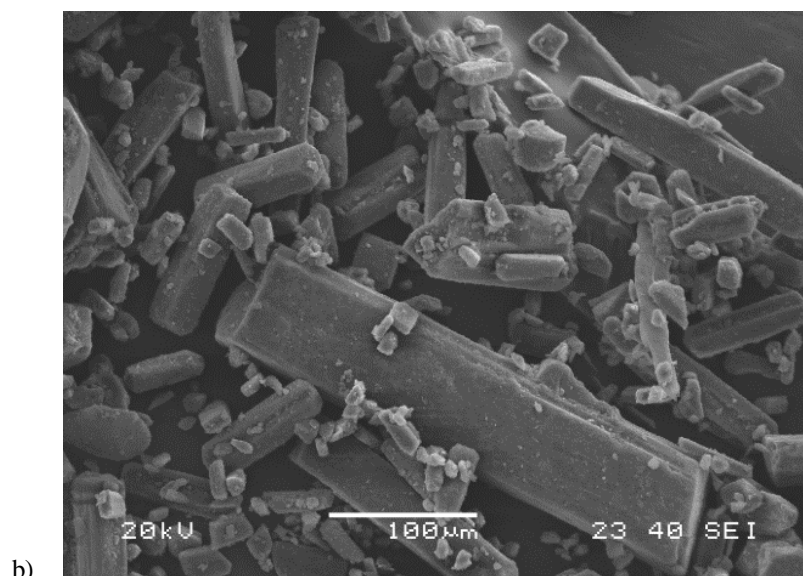
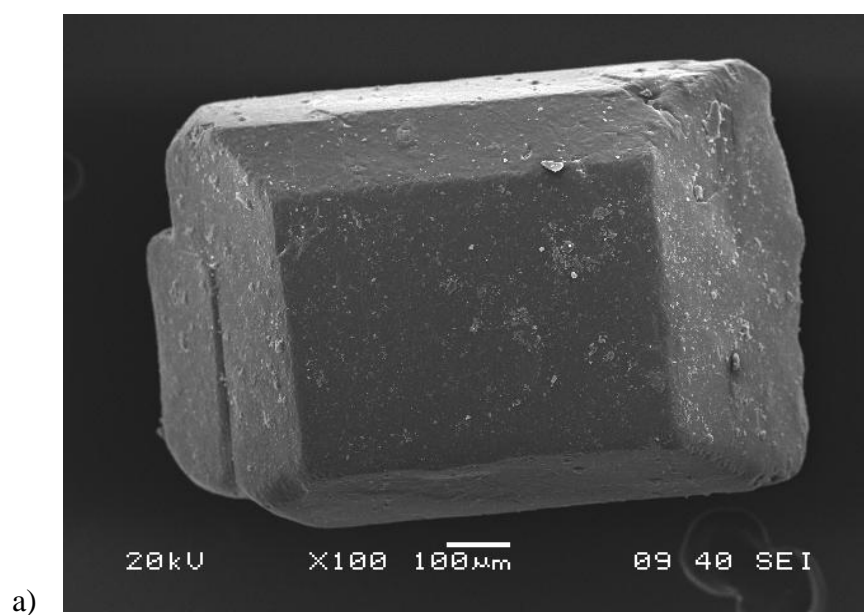


Figure 4.1 SEM images of raffinose pentahydrate. Scale bar corresponds to a) 500µm b) 100µm.

Figure 4.2 show SEM images of crystalline sucrose showing a large rectangular shaped crystalline and a large crystal agglomerate (Figure 4.2b) made up of fused smaller crystals.



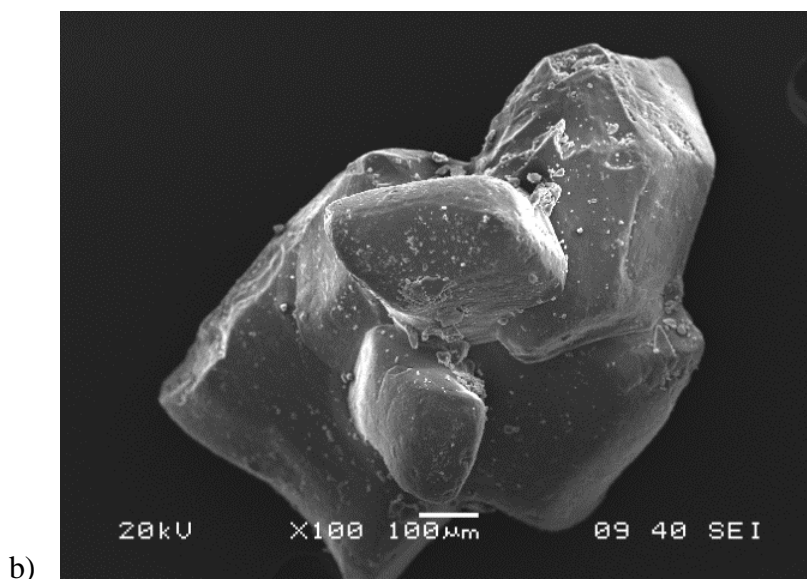


Figure 4.2 SEM images of crystalline sucrose. Scale bar corresponds to 100µm.

Generally, it is expected that amorphous particles generated via spray drying are spherical in shape. The particle morphology of amorphous samples produced in this study proved intriguing and are shown in *Figure 4.3*, *Figure 4.4* and *Figure 4.5*. Amorphous trehalose (*Figure 4.3*), raffinose (*Figure 4.4*) and sucrose (*Figure 4.5*) particles were spherical in shape and appeared solid in structure. However, SEM images for both amorphous trehalose and raffinose samples suggested that particle formation occurred because of smaller particles were being engulfed to make larger particles. It is likely that this phenomenon was because of droplet evaporation in the spray drying process. The size and morphology of particles generated by spray drying is determined by the stage at which droplet evaporation occurs (Moran and Buckton, 2007); solid particles formed are generally smaller than the droplet from which they have precipitated. Droplets with a lower solid content will be formed at a later stage in the process therefore resulting in smaller particles. This variation in rates of evaporation of different droplet sizes may help to explain the observations in amorphous trehalose and raffinose samples. Typical droplet mass median diameters in pharmaceutical spray dryers range from less than 10µm for

pulmonary applications to upwards of 100 μm , which translates to a typical dry particle diameter range of 0.5 to 50 μm (Vehring, 2008).

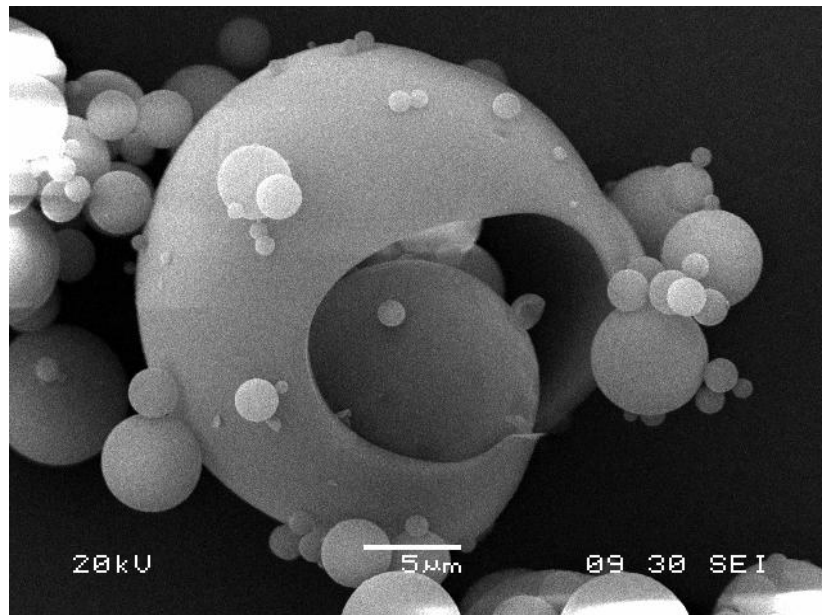


Figure 4.3 SEM images of a) amorphous trehalose. Scale bar corresponds 5 μm

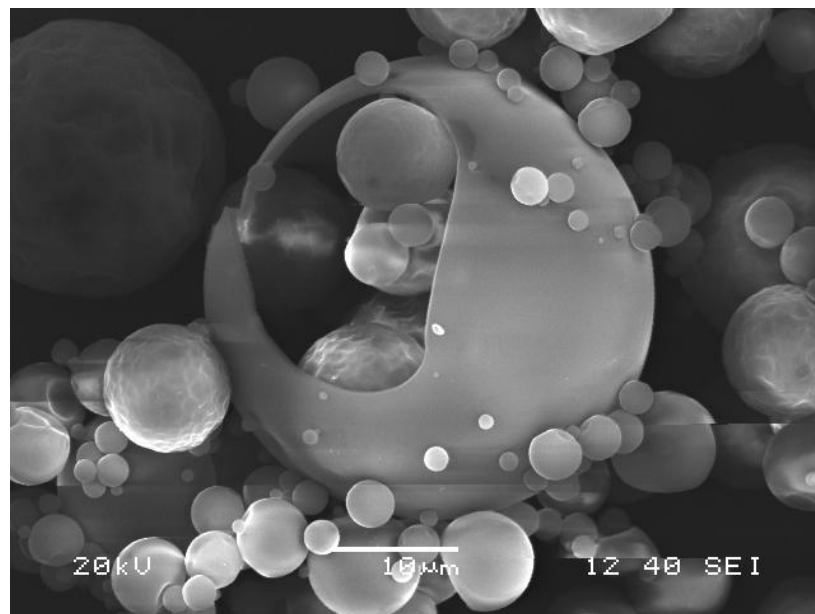


Figure 4.4 SEM images of amorphous raffinose. Scale bar corresponds to 10 μm

Amorphous sucrose particles (*Figure 4.5*) showed evidence of a high degree of particle fusion and possible evidence of deliquescence. Deliquescence (see *Chapter 1* for further

details) occurs when water is absorbed onto the particle surface enhancing molecular mobility leading to the dissolution of the amorphous solid; this process makes particles “sticky” and can promote crystallisation (Salameh and Taylor, 2005).

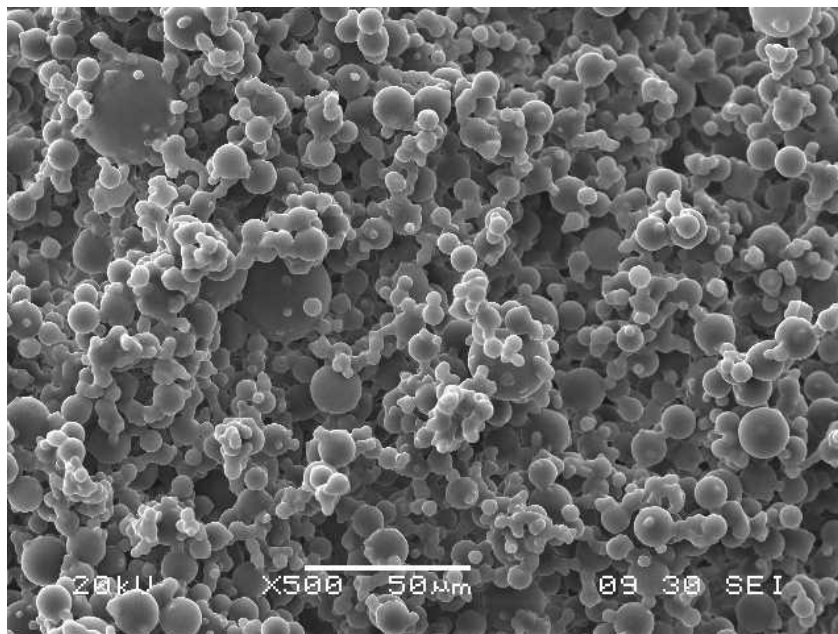


Figure 4.5 SEM image amorphous sucrose. Scale bar corresponds to 50μm

Aggregates were observed in all amorphous samples where smaller particles had fused together forming an agglomerate. This can occur when samples are close to their glass transition temperature in the spray dryer collection vessel making them sticky. Unfortunately, this can hinder product flow and stability. However, it can easily be prevented if the experimental outlet temperature can be controlled. Unfortunately, in this experiment it was not possible to control the outlet temperature.

Comparing SEM images of both amorphous and crystalline samples, it is apparent that the two forms have different morphologies and that the spray drying process results in a decrease in particle size and change a in morphology relative to crystalline samples.

Particle size analysis was performed using laser diffraction. Results presented (*Figure 4.6*, *4.7* and *4.8*) shows particle size analysis as the density distribution of particles (log of the volume size distribution) versus particle size. Raffinose pentahydrate particles (*Figure 4.6*) demonstrated a broad bi-modal distribution with the smallest crystals approximately $5\mu\text{m}$ in size and the largest particles approximately $490\mu\text{m}$ in size. Crystalline sucrose particles (*Figure 4.7*) were distributed between approximately between $400\mu\text{m}$ and $800\mu\text{m}$. It is possible that the bi-modal distribution observed in raffinose pentahydrate particle size analysis was due to the morphology of raffinose pentahydrate crystals where the length and the width possibly produced two different distributions. This event could possibly negate laser diffraction results making them unreliable.

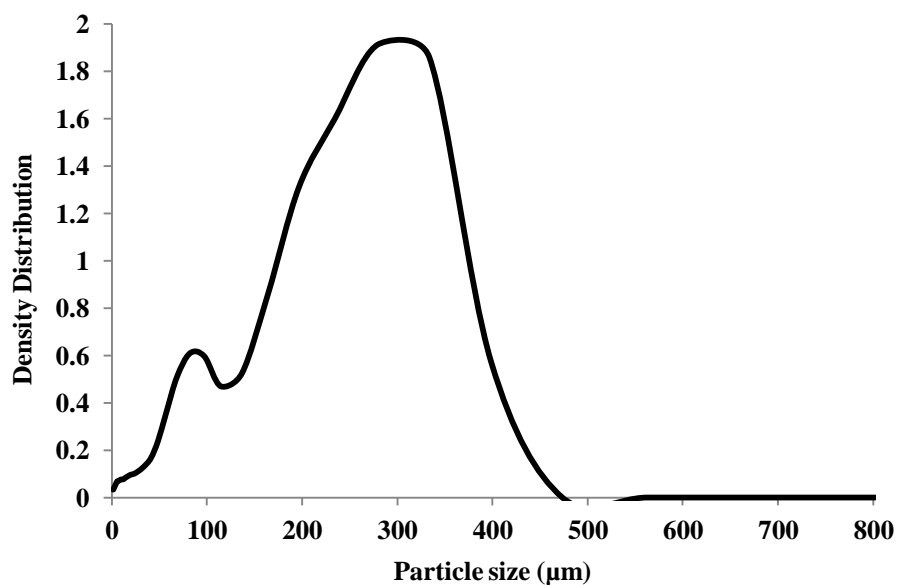


Figure 4.6 Average particle size distribution for raffinose pentahydrate

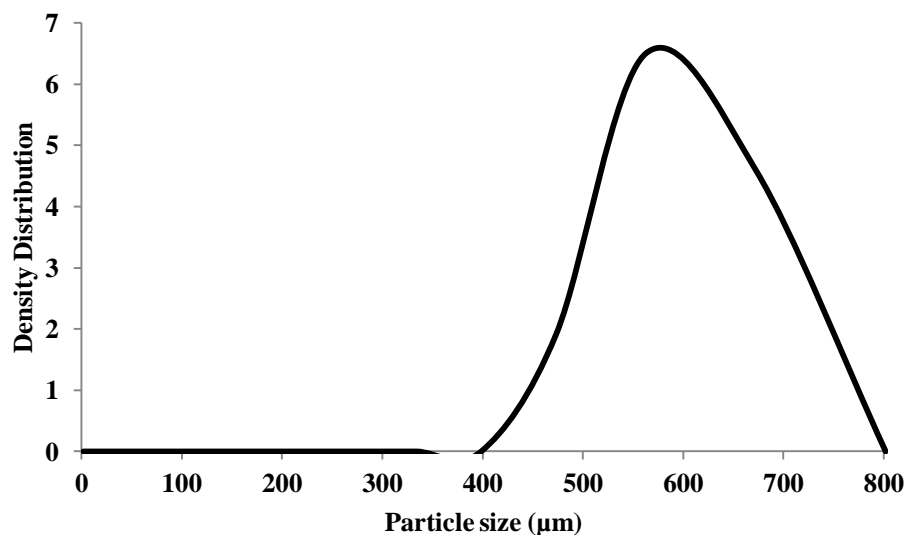


Figure 4.7 Average particle size distribution for crystalline sucrose

Spray dried amorphous particles (*Figure 4.8*) were of a more normal distribution with amorphous sucrose particles possessing a larger particle size distribution (approximately 5µm - 55µm) which could possibly be due to particle fusion and aggregate formation. Unfortunately, should aggregation occur, the laser diffraction system measures the overall size of the agglomerate instead of the size of the primary particles. Amorphous raffinose and amorphous trehalose particles were both normally distributed between 5µm-40µm and 5µm-45µm respectively. The particle size distributions for all amorphous particles generated in this study were similar, which was expected as the same spray drying conditions (i.e. same nozzle, inlet temperature and pump flow rate) were used for the preparation of each sample.

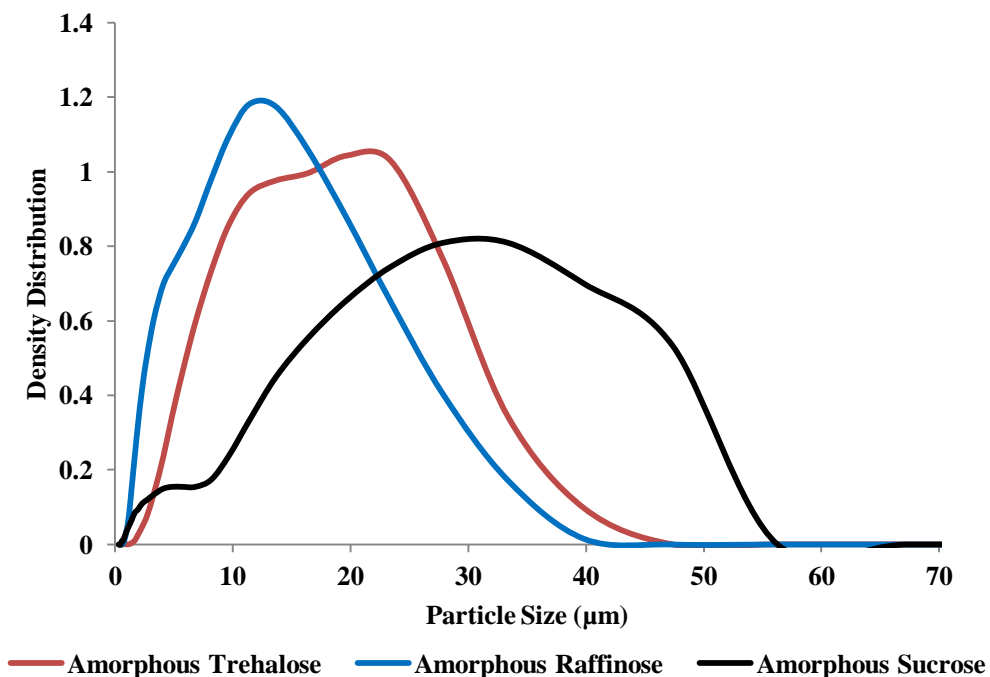


Figure 4.8 Average particle size distribution for amorphous trehalose, amorphous raffinose and amorphous sucrose

Overall, the results presented confirmed findings in SEM experiments in that crystalline and amorphous samples possess different particle size and morphology. Amorphous samples showed a reduced particle size compared with their crystalline counterparts. With raffinose pentahydrate and crystalline sucrose particles ranging from 5µm - 490µm and 2µm - 90µm (respectively). Amorphous raffinose, trehalose and sucrose particles ranged from 5µm - 45µm and 5µm - 55µm respectively.

4.3.2. X-RAY DIFFRACTION ANALYSIS OF CRYSTALLINE AND AMORPHOUS SAMPLES

Crystalline and amorphous samples of the same material are chemically identical but physically distinct. The XRPD profile for raffinose pentahydrate (*Figure 4.9*) displayed characteristic and expected peaks for raffinose pentahydrate at ca. 2θ 10.3°, 13.2° and 20.7° (Berman, 1970). Crystalline sucrose (*Figure 4.10*) showed characteristic and expected peaks at 2θ 11.6°, 13.1°, 18.8°, 19.6° and 24.6° (Hynes and Lepage, 1991).

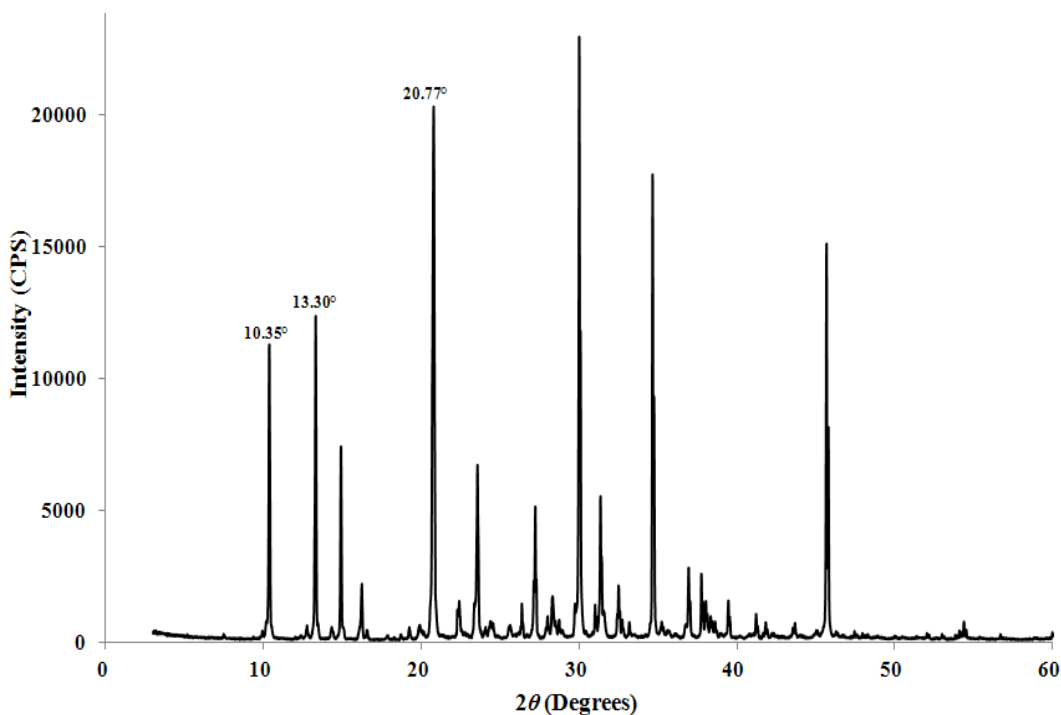


Figure 4.9 XRPD diffractogram of raffinose pentahydrate

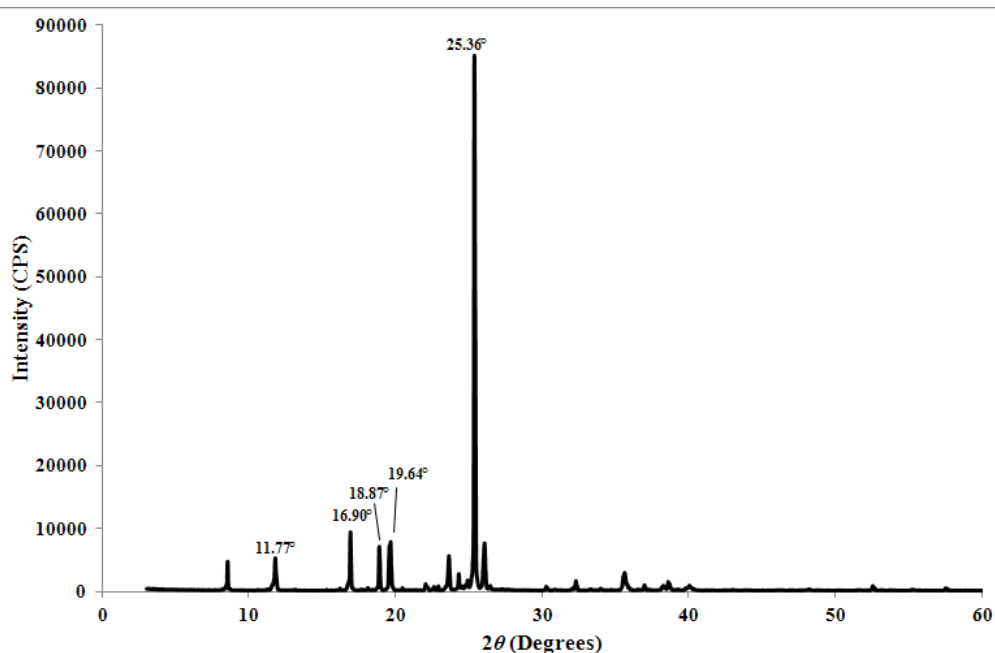


Figure 4.10 XRPD diffractogram of crystalline sucrose

It can clearly be seen that crystal sugar (raffinose pentahydrate and crystalline sucrose) diffractograms produced a series of clearly defined peaks of varying intensities which corresponds to the uniform lattice spacing and the arrangements and orientation of the molecules in agreement with the literature.

XRPD diffractograms for amorphous samples (*Figure 4.11*) showed an “amorphous halo” pattern showing no sign of peaks, indicating the absence of crystallinity (within instrument detection limits). The observed “amorphous halo” pattern occurs as a result of relative random arrangements of molecules within the amorphous materials. XRPD results for both amorphous and crystalline samples highlights the distinct differences in molecular arrangements between the two states.

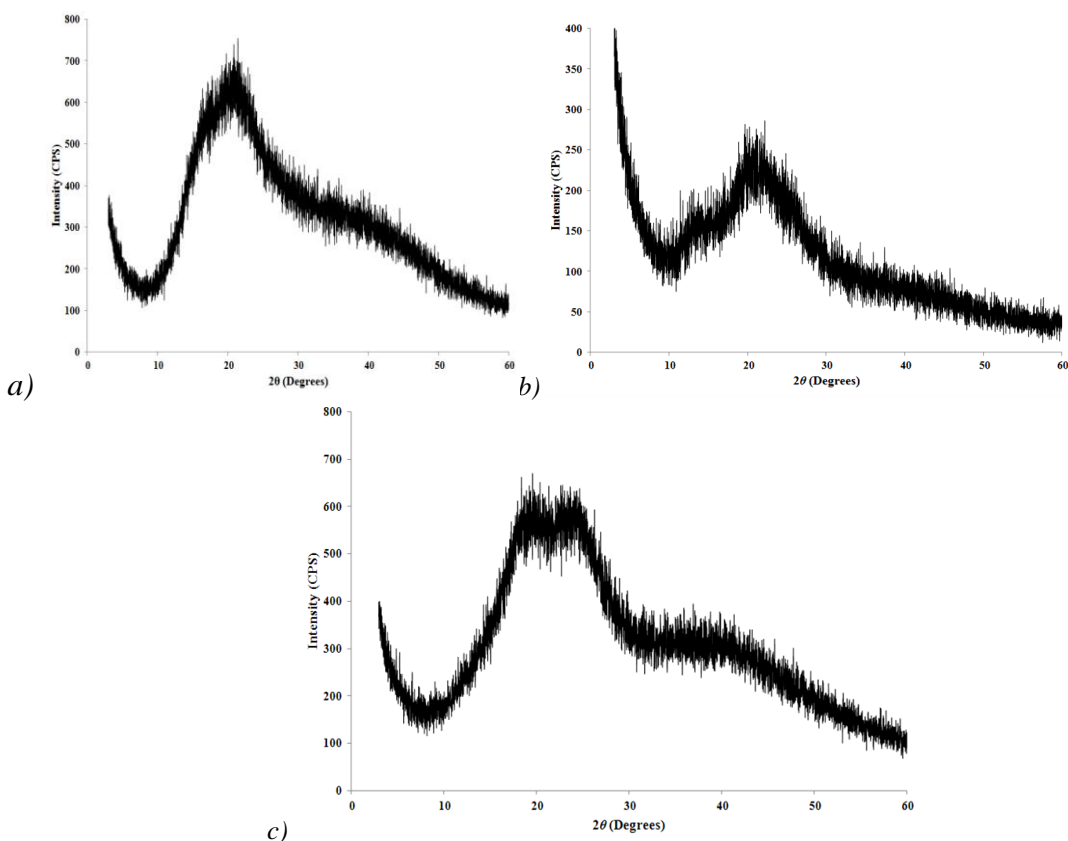


Figure 4.11 XRPD diffractogram of a) amorphous raffinose b) amorphous sucrose c) amorphous trehalose

4.3.3. SPECTROSCOPIC ANALYSIS OF CRYSTALLINE AND AMORPHOUS SAMPLES

Due to the temperatures used in the spray drying process to evaporate the solvent (in this case water), the spray-dryer glassware tended to get warm during particle processing. This includes the sample collection vessel and hence because of this there was some potential for the material produced at the start of processing to increase in temperature and re-crystallise before the run was finished. It was therefore important to check the amorphicity of the sample produced.

4.3.3.1 Crystalline Samples

ATR-FTIR spectra of raffinose pentahydrate and crystalline sucrose exhibited sharp absorption bands characteristic of crystalline sugars (*Figure 4.12*). The peak observed at

1650cm^{-1} in raffinose pentahydrate spectra (*Figure 4.12*) confirms the presence of water within its crystalline structure. A peak was not observed at 1650cm^{-1} for crystalline sucrose (*Figure 4.12*) suggesting the presence of water was not detected in ATR-FTIR studies.

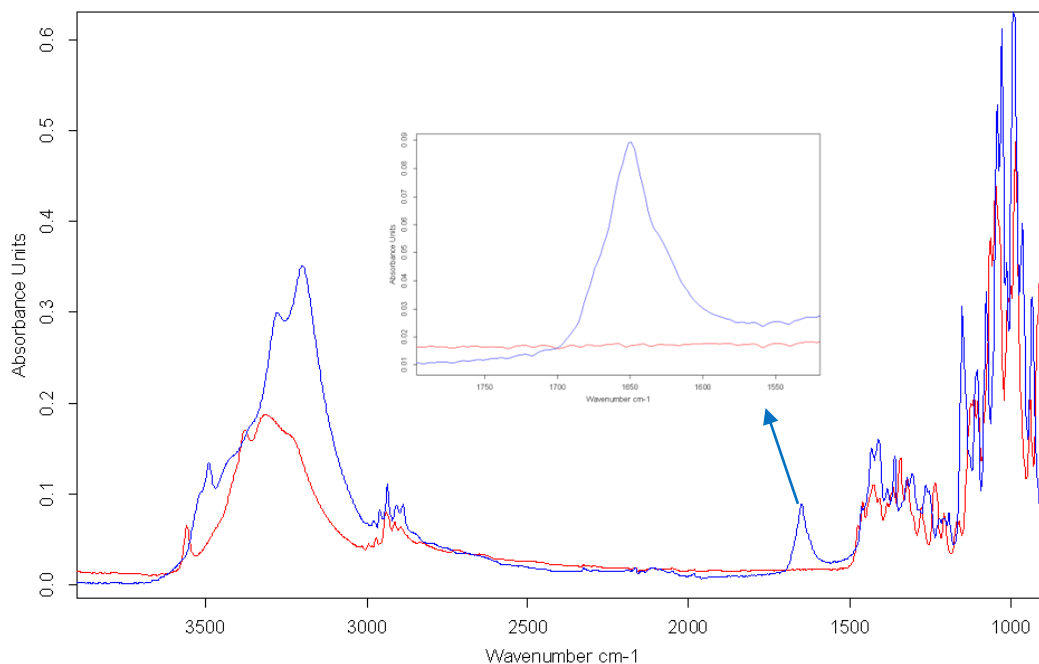


Figure 4.12 ATR-FTIR spectra of raffinose pentahydrate (*blue*) and crystalline sucrose (*red*)

4.3.3.2 Amorphous Samples

ATR-FTIR spectra of amorphous trehalose, raffinose and sucrose all exhibited broad features compared to their crystalline counterparts. Broad features are an indication of a wide range of hydrogen bond lengths and orientations within a sample. The peak observed at $\sim 1650\text{cm}^{-1}$ is an indicator of the presence of water within an amorphous sugar sample. Amorphous raffinose and trehalose samples (*Figure 4.13*) both had smaller peaks at $\sim 1650\text{cm}^{-1}$ compared to their crystalline counterparts implying as expected that these amorphous samples had lower water contents compared to their corresponding crystal

hydrate counterparts. ATR-FTIR spectra for amorphous sucrose saw an absorbance peak at $\sim 1650\text{cm}^{-1}$. These results suggested that amorphous sucrose had a greater amount of water in its structure compared to its crystalline counterpart.

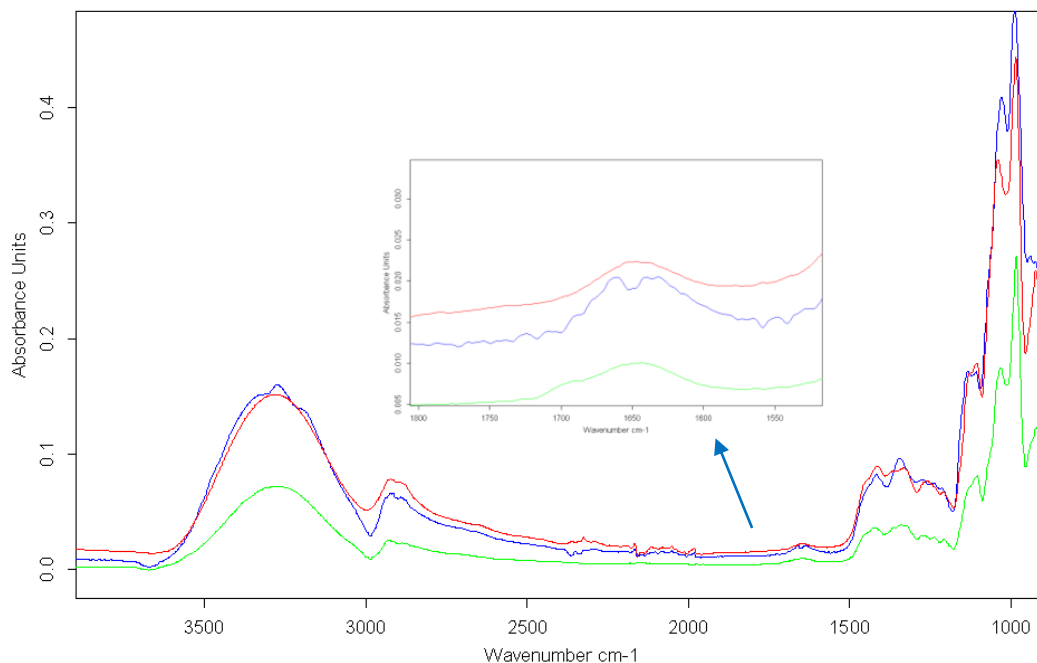


Figure 4.13 ATR- FTIR Spectra of amorphous raffinose (*blue*), amorphous sucrose (*red*) and amorphous trehalose (*green*)

Sharper and more intense peaks in a crystalline solid compared to an amorphous solid is due to a higher degree of homogeneity of intermolecular interactions, increased hydrogen bond density and strength (Wolkers et al., 2004) compared to its amorphous counterpart. ATR-FTIR experiments further confirmed evidence of no crystallisation material present in amorphous samples as all samples exhibit broad peaks. Hence, these results confirmed the generation of pure amorphous sugars by spray drying in this study.

4.3.4 THERMAL ANALYSIS OF AMORPHOUS AND CRYSTALLINE SAMPLES

In this section, thermal properties of both crystal and amorphous samples were explored using modulated temperature DSC (MTDSC) and thermogravimetric analysis (TGA). All amorphous samples were analysed using pin-holed pans. T_g values were obtained in two heating cycles to observed the true un-plasticized T_g (in the second heat).

4.3.4.1 Raffinose pentahydrate and amorphous raffinose

Figure 4.14 is typical MTDSC trace ($2^\circ\text{C}/\text{min} \pm 0.212^\circ\text{C}$ modulation over a 60 second period) and TGA weight profile ($2^\circ\text{C}/\text{min}$) for raffinose pentahydrate determined under a pin-holed pan system. A single endothermic peak was observed in the MTDSC total heat flow at (onset) 80.6°C . These results were contrary to that seen by Cheng and Lin (2006) but in agreement with reports elsewhere (Iglesias et al., 2000; Chamarthy et al., 2010). DSC experiments (performed under an open pan system) by Cheng and Lin (2006) saw three endothermic peaks at 56 , 73 and 85°C which were attributed to a step-wise sequence of weight loss of five water molecules of raffinose pentahydrate to its anhydrate form. The expected weight loss for raffinose pentahydrate is 15.27% , which is equal to five moles of water. The total weight loss observed in TGA experiment was 15.07% (*Figure 4.14b*), which equated to a loss of five moles of water. At 30°C to 67.3°C , the equivalent of one mole of water was lost, after this a further three moles of water was lost over the same temperature range as the melt endotherm observed in MTDSC studies. Finally, a further one mole of water was lost after the melt endotherm had occurred.

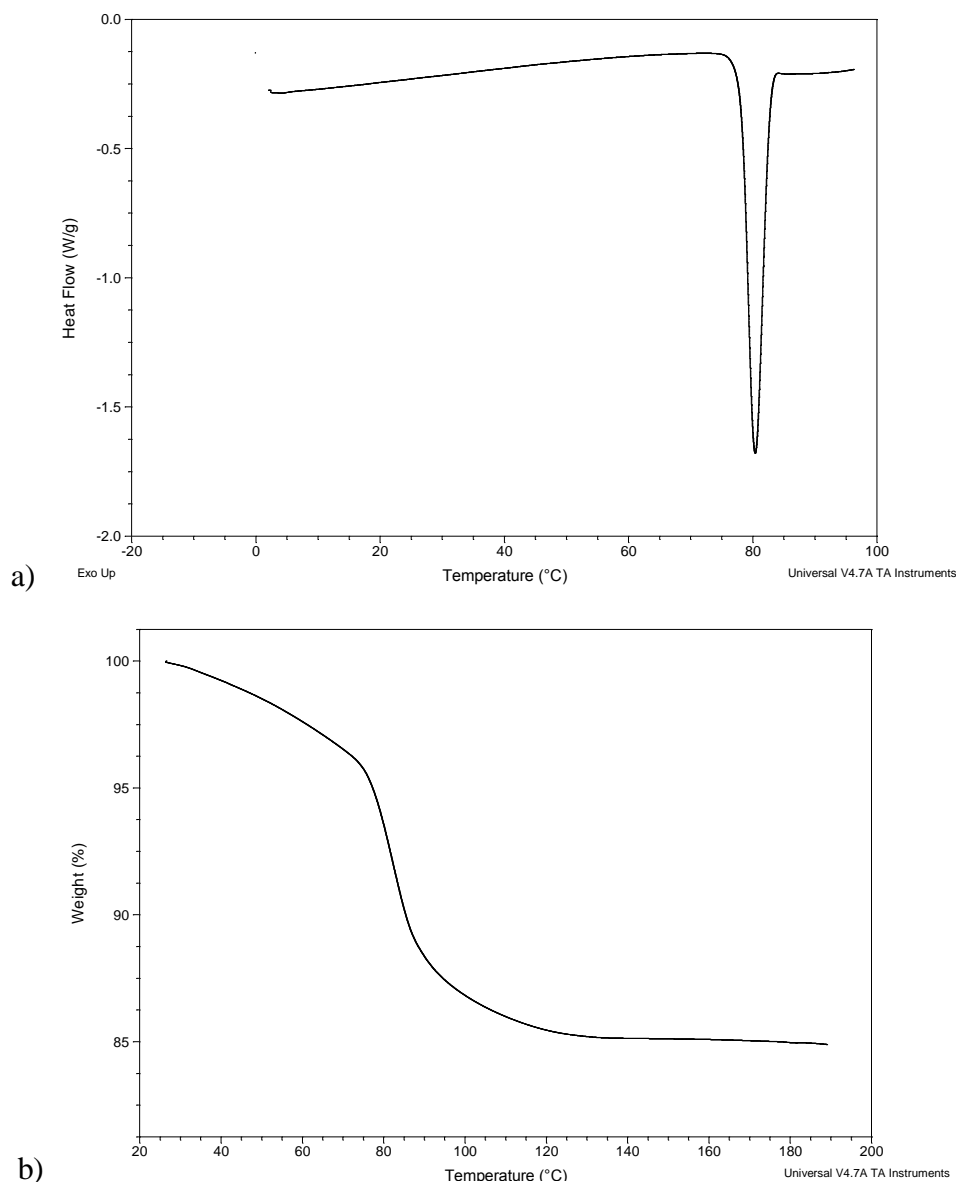


Figure 4.14 A typical MTDSC (in the total heat flow) for raffinose pentahydrate at $2^{\circ}\text{C}/\text{min} \pm 0.212^{\circ}\text{C}$ modulation over a 60 second period and b) A typical TGA weight loss profile for raffinose pentahydrate heated at $2^{\circ}\text{C}/\text{min}$ using a pin-holed pan

Three of raffinose pentahydrate's water molecules are located in a tunnel within the structure of raffinose where they act as both hydrogen donors and acceptors in a complex hydrogen bond network with raffinose (Bates et al., 2007; Salekigerhardt et al., 1995). The two other water molecules are situated outside of the tunnel and act only as hydrogen bond donors, one to raffinose and one to water and exhibit longer and weaker bonding than the

other three water molecules (Bates et al., 2007). Due to the molecular arrangement of the water molecules in a raffinose pentahydrate crystal, it could be assumed that the latter two water molecules would initially leave the structure upon dehydration at a lower temperature as they are loosely bound to the raffinose crystal structure (Kajiwara et al., 1999).

The results obtained from MTDSC, coupled with TGA data in this study, suggest initially at lower temperatures a mole of water is lost on heating. The temperature range in which three moles of water were released from raffinose pentahydrate overlapped with the endotherm observed in MTDSC. As three of the five water molecules are strongly bound to raffinose they will only be released from the crystal lattice when sufficient energy is obtained to disrupt its structure, releasing the three remaining water molecules.

A typical MTDSC trace for amorphous raffinose in the reversing heat flow signal is shown in *Figure 4.15*. A low T_g on the first heat (*Figure 4.15a*) was observed at 51.2°C (ΔC_p 0.49J/g·°C) (expected T_g : 100 to 116°C (Chamarthy et al., 2010; Miller and Lechuga-Ballesteros, 2006; Kajiwara et al., 1999)). The low T_g observed here was as a result of the plasticising effects of residual water. On the second heat a higher un-plasticized T_g (*Figure 4.15b*) was observed at 116.1°C (ΔC_p 0.37J/g·°C). TGA weight loss profile (*Figure 4.16*) determined sample water content at 2.3%.

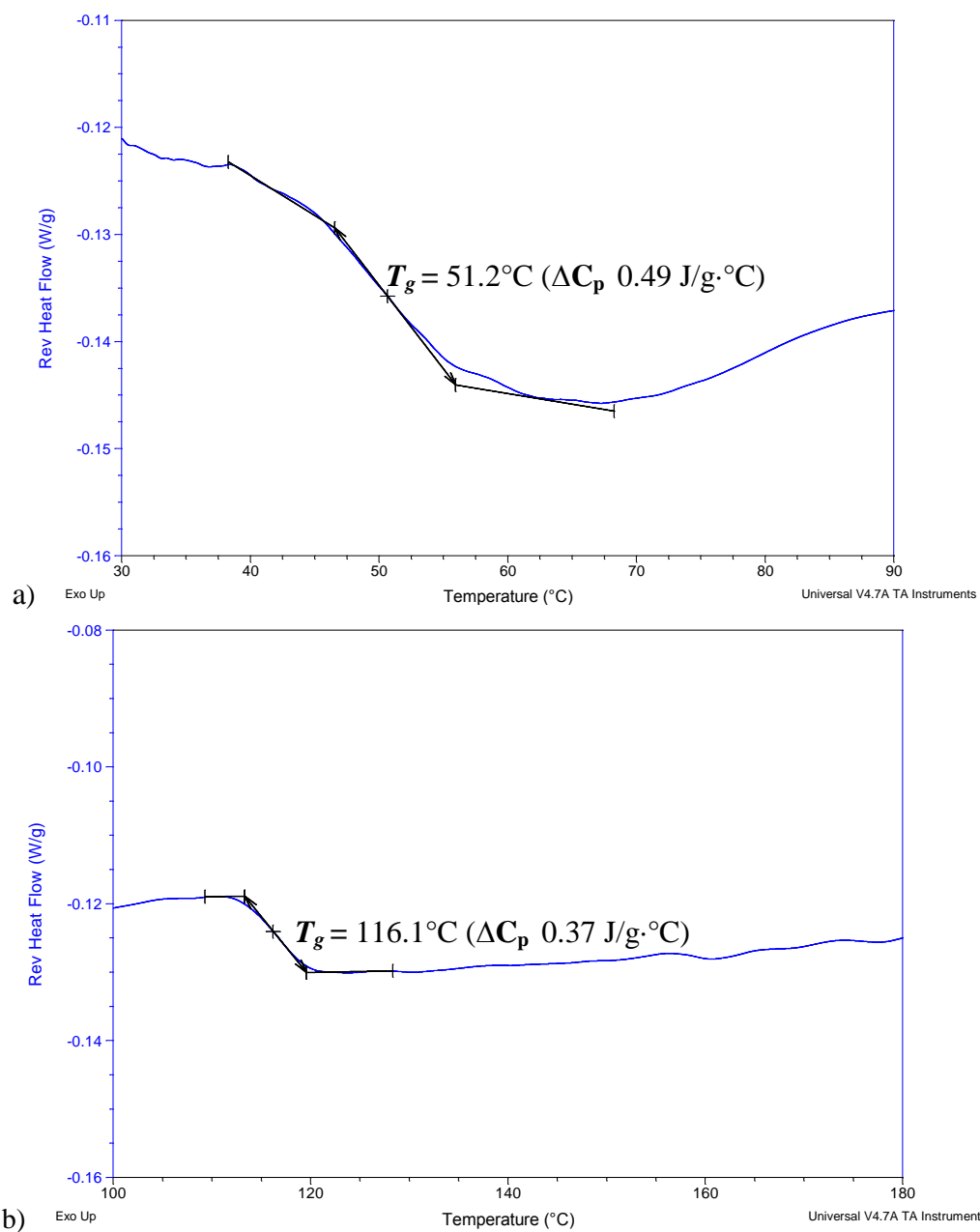


Figure 4.15 A typical MTDSC in the reversing heat flow signal for amorphous raffinose at $2^\circ\text{C}/\text{min} \pm 0.212^\circ\text{C}$ modulation over a 60 second period showing a) plasticized T_g at 51.2°C (first heat) b) un-plasticized T_g at 116.1°C using pin holed pans

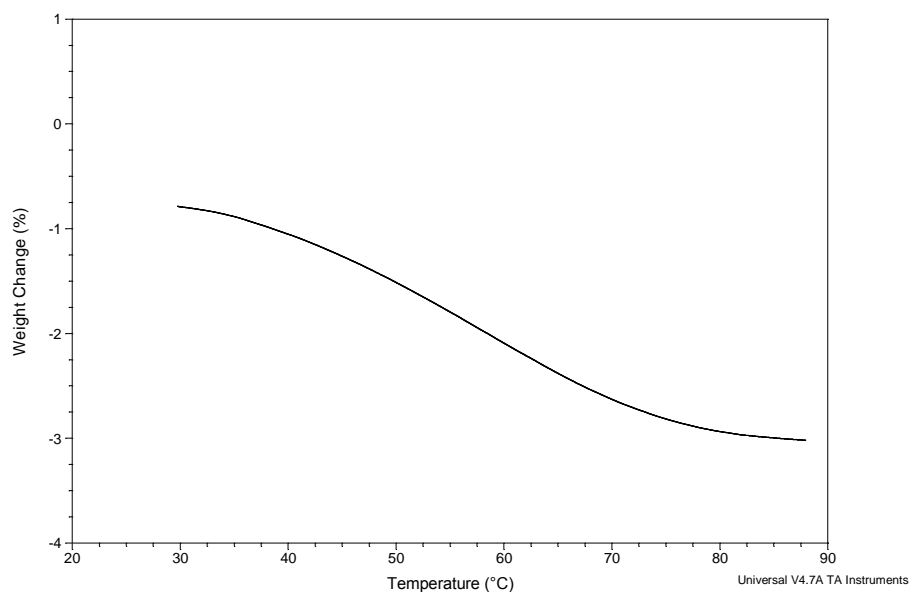


Figure 4.16 Typical TGA weight loss profile of amorphous raffinose heated at 2°C/min using a pin holed pan system

4.3.4.2 Amorphous trehalose

A typical MTDSC trace for amorphous trehalose in the reversing heat flow signal is shown in *Figure 4.17*. A low T_g on the first heat (*Figure 4.17a*) was observed at 51.8°C (ΔC_p 0.48J/g·°C) (expected $T_g = 117^\circ\text{C}$ (Jain and Roy, 2009)). The low T_g observed here was as a result of the plasticising effects of residual water. On the second heat a higher un-plasticized T_g (*Figure 4.17b*) was observed at 119.9°C (ΔC_p 0.42J/g·°C) TGA weigh loss profile (*Figure 4.18*) determined sample water content at 3.2%.

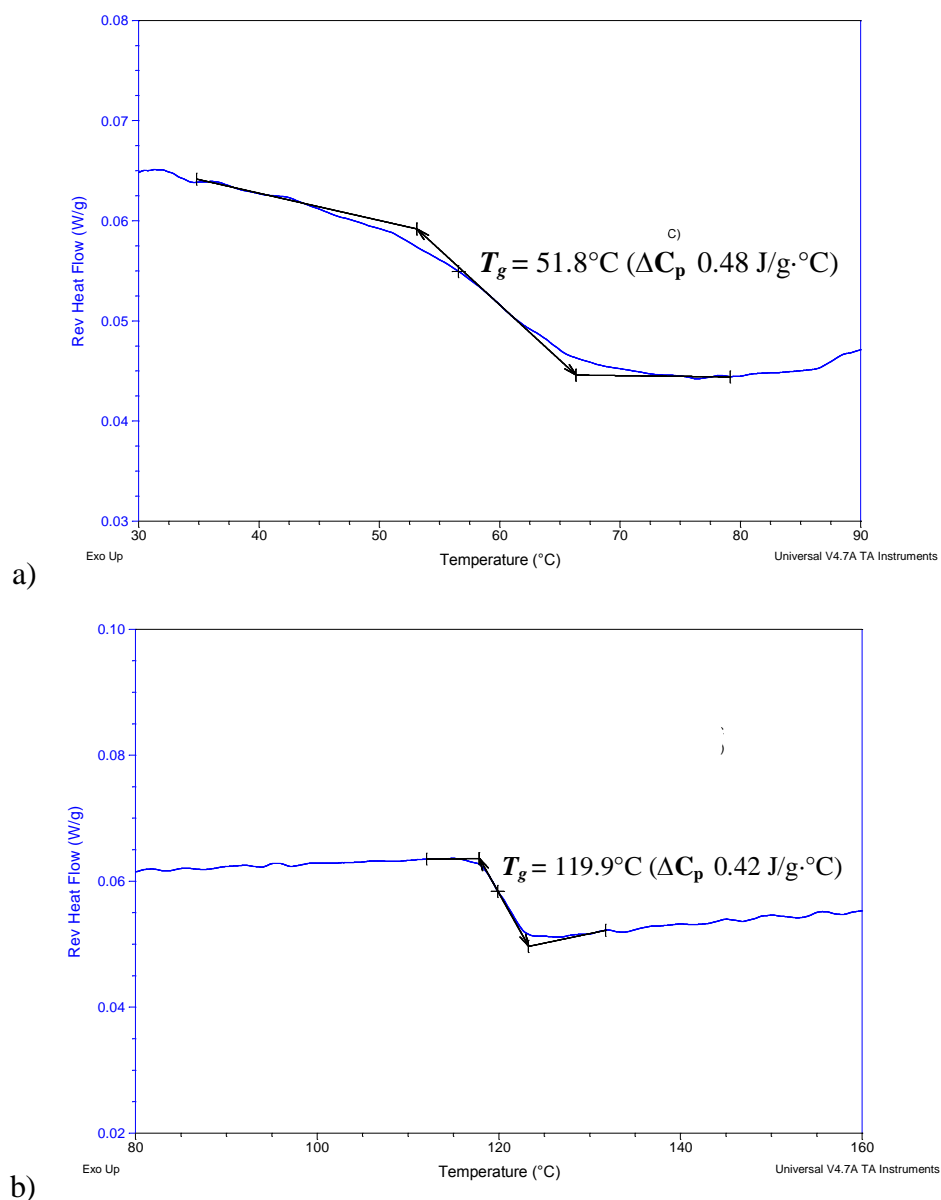


Figure 4.17 A typical MTDS C in the reversing heat flow signal for amorphous trehalose at $2^\circ\text{C}/\text{min} \pm 0.212^\circ\text{C}$ modulation over a 60 second period showing a) plasticized T_g at 51.8°C (first heat) b) un-plasticized T_g at 119.9°C using pin holed pans

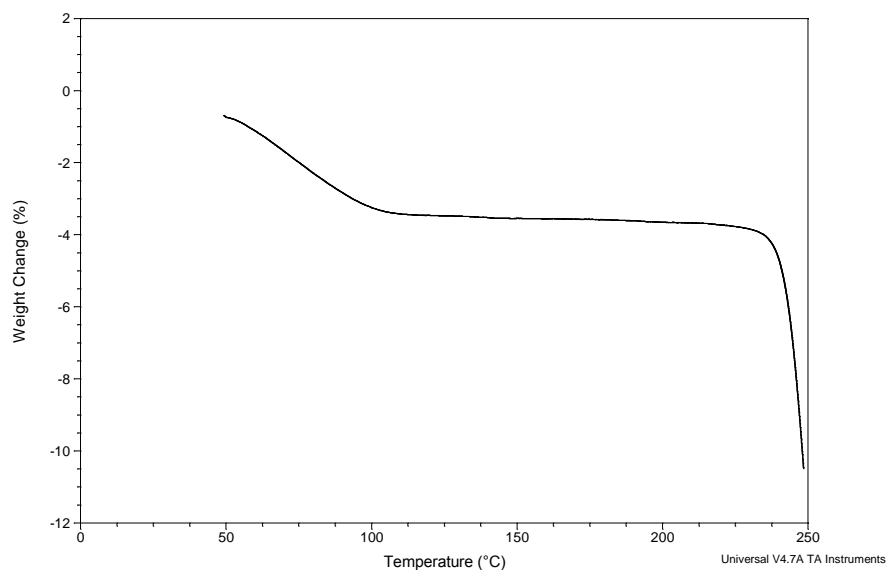


Figure 4.18 Typical TGA weight loss profile of amorphous trehalose heated at 2°C/min using a pin holed pan system

4.3.4.3 Crystalline sucrose and amorphous sucrose

A single melt endotherm was observed in the total heat flow at 181.55°C in MTDSC experiments performed on crystalline sucrose (*Figure 4.19*), which was in agreement with previous report (Roos, 1993). A small endotherm occurring just before the main melting endotherm of sucrose has been identified in previous studies conducted by Beckett et al., (2006) and Bhandari and Hartel, (2002). The presence of the endotherm has been linked to the purity of crystalline sucrose used in particular in terms of its mineral salt content, and not associated with by the presence of amorphous material within the crystalline lattice as suggested (Bhandari and Hartel, 2002). The water content observed for this crystalline sample was 0.0358%. Previous studies (Naini et al., 1998), did not detect weight loss in TGA profile which suggested crystalline sucrose did not possess water within its structure.

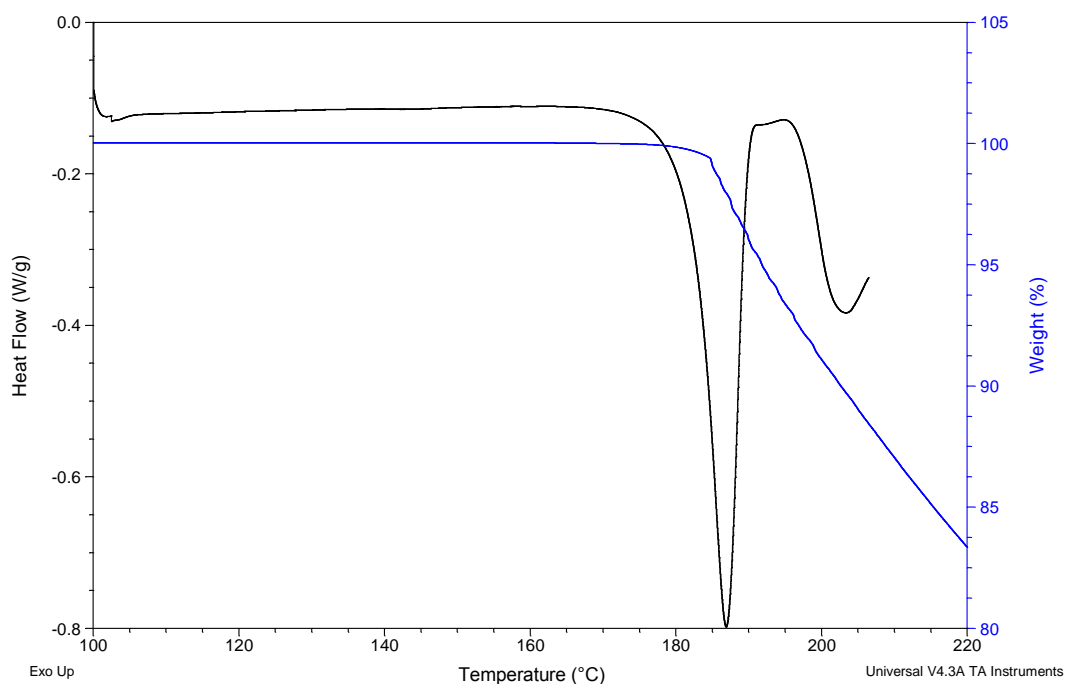


Figure 4.19 A typical MTDSC (in the total heat flow) for crystalline sucrose at $2^{\circ}\text{C}/\text{min} \pm 0.212^{\circ}\text{C}$ modulation over a 60 second period (**black** line) and a typical TGA weight loss profile for raffinose pentahydrate heated at $2^{\circ}\text{C}/\text{min}$ (**blue** line) using a pin-holed

A typical MTDSC trace for amorphous sucrose in the reversing heat flow signal is shown in *Figure 4.20*. A low T_g on the first heat (*Figure 4.20a*) was observed at 36.5°C (ΔC_p $0.70\text{J}/\text{g}\cdot^{\circ}\text{C}$). The low T_g observed here was as a result of the plasticising effects of residual water. On the second heat a higher un-plasticized T_g (*Figure 4.20b*) was observed at 63.1°C (ΔC_p $0.35\text{J}/\text{g}\cdot^{\circ}\text{C}$). TGA weigh loss profile (*Figure 4.21*) determined sample water content at 1.8%.

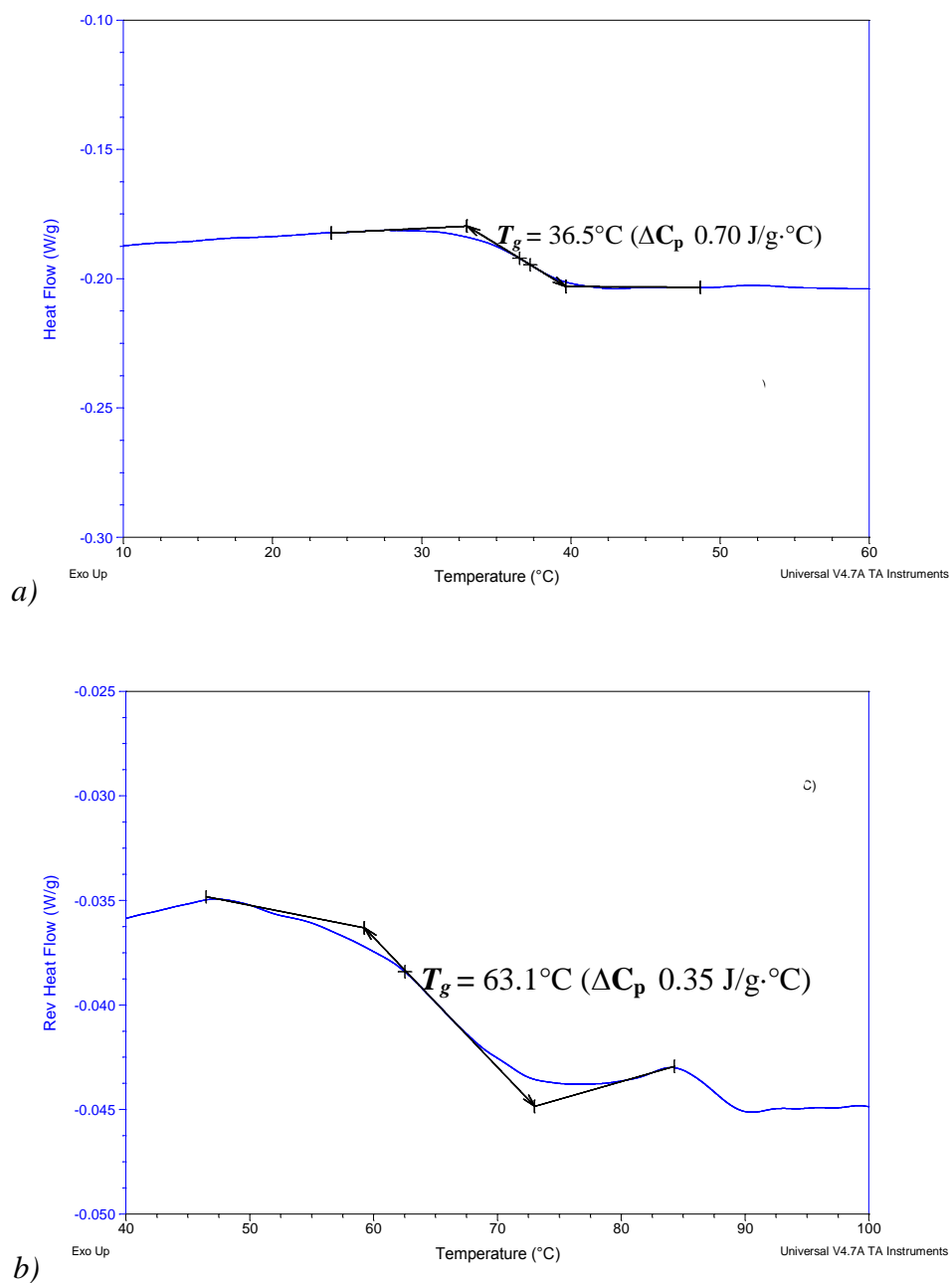


Figure 4.20 A typical MTDSC in the reversing heat flow signal for amorphous sucrose at $2^{\circ}\text{C}/\text{min} \pm 0.212^{\circ}\text{C}$ modulation over a 60 second period showing a) plasticized T_g at 36.5°C (first heat) b) un-plasticized T_g at 63.1°C using pin holed pans

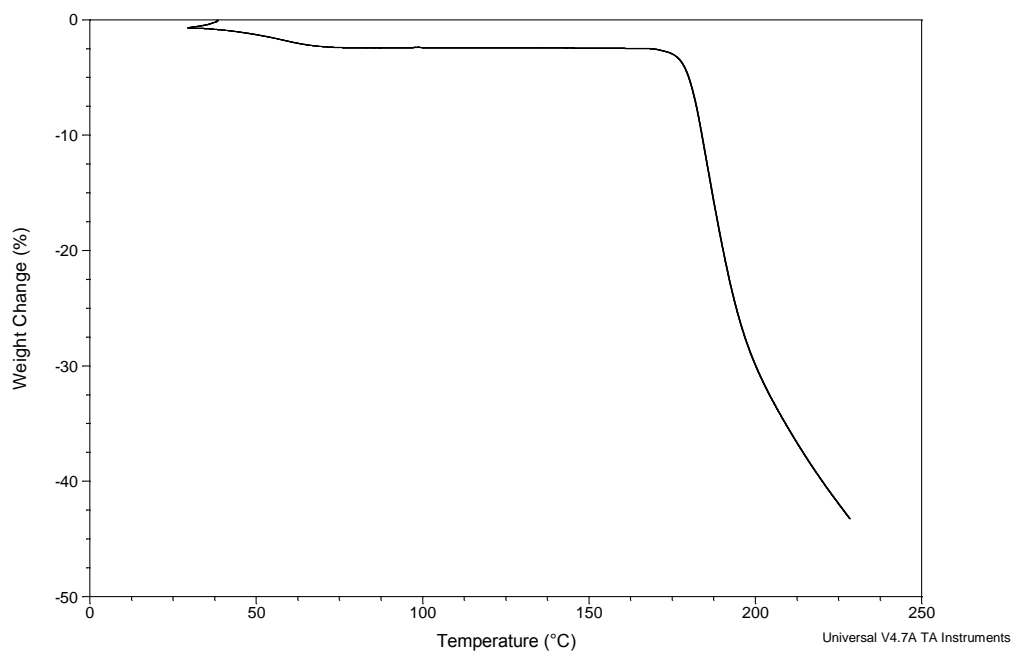


Figure 4.21 Typical TGA weight loss profile of amorphous sucrose heated at 2°C/min using a pin holed pan system

The variation in reported T_g values for amorphous sucrose (ranging from 28°C to 78°C) in the literature (summarized in *Table 4.1*) appears dependent on several factors such as sample processing, residual moisture content (Roos, 1993), and physical aging and measurement method (Yu et al., 2008). Plasticized and un-plasticized T_g values obtained in this study were comparable to literature values (though with slightly higher water contents) of amorphous sucrose samples generated by freeze drying (Ottenhof et al., 2003) and rapid drying of sugar solution (Wolkers et al., 1998) respectively.

Table 4.1 Reported literature T_g values of amorphous sucrose

T_g (°C)	ADDITIONAL INFORMATION	REFERENCE
21.8	22%RH, 4.7% water content, DSC 3°C/min Freeze dry	(<i>Ottenhof et al., 2003</i>)
33.2	11%RH, 3.3% water content, DSC 3°C/min , Freeze dry	(<i>Ottenhof et al., 2003</i>)
58.6	0%RH, 0.5% water content, DSC 3°C/min , Freeze dry	(<i>Ottenhof et al., 2003</i>)
60	Quenched melt, DSC	(<i>Mathlouthi et al., 1986</i>)
62	Rapid drying of sugar solution, VT-FTIR 1°C/min	(<i>Wolkers et al., 1998</i>)
67	DSC 5°C/min, made amorphous from melt	(<i>Roos, 1993</i>)
72.9	HyperDSC100°C/min, Spray Dry	(<i>Lappalainen et al., 2006</i>)
78	DSC 20°C/min, Freeze dry	(<i>Shamblin and Zografi, 1999</i>)

4.3.5 DYNAMIC VAPOUR SORPTION ANALYSIS OF AMORPHOUS SAMPLES

Amorphous sugars are generally hygroscopic and have a strong tendency to take up water vapour. In the presence of water, acting as a plasticiser, the T_g is lowered. This indicates that the difference between the temperature of the sample and the proximity to the glass transition will also decrease and therefore crystallisation will become progressively easier during the experiment (Hunter et al., 2010). Crystallisation is usually the limiting factor determining the amount of water vapour taken up by low molecular weight amorphous sugars (Hancock and Shamblin, 1998). Amorphous sugars in their crystalline form exists as hydrates (i.e. raffinose and trehalose). To undergo recrystallisation these amorphous sugars must acquire the minimum number of water molecules required to convert to its stable hydrate. For example, amorphous raffinose must acquire a minimum of 5 water molecules per raffinose molecule to form a stable pentahydrate. Whilst amorphous

trehalose must acquire a minimum of 2 water molecules per trehalose molecule to form a stable hydrate (Hancock and Shamblin, 1998).

4.3.5.1 Amorphous Trehalose

Figure 4.22 is a typical sorption isotherm curve for amorphous trehalose exposed to 10 to 90%RH at sequential increments of 5%RH at 25°C. The curve shows that the sample lost water at 10%RH (quantity was dependent on the original water content of the sample). From 20 to 30%RH, the sample absorbed a relatively small amount of water. Water absorption at lower humidities is likely to be absorbed onto the surface of the amorphous particles. The amount of water absorbed at 40 to 50%RH increased dramatically suggesting that at 40%RH and 50%RH water was being absorbed into the amorphous particles and not just on the surface. At 60%RH, initially the sample showed some absorption signified by an increase in weight this was quickly followed by a sharp loss of water (seen as a decrease in weight). The weight loss observed here was due to recrystallisation of the amorphous trehalose to trehalose dihydrate. The total weight change determined from 10%RH to the end of recrystallisation was 8.33%. The starting water content was 3.20%, therefore total water content by the end of the experiment was 11.53%. Gradual water loss (indicated as a decrease in the DVS profile) continued at 80%RH and 90%RH was attributed to ongoing crystallisation of small amounts of amorphous trehalose in the core as observed elsewhere (Hunter, 2009a).

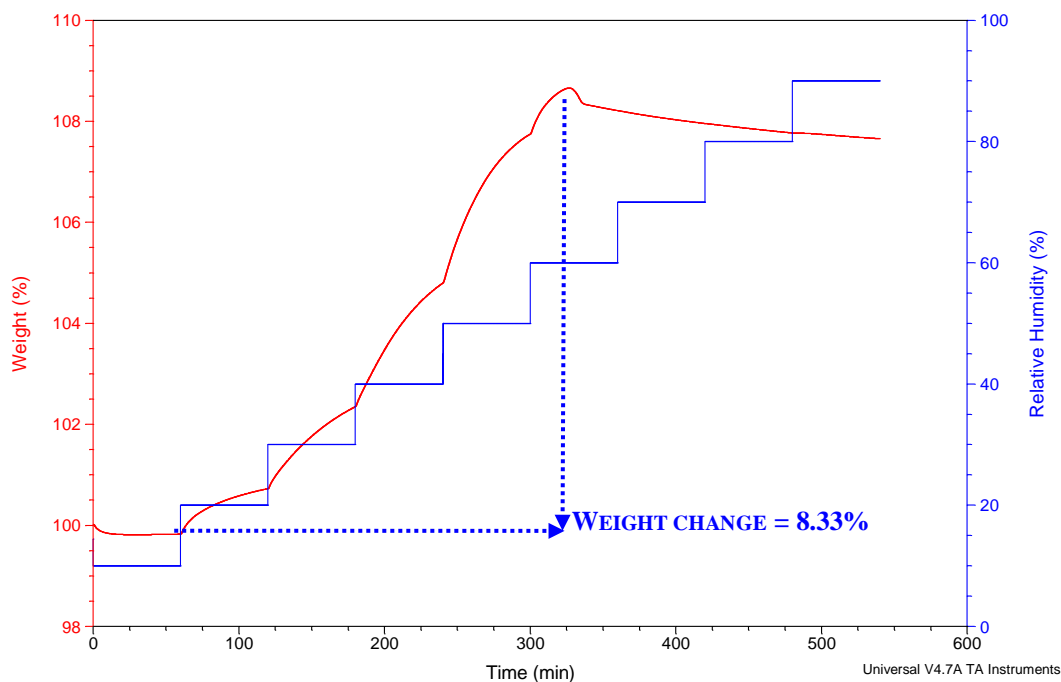


Figure 4.22 Sorption isotherm curve for amorphous trehalose exposed to 10 to 90%RH at sequential increments of 5%RH steps at 25°C

4.3.5.2 Amorphous Raffinose

Figure 4.23 is a typical sorption isotherm curve for amorphous raffinose exposed to 10 to 90%RH at sequential increments of 5%RH at 25°C. The curve shows that the sample lost a small amount of water at 10%RH signified by a decrease in weight in the DVS profile (quantity was dependent on the original water content of the sample). At 20%RH a relatively small amount of water was absorbed likely to be absorbed onto the surface of the amorphous particles. A steady increase in weight at 30 to 70%RH suggested that at these relative humidities water was being absorbed into the amorphous particles and not just on the surface. At 80%RH similar to amorphous trehalose behaviour at 60%RH, initially the sample showed some absorption signified by an increase in weight this was quickly followed by a sharp loss of water (seen as a decrease in weight). The weight loss observed here was due to recrystallisation of the amorphous raffinose to a hydrate form. The total

weight change from 10%RH to the end of recrystallisation was 11.68%. The starting water content was 2.28%, therefore total water content by the end of the experiment was 13.96%. Further weight loss was not observed at 90%RH.

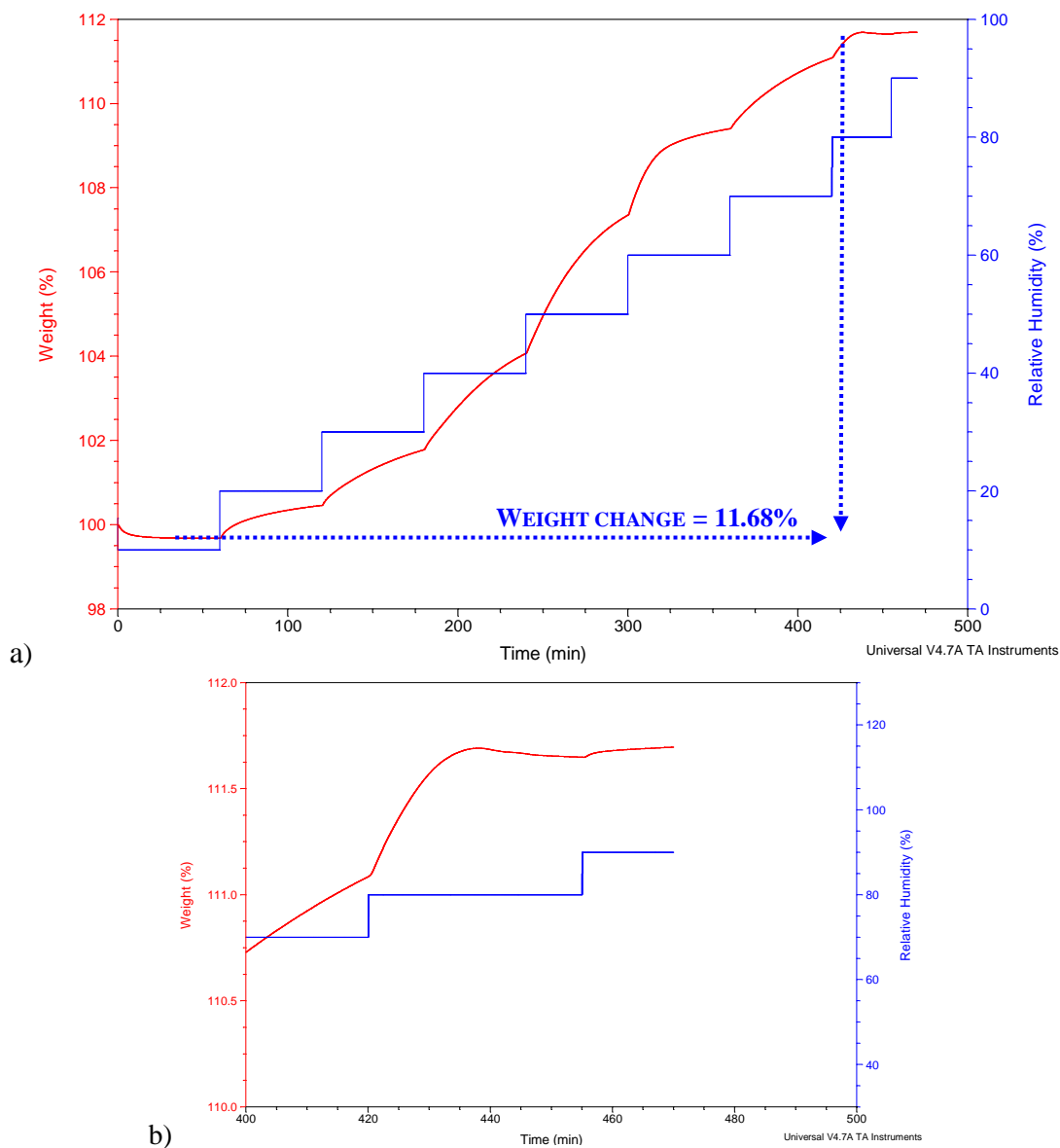


Figure 4.23 Sorption isotherm curve for amorphous raffinose exposed to 10 to 90%RH at sequential increments of 5%RH steps at 25°C b) close up crystallisation transition

4.3.5.3 Amorphous Sucrose

It was expected that amorphous sucrose would re-crystallise at a lower humidity compared to amorphous trehalose and amorphous raffinose as previous reports show humidity induced crystallization occurs at between 40%RH to 80%RH in partially amorphous sucrose (Yu et al., 2008). DVS experiments conducted on amorphous sucrose samples did not have the same DVS profile as amorphous trehalose and raffinose samples. *Figure 4.24* is a typical sorption isotherm curve for amorphous sucrose exposed to 10 to 90%RH at sequential increments of 5%RH at 25°C. The curve showed that the sample lost a small amount of water (signified as a decrease in weight) at 10% RH, (a similar behaviour was observed for both amorphous trehalose and amorphous raffinose). This was followed by a large increase in weight at 40%RH and 90%RH, a decrease in weight was not observed.

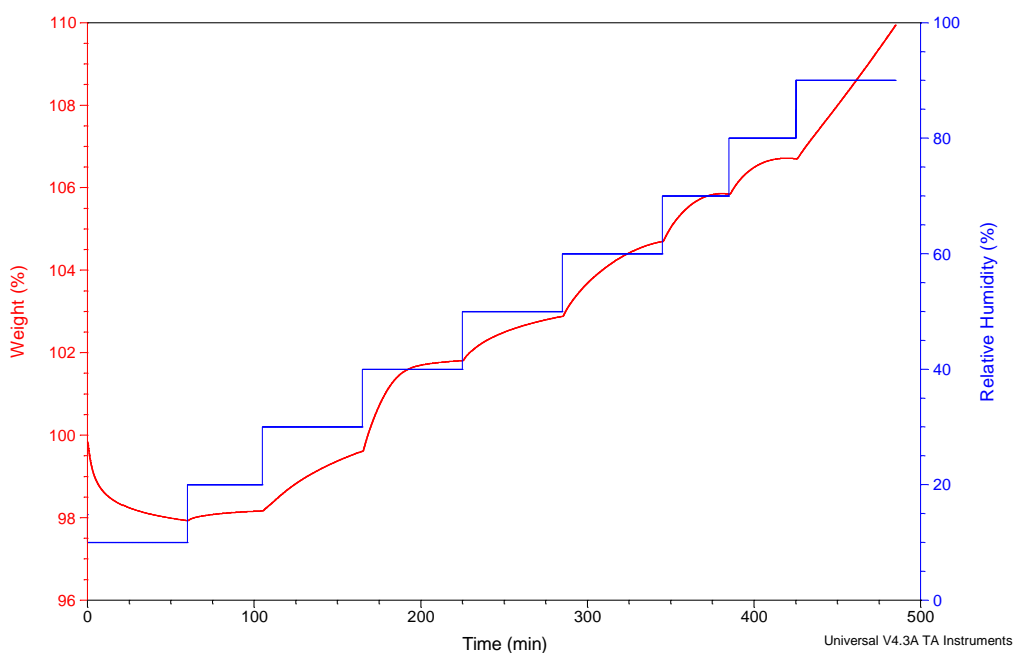


Figure 4.24 Sorption isotherm curve for amorphous sucrose exposed to 10 to 90%RH at sequential increments of 5%RH steps at 25°C

These results were not as expected. The effect of crystal formation on the water balance in amorphous system is dependent on the type of crystal to be formed (Iglesias et al., 1997). Generally, amorphous sucrose is not expected to absorb large amounts of water below its deliquescence point (75%RH) a decrease in water content below this relative humidity would indicate sucrose crystallisation (Salekigerhardt and Zograf, 1994). Though the DVS profile did not show clear evidence of recrystallisation, the sample appeared solid after DVS experiments confirming crystallisation of amorphous sucrose had occurred but was not detected.

Amorphous materials can sorb large quantities of water vapour because water moles may additionally be absorbed into the bulk of the amorphous material instead of being restricted to the particle surface. The amount of water absorbed is not directly related to the specific surface area of the solid. A decrease in the weight profile occurs as the crystalline form has a lower affinity for water than its corresponding amorphous form (Surana et al., 2004). The onset of crystallisation is the highest weight value prior to the dramatic decrease in weight observed. Factors controlling water vapour absorption for amorphous materials include the material's physico-chemical properties, such as hydrophilicity, molecular weight, experimental temperature, relative humidity and the strength and nature of any interactions between the water and amorphous molecules (Hancock and Zograf, 1996). The results detailed in this study show that each amorphous sugars would sorb different amounts of water vapour under identical experimental conditions because of their individual physico-chemical properties.

4.5 CONCLUSION

The objective of the work detailed in this chapter was to generate pure amorphous sugars (via spray drying) and characterise their physico-chemical properties using a range of diffraction, spectroscopic and thermal techniques. A summary of the results obtained in the section

Table 4.2 Summary of physico-chemical properties of crystalline samples (n=3)

	RAFFINOSE PENTAHYDRATE	CRYSTALLINE SUCROSE
PARTICLE SIZE	Bi-modal distribution 5 μ m - 490 μ m	400 μ m and 800 μ m
SEM	Large crystals and smaller crystals that appeared needle-shaped in character.	Large rectangular shaped crystals and a crystal agglomerate made up of fused smaller crystals
XRPD	Expected peaks for raffinose pentahydrate at ca. 2θ 10.3°, 13.2° and 20.7°	Expected peaks at 2θ 11.6°, 13.1°, 18.8°, 19.6° and 24.6°
ATR-FTIR	Characteristic of crystalline sugars peak observed at 1650 cm^{-1} confirming presence of water within crystalline structure	Characteristic of crystalline sugars no peak observed at 1650 cm^{-1}
DSC	Single endothermic peak was observed in the MTDSC total heat flow at (onset) 80.6°C	A single melt endotherm was observed in the total heat flow at 181.55°C in MTDSC experiments performed on crystalline sucrose
WATER CONTENT	15.07%	0.0358%.

Table 4.3 Summary of physico-chemical properties of amorphous samples ($n=3$)

	AMORPHOUS RAFFINOSE		AMORPHOUS TREHALOSE		AMORPHOUS SUCROSE	
PARTICLE SIZE	5 μ m - 45 μ m		5 μ m - 45 μ m		5 μ m -55 μ m	
SEM	Spherical particles				High degree of particle fusion	
XRPD	Amorphous halo					
ATR-FTIR	Exhibited board features compared to their crystalline counterparts					
DSC	PLASTICIZED T_g	UN- PLASTICIZED T_g	PLASTICIZED T_g	UN- PLASTICIZED T_g	PLASTICIZED T_g	UN- PLASTICIZED T_g
	51.2°C (ΔC_p 0.49J/g.°C)	116.1°C (ΔC_p 0.37J/g.°C)	51.8°C (ΔC_p 0.48J/g.°C)	119.9°C (ΔC_p 0.42J/g.°C)	36.5°C (ΔC_p 0.70J/g.°C)	63.1°C (ΔC_p 0.35J/g.°C)
WATER CONTENT	2.3%.		3.2%.		1.8%.	
DVS	Crystallisation observed		Crystallisation observed		No crystallisation observed	

In conclusion, amorphous sucrose, trehalose and raffinose were successfully generated by spray drying as confirmed by XRPD and ATR-FTIR results. Though same spray drying parameters were used for all samples, sample water contents ranged from 1.84% to 3.20%. Presence of water had a profound effect on T_g in all samples. Un-plasticized T_g values were all within expected ranges. With amorphous trehalose and raffinose displaying similar plasticized and un-plasticized T_g values. Both amorphous trehalose and raffinose had higher T_g values than sucrose. In DVS studies water induced crystallization was observed in amorphous trehalose and raffinose samples. However, crystallization was not

observed in amorphous sucrose samples though after DVS experiments sample appeared solid.

CHAPTER FIVE

**USE OF SUGAR ADDITIVES (TREHALOSE AND
RAFFINOSE) TO IMPROVE THE STABILITY OF
AMORPHOUS SUCROSE**

5.1 BACKGROUND

In the previous chapter (*Chapter 4*), the physico-chemical properties of the amorphous samples generated was determined. Both amorphous trehalose and raffinose displayed higher T_g values (as expected) compared to amorphous sucrose. These findings prompted this study whereby sucrose was co-spray dried with sugar additives, trehalose and raffinose and the effects of increasing sugar additive on amorphous sucrose stability was observed. The main objective of this study was to investigate the use of the fragility parameter m and the strength parameter D as predictors of amorphous stability of generated co-spray dried samples.

DSC experiments were conducted to calculate the activation energy for structural relaxation around T_g (ΔE_{T_g}) for all samples using the heating/cooling rate dependence of T_g (Moynihan et al., 1974). ΔE_{T_g} values obtained were then used to calculate the fragility parameter (m) (*Equation 5.1*) and strength parameter (D) (*Equation 5.2*). These parameters can be used to predict amorphous stability, as they reflect molecular mobility and interactions, although firm evidence for their predictive power is not yet available (Beckett et al., 2006; Graeser et al., 2009). Quasi-Isothermal MTDSC (Qi-MTDSC) techniques were employed to observe if co-spray dried samples existed as one or two amorphous phases evident by the presence of either one or two glass transition events.

The amorphous state can be deliberately generated to obtain higher drug bioavailability and, for excipients, is essential for stabilization of proteins and small molecules in freeze-dried and spray dried products. The advantageous properties of the amorphous state are as

a result of the thermodynamic properties of the amorphous state reflected in excess entropy, enthalpy and free energy (Graeser et al., 2009). These factors along with enhanced molecular mobility in the amorphous state unfortunately also result in physical instability (i.e. recrystallisation). Hence prevention of recrystallization from the amorphous state is of considerable interest.

Crystallisation of an amorphous sample is dependent on two stages, nucleation and crystal growth (Van Scoik and Carstensen, 1990). Cold crystallisation occurs when the amorphous sample or glass is heated beyond its T_g . When crystallisation is the instability of concern, one is more concerned with the temperature of onset of crystallisation (T_c) than the rate of crystal growth. T_c can be determined using isothermal and/or non-isothermal DSC techniques.

Amorphous physical stability may be tentatively predicted using a range of fundamental parameters especially those with an emphasis on molecular mobility; these include the "fragility" of a liquid. The fragility of a liquid is a measure of the temperature dependence of the viscosity approaching T_g . This is discussed in more detail in *Chapter 1*. The fragility parameter (m), can be described using the following equation

$$m = \frac{\Delta E_{T_g}}{(\ln(10))RT_g} \quad \text{Eq. 5.1}$$

where ΔE_{T_g} (can be calculated by using the scanning rate dependency of T_g) is the activation enthalpy for structural relaxation around the T_g and R is the gas constant (8.314 JK⁻¹mol⁻¹). A large m value indicates rapidly changing dynamics at T_g which equates to

fragile behaviour (Crowley and Zografi, 2001). Generally strong liquids have m values less than 40 whilst fragile liquids have m values greater than 75. Strong liquids have high viscosity at T_m and are resistant to structural changes, whilst fragile liquids exhibit lower viscosities at T_m and are less resistant to structural changes therefore are less stable (Baird et al., 2010). Heat capacity changes at T_g for strong liquids are small because of minimal molecular mobility; however, they are larger for fragile liquids due to greater molecular mobility changes (Angell, 1995). With reference to the melting temperature (T_m), strong liquids have higher viscosities at T_m and are resistant to structural changes. Fragile liquids exhibit lower viscosities at T_m and are therefore less resistant to structural changes (Crowley and Zografi, 2001).

D is a variable referred to as the strength parameter and can be described using the following equation

$$D = \frac{(\ln(10))m_{min}^2}{m - m_{min}} \quad \text{Eq. 5.2}$$

where m_{min} is a minimum value for m (τ at T_g is approximately 100s (measured using DSC at 10K/min) (Moynihan et al., 1974) whilst τ_0 represents a timescale of vibrational motions of approximately 10^{-14} s (Crowley and Zografi, 2001). Using these approximations m_{min} has been defined as 16 in previous studies (Crowley and Zografi, 2001). Strong liquids have large D values (greater than 30) whilst fragile liquids have relatively low D values (less than 10).

5.1.1 STUDY OBJECTIVES

Previous studies have been performed with the aim of improving the stability of an amorphous sucrose system by adding a small percentage of another sugar (Leinen and Labuza, 2006; Salekigerhardt and Zografi, 1994; Roe and Labuza, 2005) or amino acids (Lu, 2011). Whilst previous studies have evaluated the use of additives to improved temperature-induced crystallisation of amorphous sucrose, they have not investigated the effect these additive have on amorphous stability. The objective of this study was to investigate the use of the fragility parameter m and the strength parameter D as predictors of amorphous stability of generated co-spray dried samples.

5.1.2 GENERAL METHODOLOGY

Previous studies on amorphous sucrose stabilisation used high percentages of additives (up to 80%w/w) (Davidson and Sun, 2001; Salekigerhardt and Zografi, 1994). In this study sucrose was co-spray dried with trehalose and raffinose at an addition of 2.5, 4, 5.26 and 11.11%w/w of total sucrose amount (dry mass)) using the following parameters : inlet temperature of 125°C, an average pump flow rate of 3.7mL/min, 100% aspirator setting and an outlet temperature ranging from 60-80°C (not controlled). For ease of reference, samples will be referred to in terms of additive dry weight where T represents trehalose, S sucrose and R raffinose. 2.5, 4, 5.26 and 11 correspond to addition of 2.5, 4, 5.26 and 11.11%w/w trehalose and raffinose (of total sucrose amount) i.e. ST2.5, ST4, ST5.26, ST11.11 and SR2.5, SR4, SR5.26 and SR11.11.

X-ray powder diffraction (XRPD) studies were performed to confirm sample amorphicity. ATR-FTIR studies were used to compare hydrogen bond arrangement of co-spray dried samples to ensure there was no interaction between sucrose and the additive. DSC was used to calculate the activation enthalpy for structural relaxation around the T_g (ΔE_{T_g}) using the heating rate dependency of T_g . DSC experiments were conducted using pin-holed pans and T_g values were obtained at 2, 5, 10, and 20°C/min. It was essential for the cooling rate used to be equal to the subsequent heating rate, if not ΔE_{T_g} values obtained would not be accurate. Thermogravimetric analysis (TGA) was used to obtain sample water content. Full details of these techniques are outlined in *Chapter 2* unless otherwise stated in the results and discussion section.

5.2 RESULTS AND DISCUSSION

5.2.1 X-RAY DIFFRACTION ANALYSIS OF AMORPHOUS SAMPLES

Typical XRPD diffractograms are illustrated in *Figure 5.1* (amorphous sucrose), *Figure 5.2* (co-spray dried sucrose and trehalose samples) and *Figure 5.3* (co-spray dried sucrose and raffinose). It is well known that molecules in the amorphous phase are located randomly; they do however, exhibit short range molecular, translational and conformation order. The XRPD diffractograms of all the traces appeared different, though they all possessed the characteristic “amorphous halo” pattern showing no sign of peaks and therefore indicating the absence of crystallinity (within the detection limits of the technique and equipment). The differences in halo shapes can be attributed to the identification of locations of short-range molecular order within the samples. An example of this is with ST2.5 samples (*Figure 5.2*) and SR4 (*Figure 5.3*) where clear differences in

the halo pattern were observed. Should crystallisation have occurred as a result of processing, peaks representing either isolated sucrose, raffinose or trehalose crystals would have been present in diffractograms. These results show that fully amorphous samples containing a mixture of sucrose, raffinose and trehalose mixes were generated by spray drying.

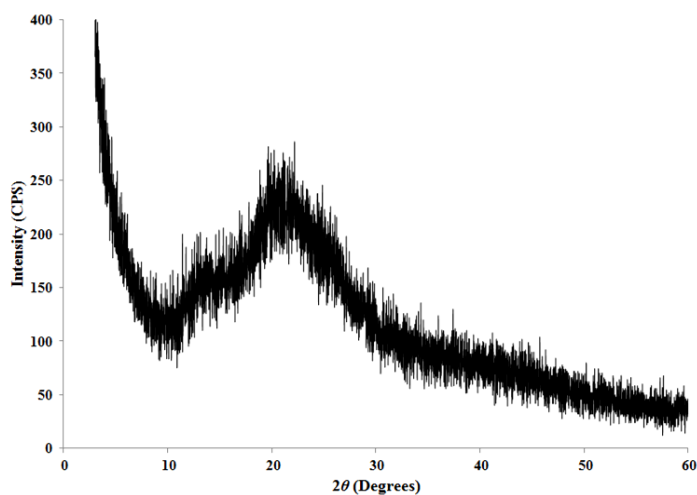


Figure 5.1 XRPD diffractogram of amorphous sucrose

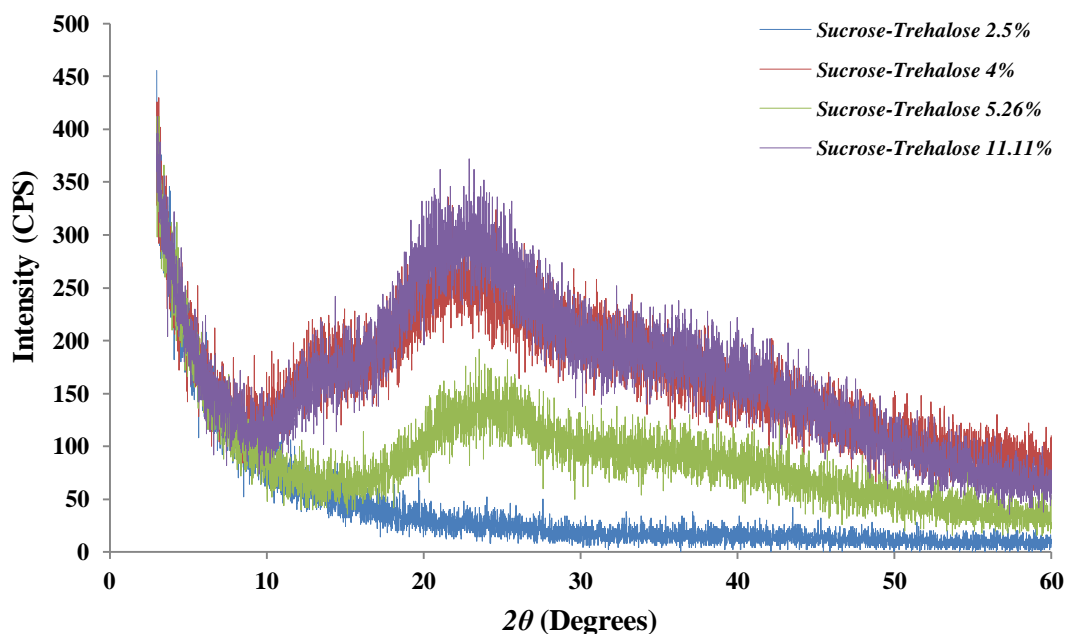


Figure 5.2 XRPD diffractogram of amorphous sucrose-trehalose samples

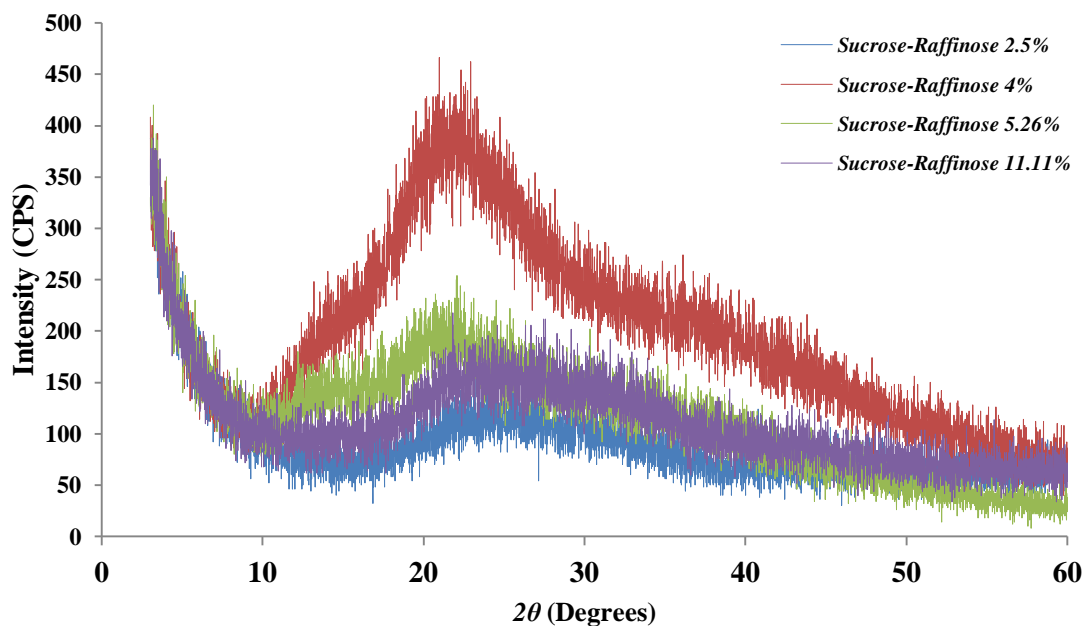


Figure 5.3 XRPD diffractogram of amorphous sucrose-raffinose samples

5.2.2 SPECTROSCOPIC ANALYSIS OF CRYSTALLINE AND AMORPHOUS SAMPLES

ATR-FTIR spectra of all co-spray samples exhibited broad features with no visible sharp peaks, leading to the conclusion that samples were entirely amorphous. Examples of the spectra are shown in *Figure 5.4* and *5.5* with amorphous sucrose spectra shown for reference. Peaks in all spectra were broad and all the sugars shared similar absorptions, i.e. between 3600 and 3000cm^{-1} which is termed the OH stretching band arising from sugar -OH groups. Due to the overlapping of absorption bands, analysis proved difficult. Differences were observed however at $\sim 1650\text{cm}^{-1}$ potentially relating to varied sample water contents.

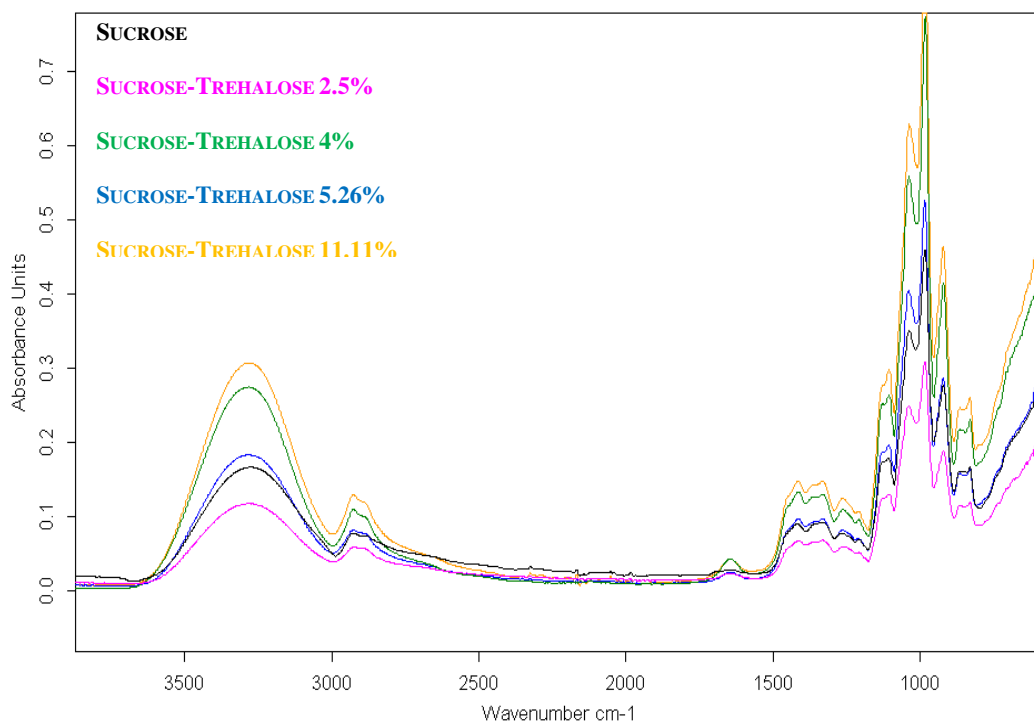


Figure 5.4 ATR-FTIR Spectra of amorphous sucrose and ST samples

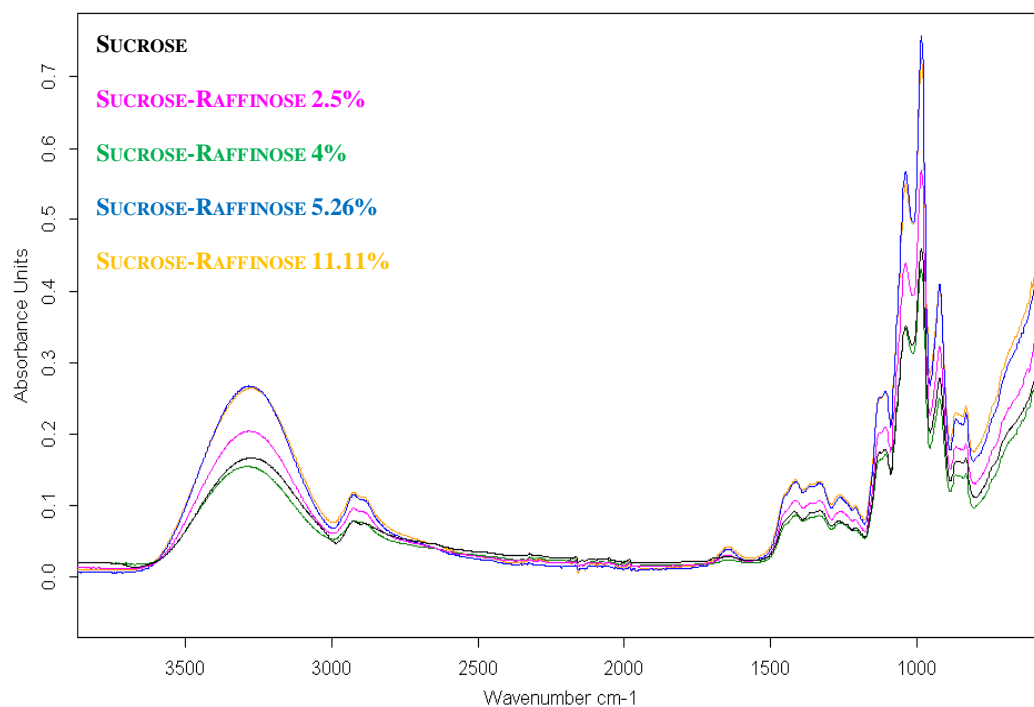


Figure 5.5 ATR-FTIR Spectra of amorphous sucrose and SR samples

5.2.3 SAMPLE WATER CONTENT

TGA studies were conducted to determine sample water content. Water content of amorphous sucrose in *Chapter 4* was 1.8% (*Figure 5.6*). ST and SR samples were generated using the same parameters used to generate amorphous sucrose samples therefore water contents were expected to be similar.

Figures 5.7 to 5.10 are TGA weight loss profiles for ST2.5 (1.2%), ST4 (1.9%), ST5.26 (2.5%) and ST11.11 (1.7%) samples. Sample water content was similar although ST5.26 samples had a slightly higher water content than the other ST samples.

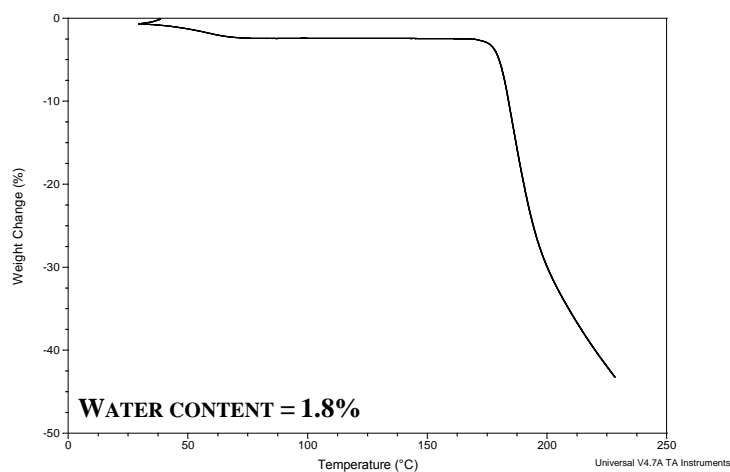


Figure 5.6 Typical TGA weight loss profile of amorphous sucrose heated at 2°C/min using a pin holed pan system

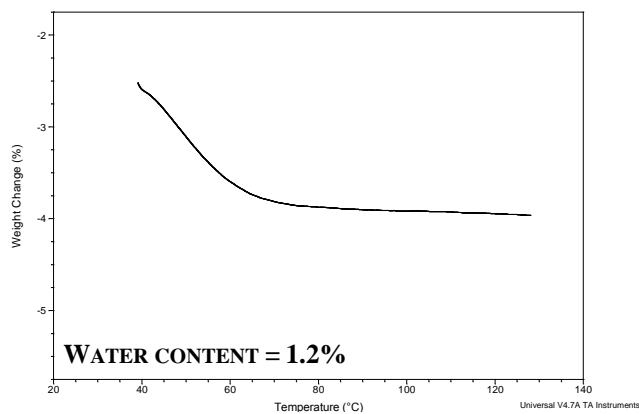


Figure 5.7 Typical TGA weight loss profile of ST2.5 heated at 2°C/min using a pin holed pan system

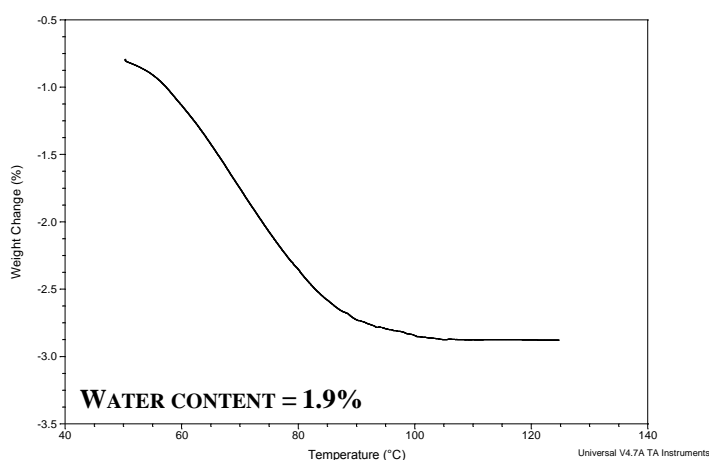


Figure 5.8 Typical TGA weight loss profile of ST4 heated at 2°C/min using a pin holed pan system

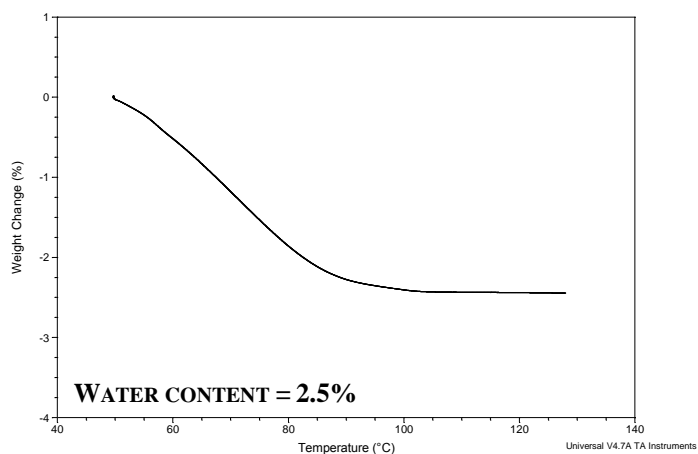


Figure 5.9 Typical TGA weight loss profile of ST5.26 heated at 2°C/min using a pin holed pan system

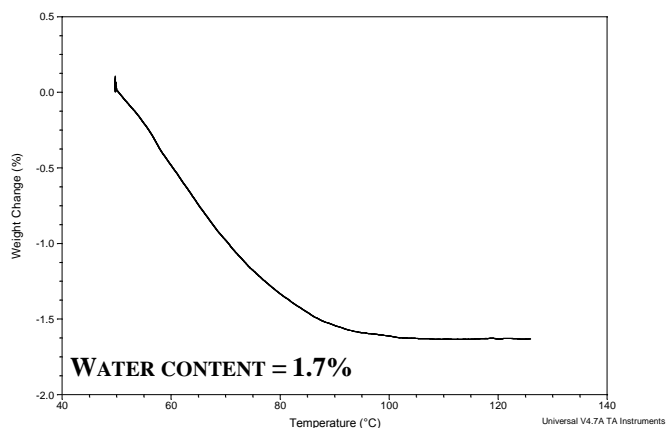


Figure 5.10 Typical TGA weight loss profile of ST11.11 heated at 2°C/min using a pin holed pan system

Figures 5.11 to 5.14 are TGA weight loss profiles for SR2.5 (1.2%), ST4 (1.9%), ST5.26 (1.8%) and ST11.11 (2.7%) samples. Sample water content was similar although SR11.11 samples had a slightly higher water content than the other SR samples.

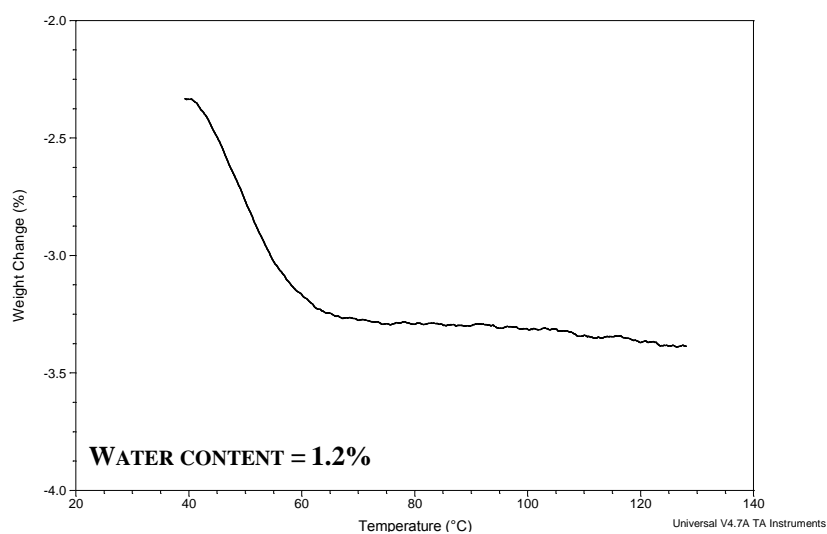


Figure 5.11 Typical TGA weight loss profile of SR2.5 heated at 2°C/min using a pin holed pan system

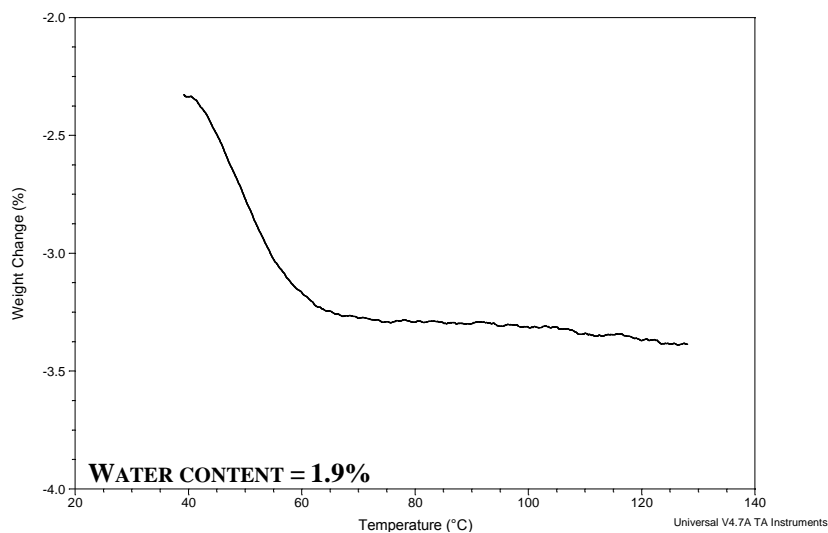


Figure 5.12 Typical TGA weight loss profile of SR4 heated at 2°C/min using a pin holed pan system

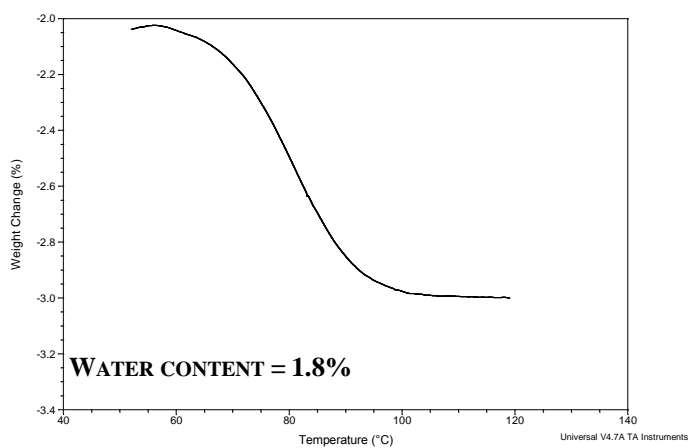


Figure 5.13 Typical TGA weight loss profile of SR5.26 heated at 2°C/min using a pin holed pan system

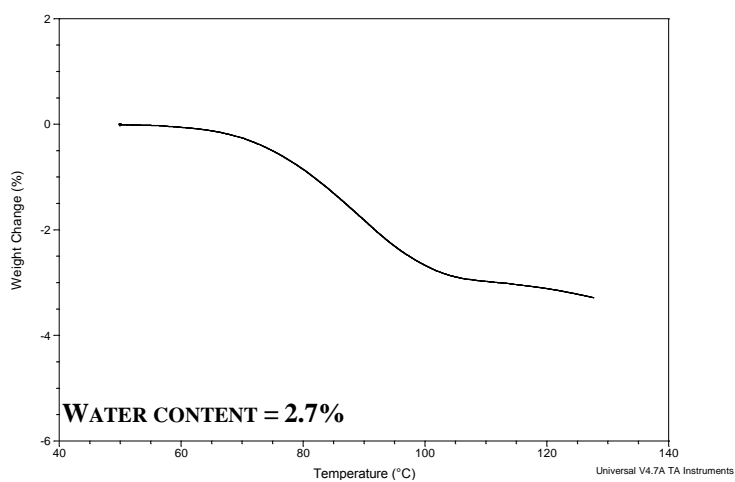


Figure 5.14 Typical TGA weight loss profile of SR11.11 heated at 2°C/min using a pin holed pan system

5.2.4 CALCULATION OF AMORPHOUS STABILITY PARAMETERS

5.2.4.1 Determination of activation enthalpy (ΔE_{T_g}) for structural relaxation around T_g (ΔE_{T_g}), calculated from the heat rate dependency of T_g

DSC experiments were conducted to calculate the activation energy for structural relaxation around T_g (ΔE_{T_g}) for all samples. In this study, ΔE_{T_g} was evaluated from the heating/cooling rate (q) dependence of T_g (Moynihan et al., 1974). The heating rate dependency of T_g is usually measured using cooling/heating rates within the range of 2.5 to 40°C/min, as either poor sensitivity or significant temperature lags are observed beyond each extreme (Crowley and Zografi, 2001). DSC experiments were conducted at 2, 5, 10 and 20°C/min samples were first heated, cooled and then heated again to obtain un-plasticised T_g values. Activation energies were evaluated using the heating rate dependency of the T_g , where T_g values were obtained in the second heat at 2, 5, 10 and 20°C/min and were plotted according *Equation 5.3*.

$$\frac{d \ln q}{d(1/T_g)} = \frac{\Delta H_{Act}}{R} \quad Eq.5.3$$

where R is the universal gas constant (8.314 JK⁻¹mol⁻¹) and q is the heating rate. ΔE_{T_g} was calculated by multiplying the gradient of the graph by the gas constant.

A typical DSC heat flow signal for amorphous sucrose samples at 2, 5, 10 and 20°C/min is provided in *Figure 5.15*. T_g values (summarised in *Table 5.1*) obtained here were used to plot the natural logarithm of the heating rate versus $1000/T_g$ (according to *Equation 5.3*) to calculate the ΔE_{T_g} and is shown in *Figure 5.16*.

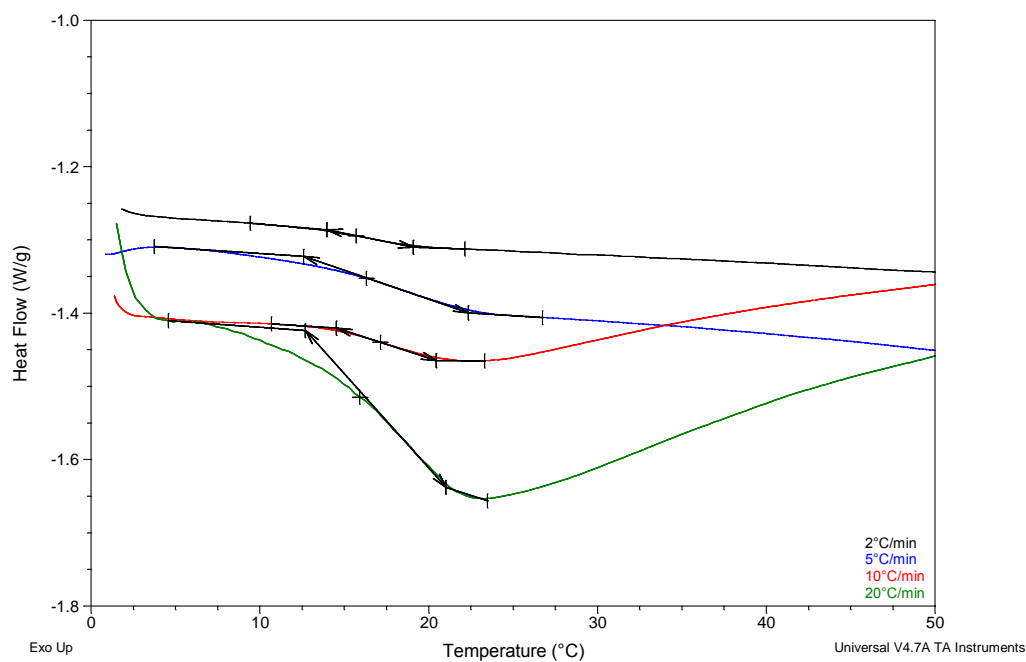


Figure 5.15 A typical DSC heat flow signal for amorphous sucrose at 2, 5, 10 and 20°C/min

Table 5.1 Summary of T_g values obtained from DSC heat flow signal for amorphous sucrose at 2, 5, 10 and 20°C/min

Heating rate, q (K/min)	$\ln q$	T_g (°C)	T_g (K)	$1000/T_g$ (K ⁻¹)
2	0.6931	14.89	287.89	3.4735
5	1.6094	16.75	289.75	3.4513
10	2.3026	17.43	290.43	3.4432
20	2.9957	18.87	291.87	3.4262

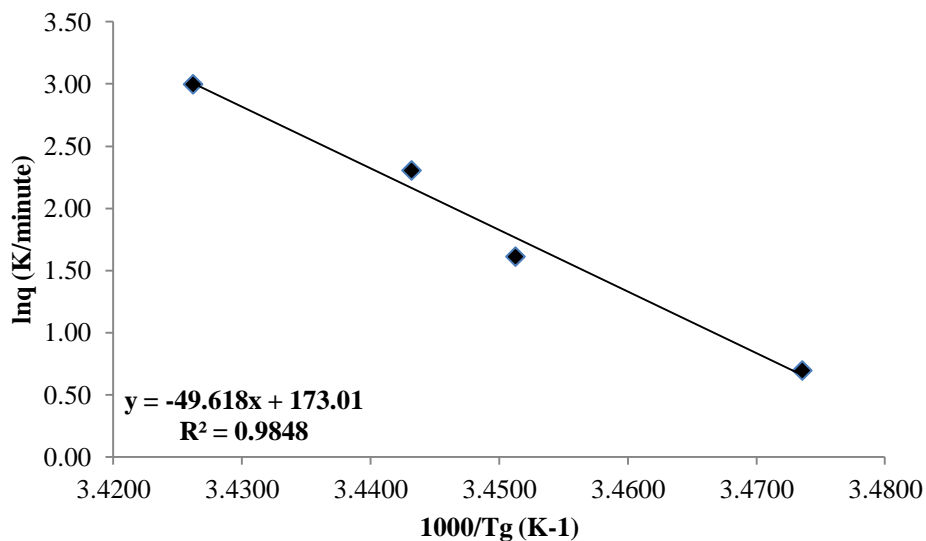
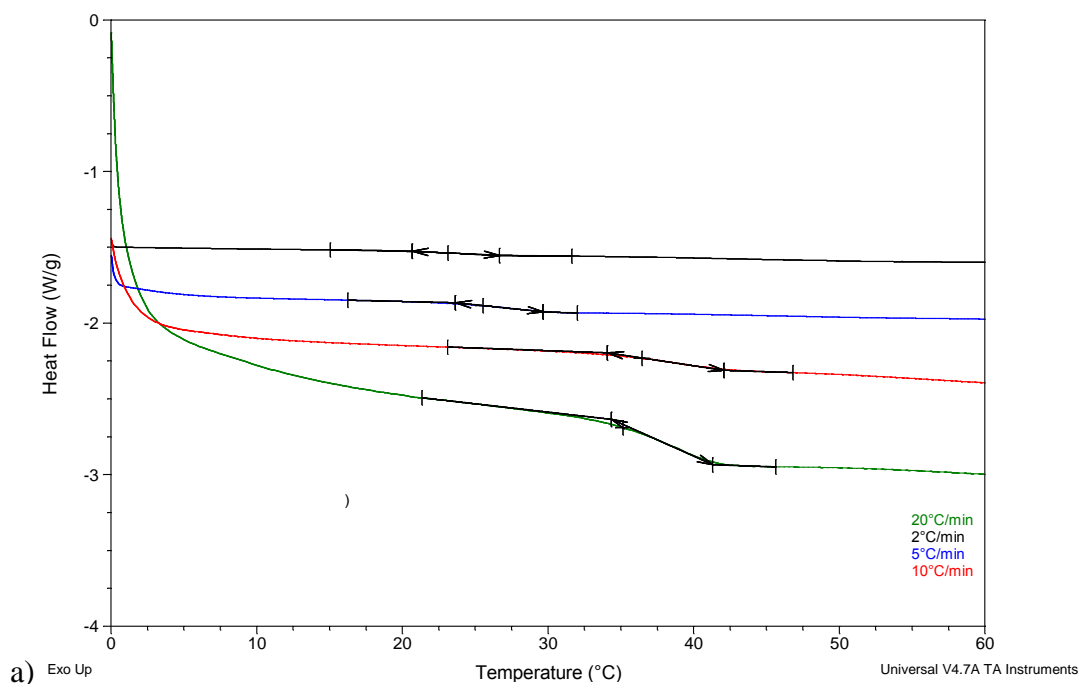


Figure 5.16 Activation energy determination from DSC heating rate experiments on amorphous sucrose.

A typical DSC heat flow signal for ST2.5 samples at 2, 5, 10 and 20K/min is provided in *Figure 5.17*. T_g values (summarised in *Table 5.2*) obtained here were used to plot the natural logarithm of the heating rate versus $1000/T_g$ (according to *Equation 5.3*) to calculate the ΔE_{T_g} and is shown in *Figure 5.18*.



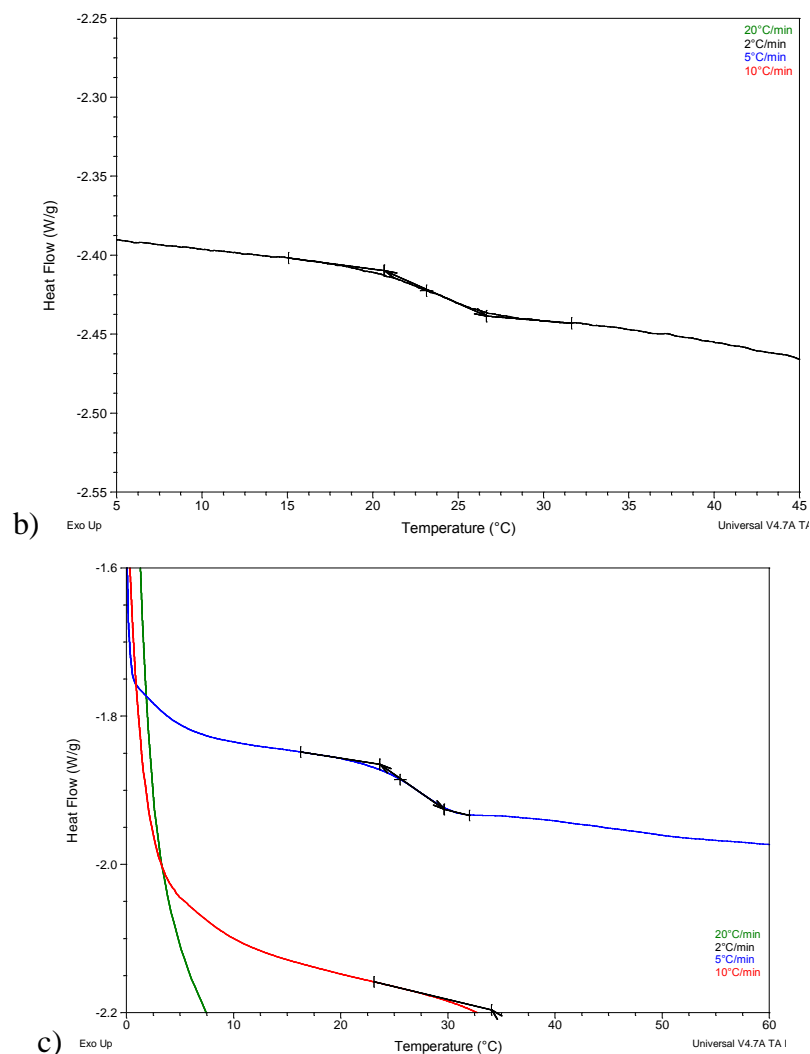
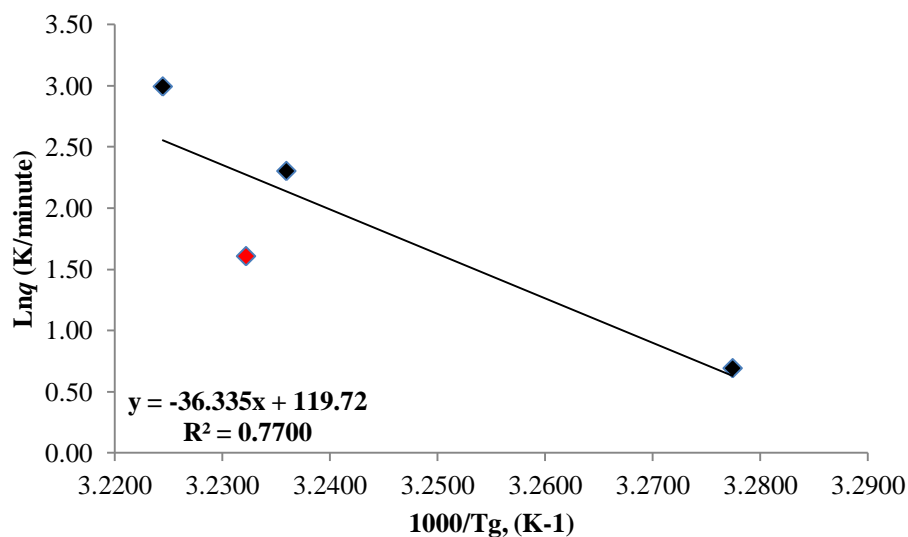


Figure 5.17 A typical DSC heat flow signal for ST2.5 a) at 2,5,10 and 20°C/min b) close up of DSC heat flow signal at 2°C/min and at c)5°C/min

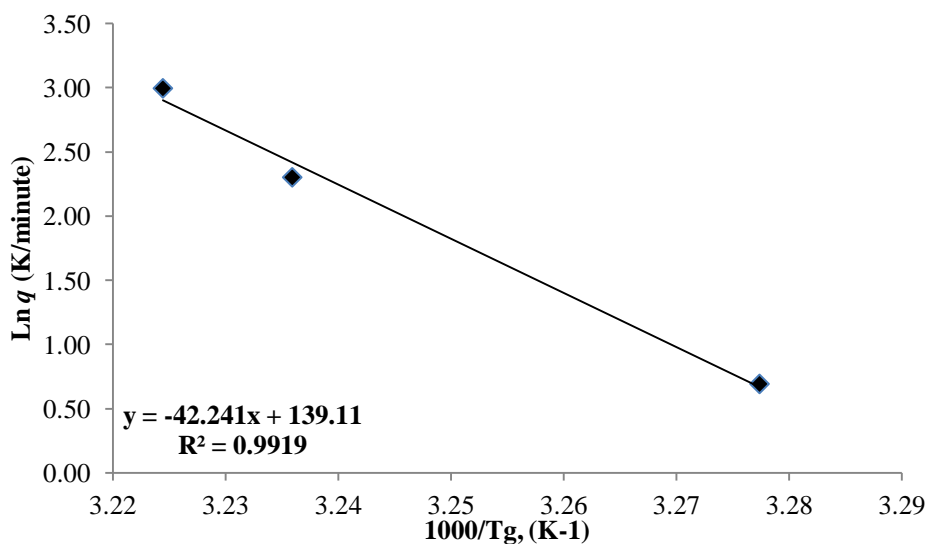
Table 5.2 Summary of T_g values obtained from DSC heat flow signal for ST2.5 at 2, 5, 10 and 20°C/min

Heating rate, q (K/min)	$\ln q$	$T_g(^{\circ}\text{C})$	$T_g(\text{K})$	$1000/T_g$ (K^{-1})
2	0.6931	32.12	305.12	3.2774
5	1.6094	36.39	309.39	3.2322
10	2.3026	36.03	309.03	3.2359
20	2.9957	37.13	310.13	3.2245

Figure 5.18a is a plot of the natural logarithm of the heating rate versus $1/T_g$ for ST2.5. The R^2 value was 0.7700. This low R^2 value was due to the data point correlating the T_g observed at $5^\circ\text{C}/\text{min}$ (data point is shown in red in Figure 5.18a). This plot was removed and the line of best fit was recalculated (Figure 5.18b) the new R^2 value was 0.9919, the gradient of this line was used to calculate the ΔE_{T_g} .



a)



b)

Figure 5.18 Activation energy determination from DSC heating rate experiments on ST2.5.a) with 2.5, 10 and $20^\circ\text{C}/\text{min}$ values plotted b) with 2, 10 and $20^\circ\text{C}/\text{min}$ values plotted

A typical DSC heat flow signal for ST4 samples at 2, 5, 10 and 20°C/min is provided in *Figure 5.19*. T_g values (summarised in *Table 5.3*) obtained here were used to plot the natural logarithm of the heating rate versus $1000/T_g$ (according to *Equation 5.3*) to calculate the ΔE_{T_g} and is shown in *Figure 5.20*.

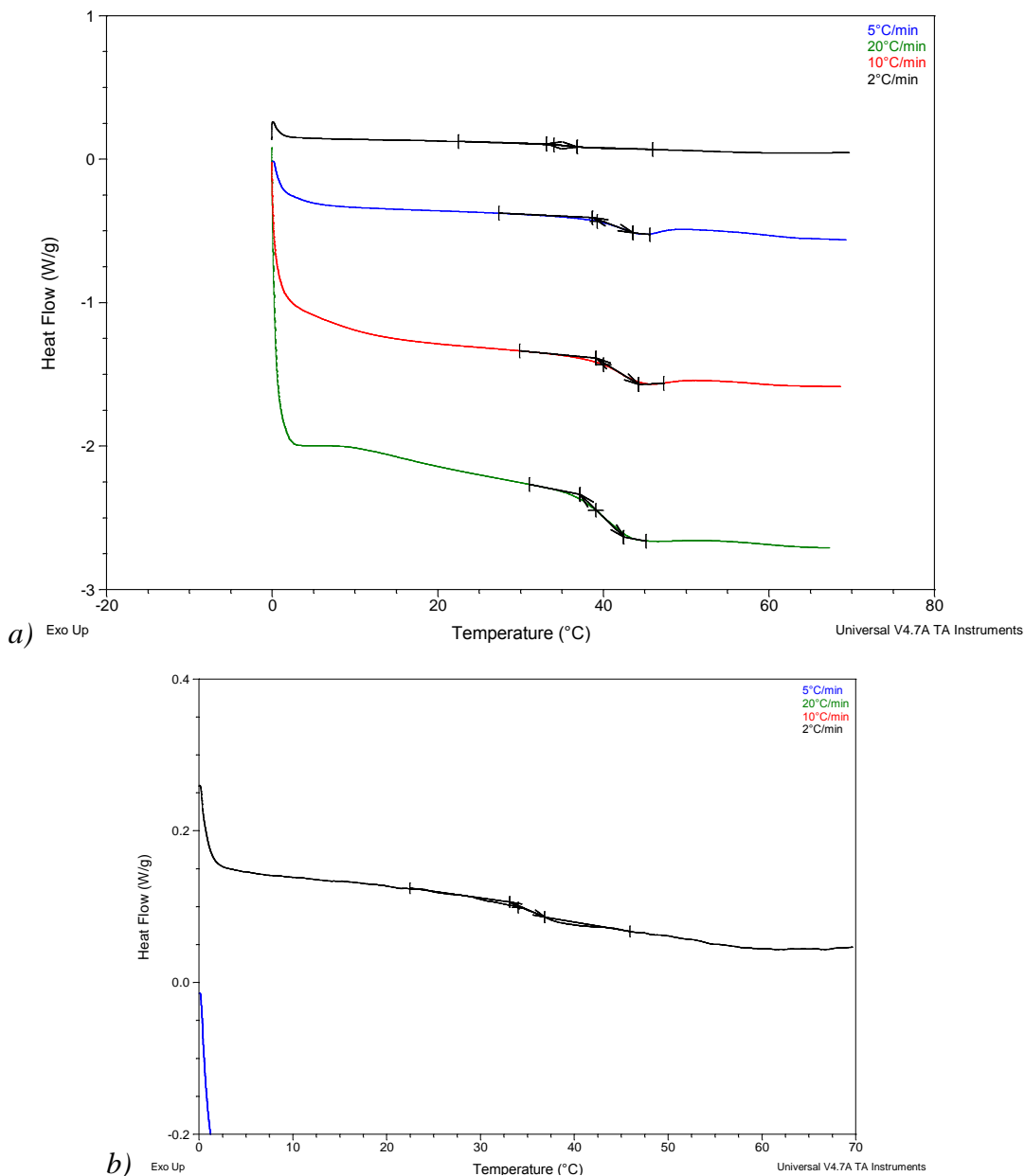


Figure 5.19 A typical DSC heat flow signal for ST4 a) at 2,5,10 and 20°C/min b) close up of DSC heat flow signal at 2°C/min

Table 5.3 Summary of T_g values obtained from DSC heat flow signal for ST4 at 2, 5, 10 and 20°C/min

Heating rate , q (K/min)	$\ln q$	$T_g(^{\circ}\text{C})$	$T_g(\text{K})$	$1000/T_g (\text{K}^{-1})$
2	0.6931	33.4	306.4	3.2637
5	1.6094	39.03	312.03	3.2048
10	2.3026	40.11	313.11	3.1938
20	2.9957	41.84	314.84	3.1762

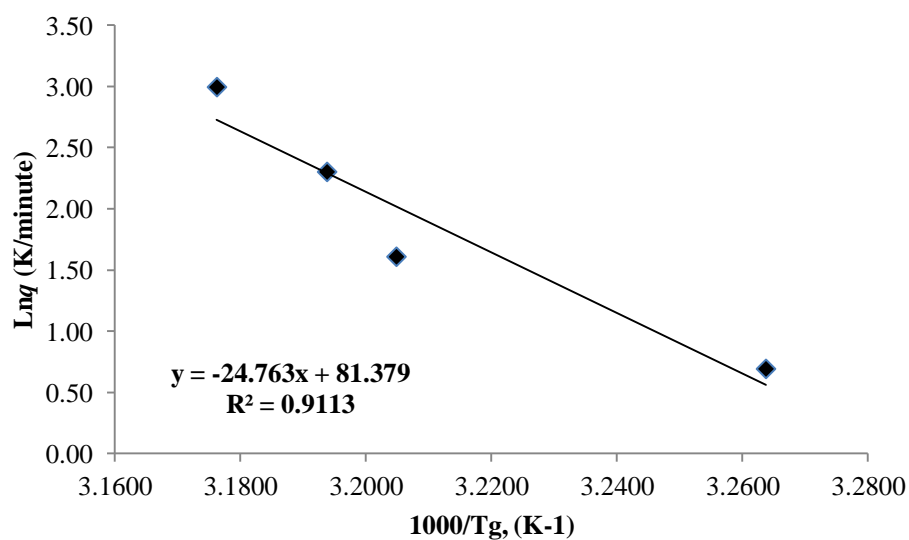


Figure 5.20 Activation energy determination from DSC heating rate experiments on ST4

A typical DSC heat flow signal for ST5.26 samples at 2, 5, 10 and 20°C/min is provided in *Figure 5.21*. T_g values (summarised in *Table 5.4*) obtained here were used to plot the natural logarithm of the heating rate versus $1000/T_g$ (according to *Equation 5.3*) to calculate the ΔE_{T_g} and is shown in *Figure 5.22*.

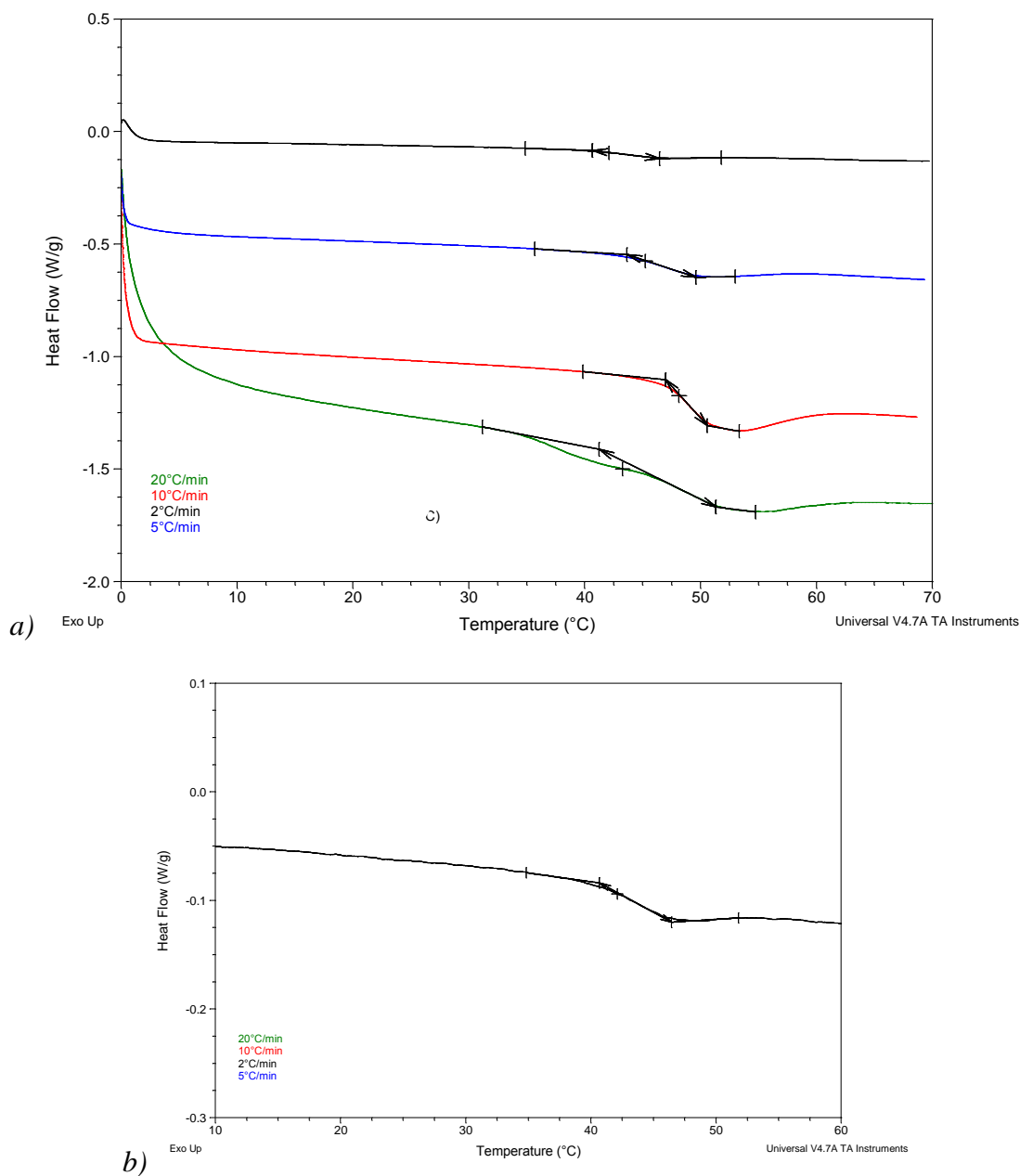
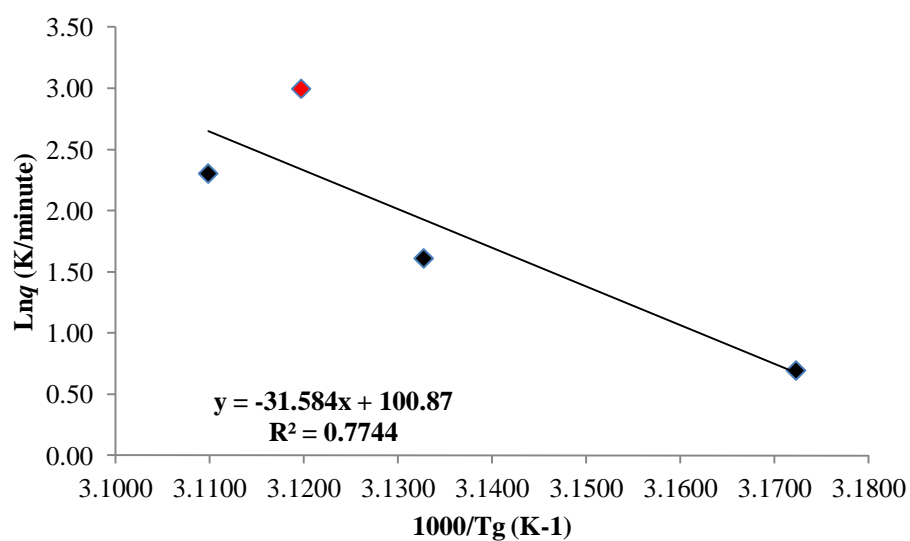


Figure 5.21 A typical DSC heat flow signal for ST5.26 a) at 2,5,10 and 20°C/min b) close up of DSC heat flow signal at 2°C/min

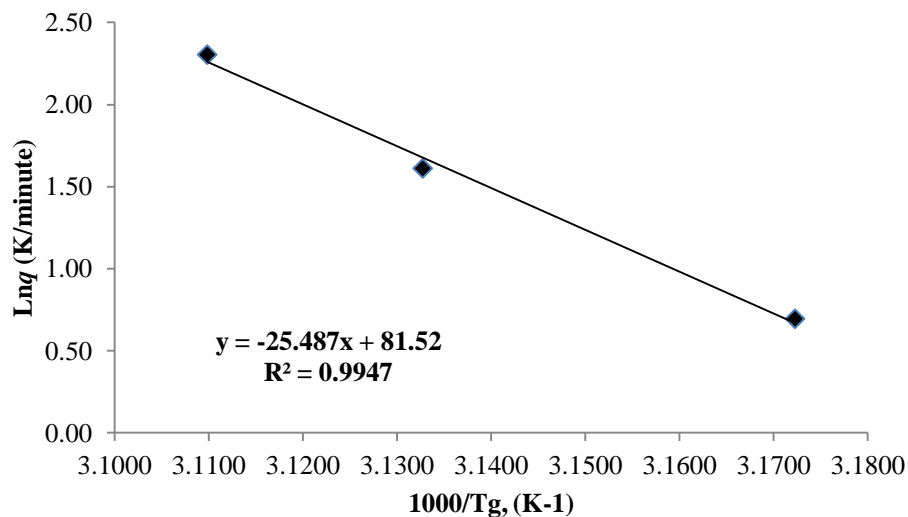
Table 5.4 Summary of T_g values obtained from DSC heat flow signal for ST5.26 at 2, 5, 10 and 20°C/min

Heating rate, q (K/min)	Ln q	T _g (K)	T _g (K)	1000/T _g (K ⁻¹)
2	0.6931	42.23	315.23	3.1723
5	1.6094	46.21	319.21	3.1327
10	2.3026	48.56	321.56	3.1098
20	2.9957	47.54	320.54	3.1197

Figure 5.22a is a plot of the natural logarithm of the heating rate versus $1/T_g$ for ST2.5. The R^2 value was 0.7744. This low R^2 value was due to the data point correlating the T_g observed at 20°C/min (data point is shown in red). This data point was removed and the line of best fit was recalculated (Figure 5.22b) the new R^2 value was 0.9919, the gradient of this line was used to calculate the ΔE_{T_g} .



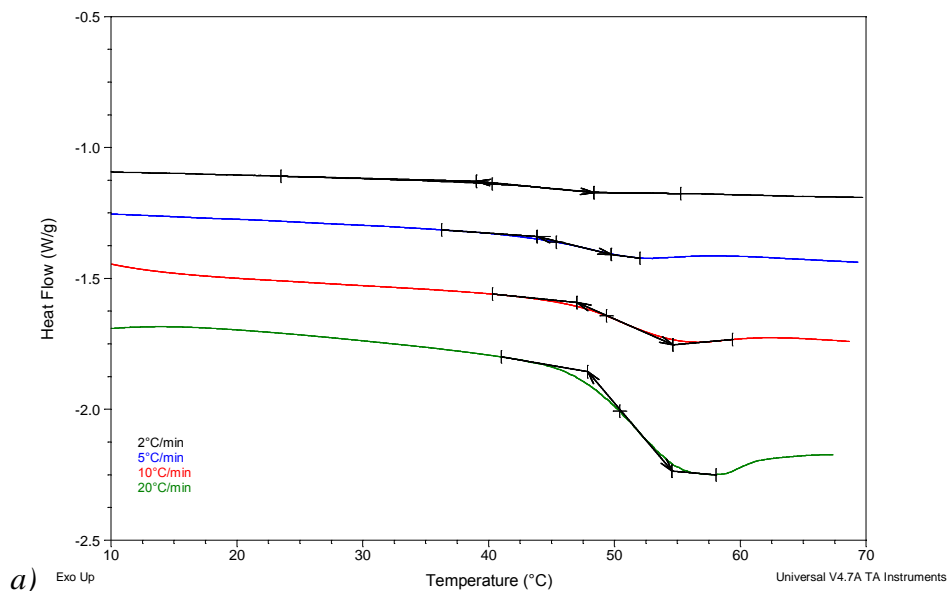
a)



b)

Figure 5.22 Activation energy determination from DSC heating rate experiments on ST5.26.a) with 2.5, 10 and 20°C/min values plotted b) with 2, 5 and 10°C/min values plotted

A typical DSC heat flow signal for ST11.11 samples at 2, 5, 10 and 20°C/min is provided in *Figure 5.23*. T_g values (summarised in *Table 5.5*) obtained here were used to plot the natural logarithm of the heating rate versus $1000/T_g$ (according to *Equation 5.3*) to calculate the ΔE_{T_g} and is shown in *Figure 5.24*.



a)

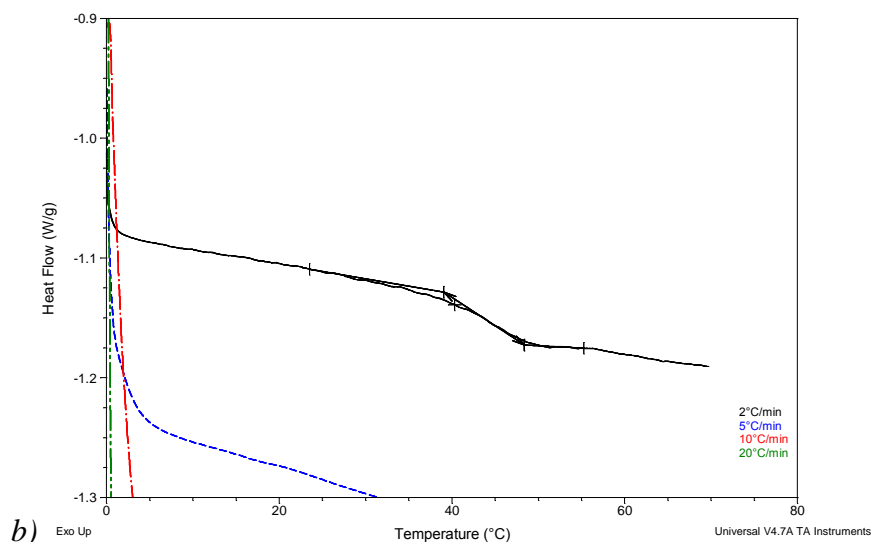


Figure 5.23 A typical DSC heat flow signal for ST11.11 a) at 2,5,10 and 20°C/min b) close up of DSC heat flow signal at 2°C/min

Table 5.5 Summary of T_g values obtained from DSC heat flow signal for ST5.26 at 2, 5, 10 and 20°C/min

Heating rate, q (K/min)	Ln q	T_g (K)	T_g (K)	$1000/T_g$ (K ⁻¹)
2	0.6931	42.16	315.16	3.1730
5	1.6094	46.39	319.39	3.1310
10	2.3026	50.17	323.17	3.0943
20	2.9957	50.82	323.82	3.0881

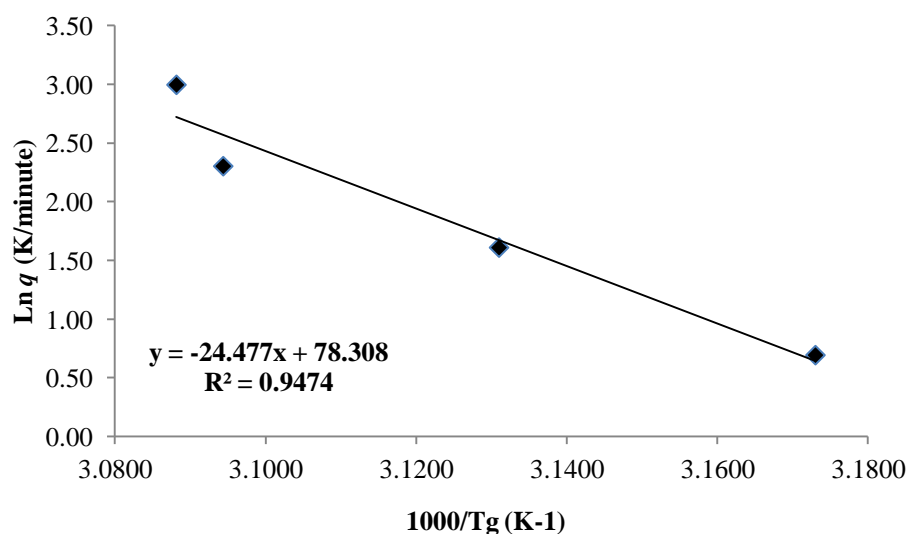


Figure 5.24 Activation energy determination from DSC heating rate experiments on ST11.11

The activation enthalpy of structural relaxation at T_g , ΔE_{T_g} was calculated by multiplying the gradient values obtained from the natural logarithm of the heating rate versus $1000/T_g$ by the gas constant, R ($8.314\text{JK}^{-1}\text{mol}^{-1}$) as per *Equation 5.3*. These results are presented in *Table 5.6*.

Table 5.6 ΔE_{T_g} calculated from the heating rate dependency of T_g for Amorphous Sucrose and ST samples

SAMPLE	GRADIENT	ACTIVATION ENTHALPY OF STRUCTURAL RELAXATION AT T_g ,
		ΔE_{T_g} (kJ/mol)
Sucrose	49.618	413
ST2.5	42.241	351
ST4	24.763	206
ST5.26	31.584	263
ST11.11	24.477	204

A typical DSC heat flow signal for SR2.5 samples at 2, 5, 10 and 20K/min is provided in *Figure 5.25*. T_g values (summarised in *Table 5.7*) obtained here were used to plot the natural logarithm of the heating rate versus $1000/T_g$ (according to *Equation 5.3*) to calculate the ΔE_{T_g} and is shown in *Figure 5.26*.

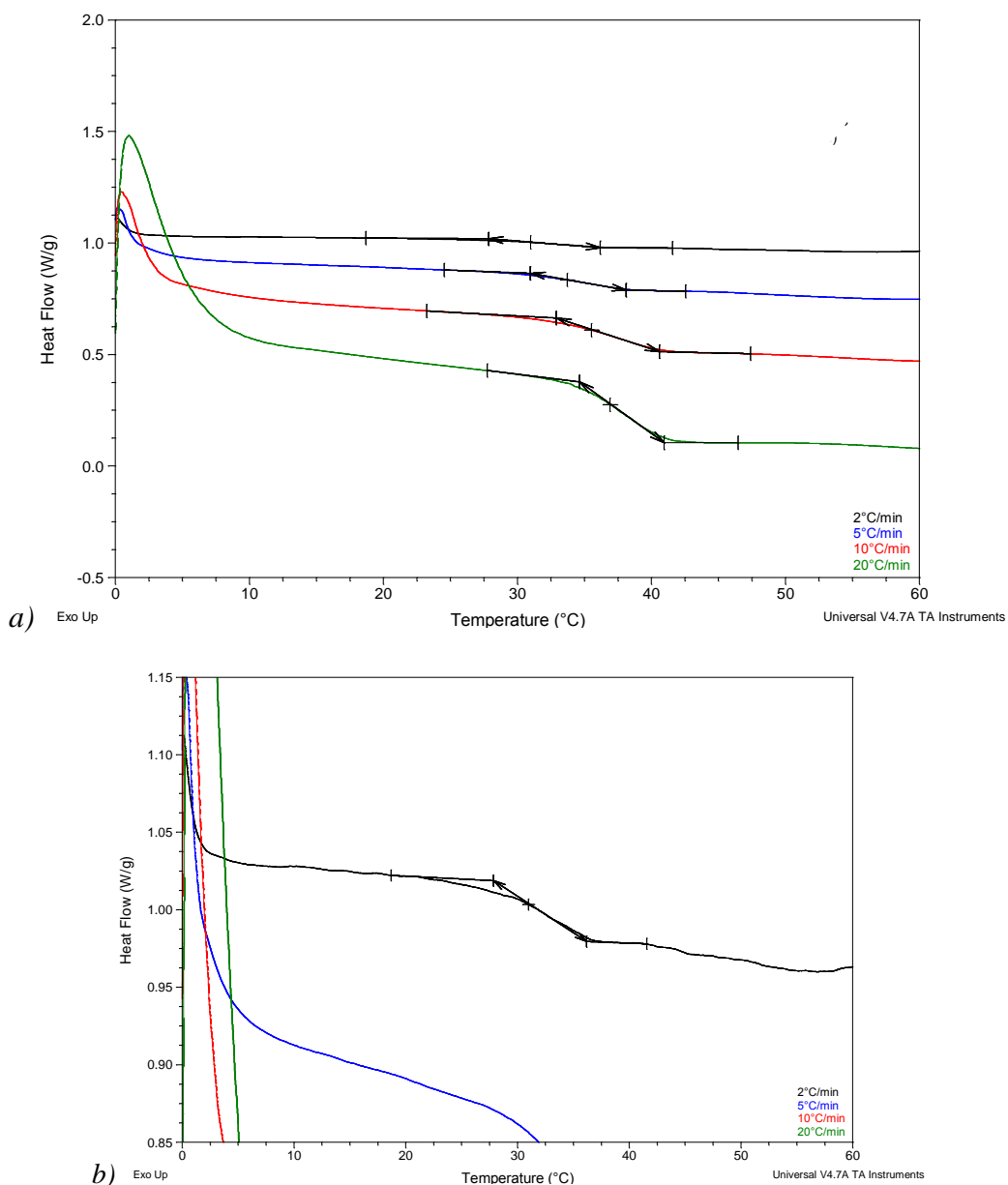


Figure 5.25 A typical DSC heat flow signal for SR2.5 a) at 2,5,10 and 20°C/min b) close up of DSC heat flow signal at 2°C/min

Table 5.7 Summary of T_g values obtained from DSC heat flow signal for SR2.5 at 2, 5, 10 and 20°C/min

Heating rate, q (K/min)	Ln q	T_g (K)	T_g (K)	$1000/T_g$ (K ⁻¹)
2	0.6931	32.785	305.785	3.2703
5	1.6094	34.08	307.08	3.2565
10	2.3026	36.305	309.305	3.2331
20	2.9957	37.095	310.095	3.2248

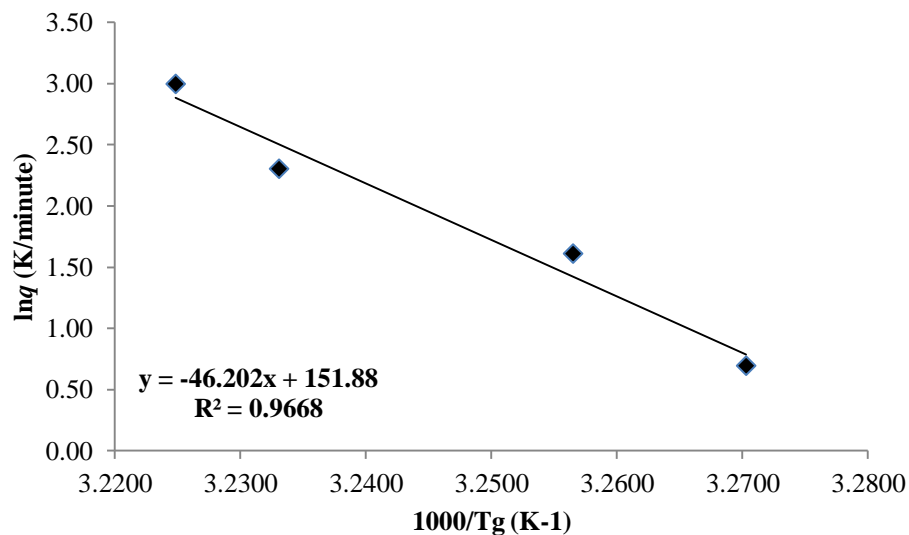
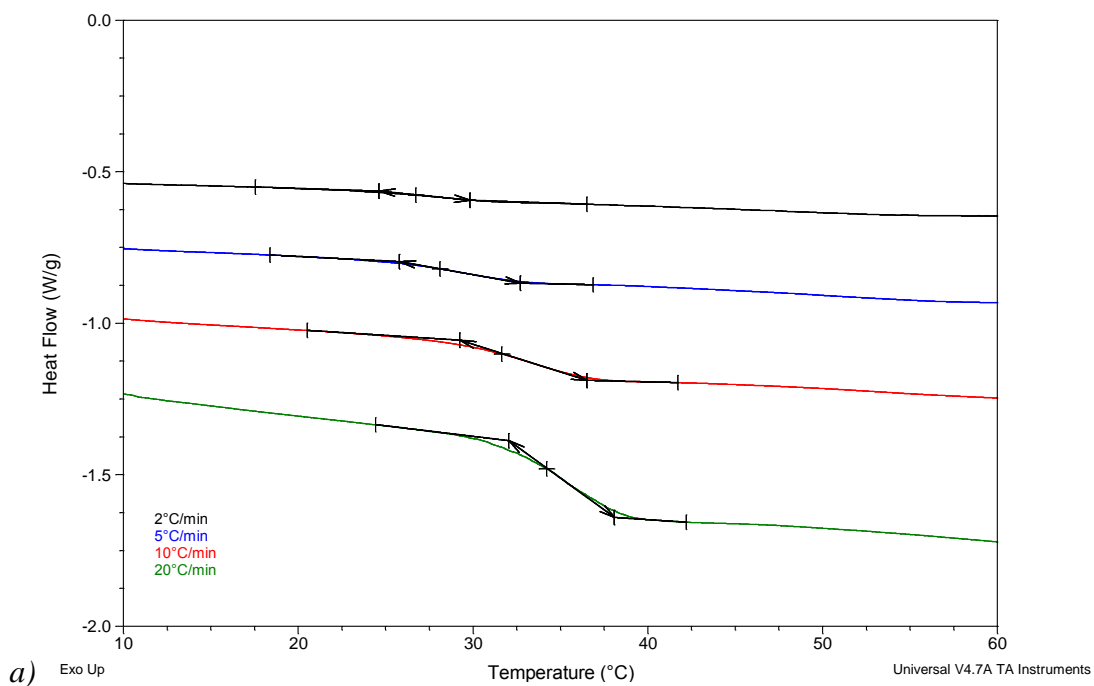


Figure 5.26 Activation energy determination from DSC heating rate experiments on SR2.5

A typical DSC heat flow signal for SR4 samples at 2, 5, 10 and 20°C/min is provided in *Figure 5.27*. T_g values (summarised in *Table 5.8*) obtained here were used to plot the natural logarithm of the heating rate versus $1000/T_g$ (according to *Equation 5.3*) to calculate the ΔE_{T_g} and is shown in *Figure 5.28*.



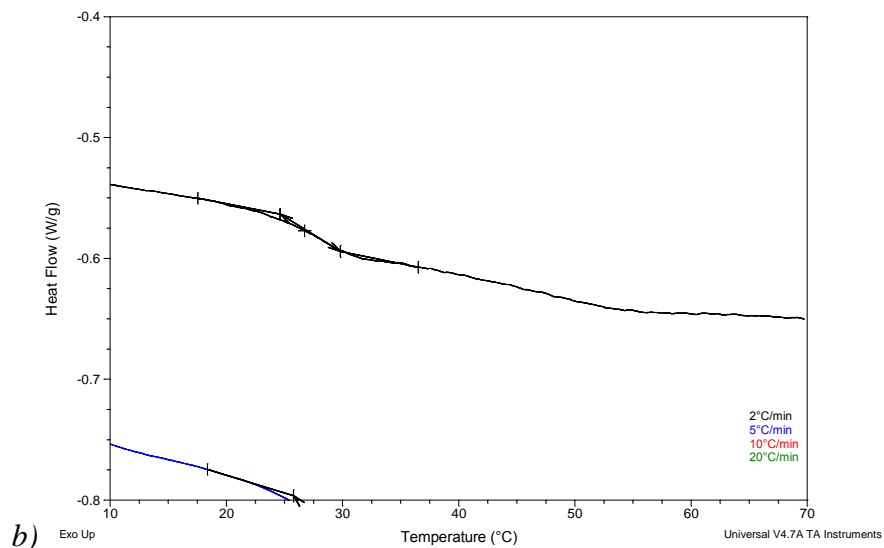


Figure 5.27 A typical DSC heat flow signal for SR4 a) at 2,5,10 and 20°C/min b) close up of DSC heat flow signal at 2°C/min

Table 5.8 Summary of T_g values obtained from DSC heat flow signal for SR4 at 2, 5, 10 and 20°C/min

Heating rate, q (K/min)	Ln q	$T_g(K)$	$T_g(K)$	$1000/T_g (K^{-1})$
2	0.6931	25.705	298.705	3.3478
5	1.6094	28.595	301.595	3.3157
10	2.3026	31.635	304.635	3.2826
20	2.9957	33.625	306.625	3.2613

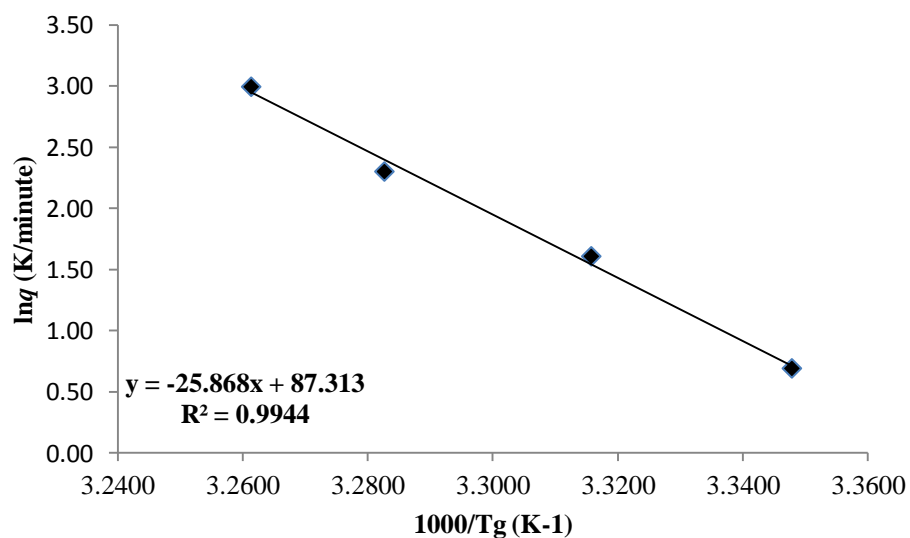


Figure 5.28 Activation energy determination from DSC heating rate experiments on SR4

A typical DSC heat flow signal for SR5.26 samples at 2, 5, 10 and 20°C/min is provided in *Figure 5.29*. T_g values (summarised in *Table 5.9*) obtained here were used to plot the natural logarithm of the heating rate versus $1000/T_g$ (according to *Equation 5.3*) to calculate the ΔE_{T_g} and is shown in *Figure 5.30*.

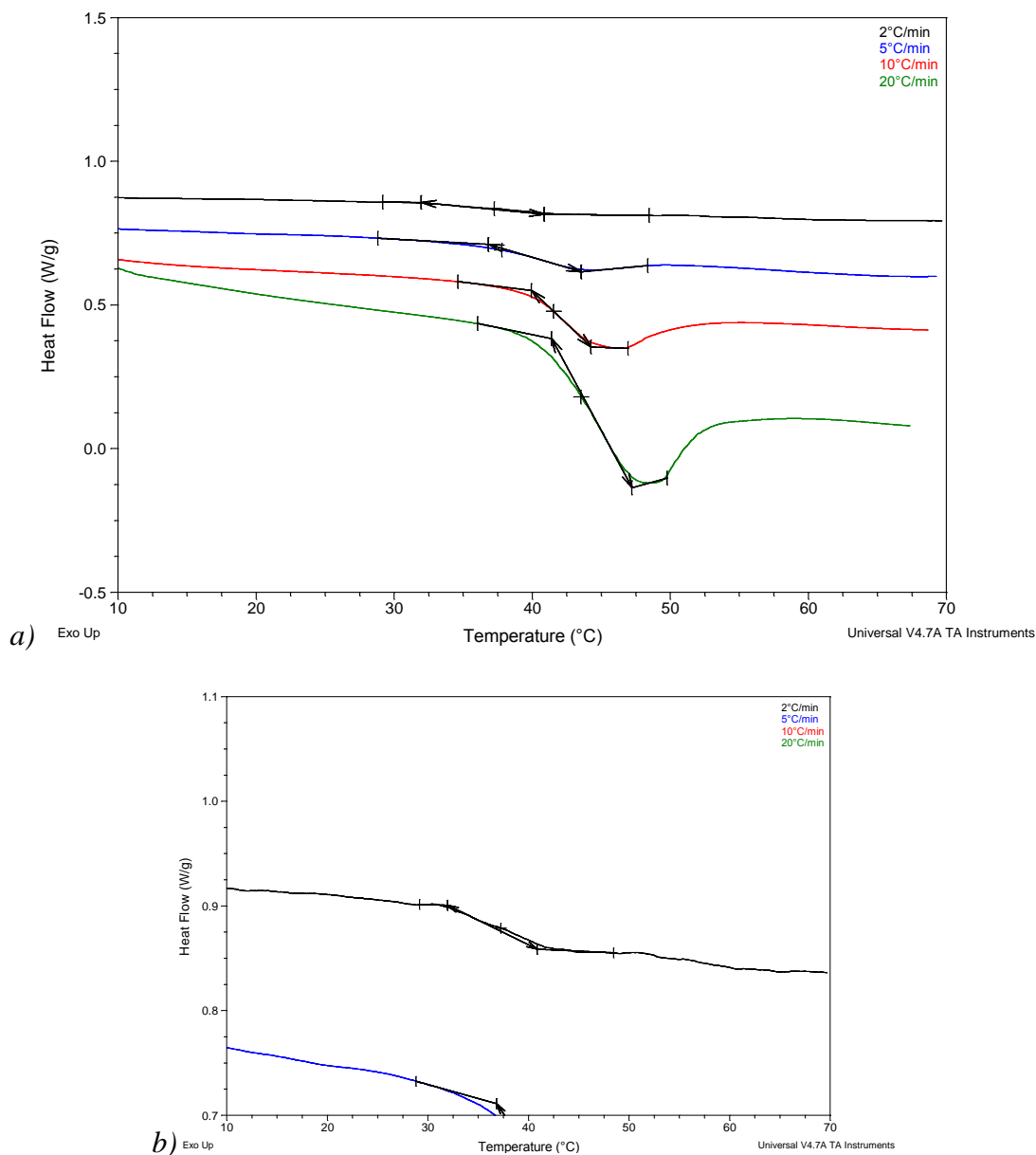


Figure 5.29 A typical DSC heat flow signal for SR5.26 a) at 2,5,10 and 20°C/min b) close up of DSC heat flow signal at 2°C/min

Table 5.9 Summary of T_g values obtained from DSC heat flow signal for SR5.26 at 2, 5, 10 and 20°C/min

Heating rate, q (K/min)	Ln q	T_g (K)	T_g (K)	1000/ T_g (K ⁻¹)
2	0.6931	37	310	3.2258
5	1.6094	39.41	312.41	3.2009
10	2.3026	41.46	314.46	3.1801
20	2.9957	43.26	316.26	3.1620

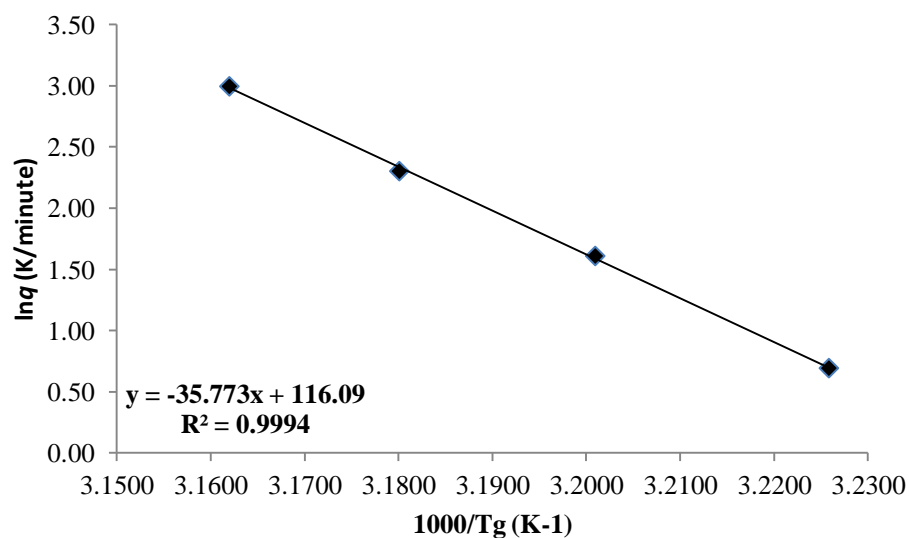


Figure 5.30 Activation energy determination from DSC heating rate experiments on SR5.26

A typical DSC heat flow signal for SR11.11 samples at 2, 5, 10 and 20°C/min is provided in *Figure 5.31*. T_g values (summarised in *Table 5.10*) obtained here were used to plot the natural logarithm of the heating rate versus $1000/T_g$ (according to *Equation 5.3*) to calculate the ΔE_{T_g} and is shown in *Figure 5.32*.

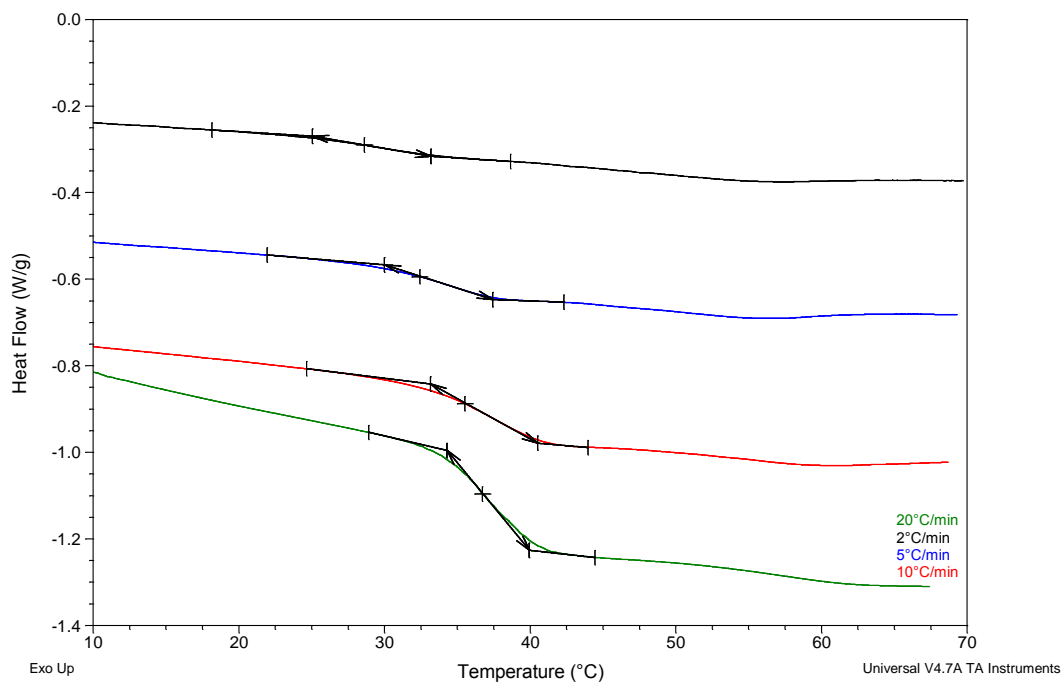


Figure 5.31 A typical DSC heat flow signal for SR11.11 at 2, 5, 10 and 20°C/min

Table 5.10 Summary of T_g values obtained from DSC heat flow signal for SR11.11 at 2, 5, 10 and 20°C/min

Heating rate, q (K/min)	$\ln q$	T_g (K)	T_g (K)	$1000/T_g$ (K ⁻¹)
2	0.6931	26.84	299.835	3.3352
5	1.6094	31.78	304.775	3.2811
10	2.3026	36.20	309.2	3.2342
20	2.9957	36.56	309.56	3.2304

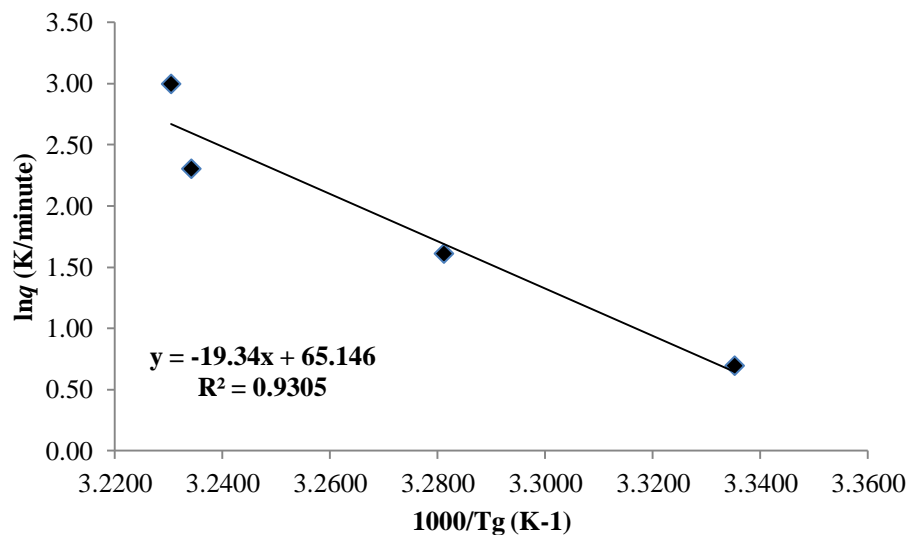


Figure 5.32 Activation energy determination from DSC heating rate experiments on SR11.11

The activation enthalpy of structural relaxation at T_g , ΔE_{T_g} was calculated by multiplying the gradient values obtained from the natural logarithm of the heating rate versus $1000/T_g$ by the gas constant, R ($8.314 \text{ JK}^{-1} \text{ mol}^{-1}$) as per *Equation 5.3*. These results are presented in *Table 5.11*.

Table 5.11 ΔE_{T_g} calculated from the heating rate dependency of T_g for Amorphous Sucrose and SR samples

SAMPLE	GRADIENT	ACTIVATION ENTHALPY OF
		STRUCTURAL RELAXATION AT T_g , ΔE_{T_g} (kJ/mol)
Sucrose	49.618	413
SR2.5	46.202	384
SR4	25.868	215
SR5.26	35.773	297
SR11.11	19.34	161

Table 5.12 is a summary of the activation enthalpy of structural relaxation at T_g for amorphous sucrose, ST and SR samples. Structural relaxation in a glass-forming liquid refers to the kinetically restricted re-arrangement of the liquid structure in response to changes in external variables such as temperature. It is generally thought that the atomic or molecular re-arrangements taking place during structural relaxation are similar to those occurring during viscous flow in response to a shear stress (Moynihan et al., 1996). In general, increasing percentage of sugar additive (trehalose and raffinose) reduced ΔE_{T_g} values from 412kJ/mol in pure amorphous sucrose samples to 204kJ/mol for ST11.11 and 161kJ/mol for SR11.11. In the amorphous state, low free volume results in large activation energy for molecular motions. As temperature is increased, the free volume is increased which facilitates molecular motion as well as lowers activation energy (Dranca et al., 2009).

Table 5.12 ΔE_{T_g} calculated from the heating rate dependency of T_g for Amorphous Sucrose with or without sugar additive

% SUGAR ADDITIVE	ACTIVATION ENTHALPY OF STRUCTURAL RELAXATION AT T_g , ΔE_{T_g} (kJ/mol)	
	TREHALOSE	RAFFINOSE
0	412	
2.5	351	384
4.0	206	215
5.26	263	297
11.11	204	161

ΔE_{T_g} values obtained from this study were used to calculate the fragility parameter (m) (Equation 5.1) and strength parameter (D) (Equation 5.2).

5.2.4.2 Calculation of fragility and strength parameters

The fragility and strength parameters for all samples were calculated as per Equation 5.1 and Equation 5.2 respectively. Strength parameter D was calculated using an m_{\min} value of 16 and m_{\min} value determined using T_g values obtained from this study. It was assumed that τ at T_g was approximately 100s (Moynihan et al., 1974) whilst τ_0 represented a timescale of vibrational motions of approximately 10^{-14} s (Crowley and Zografi, 2001). Calculated m_{\min} for samples was 17 expected for ST5.26 and ST11.11 formulations which had an m_{\min} value of 18. Values obtained using $m_{\min} = 16$ gave lower D values than calculated m_{\min} however, the trends were still the same.

The results for amorphous sucrose, ST and SR samples are summarised both Table 5.13, Table 5.14 and Table 5.15. Strong liquids have fragility (m) values less than 40, strength (D) values greater than 30 whilst fragile liquids have m values greater than 75, D values less than 10. A clear relationship was not established between the percentage of sugar additive and m and D . However, some trends were apparent. SR4, SR11.11, ST4 and ST11.11 samples had m values less than 40 and were therefore identified as strong liquids. Whilst using D , SR11.11, ST4 and ST11.11 samples appeared to be strong liquids by possessing D values greater than 30. The results in this study showed that at the highest percentage sugar additive (i.e. SR11.11 and ST11.11), the highest values of D and the lowest values of m were observed. Both m and D parameters indicated that both SR11.11 and ST11.11 were the strongest glass formers and would therefore be associated with greater amorphous sucrose stability.

Table 5.13 Calculated fragility parameter, m (Eq.5.1) using ΔE_{T_g} calculated from the heating rate dependency of T_g for Amorphous Sucrose, ST and SR samples

	ΔE_{T_g} (J/mol)	ln10	T_g (K) (at 10K/min)	ln10RT_g	m
Sucrose	412000	2.3026	290.43	5559.94	74
ST2.5	351000		309.03	5916.01	59
ST4	206000		313.11	5994.12	34
ST5.26	263000		321.56	6155.89	43
ST11	204000		323.17	6186.71	33
SR2.5	384000		309.305	5921.28	65
SR4	215000		304.635	5831.88	37
SR5.26	297000		314.46	6019.96	49
SR11	161000		309.2	5919.27	27

Table 5.14 Calculated strength parameter, D (Eq.5.2) using ΔE_{T_g} calculated from the heating rate dependency of T_g for Amorphous Sucrose, ST and SR samples using $m_{min} = 16$

	ln10	m	m_{min}^2	$m - m_{min}$	D
Sucrose	2.3026	74	256	58	10
ST2.5		59		43	14
ST4		34		18	32
ST5.26		43		27	22
ST11		33		17	35
SR2.5		65		49	12
SR4		37		21	28
SR5.26		49		33	18
SR11		27		11	53

Table 5.15 Calculated strength parameter, D (Eq.5.2) using ΔE_{T_g} calculated from the heating rate dependency of T_g for Amorphous Sucrose, ST and SR samples using m_{min} from data

	ln10	m	m_{min}	m_{min}^2	$m - m_{min}$	D
Sucrose	2.3026	74	17	305	57	12
ST2.5		59	17	306	42	17
ST4		34	17	306	17	42
ST5.26		43	18	307	25	28
ST11		33	18	307	15	46
SR2.5		65	17	306	47	15
SR4		37	17	306	19	36
SR5.26		49	17	306	32	22
SR11		27	17	306	10	73

5.2.4.4 Characterisation using quasi-isothermal modulated temperature dsc

Qi-MTDSC is a variant of MTDSC where the experimental temperature is modulated around a constant underlying temperature for a specified time, after which the temperature is incrementally ramped up or down so as to obtain a profile through a transition (Manduva et al., 2008). The effect of heating rate is negated by holding the sample at a range of selected temperatures about which the sample is modulated. Further details of this technique are described in *Chapter 2*. Qi-MTDSC experiments were conducted on all samples generated to identify if co-spray dried samples existed as a single mixed amorphous system (indicated by observation of one glass transition event) or if the sugars existed as separate amorphous phases (indicated by observation of two glass transition events). Qi-MTDSC experiments identified that ST2.5, ST11.11 and SR4 existed in separate amorphous phases indicated by the identification of two glass transition events.

As discussed previously, in a study conducted by Verdonck et al., (1999), PET was heated below its T_g an increase in heat capacity was observed and corresponding to the devitrification of PET at T_g . A decrease in heat capacity was detected as the sample reached a temperature where cold crystallisation occurred (Verdonck et al., 1999).

Typical Qi-MTDSC traces, reversing heat capacity signal as a function of time at a temperature modulation of $\pm 1^\circ\text{C}$, 20 minute isothermal periods with 3°C increments from 0°C to 130°C for all samples are shown in *Figure 5.33* to *Figure 5.39*. Samples were evaluated once residual water had been driven off prior to experiment.

An increase in heat capacity characteristic of a glass transition event was observed from 67.97°C to 81.98°C for amorphous sucrose (*Figure 5.33*). This was followed by an abrupt decrease in heat capacity at 103.99°C characteristic of a cold crystallisation event.

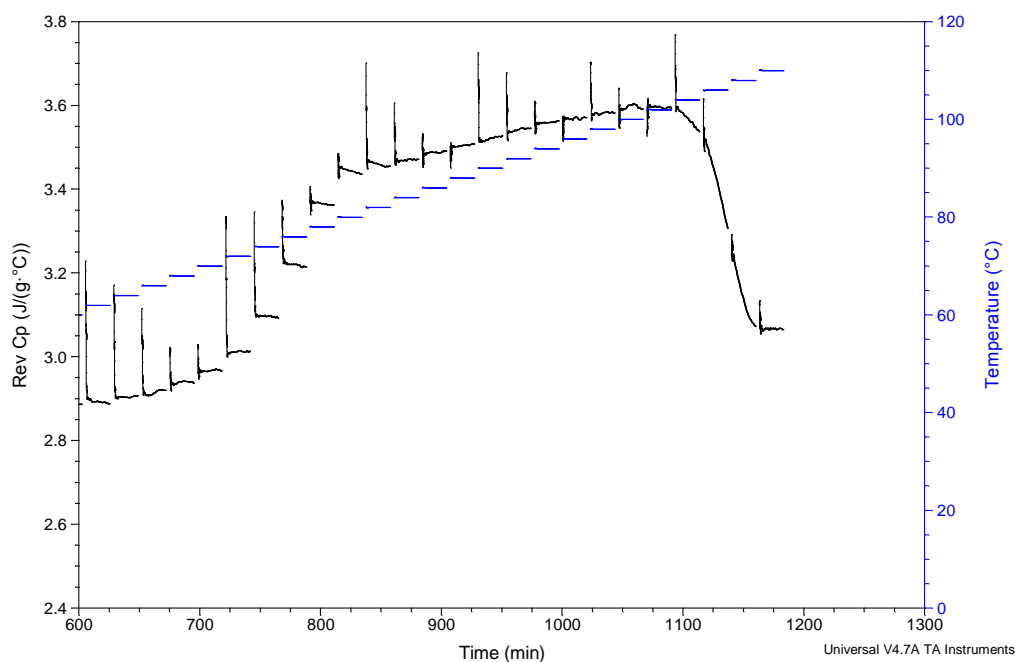


Figure 5.33 Typical Qi-MTDSC reversing heat capacity (as a function of time) signal of amorphous sucrose at a temperature modulation of $\pm 1^\circ\text{C}$, 20 minute isothermal periods with 2°C increments using a pin-holed pan

Qi-MTDSC experiments conducted on ST2.5 (*Figure 5.34*) showed evidence of two glass transitions occurring prior to cold crystallisation. The heat capacity increased in a manner characteristic of a glass transition event at 17.91°C to 47.91°C. Heat capacity appeared to plateau from 47.91°C to 53.91°C. A small decline in heat capacity was observed at 59.91°C which could have been due to molecular re-arrangement. This was followed by an increase in heat capacity at 71.91°C to 95.91°C characteristic of a glass transition. At 98.91°C heat capacity dramatically decreased characteristic of cold crystallization. In this sample, it can be assumed that this first glass transition event identified in Qi-MTDSC

experiments corresponds to the glass transition of sucrose. The small decrease in heat capacity observed at 59.91°C is likely to correspond to molecular re-arrangement of sucrose molecules towards its more stable crystalline form. However, the presence of trehalose molecules (with increased molecular mobility as it approaches its T_g) could have further slowed molecular mobility of sucrose molecules and therefore delaying re-arrangement to its crystalline form. The second glass transition observed is assumed to be the glass transition of amorphous trehalose.

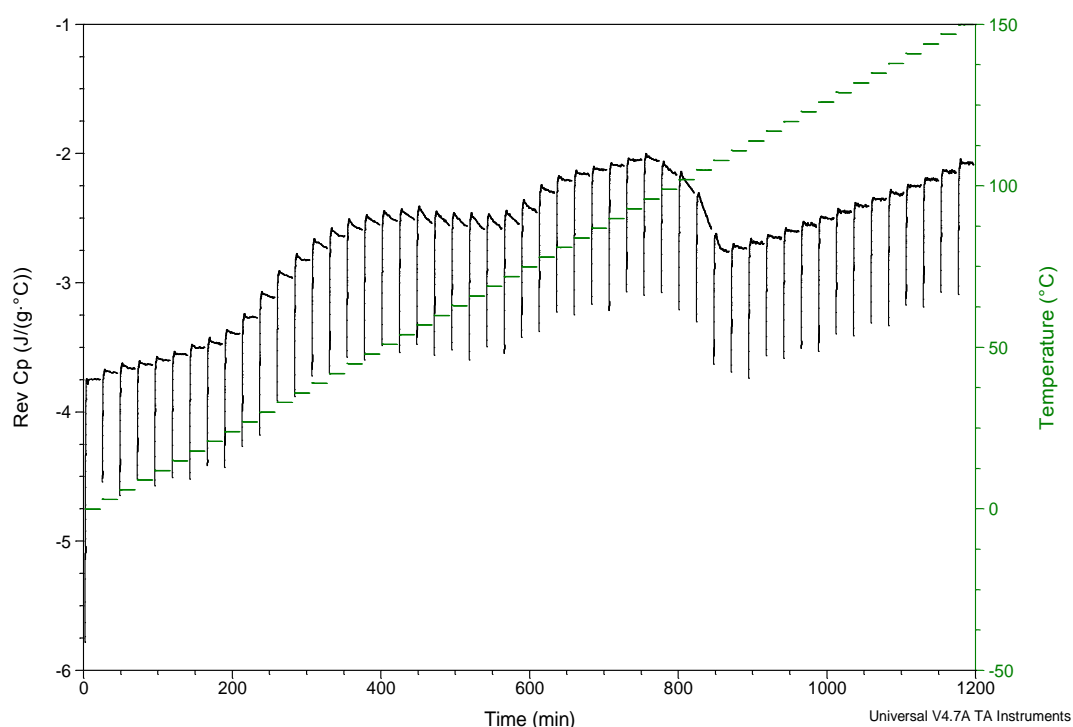


Figure 5.34 Typical Qi-MTDSC reversing heat capacity (as a function of time) signal of ST2.5 at a temperature modulation of $\pm 1^\circ\text{C}$, 20 minute isothermal periods with 2°C increments using a pin-holed pan

Qi-MTDSC experiments conducted on ST4 and ST5.26 both depicted in *Figure 5.35a* and *b* saw an increase in heat capacity characteristic of a glass transition at 68.91°C to 83.92°C and 68.97°C to 89.98°C respectively. This was followed by a dramatic decrease in heat

capacity characteristic of a cold crystallisation event at 107.91°C and 101.98°C respectively.

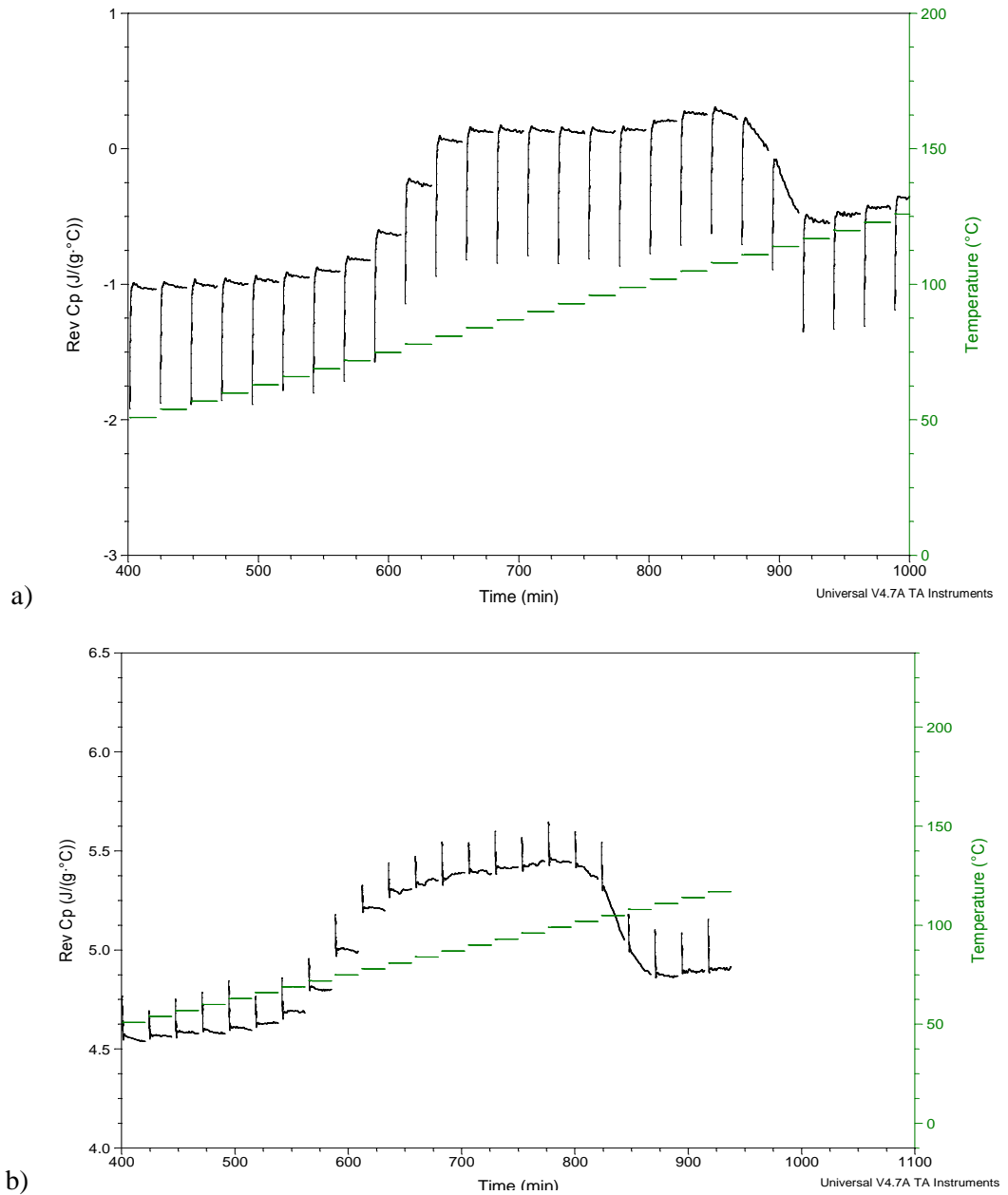


Figure 5.35 Typical Q_i -MTDSC reversing heat capacity (as a function of time) signal at a temperature modulation of $\pm 1^\circ\text{C}$, 20 minute isothermal periods with 2°C increments for a) ST4 b) ST5.26 using a pin-holed pan

Qi-MTDSC experiments conducted on ST11.11 (Figure 5.36) showed evidence of two glass transition events similar to observe trend in ST2.5 samples. An increase in heat capacity was observed at 65.92°C to 86.98°C, followed by another increase at 92.98°C to 110.98°C. A change in heat capacity was not observed until a gradual decrease at 122.99°C to 134°C. The first glass transition event was attributed to the glass transition of amorphous sucrose whilst the second event was attributed to the glass transition of amorphous trehalose.

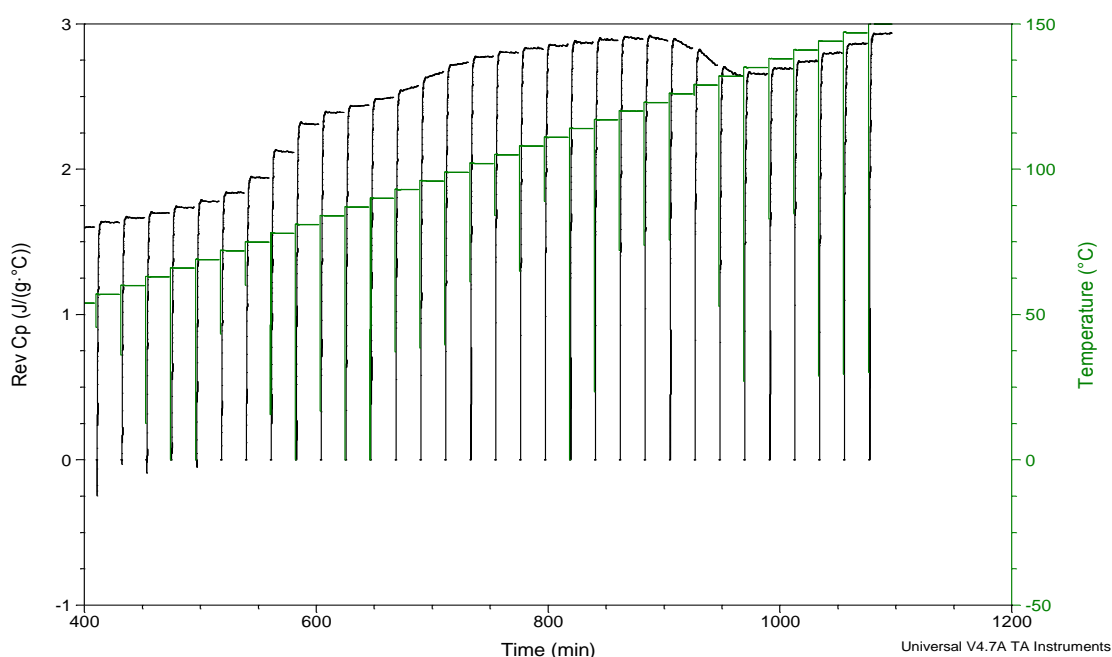


Figure 5.36 Typical Qi-MTDSC reversing heat capacity (as a function of time) signal of ST11.11 at a temperature modulation of $\pm 1^\circ\text{C}$, 20 minute isothermal periods with 2°C increments using a pin-holed pan

Qi-MTDSC experiments conducted on SR2.5 and SR5.26 (Figure 5.37 a and b) both saw similar responses an increase in heat capacity characteristic of a glass transition was observed at 14.92°C to 47.91°C and at 62.96°C to 80.97°C respectively. This was followed by a decrease in heat capacity occurring at 50.91°C to 68.91°C for SR2.5 and 113.98°C to 122.99°C for SR5.26 samples.

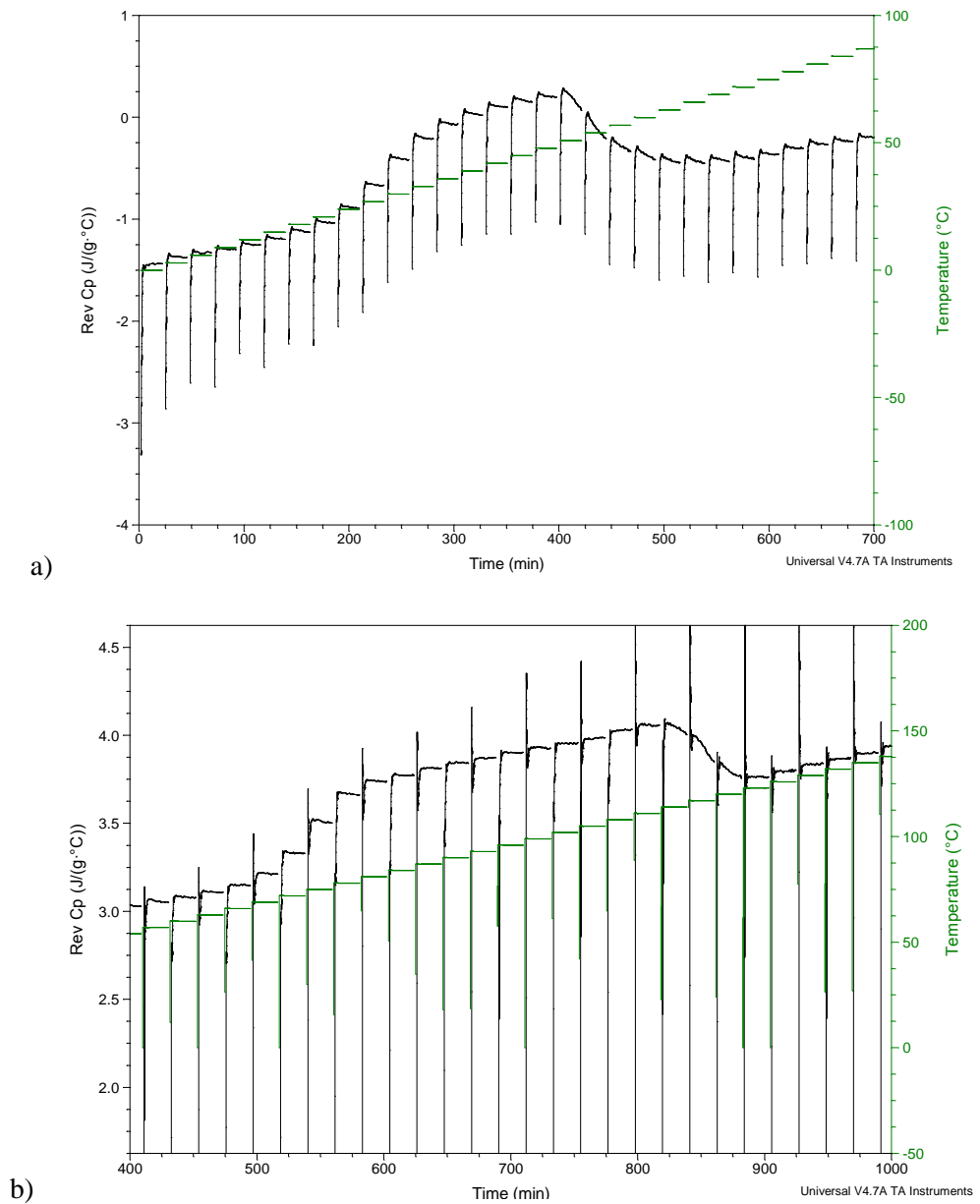


Figure 5.37 Typical *Qi*-MTDSC reversing heat capacity (as a function of time) signal at a temperature modulation of $\pm 1^\circ\text{C}$, 20 minute isothermal periods with 2°C increments for a) SR2.5 b) SR5.26 using a pin-holed pan

SR4 thermal profile obtained from *Qi*-MTDSC experiments (Figure 5.38), displayed evidence of two glass transitions occurring before crystallisation. The first was observed by an increase in heat capacity at 32.95°C to 68.97°C and another at 74.97°C to 83.98°C .

Further increase in heat capacity was observed to 110.99°C, which was then followed by a dramatic decrease in heat capacity at 113.99°C.

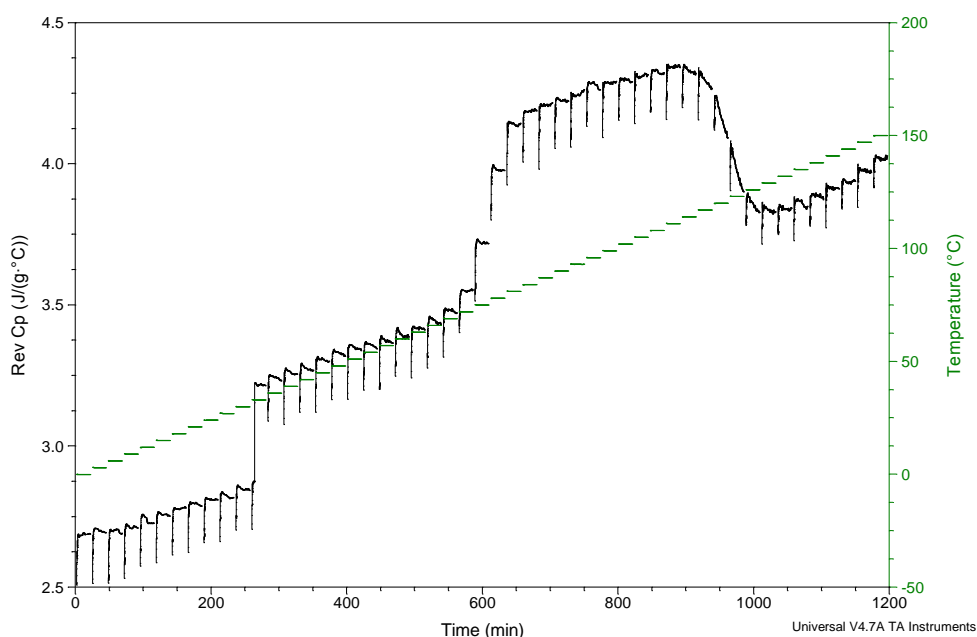


Figure 5.38 Typical Qi-MTDSC reversing heat capacity (as a function of time) signal of SR4 at a temperature modulation of $\pm 1^\circ\text{C}$, 20 minute isothermal periods with 2°C increments using a pin-holed pan

SR11.11 thermal profile obtained from Qi-MTDSC experiments (Figure 5.39) proved intriguing, an increase in heat capacity was observed at 11.93°C to 20.94°C after which no further changes in heat capacity were identified. These results did not confirm the presence of a crystallisation event.

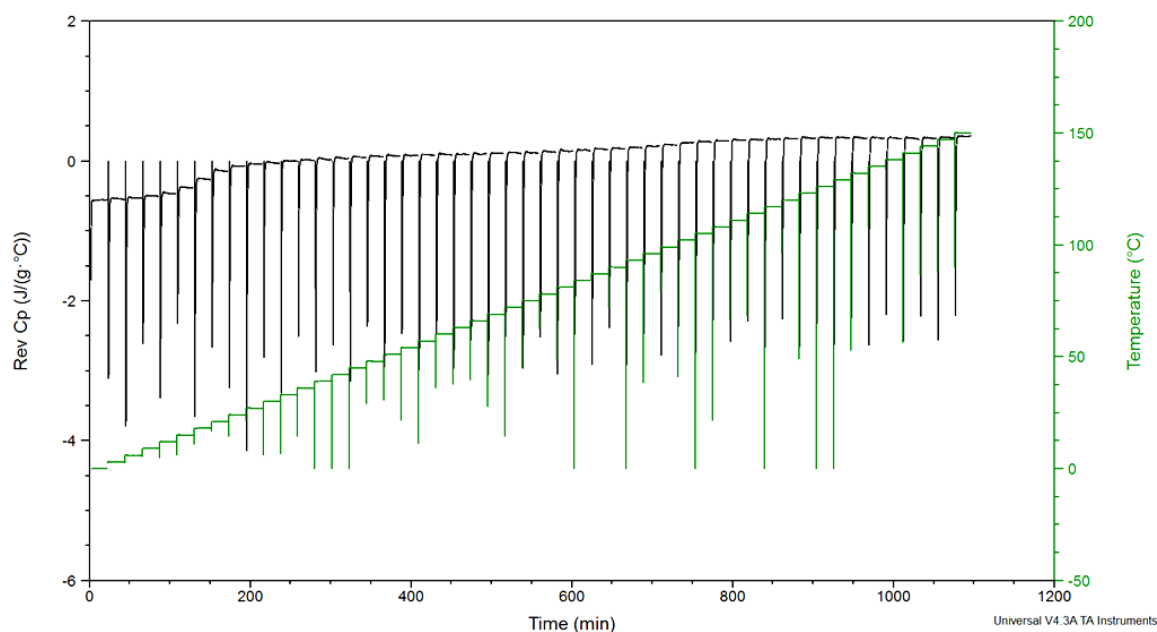


Figure 5.39 Typical Qi-MTDSC reversing heat capacity (as a function of time) signal of SR11.11 at a temperature modulation of $\pm 1^\circ\text{C}$, 20 minute isothermal periods with 2°C increments using a pin-holed pan

In this section Qi-MTDSC experiments were conducted on all samples to identify if co-spray dried samples existed as a single mixed amorphous system (indicated by a single glass transition event) or if the sugars co-existed as separate amorphous phases (indicated by the observation of two glass transition events).

Qi-MTDSC experiments identified that the following samples as existing in separate amorphous phases ST2.5, ST11.11 and SR4 indicated by the identification of two glass transition events. Qi-MTDSC experiments were also able to confirm the absence of a crystallisation event in SR11.11 samples. These promising results propose low nucleation rates in SR11.11 samples compared to other samples generated. This phenomenon has been observed elsewhere (Salekigerhardt and Zografis, 1994), where raffinose at 10% additive (equivalent to 6.8mol %) showed no indication of crystallisation.

5.3 CONCLUSION

In the previous chapter (*Chapter 4*), the physico-chemical properties of the amorphous samples generated was determined. These findings prompted this study whereby sucrose was co-spray dried with sugar additives, trehalose and raffinose. The main objective of this study was to investigate the use of the fragility parameter m and the strength parameter D as potential predictors of physical stability of generated co-spray dried samples.

ΔE_{T_g} values obtained from DSC experiments saw a general trend with increasing percentage of sugar additive (trehalose and raffinose). ΔE_{T_g} values were reduced from 412kJ/mol in pure amorphous sucrose samples to 204kJ/mol for ST11.11 and 161kJ/mol for SR11.11. ΔE_{T_g} values were then used to calculate the fragility parameter (m) (*Equation 5.1*) and strength parameter (D) (*Equation 5.2*).

Both m and D parameters indicated that both SR11.11 and ST11.11 were the strongest glass formers and would therefore be associated with greater amorphous sucrose stability.

Qi-MTDSC experiments identified that the following samples as existing in separate amorphous phases ST2.5, ST11.11 and SR4 indicated by the identification of two glass transition events. These results suggest this property may play a role in impeding crystallisation of amorphous sucrose. Though, further studies would be required to confirm this. Qi-MTDSC experiments also saw the absence of a crystallisation event in SR11.11 samples.

In conclusion, in this study the potential for raffinose and trehalose to improve the stability of amorphous sucrose has been examined. m , D were used as theoretical predictors of amorphous stability. Addition of both trehalose and raffinose appeared to improve predicted amorphous stability with greatest effect at the highest concentrations.

CHAPTER SIX

**OBSERVING THE ABILITY OF TREHALOSE,
RAFFINOSE AND SUCROSE TO PREVENT
DEGRADATION OF SPRAY DRIED PLASMID DNA**

6.1 BACKGROUND

Results in the previous chapter showed that addition of trehalose and raffinose improved predicted stability of amorphous sucrose formulations. In this chapter the potential for these sugar-based formulations in preserving the structural integrity of spray dried pDNA was explored.

Systemic delivery of a biopharmaceutical by pulmonary delivery allows for rapid and predictable onset of action, avoidance of first-pass hepatic metabolism and degradation within the gastrointestinal tract. This approach is particularly suitable for the treatment of localised pulmonary diseases (e.g. chronic obstructive pulmonary diseases) as lower dosages are required compared to the oral route, therefore potential side effects are reduced (Kuruba et al., 2009; Timsina et al., 1994).

Spray-drying can be used to develop biopharmaceutical particles for the pulmonary delivery. Spray-drying nucleic acids runs the risk of loss of biological activity, sample instability as well as thermal degradation, as a result of shearing stresses in the spray drying nozzle (Levy et al., 1999). A temperature difference of approximately 15°C exists between the hot drying air and droplet surface, therefore the temperature experienced by the droplets is generally lower than the temperature of the drying air. This is due to evaporative cooling (Shoyele and Cawthome, 2006).

Carbohydrates such as raffinose and trehalose have the ability to stabilize and protect biological molecules (Quaak et al., 2010; Li et al., 2005). The protective properties of

these non-condensing agents have been ascribed to both specific and kinetic effects. At a specific level, they interact with biological structures and stabilise them during drying. During the drying process, hydrogen bonds between bio-molecules and sugar replace essential water molecules therefore retaining the structure of the biological molecule. At the kinetic level, these sugars form an amorphous matrix surround the bio-molecules influencing the kinetics of reactions responsible for its deteriorations during storage (Schebor et al., 2010).

6.2 STUDY OBJECTIVE

The first object in this study was to evaluate the percentage degradation of pDNA spray dried in the presence of trehalose, raffinose and HPMC. Within this objective the effects of trehalose, raffinose and HPMC on A549 cells was explored by performing an MTT assay. A549 cells were used as pDNA formulations generated were intended for pulmonary delivery therefore it is important to ensure the materials used did not cause any cell cytotoxicity. Transfection studies were then performed using A549 cells and HeLa cells.

The second objective of this study was to evaluate the percentage degradation of pDNA spray dried in the presence of sucrose, SR2.5, SR11.11, ST2.5 and ST11.11 formulations designed in *Chapter 5*. Sucrose, trehalose and raffinose are well known cryoprotectants, therefore, it was expected that the addition of trehalose and raffinose to sucrose formulations would enhance the overall protective ability of spray dried pDNA minimising DNA degradation caused by the spray drying process.

6.3 METHODOLOGY

pDNA was extracted, purified and quantified as detailed in *Chapter 2*. Purified pDNA was obtained as a concentration of 2.17mg/mL and 1.92mg/mL with a purity assessed by its A260/A280 ratio of 1.92 and 1.91 respectively. 100µg pDNA was co-spray dried with a 10% w/v aqueous solution of HPMC (inert, non-protective carrier for pDNA), raffinose, trehalose, sucrose, ST2.5,11.11 and SR2.5,11.11 samples using the following parameters: inlet temperature of 125°C an average pump flow rate of 3.7mL/min, 100% aspirator setting and an outlet temperature ranging from 60-80°C (not controlled).

Spray-dried pDNA powder samples were stored at -20°C prior to analysis. After spray drying, powders were dissolved in sterile deionised water and an amount equivalent to 1µg of pDNA was cut using *StuI*, *HindIII*, *BamH* and *NotI* restriction enzymes resulting in 5 DNA fragments of 2780, 2000, 1200, 600 and 700 base pairs. pDNA digests were subjected to gel electrophoresis using 2% agarose gels to separate pDNA fragments. Gels were visualised using a G:Box gel imaging system, and were analysed using GeneTools version 4.01 and ImageJ 1.45s. ImageJ was used to evaluate percentage degradation by densitometric analysis of the ethidium bromide stained DNA bands from spray dried pDNA formulations relative to equal amounts of extracted pDNA (pDNA not subjected to spray drying) processed in an identical manner.

6.4 RESULTS AND DISCUSSION

6.4.1 MTT ASSAY AND TRANSFECTION STUDIES

MTT assays was conducted using trehalose, raffinose (1, 3, 5 and 10%w/v) and HPMC solutions (0.2, 0.6, 1 and 2%w/v) to determine if these materials had any effect on cell viability (24hour MTT exposure). Full details of this technique are outline in *Chapter 2*, MTT assay plate are shown in *Appendix 2.3 (Figure A.2)* and graphical presentation of results are depicted in *Figure 6.1*.

MTT assay results saw that each of the three excipients (trehalose, raffinose and HPMC) exerted concentration dependent cytotoxicity as demonstrated by reductions in the mitochondrial reduction of the MTT probe. Of the three excipients tested HPMC was the most potent at reducing cell viability. The application of 0.2% w/v HPMC causing a ~35% reduction in cell viability, increasing to a ~70% reduction by the 2% w/v solution. The application of 1% w/v raffinose and trehalose caused a ~23% and ~14% reduction in cell viability which increased to ~65% and ~69% reduction by 10%w/v solutions respectfully.

Observation of cells under the microscope after 48hours exposure did not however show any visible evidence of cell death. This indicates that the nature of the cytotoxicity was subtle enough to disrupt the mitochondrial integrity of the A549 cells but was insufficient to cause gross damage to the cells which can cause cell detachment. To date there is not literature evidence available to support these findings in this study.

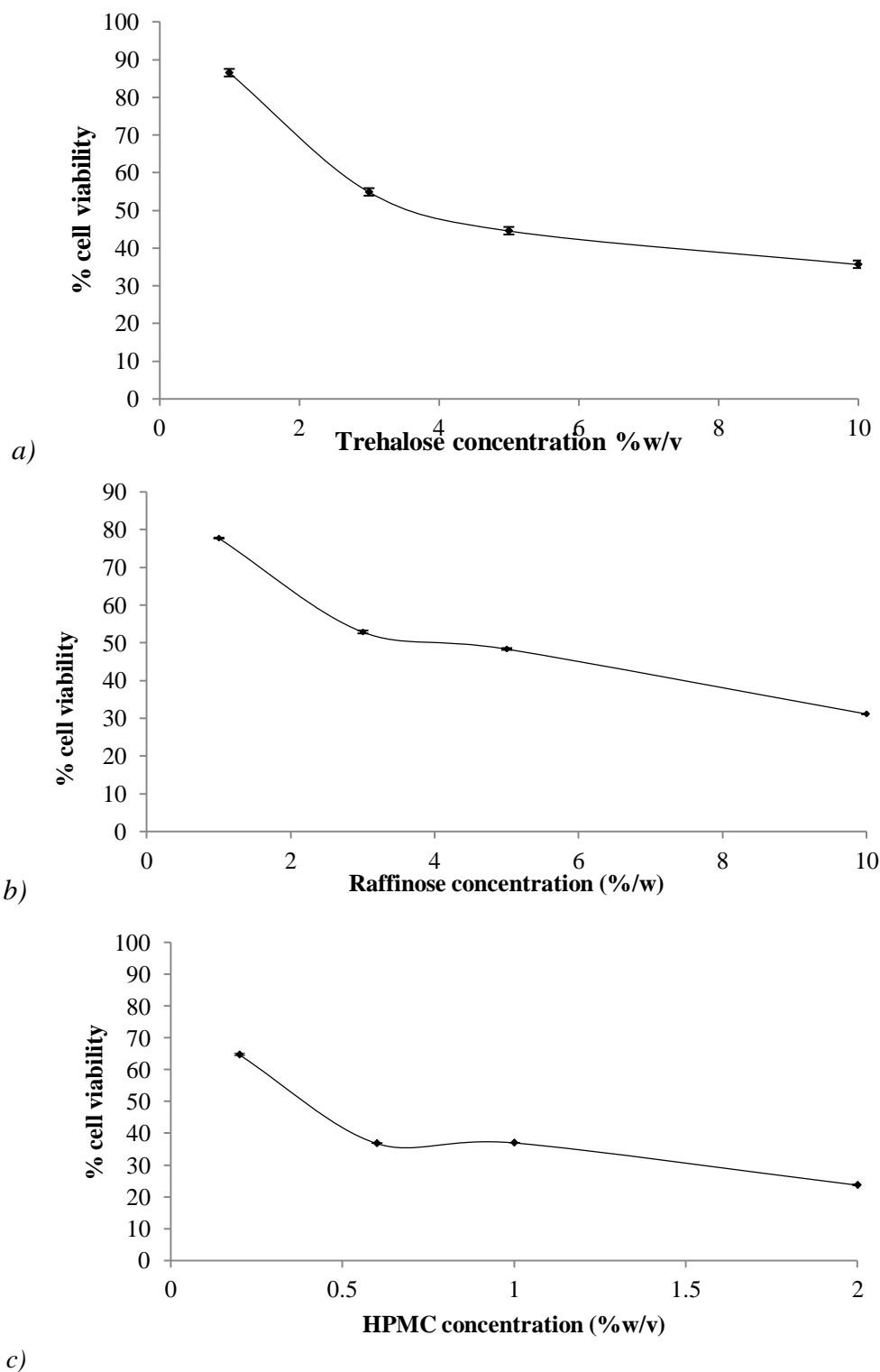


Figure 6.1 Cytotoxicity of a) trehalose b) raffinose and c) HPMC on A549 cells (24hour MTT exposure) assessed by MTT assay. The % cell viability was compared to control cells ($n = 3$, error bars represent standard deviation of mean)

Transfection studies performed using the cancerous lung epithelial cell line, A549 (method used detailed in *Appendix 2.5*) did not prove successful (*Figure 6.2a*). The faint green color in *Figure 6.2a* is due to cellular autofluorescence which is commonly observed at high laser power and long exposure times.

Identical transfection experiments performed using the non-pulmonary HeLa cell line (*Appendix 2.6*) proved successful with the addition of sodium butyrate which can be added to increase the efficiency of a transfection (Goldstein et al., 1989)(*Figure 6.2b*). Application of 10 μ g of pEGFP Arrestin 2 (control) at a total pDNA dose per well of 3.3 μ g gave a low transfection efficiency as evidenced by a low number of GFP positive cells (green in *Figure 6.2b*). Application of 10 μ g of pEGFP Arrestin 2 spray dried at 125 $^{\circ}$ C inlet temperature in the presence of trehalose (total pDNA dose per well of 3.3 μ g) gave a low transfection efficiency as well as evidence of cellular autofluorescence (*Figure 6.2c*). Application of 10 μ g of pEGFP Arrestin 2 spray dried at 125 $^{\circ}$ C inlet temperature in the presence of either raffinose or HPMC (*Figure 6.2d* and *6.2e*) did not show any evidence of transfection. However, both samples showed evidence of cellular autofluorescence.

These results suggested pEGFP Arrestin 2 spray dried at 125 $^{\circ}$ C inlet temperature in the presence of trehalose retained its biological functionality as opposed to pEGFP Arrestin 2 spray dried in the presence of raffinose and HPMC.

Further transfection experiments were not conducted due to time restrictions.

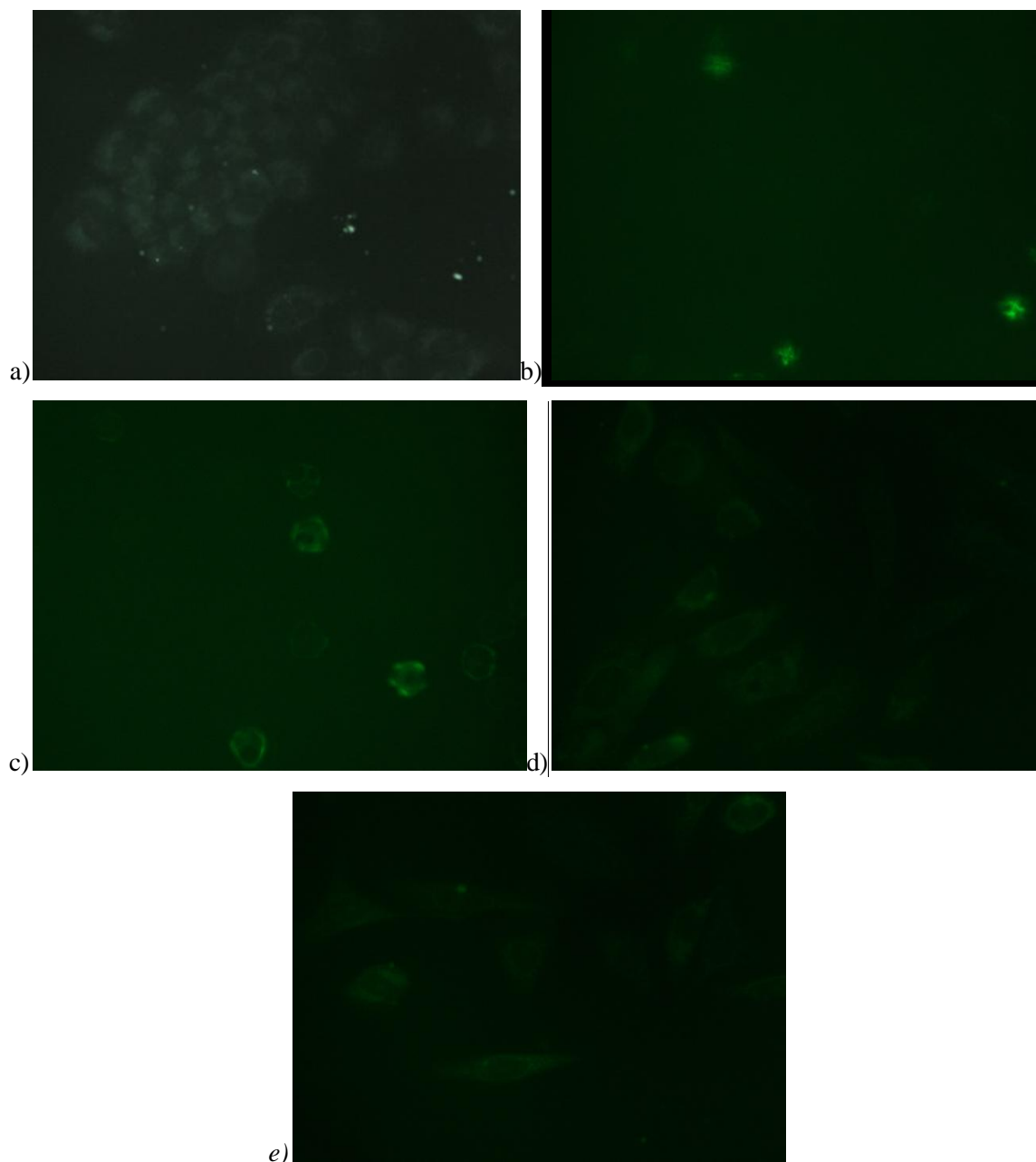


Figure 6.2 a) Showing unsuccessful transfection studies using A549 cells (control using 10 μ g of pEGFP Arrestin 2) showing non-specific fluorescence b) Showing successful transfection of HeLa cells (control using 10 μ g of pEGFP Arrestin 2) showing low transfection efficiency c) Showing successful transfection of HeLa cells using 10 μ g of pEGFP Arrestin 2 spray dried in the presence of 10%w/v trehalose d) Showing unsuccessful transfection studies using HeLa cells 10 μ g of pEGFP Arrestin 2 spray dried in the presence of 10%w/v raffinose e) 10 μ g of pEGFP Arrestin 2 spray dried in the presence of 2%w/v HPMC

6.4.2 CO-SPRAY DRYING pDNA WITH TREHALOSE AND RAFFINOSE AT 125°C

Figure 6.3 shows 2% agarose gel electrophoresis of spray dried powders containing linearized pEGFP-Arrestin-2 by digestion with restriction enzymes. By this process pDNA was cut into 5 DNA fragments of 2780, 2000, 1200, 600 and 700 base pairs. Analysis of data in this manner was chosen to assess the full effects of the spray drying process on the pDNA molecule.

The band seen at 2780 bp was visible in all samples, the 2000 bp band was visible in all formulations (at a greatly reduced intensity with pDNA co-spray dried with HPMC) except for pDNA co-spray dried with raffinose the bands at 1200, 600 and 700 bp were all visible in all formulations albeit at varied intensities. The band at 2000 bp not observed in pDNA co-spray dried in the presence of raffinose was suspected to be due to insufficient digest as the band seen at 2780bp had a stronger than expected intensity. These results indicated that pDNA was degraded by the spray drying process at 125°C when observing differences between lanes 1 to 3 and lane 4 (pDNA without spray drying).

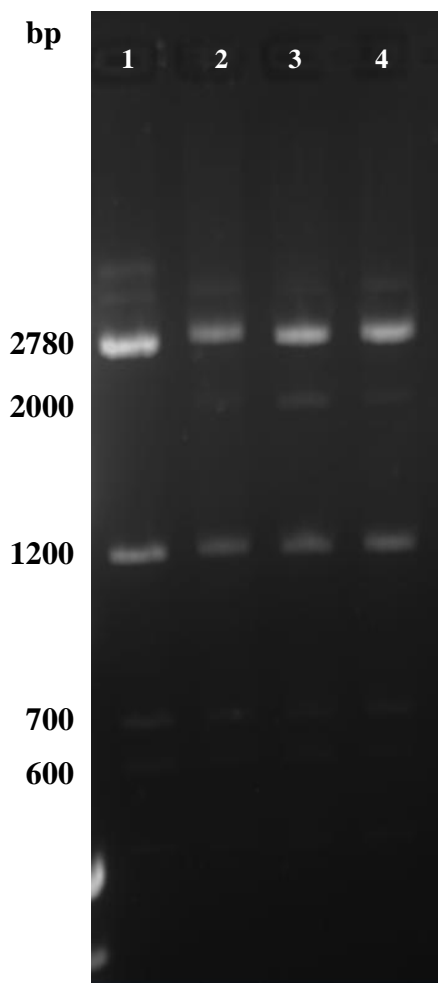


Figure 6.3 2% agarose gel electrophoresis of spray dried powders containing linearized pEGFP-Arrestin-2 by digestion with restriction enzymes. Lane 1 Raffinose co-spray dried with pDNA Lane 2 HPMC co-spray dried with pDNA; Lane 3: Trehalose co-spray dried with pDNA and Lane 4 pEGFP Arrestin 2 (without spray drying) at 125°C

ImageJ was used to evaluate percentage degradation by densitometric analysis of the ethidium bromide stained DNA bands from spray dried pDNA formulations relative to equal amounts of extracted pDNA (pDNA not subjected to spray drying) processed in an identical manner. These results were then calculated as percentage degradation (% degradation). In this study, HPMC was co-spray dried with pDNA where it was used as a carrier for pDNA as spray drying pDNA alone did not result in visible particles in the

spray drying collecting chamber. This is likely to be due to low mass (500 μ g of extracted pEGFP Arrestin 2 pDNA) used.

At 125 $^{\circ}$ C inlet temperature (Figure 6.4) 53% of pDNA co-spray dried with HPMC was degraded. Addition of both trehalose and raffinose reduced the percentage degraded from 53% (HPMC control) to 22% (trehalose) and 30% (raffinose).

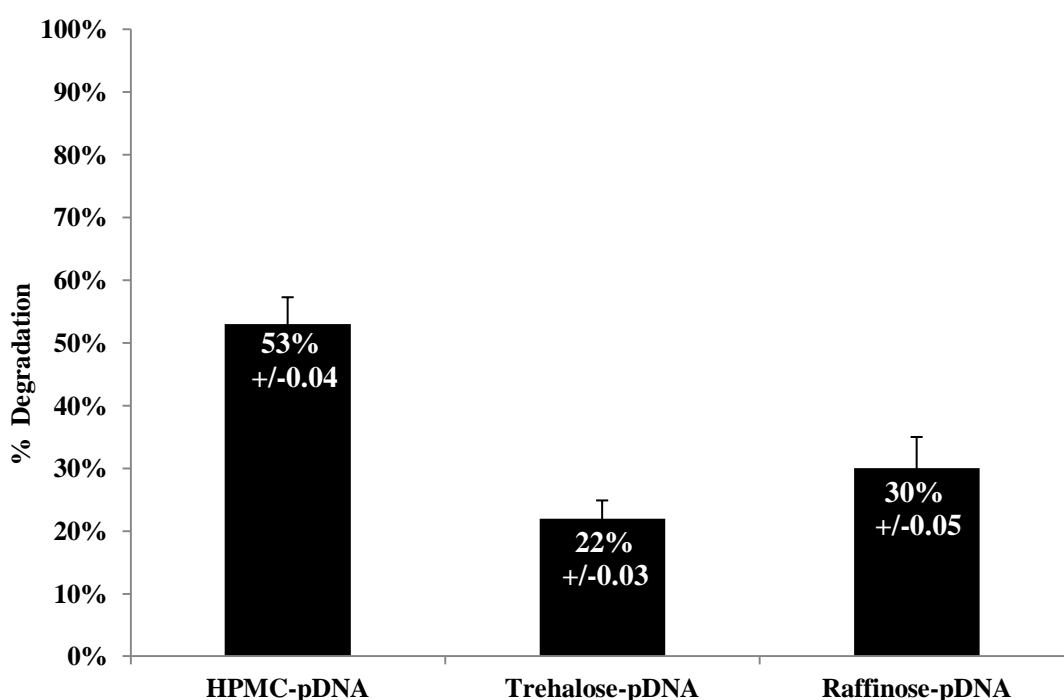


Figure 6.4 Degradation of pDNA co-spray dried with HPMC, trehalose and raffinose at 125 $^{\circ}$ C spray drying inlet temperature ($n = 3$, error bars represent standard deviation of mean).

As discussed earlier, spray drying nucleic acids like pDNA can result in loss of biological activity and thermal degradation as a result of shearing stressing in the spray drying nozzle. These promising results indicate that co-spray pDNA in the presence of either trehalose and raffinose offered protection ($\sim 78\%$ trehalose, $\sim 70\%$ raffinose) and reduced pDNA

degradation to a greater extent than in the presence of HPMC which in this study was used as a carrier of pDNA and was not expect to possess any protective properties.

6.4.3 CO-SPRAY DRYING SR2.5, SR11.11, ST2.5 AND ST11.11 WITH PDNA AT 125°C

Figure 6.5 shows 2% agarose gel electrophoresis of spray dried powders containing linearized pEGFP-Arrestin-2 by digestion with restriction enzymes. By this process pDNA was cut into 5 DNA fragments of 2780, 2000, 1200, 600 and 700 base pairs. A band was visible in all sucrose, ST and SR samples at 2780bp at varied intensities. SR2.5, ST11.11 and SR11.11 co-spray dried formulations had faint bands visible at 1200bp. No other bands were visible in formulation digests.

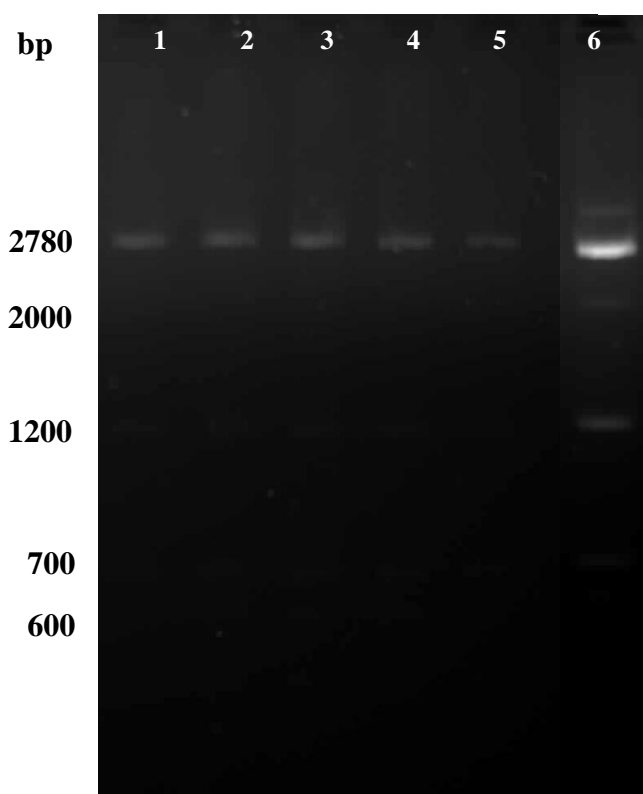


Figure 6.5 2% agarose gel electrophoresis of spray dried powders containing linearized pEGFP-Arrestin-2 by digestion with restriction enzyme. Lane 1 Sucrose co-spray dried with pDNA; Lane 2 ST2.5 co-spray dried with pDNA; Lane 3 ST11.11co-spray dried with pDNA; Lane 4 SR2.5co-spray dried with pDNA; Lane 5 SR11.11co-spray dried with pDNA and Lane 6 pEGFP Arrestin 2 (without spray drying) at 125°C

As with previous studies detailed in this Chapter, ImageJ was used to evaluate percentage degradation by densitometric analysis of the ethidium bromide stained DNA bands from spray dried pDNA formulations relative to equal amounts of extracted pDNA (pDNA not subjected to spray drying) processed in an identical manner. These results were then calculated as percentage degradation (% degradation) and are presented in *Figure 6.6*. It can clearly be seen that pDNA spray dried in the presence of sucrose, ST and SR formulations did not prevent pDNA degradation as effectively as trehalose and raffinose alone. pDNA spray dried in the presence of sucrose saw 90% degradation. Addition of ST and SR formulations appeared to reduce this with SR11.11 formulations showing 80% degradation compared to 90% seen with sucrose formulations. Surprisingly, HPMC appeared to prevent pDNA degradation at a greater extent (53% degradation) than sucrose, ST and SR formulations. This was not expected as HPMC was used as a carrier for pDNA and was not expected to exert a protective property as there are no literature reports of this phenomenon.

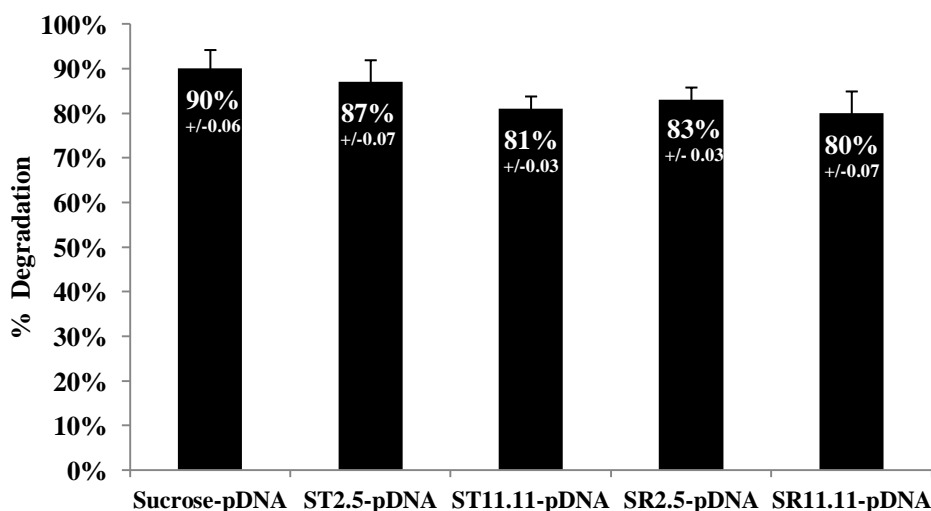


Figure 6.6 Percentage degradation plot of sucrose, ST2.5, SR2.5, ST11.11 and SR11.11 co-spray dried with pDNA at 125 °C spray drying inlet temperature ($n = 3$, error bars represent standard deviation of mean)

Previous studies observing the effects of sucrose (Kuo, 2003; Quaak et al., 2010) and trehalose (Quaak et al., 2010) at higher concentrations (~20%-30%) used compared to in this study, have illustrated the use of these sugars in protecting pDNA. However, experiments conducted by Quaak et al., (2010) involved the assessment of the effect of disaccharides on naked pDNA stability after freeze-drying. Kuo, (2003) co-spray dried pCMV-luc (a plasmid which contains the luciferase reporter gene under the control of the CMV promoter) with 20%w/v or 30%w/v sucrose solutions and observed the effects the outlet temperature (at 56, 69, 94 and 122°C) had on the structural integrity of the pDNA used. Results in their study saw the integrity of pDNA was changed by the spray-drying process even when spray drying outlet temperature was decreased to 56°C. In this study the outlet temperature was not controlled as this function was not available on the spray dryer used. However, direct comparisons between their results and results detailed in this chapter are not possible as the inlet temperature used in Kuo, (2003) study was not stated.

6.5 CONCLUSION

The first object in this study was to compare the ability of raffinose and trehalose to prevent plasmid DNA (pDNA) degradation of spray dried DNA. Within this objective the effects of trehalose, raffinose and HPMC on A549 cells was explored by performing an MTT assay as well a transfection studies using A549 cells and HeLa cells.

The second objective of this study was to co-spray drying pDNA with sucrose, SR2.5, SR11.11, ST2.5 and ST11.11 formulations designed in *Chapter 5*. Sucrose, trehalose and raffinose are well known cryoprotectants it was expected that the addition of trehalose and

raffinose to the sucrose formulation would enhance its protective function over spray dried pDNA and therefore minimising DNA degradation caused by the spray drying process.

Results from the MTT assay performed on A549 cells using trehalose, raffinose and HPMC solutions suggested reduction in cell viability with increasing concentration of all three materials. Transfection studies were attempted with A549 cells however, did not prove successful. Transfection studies using non-pulmonary HeLa cell line proved successful. These results saw transfection efficiency in pDNA spray dried in the presence of trehalose however, transfection efficiency was not observed in pDNA spray dried in the presence of raffinose or HPMC. The results detailed in this study have shown that spray drying pDNA in the presence of sucrose, raffinose, trehalose and surprisingly HPMC results in a prevention of pDNA degradation though, this occurs to a greater extent with trehalose and raffinose. pDNA spray-dried in the presence of sucrose, SR and ST formulations did not show ideal characteristics as % degradation was greater in these samples than with trehalose, raffinose and HPMC. Prevention of pDNA degradation of pDNA spray dried in the presence of HPMC appeared

CHAPTER SEVEN

THESIS CONCLUSIONS AND RECOMMENDATIONS

FOR FUTURE WORK

7.1 THESIS CONCLUSIONS

The overall aim of the research detailed in this thesis was to design and analyze sugar-based (trehalose, raffinose and sucrose) carrier systems for the protection of naked pDNA formulations generated by spray drying. The work detailed in this thesis was composed of three main areas.

The first area (detailed in *Chapter 3*) focused on investigating the inter-conversion properties of trehalose dihydrate to observe if an in-depth understanding of its physical properties will provide an insight into its bio-protective properties. Within this area, the first objective addressed the influence of inter-batch variation on the thermal response of trehalose dihydrate. The influences of batch variation of trehalose dihydrate had been briefly explored by Armstrong et al., (1996) where results showed that whilst sample presentation and experimental conditions could influence the thermal response, sample origin can also have affect on the crystal texture and consequently the observed thermal response. At the time of this thesis further studies investigating the thermal transitions of α,α -trehalose dihydrate had not taken into account the possible contribution of inter-batch or intra-batch variations contributing to the thermal response. Only preference in purchasing choice had briefly been addressed by Macdonald and Johari (2000). In *Chapter 3, Section 3.2*, a series of thermal, spectroscopic and X-ray diffraction techniques were conducted on three α,α -trehalose dihydrate batches obtained from two different manufacturers, Sigma-Aldrich (Sigma A and Sigma B) and Acros Organics (Acros batch). The results showed that a high level of inter-batch variability existed between trehalose dihydrate batches tested. Results obtained showed that Sigma B and Acros batches differed from Sigma A particles. XRPD data suggested structural variations between the

batches indicating that the crystalline structure of the batches were not entirely similar. Overall, physico-chemical characterisation of batches did not shed light on reason for batch variability. Differences observed in this study could have been due to the raw materials used, manufacturing process or impurities un-detectable using spectroscopic and thermal techniques.

A recent review (Ohtake and Wang, 2011) on the use of trehalose suggested that the purification process of trehalose dihydrate is related to its intended use. With purification of trehalose for use in food applications lower than that intended for pharmaceutical products. Variations in the levels of purity can increase the presence of impurities like arsenic, heavy metals, microbes, reducing sugars and endotoxin (Ohtake and Wang, 2011). Special attention is required if the raw materials are produced from a tapioca source (starch extracted from cassava native to South America), as there is risk that cyanide may be present.

Inter-batch variability is an issues if the variability has a significant impact on data interpretation or (if used as part of a formulation) if these difference would have a significant impact on formulation performance. Investigating the latter was outside the objectives of this study; however, results in this section did show that inter-batch variability had an impact on data interpretation of the properties of trehalose dihydrate. These intriguing results illustrated the effect inter-batch variability could have on data interpretation. It was concluded that in order to have a clearer understanding of the thermal transitions α,α -trehalose dihydrate standardised forms where required to eliminate

any processing effects and produce reproducible data providing clearer insight into the thermal transitions of α,α -trehalose dihydrate not influenced by inter-batch variations.

The second objective (based on results from *Chapter 3, Section 3.2*) was to generate and characterise two standardised forms of α,α -trehalose dihydrate by performing a series of thermal, spectroscopic and X-ray diffraction techniques. This work described in *Chapter 3, Section 3.3*, led to the identification of a polymorphic form of α,α -trehalose dihydrate which was characterised and is described in *Chapter 3, Section 3.3.4.5*

The main objective of this section was to generate standardised forms of trehalose dihydrate and characterise samples with an aim to gain a further and clearer understanding of the thermal transitions of trehalose dihydrate with a focus on the transitions that occur between 30°C to 160°C. The results detailed in this study showed that the two standardised forms generated had different thermal responses. Dehydration of T_{h1} resulted in structural collapse leading to the generation of an amorphous form. Further heating lead to the re-crystallisation of T_{β} confirmed by the subsequent melt at ~210°C. In contrast, dehydration of T_{h2} resulted in the structural collapse and molecular re-arrangement to T_{hx} further heating resulted in generation of an amorphous liquid. The discovery of T_{hx} which appeared to be an anhydrate (possible T_{α} and T_{β}) and amorphous mixture (from XRPD data) confirmed the existence of an intermediary crystalline state with an XRPD profile that has not been identified in the literature. These promising results which were not influenced by inter-batch variability has provided a clearer understanding of the thermal transitions of trehalose showing two possible routes in which it can convert in a bid to protect delicate biological molecules

Sussich and Cesaro, (2008) used the time-temperature transition (TTT) principle to shed light on the biological relevance of the physical properties of trehalose. They propose that using this principle transformation time scales measured at high temperatures within a calorimeter have a counterpart in slower phenomena occurring at nature temperatures (Sussich and Cesaro, 2008). The TTT principle (is also referred to as the time-temperature superposition principle (TTS)) is well known in polymer science. First proposed by Lenderman (1943) and later further developed by Williams et al., (1955). The underlying principle is that processes involved in molecular relaxation or molecular re-arrangement in viscoelastic materials (like polymers) occur at faster rates at higher temperatures and are equivalent between time and temperature. Therefore the time which these processes occur can be reduced if the measurement is conducted at elevated temperatures and resultant data is transposed to lower temperatures. TTS appears to only be valid for materials with thermorheological simplicity like polymers (Dealy J and Plazek D, 2009). Therefore application of TTS to the thermal transitions of trehalose is questionable and not applicable as trehalose is not known to display thermorheological simplicity.

The findings in this study have an implication on both past and future experiments conducted on trehalose dihydrate. The findings in this thesis raise the question of the authenticity of previous results obtained with the identification of various anhydrous polymorphs. The future use of the standardised forms generated in this study will minimise variations in polymorphs identified. Like in the case of Nagase et al., who in 2002 reported the discovery of a new anhydrous polymorph T_K but later in 2008, concluded that T_K was identical to T_α though generated by a different route.

Within the second area of this thesis, the first objective described in *Chapter 4*, was to generate pure amorphous sugars (via spray drying) and characterise their physico-chemical properties using a range of diffraction, spectroscopic and thermal techniques. The second objective described in *Chapter 5*, was to investigate the use of the fragility parameter m and the strength parameter D as potential predictors of amorphous stability of generated co-spray dried samples. Quasi-Isothermal MTDSC (Qi-MTDSC) techniques were employed to observe if co-spray dried samples existed as one or two amorphous phases evident by the presence of either one or two glass transition events.

These results showed that the addition of both raffinose and trehalose had an overall positive effect on the predicted stability of amorphous sucrose formulations, with greatest effect at the highest concentrations. According to Qi-MTDSC data ST2.5, ST11.11 and SR4 existed in separate amorphous phases indicated by the identification of two glass transition events. These results intriguing results suggest this property may play a role in impeding crystallisation of amorphous sucrose. Qi-MTDSC experiments also saw the absence of a crystallisation event in SR11.11 samples.

It was concluded that ST11.11 and SR11.11 formulations were the strongest glasses and therefore possessed greater amorphous stability.

The third area of this thesis was to evaluate the degree of degradation of plasmid DNA spray dried in the presence of amorphous sugars. Within this area (detailed in *Chapter 6*), the first objective was to evaluate the percentage degradation of plasmid DNA spray dried in the presence of trehalose and raffinose. The second objective was to observe the effects

of trehalose and raffinose on A549 cells was explored by performing an MTT assay. A549 cells were used as pDNA formulations generated were intended for pulmonary delivery therefore it is important to ensure the materials used did not cause any cell cytotoxicity. Transfection studies were then performed using A549 cells and HeLa cells. The third objective within this area was to evaluate the percentage degradation of pDNA spray dried in the presence of sucrose, SR2.5, SR11.11, ST2.5 and ST11.11 formulations designed in *Chapter 5*.

Results from the MTT assay performed on A549 cells using trehalose, raffinose and HPMC solutions suggested reduction in cell viability with increasing concentration of all three materials. Transfection of A549 cells was not successful, however, transfection in a non-pulmonary cell line (HeLa) cells was successful. Transfection of pDNA spray dried in the presence of trehalose in HeLa cells was successful.

The results detailed in this study have shown that spray drying pDNA in the presence of sucrose, raffinose, trehalose and surprisingly HPMC resulted in a prevention of pDNA degradation though, this occurs to a greater extent with trehalose and raffinose. The results obtained from this study indicated that co-spray drying pDNA with either trehalose or raffinose over sucrose could reduce thermal degradation and structural changes that can occur as a result of the spray drying process, though further formulation strategies and manipulation of processing parameters are required to optimize formulation.

Overall, two key messages can be concluded from the work detailed in this thesis. Firstly, the observed thermal transitions of α,α -trehalose dihydrate can be influenced by environmental factors as well as inter-batch variability which can affect the authenticity of polymorphous and amorphous forms identified. The use of the standardised forms generated in this study would result in a clearer understanding of the physical properties of trehalose dihydrate which could lead to a better understanding of its bio-protective properties.

Secondly, addition of raffinose and trehalose to amorphous sucrose formulations improved the predicted amorphous stability of the formulations. These promising results could have an effect on future formulation strategies involving amorphous sucrose stability. As previous work has focused on the ability of these additives to improve onset of crystallisation studies are yet to be conducted on the use of thermodynamic parameters to predict amorphous stability.

7.2 RECOMMENDATIONS FOR FUTURE WORK

Whilst conducting the experiments in this thesis possible areas for further research were highlighted. It was not possible to explore these areas as they were either outside the objectives of this thesis or beyond the scope of time available. Recommendations for future work have been categorised by chapter.

Chapter 3 – Generation and Characterisation of Standardised Forms of Trehalose Dihydrate

The majority of the work conducted on T_{h1} and T_{h2} was conducted on pin-holed pans, it would be of interest to repeat these experiments and compare the effect of pan type on the thermal response during slow heat/cool MTDSC experiments and Qi-MTDSC experiments. An investigation observing the effects of dehydrating T_{h1} and T_{h2} at temperatures correlating the occurrence of the low temperature endotherms observed in MTDSC traces could prove insightful.

Full characterisation of T_{hx} in the same manner as T_{h1} and T_{h2} would be essential in mapping out the inter-conversion process of trehalose.

Many studies conducted on trehalose dihydrate have been conducted on α,α -trehalose dihydrate. However, there are not many studies investigating the thermal transitions of α,β -trehalose an isomer of α,α -trehalose where two glucose molecules are linked through α - β 1 \rightarrow 1-glycosidic bond. α,β -trehalose can be obtained as a mono-hydrate or as an anhydrous crystal. It would be of interest and importance in understanding trehalose to characterize this isomer.

Chapter 5 – Use of Sugar Additives (trehalose and raffinose) to Improve the Stability of Amorphous Sucrose

Having predicted improved amorphous stability by addition of sugar additives, the next stage would be to compare predicted stability to actual stability. This would be conducted by evaluating the onset of crystallisation time in samples and performing stability studies over a period of time.

Chapter 6 - Observing the ability of sucrose, raffinose and trehalose to preserve the structural integrity of spray dried plasmid DNA

The results obtained in this preliminary study could prove insightful for future formulations. As the transfection protocol for A549 cells was not successful in this study future experiments could be adapted to use the transfection agent Lipofectamine[®] as opposed to using the electroporation method used in this study. Alternatively, formulations strategies could be employed to explore the addition of a cationic agent for example chitosan to improve stability as well as possibly aid transfection of pDNA into the cell.

Further experiments could be conducted using different spray drying parameters for example lowering the inlet temperatures. However, this might compromise formulation physical stability as reduced inlet temperatures would result in higher water contents leading to increased risk of crystallisation.

Once the ideal formulation has been identified for pulmonary delivery, it would be essential to conduct *in vitro* powder aerosolization and deposition characterisation. This would involve using a two-stage glass impinger used to represent the upper and lower respiratory tract and is used to assess drug delivery from a delivery device. In addition, cellular studies as a tool for biological evaluation of the formulation safety, stability and efficacy would be conducted. This will involve conducting an MTT assay and transfection studies using A549 cells.

REFERENCES

AHLQVIST, M. U. A. & TAYLOR, L. S. 2002. Water diffusion in hydrated crystalline and amorphous sugars monitored using H/D exchange. *Journal of Pharmaceutical Sciences*, 91, 690-698.

AIGNER, A. 2007. Applications of RNA interference: current state and prospects for siRNA-based strategies in vivo. *Applied Microbiology and Biotechnology*, 76, 9-21.

ALDOUS, B. J., AUFFRET, A. D. & FRANKS, F. 1995. THE CRYSTALLIZATION OF HYDRATES FROM AMORPHOUS CARBOHYDRATES. *Cryo-Letters*, 16, 181-186.

ANDERSON, W. F. 1984. PROSPECTS FOR HUMAN-GENE THERAPY. *Science*, 226, 401-409.

ANGELL, C. A. 1995. FORMATION OF GLASSES FROM LIQUIDS AND BIOPOLYMERS. *Science*, 267, 1924-1935.

ANGELL, C. A. 2002. Liquid fragility and the glass transition in water and aqueous solutions. *Chemical Reviews*, 102, 2627-2649.

ARMSTRONG, C. L., FORBES, R. T., BLAIR, J. & YORK, P. 1996. Thermal behaviour of alpha,alpha-trehalose dihydrate batches. *European Journal of Pharmaceutical Sciences*, 4, S181.

AULTON M E & TAYLOR, K. (eds.) 2001. *Pharmaceutics: The Science of Dosage Form Design* Churchill Livingstone.

AUTHELIN, J. R. 2005. Thermodynamics of non-stoichiometric pharmaceutical hydrates. *International Journal of Pharmaceutics*, 303, 37-53.

BADRINARAYANAN, P., ZHENG, W., LI, Q. & SIMON, S. L. 2007. The glass transition temperature versus the fictive temperature. *Journal of Non-Crystalline Solids*, 353, 2603-2612.

References

BAIRD, J. A., VAN EERDENBRUGH, B. & TAYLOR, L. S. 2010. A Classification System to Assess the Crystallization Tendency of Organic Molecules from Undercooled Melts. *Journal of Pharmaceutical Sciences*, 99, 3787-3806.

BATES, S., KELLY, R. C., IVANISEVIC, I., SCHIELDS, P., ZOGRAFI, G. & NEWMAN, A. W. 2007. Assessment of defects and amorphous structure produced in raffinose pentahydrate upon dehydration. *Journal of Pharmaceutical Sciences*, 96, 1418-1433.

BAUER, J., SPANTON, S., HENRY, R., QUICK, J., DZIKI, W., PORTER, W. & MORRIS, J. 2001. Ritonavir: An extraordinary example of conformational polymorphism. *Pharmaceutical Research*, 18, 859-866.

BECKETT, S. T., FRANCESCONI, M. G., GEARY, P. M., MACKENZIE, G. & MAULNY, A. P. E. 2006. DSC study of sucrose melting. *Carbohydrate Research*, 341, 2591-2599.

BERMAN, H. M. 1970. CRYSTAL STRUCTURE OF A TRISACCHARIDE, RAFFINOSE PENTAHYDRATE. *Acta Crystallographica Section B-Structural Crystallography and Crystal Chemistry*, B 26, 290-&.

BERTHOMIEU, C. & HIENERWADEL, R. 2009. Fourier transform infrared (FTIR) spectroscopy. *Photosynthesis Research*, 101, 157-170.

BHANDARI, B. R. & HARTEL, R. W. 2002. Co-crystallization of Sucrose at High Concentration in the Presence of Glucose and Fructose. *Journal of Food Science*, 67, 1797-1802.

BLOOMFIELD, V. A. 1991. Condensation of DNA by multivalent cations: Considerations on mechanism. *Biopolymers*, 31, 1471-1481.

BLOOMFIELD, V. A. 1996. DNA condensation. *Current Opinion in Structural Biology*, 6, 334-341.

References

BORDE, B., BIZOT, H., VIGIER, G. & BULEON, A. 2002. Calorimetric analysis of the structural relaxation in partially hydrated amorphous polysaccharides. I. Glass transition and fragility. *Carbohydrate Polymers*, 48, 83-96.

BRITISHPHARMACOPOEIA 2012. Volume V Appendix XVII B. Sieves and Filters. *In: PHARMACOPOEIA, B. (ed.) British Pharmacopoeia* British Pharmacopoeia

BROWN, G. M., ROHRER, D. C., BERKING, B., BEEVERS, C. A., GOULD, R. O. & SIMPSON, R. 1972. CRYSTAL-STRUCTURE OF ALPHA,ALPHA-TREHALOSE DIHYDRATE FROM 3 INDEPENDENT X-RAY DETERMINATIONS. *Acta Crystallographica Section B-Structural Science*, B 28, 3145-3158.

BRUKEROPTICS 2008. Fourier Transform Infrared Spectroscopy. *Bruker Optics*.

BÜCHI 2003. Training Papers Spray Drying. *In: AG, B. (ed.)*.

CESARO, A., DE GIACOMO, O. & SUSSICH, F. Year. Water interplay in trehalose polymorphism. *In: 4th International Workshop on Water in Foods, Mar 27-28 2006 Brussels, BELGIUM. 1318-1328.*

CHAMARTHY, S. P., KHALEF, N., TRASI, N., BAKRI, A., CARVAJAL, M. T. & PINAL, R. 2010. The effect of dehydration conditions on the functionality of anhydrous amorphous raffinose. *European Journal of Pharmaceutical Sciences*, 40, 171-178.

CHENG, W. T. & LIN, S. Y. 2006. Processes of dehydration and rehydration of raffinose pentahydrate investigated by thermal analysis and FT-IR/DSC microscopic system. *Carbohydrate Polymers*, 64, 212-217.

CHOW, A. H. L., TONG, H. H. Y., CHATTOPADHYAY, P. & SHEKUNOV, B. Y. 2007. Particle engineering for pulmonary drug delivery. *Pharmaceutical Research*, 24, 411-437.

CLARKE, A. 2002. Microscopy techniques for materials science. CRC Press.

References

COHEN, M. H. & TURNBULL, D. 1959. MOLECULAR TRANSPORT IN LIQUIDS AND GLASSES. *Journal of Chemical Physics*, 31, 1164-1169.

COLEMAN, N. J. & CRAIG, D. Q. M. 1996. Modulated temperature differential scanning calorimetry: A novel approach to pharmaceutical thermal analysis. *International Journal of Pharmaceutics*, 135, 13-29.

COLONNA, C., CONTI, B., GENTA, I. & ALPAR, O. H. 2008. Non-viral dried powders for respiratory gene delivery prepared by cationic and chitosan loaded liposomes. *International Journal of Pharmaceutics*, 364, 108-118.

CRAIG, D. Q. M., ROYALL, P. G., KETT, V. L. & HOPTON, M. L. 1999. The relevance of the amorphous state to pharmaceutical dosage forms: glassy drugs and freeze dried systems. *International Journal of Pharmaceutics*, 179, 179-207.

CROOKE, S. T. 1999. Molecular mechanisms of action of antisense drugs. *Biochimica Et Biophysica Acta-Genes Structure and Expression*, 1489, 31-44.

CROWE, J. H., CARPENTER, J. F. & CROWE, L. M. 1998. THE ROLE OF VITRIFICATION IN ANHYDROBIOSIS. *Annual Review of Physiology*, 60, 73-103.

CROWE, J. H., HOEKSTRA, F. A. & CROWE, L. M. 1992. ANHYDROBIOSIS. *Annual Review of Physiology*, 54, 579-599.

CROWE, L. M. 2002. Lessons from nature: the role of sugars in anhydrobiosis. *Comparative Biochemistry and Physiology a-Molecular and Integrative Physiology*, 131, 505-513.

CROWE, L. M., REID, D. S. & CROWE, J. H. 1996. Is trehalose special for preserving dry biomaterials? *Biophysical Journal*, 71, 2087-2093.

CROWLEY, K. J. & ZOGRAFI, G. 2001. The use of thermal methods for predicting glass-former fragility. *Thermochimica Acta*, 380, 79-93.

References

- CUE, C. C., SALVADOR, A. R. R., MORALES, S. A., RODRIGUEZ, F. L. F. & GONZALEZ, P. P. 2001. Raffinose-sucrose crystal interaction modelling. *Journal of Crystal Growth*, 231, 280-289.
- DAVIDSON, P. & SUN, W. Q. 2001. Effect of sucrose/raffinose mass ratios on the stability of co-lyophilized protein during storage above the T-g. *Pharmaceutical Research*, 18, 474-479.
- DE GIACOMO, O. Z. 2008. *Molecular Mobility of Trehalose in Relation to its Bioprotective Action*. University of Trieste.
- DEALY J, P. D. & PLAZEK D 2009. Time-Temperature Superposition - A Users Guide. *Rheology Bulletin*, 78.
- DEMUTH, P. C., SU, X., SAMUEL, R. E., HAMMOND, P. T. & IRVINE, D. J. 2010. Nano-Layered Microneedles for Transcutaneous Delivery of Polymer Nanoparticles and Plasmid DNA. *Advanced Materials*, 22, 4851-+.
- DING, S. P., FAN, J., GREEN, J. L., LU, Q., SANCHEZ, E. & ANGELL, C. A. 1996. Vitrification of trehalose by water loss from its crystalline dihydrate. *Journal of Thermal Analysis*, 47, 1391-1405.
- DRANCA, I., BHATTACHARYA, S., VYAZOVKIN, S. & SURYANARAYANAN, R. 2009. Implications of Global and Local Mobility in Amorphous Sucrose and Trehalose as Determined by Differential Scanning Calorimetry. *Pharmaceutical Research*, 26, 1064-1072.
- DUPRAY, V., BERTON, B., OSSART, S., ATMANI, H., PETIT, M. N. & COQUEREL, G. 2009. Concomitant dehydration mechanisms in single crystals of alpha,alpha-trehalose. *Carbohydrate Research*, 344, 2539-2546.
- DURLAND, R. H. & EASTMAN, E. M. 1998. Manufacturing and quality control of plasmid-based gene expression systems. *Advanced Drug Delivery Reviews*, 30, 33-48.

References

EDIGER, M. D., ANGELL, C. A. & NAGEL, S. R. 1996. Supercooled liquids and glasses. *Journal of Physical Chemistry*, 100, 13200-13212.

EGERTON, R. F. 2005. Physical principles of electron microscopy : an introduction to TEM, SEM, and AEM. Springer.

ERNST, N., ULRICHSKOTTER, S., SCHMALIX, W. A., RADLER, J., GALNEDER, R., MAYER, E., GERSTING, S., PLANK, C., REINHARDT, D. & ROSENECKER, J. 1999. Interaction of liposomal and polycationic transfection complexes with pulmonary surfactant. *Journal of Gene Medicine*, 1, 331-340.

EVANS, R. K., XU, Z., BOHANNON, K. E., WANG, B., BRUNER, M. W. & VOLKIN, D. B. 2000. Evaluation of degradation pathways for plasmid DNA in pharmaceutical formulations via accelerated stability studies. *Journal of Pharmaceutical Sciences*, 89, 76-87.

FATTAL, E. & BOCHOT, A. 2006. Ocular delivery of nucleic acids: antisense oligonucleotides, aptamers and siRNA. *Advanced Drug Delivery Reviews*, 58, 1203-1223.

FOX, T. G. & FLORY, P. J. 1950. 2ND-ORDER TRANSITION TEMPERATURES AND RELATED PROPERTIES OF POLYSTYRENE .1. INFLUENCE OF MOLECULAR WEIGHT. *Journal of Applied Physics*, 21, 581-591.

FURUKI, T., KISHI, A. & SAKURAI, M. 2005. De- and rehydration behavior of alpha,alpha-trehalose dihydrate under humidity-controlled atmospheres. *Carbohydrate Research*, 340, 429-438.

GABBOTT, P., CLARKE, P., MANN, T., ROYALL, P. & SHERGILL, S. 2003. A high-sensitivity, high-speed DSC technique: Measurement of amorphous lactose. *American Laboratory*, 35, 17-+.

GAISFORD, S. 2008. Fast-scan differential scanning calorimetry. *European Pharmaceutical Review*, 83-89.

References

GAMBLE, J. F., CHIU, W.-S., GRAY, V., TOALE, H., TOBYN, M. & WU, Y. 2010. Investigation into the Degree of Variability in the Solid-State Properties of Common Pharmaceutical Excipients-Anhydrous Lactose. *Aaps Pharmscitech*, 11, 1552-1557.

GARCIA-CANAS, V., GONZALEZ, R. & CIFUENTES, A. 2002. Highly reproducible capillary gel electrophoresis (CGE) of DNA fragments using uncoated columns. Detection of genetically modified maize by PCR-CGE. *Journal of Separation Science*, 25, 577-583.

GEWIRTZ, A. M. 2007. On future's doorstep: RNA interference and the pharmacopeia of tomorrow. *Journal of Clinical Investigation*, 117, 3612-3614.

GIL, A. M., BELTON, P. S. & FELIX, V. 1996. Spectroscopic studies of solid alpha-alpha trehalose. *Spectrochimica Acta Part a-Molecular and Biomolecular Spectroscopy*, 52, 1649-1659.

GOLDSTEIN, S., FORDIS, C. M. & HOWARD, B. H. 1989. ENHANCED TRANSFECTION EFFICIENCY AND IMPROVED CELL-SURVIVAL AFTER ELECTROPORATION OF G2/M-SYNCHRONIZED CELLS AND TREATMENT WITH SODIUM-BUTYRATE. *Nucleic Acids Research*, 17, 3959-3971.

GORDON, M. & TAYLOR, J. S. 1952. IDEAL COPOLYMERS AND THE 2ND-ORDER TRANSITIONS OF SYNTHETIC RUBBERS .1. NON-CRYSTALLINE COPOLYMERS. *Journal of Applied Chemistry*, 2, 493-500.

GOUGH, W., RICHARDS, J.P.G., WILLIAMS, R.P. 1995. *Vibrations and Waves*, Prentice Hall.

GRAESER, K. A., PATTERSON, J. E., ZEITLER, J. A., GORDON, K. C. & RADES, T. 2009. Correlating thermodynamic and kinetic parameters with amorphous stability. *European Journal of Pharmaceutical Sciences*, 37, 492-498.

GRANSKE, F. 2008. Absorbance DNA Quantitation Using BMG LABTECH's POLARstar Omega Microplate Reader. *BMG LABTECH, Offenburg, Germany*.

References

GUINOT, S. & LEVEILLER, F. 1999. The use of MTDSC to assess the amorphous phase content of a micronised drug substance. *International Journal of Pharmaceutics*, 192, 63-75.

HALEBLIA.J & MCCRONE, W. 1969. PHARMACEUTICAL APPLICATIONS OF POLYMORPHISM. *Journal of Pharmaceutical Sciences*, 58, 911-&.

HALHAL, M., RENARD, G., COURTOIS, Y., BENEZRA, D. & BEHAR-COHEN, F. 2004. Iontophoresis: from the lab to the bed side. *Experimental Eye Research*, 78, 751-757.

HALLBRUCKER, A., MAYER, E. & JOHARI, G. P. 1989. GLASS-TRANSITION IN PRESSURE-AMORPHIZED HEXAGONAL ICE - A COMPARISON WITH AMORPHOUS FORMS MADE FROM THE VAPOR AND LIQUID. *Journal of Physical Chemistry*, 93, 7751-7752.

HANCOCK, B. C. & SHAMBLIN, S. L. 1998. Water vapour sorption by pharmaceutical sugars. *Pharmaceutical Science & Technology Today*, 1, 345-351.

HANCOCK, B. C. & ZOGRAF, G. 1996. Characteristics and significance of the amorphous state in pharmaceutical systems. *Journal of Pharmaceutical Sciences*, 86, 1-12.

HANCOCK, B. C. & ZOGRAFI, G. 1994. THE RELATIONSHIP BETWEEN THE GLASS-TRANSITION TEMPERATURE AND THE WATER-CONTENT OF AMORPHOUS PHARMACEUTICAL SOLIDS. *Pharmaceutical Research*, 11, 471-477.

HASSEL, R. L. & HESSE, N. D. 2007. Dynamic Vapor Sorption Characterization of Pharmaceutical Recrystallization. *TA Instruments*.

HERNANDEZ GARCIA, A. 2011. Anhydrobiosis in bacteria: From physiology to applications. *Journal of Biosciences*, 36, 939-950.

HILL, V. L., CRAIG, D. Q. M. & FEELY, L. C. 1998. Characterisation of spray-dried lactose using modulated differential scanning calorimetry. *International Journal of Pharmaceutics*, 161, 95-107.

References

HILL, V. L., CRAIG, D. Q. M. & FEELY, L. C. 1999. The effects of experimental parameters and calibration on MTDSC data. *International Journal of Pharmaceutics*, 192, 21-32.

HODGE, I. M. 1996. Strong and fragile liquids - A brief critique. *Journal of Non-Crystalline Solids*, 202, 164-172.

HOGAN, S. E. & BUCKTON, G. 2001. Water sorption/desorption - near IR and calorimetric study of crystalline and amorphous raffinose. *International Journal of Pharmaceutics*, 227, 57-69.

HORVAT, M. 2003. *EFFECT OF PARTICLE SIZE ON PHYSICO-CHEMICAL PROPERTIES OF TREHALOSE-PARACETAMOL MIXTURE*.

HUNTER, N. E. 2009a. *A spectroscopic and kinetic investigation into sugar glasses*. Doctor of Philosophy, University of East Anglia.

HUNTER, N. E. 2009b. *A Spectroscopic and Kinetic Investigation into Sugar Glasses*.

HUNTER, N. E., FRAMPTON, C. S., CRAIG, D. Q. M. & BELTON, P. S. 2010. The use of dynamic vapour sorption methods for the characterisation of water uptake in amorphous trehalose. *Carbohydrate Research*, 345, 1938-1944.

HYNES, R. C. & LEPAGE, Y. 1991. SUCROSE, A CONVENIENT TEST CRYSTAL FOR ABSOLUTE STRUCTURES. *Journal of Applied Crystallography*, 24, 352-354.

IGLESIAS, H. A., CHIRIFE, J. & BUERA, M. P. 1997. Adsorption isotherm of amorphous trehalose. *Journal of the Science of Food and Agriculture*, 75, 183-186.

IGLESIAS, H. A., SCHEBOR, C., BUERA, M. P. & CHIRIFE, J. 2000. Sorption isotherm and calorimetric behavior of amorphous/crystalline raffinose-water systems. *Journal of Food Science*, 65, 646-650.

INFOMETRIX 2008. *Pirouette User Guide: Multivariate Data Analysis*. In: INFOMETRIX, I. (ed.).

References

- JAIN, N. K. & ROY, I. 2009. Effect of trehalose on protein structure. *Protein Science*, 18, 24-36.
- JOHNSON, K. A. 1997. Preparation of peptide and protein powders for inhalation. *Advanced Drug Delivery Reviews*, 26, 3-15.
- JONES, K. J., KINSHOTT, I., READING, M., LACEY, A. A., NIKOLOPOULOS, C. & POLLOCK, H. M. 1997. The origin and interpretation of the signals of MTDSC. *Thermochimica Acta*, 305, 187-199.
- JONES, M. D., HOOTON, J. C., DAWSON, M. L., FERRIE, A. R. & PRICE, R. 2006. Dehydration of trehalose dihydrate at low relative humidity and ambient temperature. *International Journal of Pharmaceutics*, 313, 87-98.
- JUDOVITS, L. & GUPTA, R. 2011. Detection of obscured glass transitions by QiDSC. *Journal of Thermal Analysis and Calorimetry*, 106, 299-303.
- KACURÁKOVÁ, M. & MATHLOUTHI, M. 1996. FTIR and laser-Raman spectra of oligosaccharides in water: characterization of the glycosidic bond. *Carbohydrate Research*, 284, 145-157.
- KAJIWARA, K. & FRANKS, F. 1997. Crystalline and amorphous phases in the binary system water-raffinose. *Journal of the Chemical Society-Faraday Transactions*, 93, 1779-1783.
- KAJIWARA, K., FRANKS, F., ECHLIN, P. & GREER, A. L. 1999. Structural and dynamic properties of crystalline and amorphous phases in raffinose-water mixtures. *Pharmaceutical Research*, 16, 1441-1448.
- KANG, D., CHUNG, D. S., KANG, S. H. & KIM, Y. 2005. Separation of DNA with hydroxypropylmethyl cellulose and poly(ethylene oxide) by capillary gel electrophoresis. *Microchemical Journal*, 80, 121-125.
- KATAS, H. & ALPAR, H. O. 2006. Development and characterisation of chitosan nanoparticles for siRNA delivery. *Journal of Controlled Release*, 115, 216-225.

References

KAUZMANN, W. 1948. THE NATURE OF THE GLASSY STATE AND THE BEHAVIOR OF LIQUIDS AT LOW TEMPERATURES. *Chemical Reviews*, 43, 219-256.

KAWAI, K., HAGIWARA, T., TAKAI, R. & SUZUKI, T. 2004. Maillard Reaction rate in various glassy matrices. *Bioscience Biotechnology and Biochemistry*, 68, 2285-2288.

KETT, V. 2000. *An Investigation Into Amorphous Sucrose Systems Using Modulated Temperature Differential Scanning Calorimetry*. Doctor of Philosophy, University of London.

KETTNER-BUHROW, D., DITTRICH-BREIHZOLZ, O., SCHNEIDER, H., WOLTER, S., RESCH, K. & KRACHT, M. 2006. Small interfering RNAs generated by recombinant dicer induce inflammatory gene expression independent from the TAK1-NF kappa B-MAPK signaling pathways. *Biochemical and Biophysical Research Communications*, 347, 566-573.

KHANKARI, R. K. & GRANT, D. J. W. 1995. PHARMACEUTICAL HYDRATES. *Thermochimica Acta*, 248, 61-79.

KLUG, H. P. & ALEXANDER, L. E. 1954. *X-Ray Diffraction Procedures: For Polycrystalline and Amorphous Materials*, A Wiley-Interscience Publication.

KUMAR, P. & CLARK, M. 2005. Clinical medicine: Chapter 14 Respiratory Diseases.

KUO, J. H. S. 2003. The effect of protective agents on the stability of plasmid DNA by the process of spray-drying. *Journal of Pharmacy and Pharmacology*, 55, 301-306.

KURUBA, R., WILSON, A., GAO, X. & LI, S. 2009. Targeted Delivery of Nucleic Acid-Based Therapeutics to the Pulmonary Circulation. *Aaps Journal*, 11, 23-30.

LAI, H. L., PITT, K. & CRAIG, D. Q. M. 2010. Characterisation of the thermal properties of ethylcellulose using differential scanning and quasi-isothermal calorimetric approaches. *International Journal of Pharmaceutics*, 386, 178-184.

References

- LAMMERT, A. M., SCHMIDT, S. J. & DAY, G. A. 1998. Water activity and solubility of trehalose. *Food Chemistry*, 61, 139-144.
- LANDIN, M., MARTINEZPACHECO, R., GOMEZAMOZA, J. L., SOUTO, C., CONCHEIRO, A. & ROWE, R. C. 1993a. EFFECT OF BATCH VARIATION AND SOURCE OF PULP ON THE PROPERTIES OF MICROCRYSTALLINE CELLULOSE. *International Journal of Pharmaceutics*, 91, 133-141.
- LANDIN, M., MARTINEZPACHECO, R., GOMEZAMOZA, J. L., SOUTO, C., CONCHEIRO, A. & ROWE, R. C. 1993b. EFFECT OF COUNTRY-OF-ORIGIN ON THE PROPERTIES OF MICROCRYSTALLINE CELLULOSE. *International Journal of Pharmaceutics*, 91, 123-131.
- LAPPALAINEN, M., PITKANEN, I. & HARJUNEN, P. 2006. Quantification of low levels of amorphous content in sucrose by hyperDSC. *International Journal of Pharmaceutics*, 307, 150-155.
- LEINEN, K. M. & LABUZA, T. P. 2006. Crystallization inhibition of an amorphous sucrose system using raffinose. *Journal of Zhejiang University. Science. B*, 7, 85-9.
- LERK, C. F. 1993. CONSOLIDATION AND COMPACTION OF LACTOSE. *Drug Development and Industrial Pharmacy*, 19, 2359-2398.
- LEVY, M. S., COLLINS, I. J., YIM, S. S., WARD, J. M., TITCHENER-HOOKER, N., SHAMLOU, P. A. & DUNNILL, P. 1999. Effect of shear on plasmid DNA in solution. *Bioprocess Engineering*, 20, 7-13.
- LI, H., LABEAN, T. H. & LEONG, K. W. 2011. Nucleic acid-based nanoengineering: novel structures for biomedical applications. *Interface Focus*, 1, 702-724.
- LI, H. Y., SEVILLE, P. C., WILLIAMSON, I. J. & BIRCHALL, J. C. 2005. The use of absorption enhancers to enhance the dispersibility of spray-dried powders for pulmonary gene therapy. *Journal of Gene Medicine*, 7, 1035-1043.

References

LI, J., LI, X., ZHANG, Y., ZHOU, X. K., YANG, H. S., CHEN, X. C., WANG, Y. S., WEI, Y. Q., CHEN, L. J., HU, H. Z. & LIU, C. Y. 2010. Gene therapy for psoriasis in the K14-VEGF transgenic mouse model by topical transdermal delivery of interleukin-4 using ultradeformable cationic liposome. *Journal of Gene Medicine*, 12, 481-490.

LU, E. 2011. *Stabilization of Amorphous Pharmaceuticals by Excipients*.

MAA, Y. F., NGUYEN, P. A., ANDYA, J. D., DASOVICH, N., SWEENEY, T. D., SHIRE, S. J. & HSU, C. C. 1998. Effect of spray drying and subsequent processing conditions on residual moisture content and physical/biochemical stability of protein inhalation powders. *Pharmaceutical Research*, 15, 768-775.

MACDONALD, C. & JOHARI, G. P. 2000. Glass-softening of trehalose and calorimetric transformations in its liquid state. *Journal of Molecular Structure*, 523, 119-132.

MANDUVA, R., KETT, V. L., BANKS, S. R., WOOD, J., READING, M. & CRAIG, D. Q. M. 2008. Calorimetric and spatial characterization of polymorphic transitions in caffeine using quasi-isothermal MTDSC and localized thermomechanical analysis. *Journal of Pharmaceutical Sciences*, 97, 1285-1300.

MASTERS, K. 1976. *Spray Drying Handbook*, George Godwin Ltd.

MATHLOUTHI, M., CHOLLI, A. L. & KOENIG, J. L. 1986. SPECTROSCOPIC STUDY OF THE STRUCTURE OF SUCROSE IN THE AMORPHOUS STATE AND IN AQUEOUS-SOLUTION. *Carbohydrate Research*, 147, 1-9.

MCGARVEY, O. S., KETT, V. L. & CRAIG, D. Q. M. 2003. An investigation into the crystallization of alpha,alpha-trehalose from the amorphous state. *Journal of Physical Chemistry B*, 107, 6614-6620.

MILLER, D. P. & LECHUGA-BALLESTEROS, D. 2006. Rapid assessment of the structural relaxation behavior of amorphous pharmaceutical solids: Effect of residual water on molecular mobility. *Pharmaceutical Research*, 23, 2291-2305.

References

MISHIMA, O., CALVERT, L. D. & WHALLEY, E. 1985. AN APPARENTLY 1ST-ORDER TRANSITION BETWEEN 2 AMORPHOUS PHASES OF ICE INDUCED BY PRESSURE. *Nature*, 314, 76-78.

MOLLER, J. T. & FREDSTED, S. 2009. A Primer on Spray Drying. *Chemical Engineering*, 116, 34-40.

MORAN, A. & BUCKTON, G. 2007. Adjusting and understanding the properties and crystallisation behaviour of amorphous trehalose as a function of spray drying feed concentration. *International Journal of Pharmaceutics*, 343, 12-17.

MORETON, C. 2009. Functionality and performance of excipients in a quality-by-design world: obtaining information on excipient variability for formulation design space. *Am Pharm Rev*, 12, 28-33.

MOYNIHAN, C. T., EASTEAL, A. J., WILDER, J. & TUCKER, J. 1974. DEPENDENCE OF GLASS-TRANSITION TEMPERATURE ON HEATING AND COOLING RATE. *Journal of Physical Chemistry*, 78, 2673-2677.

MOYNIHAN, C. T., LEE, S. K., TATSUMISAGO, M. & MINAMI, T. 1996. Estimation of activation energies for structural relaxation and viscous flow from DTA and DSC experiments. *Thermochimica Acta*, 280, 153-162.

NAGASE, H., ENDO, T., UEDA, H. & NAKAGAKI, M. 2002. An anhydrous polymorphic form of trehalose. *Carbohydrate Research*, 337 167-173.

NAGASE, H., OGAWA, N., ENDO, T., SHIRO, M., UEDA, H. & SAKURAI, M. 2008. Crystal structure of an anhydrous form of trehalose: Structure of water channels of trehalose polymorphism. *Journal of Physical Chemistry B*, 112, 9105-9111.

NAINI, V., BYRON, P. R. & PHILLIPS, E. M. 1998. Physicochemical stability of crystalline sugars and their spray-dried forms: Dependence upon relative humidity and suitability for use in powder inhalers. *Drug Development and Industrial Pharmacy*, 24, 895-909.

References

OHTAKE, S. & WANG, Y. J. 2011. Trehalose: Current Use and Future Applications. *Journal of Pharmaceutical Sciences*, 100, 2020-2053.

OTSUKA, M., OHTANI, H., OTSUKA, K. & KANENIWA, N. 1993. EFFECT OF HUMIDITY ON SOLID-STATE ISOMERIZATION OF VARIOUS KINDS OF LACTOSE DURING GRINDING. *Journal of Pharmacy and Pharmacology*, 45, 2-5.

OTTENHOF, M. A., MACNAUGHTAN, W. & FARHAT, I. A. 2003. FTIR study of state and phase transitions of low moisture sucrose and lactose. *Carbohydrate Research*, 338, 2195-2202.

PATIL, S., RHODES, D. & BURGESS, D. 2005. DNA-based therapeutics and DNA delivery systems: A comprehensive review. *The AAPS Journal*, 7, E61-E77.

PEARTON, M., ALLENDER, C., BRAIN, K., ANSTEY, A., GATELEY, C., WILKE, N., MORRISSEY, A. & BIRCHALL, J. 2008. Gene Delivery to the Epidermal Cells of Human Skin Explants Using Microfabricated Microneedles and Hydrogel Formulations. *Pharmaceutical Research*, 25, 407-416.

PERKINELMER 2005. FT-IR Spectroscopy: Attenuated Total Reflection. *PerkinElmer: Life and Analytical Sciences*.

POCKETT, J. 2004. *CRYSTALLINITY IN LINEAR POLYAMIDES: A STUDY USING MELT BLENDING WITH SMALL-MOLECULE DILUENTS*. Degree of Doctor of Philosophy, University of South Australia.

POOLE, P. H., GRANDE, T., ANGELL, C. A. & MCMILLAN, P. F. 1997. Polymorphic phase transitions in liquids and glasses. *Science*, 275, 322-323.

PRZYBYLOWSKI, M., BARTIDO, S., BORQUEZ-OJEDA, O., SADELAIN, M. & RIVIÈRE, I. 2007. Production of clinical-grade plasmid DNA for human Phase I clinical trials and large animal clinical studies. *Vaccine*, 25, 5013-5024.

QIAGEN® 2005. QIAGEN® Plasmid Purification Handbook. In: N, Q. I. A. G. E. (ed.) www.Qiagen.com Third Edition ed.

References

QUAAK, S. G. L., HAANEN, J. B. A. G., BEIJNEN, J. H. & NUIJEN, B. 2010. Naked Plasmid DNA Formulation: Effect of Different Disaccharides on Stability after Lyophilisation. *Aaps Pharmscitech*, 11, 344-350.

RABUSSAY, D., DEV, N. B., FEWELL, J., SMITH, L. C., WIDERA, G. & ZHANG, L. 2003. Enhancement of therapeutic drug and DNA delivery into cells by electroporation. *Journal of Physics D-Applied Physics*, 36, 348-363.

RANI, M., GOVINDARAJAN, R., SURANA, R. & SURYANARAYANAN, R. 2006. Structure in dehydrated trehalose dihydrate - Evaluation of the concept of partial crystallinity. *Pharmaceutical Research*, 23, 2356-2367.

RAW, A. S., FURNESS, M. S., GILL, D. S., ADAMS, R. C., HOLCOMBE, F. O. & YU, L. X. 2004. Regulatory considerations of pharmaceutical solid polymorphism in abbreviated new drug applications (ANDAs). *Advanced Drug Delivery Reviews*, 56, 397-414.

READING, M., ELLIOTT, D. & HILL, V. L. 1993. A NEW APPROACH TO THE CALORIMETRIC INVESTIGATION OF PHYSICAL AND CHEMICAL-TRANSITIONS. *Journal of Thermal Analysis*, 40, 949-955.

REDWAY. 2012. *Gene Manipulation & Recombinant DNA* [Online]. Available: <http://www2.wmin.ac.uk/~redwayk/lectures/analysis.htm> [Accessed 16 February 2012 2012].

REGNIER, V., TAHIRI, A., ANDRE, N., LEMAITRE, M., LE DOAN, T. & PREAT, V. 2000. Electroporation-mediated delivery of 3'-protected phosphodiester oligodeoxynucleotides to the skin. *Journal of Controlled Release*, 67, 337-346.

REISENER, H. J., GOLDSCHMID, H. R., LEDINGHAM, G. A. & PERLIN, A. S. 1962. Formation of trehalose and polyols by wheat stem rust (*Puccinia graminis tritici*) uredospores. *Canadian journal of biochemistry and physiology*, 40, 1248-1251.

References

ROE, K. D. & LABUZA, T. P. 2005. Glass transition and crystallization of amorphous trehalose-sucrose mixtures. *International Journal of Food Properties*, 8, 559-574.

ROGERS, T. L., JOHNSTON, K. P. & WILLIAMS, R. O. 2001. Solution-based particle formation of pharmaceutical powders by supercritical or compressed fluid CO₂ and cryogenic spray-freezing technologies. *Drug Development and Industrial Pharmacy*, 27, 1003-1015.

ROOS, Y. H. 1993. MELTING AND GLASS TRANSITIONS OF LOW-MOLECULAR-WEIGHT CARBOHYDRATES. *Carbohydrate Research*, 238, 39-48.

ROWE, R. C., MCKILLOP, A. G. & BRAY, D. 1994. THE EFFECT OF BATCH AND SOURCE VARIATION ON THE CRYSTALLINITY OF MICROCRYSTALLINE CELLULOSE. *International Journal of Pharmaceutics*, 101, 169-172.

SAKURAI, H., KAWABATA, K., SAKURAI, F., NAKAGAWA, S. & MIZUGUCHI, H. 2008. Innate immune response induced by gene delivery vectors. *International Journal of Pharmaceutics*, 354, 9-15.

SALAMEH, A. K. & TAYLOR, L. S. 2005. Deliquescence in binary mixtures. *Pharmaceutical Research*, 22, 318-324.

SALEKIGERHARDT, A., STOWELL, J. G., BYRN, S. R. & ZOGRAFI, G. 1995. HYDRATION AND DEHYDRATION OF CRYSTALLINE AND AMORPHOUS FORMS OF RAFFINOSE. *Journal of Pharmaceutical Sciences*, 84, 318-323.

SALEKIGERHARDT, A. & ZOGRAFI, G. 1994. NONISOTHERMAL AND ISOTHERMAL CRYSTALLIZATION OF SUCROSE FROM THE AMORPHOUS STATE. *Pharmaceutical Research*, 11, 1166-1173.

SANDS, D. E. 1993. *Introduction to Crsytallography*, Dover Publications.

SAUER P, M. M., KANG J 1998. Quantitation of DNA. *Qiagen News*, 2.

References

SCHEBOR, C., FLORENCIA MAZZOBRE, M. & DEL PILAR BUERA, M. 2010. Glass transition and time-dependent crystallization behavior of dehydration bioprotectant sugars. *Carbohydrate Research*, 345, 303-308.

SEVILLE, P. C., KELLAWAY, I. W. & BIRCHALL, J. C. 2002. Preparation of dry powder dispersions for non-viral gene delivery by freeze-drying and spray-drying. *Journal of Gene Medicine*, 4, 428-437.

SHAFIZAD.F & SUSOTT, R. A. 1973. CRYSTALLINE TRANSITIONS OF CARBOHYDRATES. *Journal of Organic Chemistry*, 38, 3710-3715.

SHAMBLIN, S. L., TANG, X. L., CHANG, L. Q., HANCOCK, B. C. & PIKAL, M. J. 1999. Characterization of the time scales of molecular motion in pharmaceutically important glasses. *Journal of Physical Chemistry B*, 103, 4113-4121.

SHAMBLIN, S. L. & ZOGRAFI, G. 1998. Enthalpy relaxation in binary amorphous mixtures containing sucrose. *Pharmaceutical Research*, 15, 1828-1834.

SHAMBLIN, S. L. & ZOGRAFI, G. 1999. The effects of absorbed water on the properties of amorphous mixtures containing sucrose. *Pharmaceutical Research*, 16, 1119-1124.

SHOYELE, S. A. & CAWTHOME, S. 2006. Particle engineering techniques for inhaled biopharmaceuticals. *Advanced Drug Delivery Reviews*, 58, 1009-1029.

SIMPERLER, A., KORNHERR, A., CHOPRA, R., BONNET, P. A., JONES, W., MOTHERWELL, W. D. S. & ZIFFERER, G. 2006. Glass transition temperature of glucose, sucrose, and trehalose: An experimental and in silico study. *Journal of Physical Chemistry B*, 110, 19678-19684.

SKLAN, E. H. & GLENN, J. S. 2007. The power of silence: Application of small interfering RNAs to gastrointestinal diseases. *Gastroenterology*, 132, 2291-2295.

SON, Y. J. & MCCONVILLE, J. T. 2008. Advancements in dry powder delivery to the lung. *Drug Development and Industrial Pharmacy*, 34, 948-959.

References

STEPHENSON, G. A., GROLEAU, E. G., KLEEMANN, R. L., XU, W. & RIGSBEE, D. R. 1998. Formation of isomorphous desolvates: Creating a molecular vacuum. *Journal of Pharmaceutical Sciences*, 87, 536-542.

SUN, W. Q., DAVIDSON, P. & CHAN, H. S. O. 1998. Protein stability in the amorphous carbohydrate matrix: relevance to anhydrobiosis. *Biochimica Et Biophysica Acta-General Subjects*, 1425, 245-254.

SURANA, R., PYNE, A. & SURYANARAYANAN, R. 2004. Effect of preparation method on physical properties of amorphous trehalose. *Pharmaceutical Research*, 21, 1167-1176.

SUSSICH, F., BORTOLUZZI, S. & CESARO, A. 2002. Trehalose dehydration under confined conditions. *Thermochimica Acta*, 391, 137-150.

SUSSICH, F. & CESARO, A. 2008. Trehalose amorphization and recrystallization. *Carbohydrate Research*, 343, 2667-2674.

SUSSICH, F., PRINCIVALLE, F. & CESARO, A. 1999. The interplay of the rate of water removal in the dehydration of alpha,alpha-trehalose. *Carbohydrate Research*, 322, 113-119.

SUSSICH, F., URBANI, R., PRINCIVALLE, F. & CESARO, A. 1998. Polymorphic amorphous and crystalline forms of trehalose. *Journal of the American Chemical Society*, 120, 7893-7899.

SUZUKI, T., OHSUMI, S. & MAKINO, K. 1994. MECHANISTIC STUDIES ON DEPURINATION AND APURINIC SITE CHAIN BREAKAGE IN OLIGODEOXYRIBONUCLEOTIDES. *Nucleic Acids Research*, 22, 4997-5003.

SYMPATEC. 2012. *LaserDiffraction Particle Size Analysis* [Online]. Available: <http://www.sympatec.com/EN/LaserDiffraction/LaserDiffraction.html> [Accessed 14th of January 2012 2012].

References

TALSMA, H., CHERNG, J. Y., LEHRMANN, H., KURSA, M., OGRIS, M., HENNINK, W. E., COTTEN, M. & WAGNER, E. 1997. Stabilization of gene delivery systems by freeze-drying. *International Journal of Pharmaceutics*, 157, 233-238.

TAYLOR, L. S. & YORK, P. 1998. Effect of particle size and temperature on the dehydration kinetics of trehalose dihydrate. *International Journal of Pharmaceutics*, 167, 215-221.

THOMAS, L. C. 2005. Modulated DSC® Paper #2, Modulated DSC® Basics; Calculation and Calibration of MDSC® Signals. TA INSTRUMENTS.

THOMAS, M., LU, J. J., CHEN, J. Z. & KLIBANOV, A. M. 2007. Non-viral siRNA delivery to the lung. *Advanced Drug Delivery Reviews*, 59, 124-133.

TIMSINA, M. P., MARTIN, G. P., MARRIOTT, C., GANDERTON, D. & YIANNESKIS, M. 1994. DRUG-DELIVERY TO THE RESPIRATORY-TRACT USING DRY POWDER INHALERS. *International Journal of Pharmaceutics*, 101, 1-13.

TSE, M. T., BLATCHFORD, C. & ALPAR, H. O. 2009. Evaluation of different buffers on plasmid DNA encapsulation into PLGA microparticles. *International Journal of Pharmaceutics*, 370, 33-40.

UHEREK, C. & WELS, W. 2000. DNA-carrier proteins for targeted gene delivery. *Advanced Drug Delivery Reviews*, 44, 153-166.

VAN SCOIK, K. G. & CARSTENSEN, J. T. 1990. Nucleation phenomena in amorphous sucrose systems. *International Journal of Pharmaceutics*, 58, 185-196.

VEHRING, R. 2008. Pharmaceutical particle engineering via spray drying. *Pharmaceutical Research*, 25, 999-1022.

VERDONCK, E., SCHAAP, K. & THOMAS, L. C. 1999. A discussion of the principles and applications of Modulated Temperature DSC (MTDSC). *International Journal of Pharmaceutics*, 192, 3-20.

References

VIPPAGUNTA, S. R., BRITAIN, H. G. & GRANT, D. J. W. 2001. Crystalline solids. *Advanced Drug Delivery Reviews*, 48, 3-26.

WALSH, G. 2002. Biopharmaceuticals and biotechnology medicines: an issue of nomenclature. *European Journal of Pharmaceutical Sciences*, 15, 135-138.

WALTHER, W. & STEIN, U. 2000. Viral vectors for gene transfer - A review of their use in the treatment of human diseases. *Drugs*, 60, 249-271.

WALTHER, W., STEIN, U., VOSS, C., SCHMIDT, T., SCHLEEF, M. & SCHLAG, P. M. 2003. Stability analysis for long-term storage of naked DNA: impact on nonviral in vivo gene transfer. *Analytical Biochemistry*, 318, 230-235.

WANG, X., XU, W., MOHAPATRA, S., KONG, X., LI, X., LOCKEY, R. F. & MOHAPATRA, S. S. 2008. Prevention of airway inflammation with topical cream containing imiquimod and small interfering RNA for natriuretic peptide receptor. *Genet Vaccines Ther*, 6, 7.

WATSON, J. D. & CRICK, F. H. C. 1953. MOLECULAR STRUCTURE OF NUCLEIC ACIDS - A STRUCTURE FOR DEOXYRIBOSE NUCLEIC ACID. *Nature*, 171, 737-738.

WILLART, J. F., DANEDE, F., DE GUSSEME, A., DESCAMPS, M. & NEVES, C. 2003. Origin of the dual structural transformation of trehalose dihydrate upon dehydration. *Journal of Physical Chemistry B*, 107, 11158-11162.

WILLART, J. F. & DESCAMPS, M. 2008. Solid State Amorphization of Pharmaceuticals. *Molecular Pharmaceutics*, 5, 905-920.

WOLKERS, W. F., OLDENHOF, H., ALBERDA, M. & HOEKSTRA, F. A. 1998. A Fourier transform infrared microspectroscopy study of sugar glasses: application to anhydrobiotic higher plant cells. *Biochimica Et Biophysica Acta-General Subjects*, 1379, 83-96.

References

WOLKERS, W. F., OLIVER, A. E., TABLIN, F. & CROWE, J. H. 2004. A fourier-transform infrared spectroscopy study of sugar glasses. *Carbohydrate Research*, 339, 1077-1085.

XU, L. & ANCHORDOQUY, T. 2010. Drug delivery trends in clinical trials and translational medicine: Challenges and opportunities in the delivery of nucleic acid-based therapeutics. *Journal of Pharmaceutical Sciences*, 100, 38-52.

YANG, W., PETERS, J. I. & WILLIAMS, R. O. 2008. Inhaled nanoparticles - A current review. *International Journal of Pharmaceutics*, 356, 239-247.

YOSHIOKA, S. & ASO, Y. 2007. Correlations between molecular mobility and chemical stability during storage of amorphous pharmaceuticals. *Journal of Pharmaceutical Sciences*, 96, 960-981.

YU, X., KAPPES, S. M., BELLO-PEREZ, L. A. & SCHMIDT, S. J. 2008. Investigating the moisture sorption behavior of amorphous sucrose using a dynamic humidity generating instrument. *Journal of Food Science*, 73, E25-E35.

YU, Z. S., GARCIA, A. S., JOHNSTON, K. P. & WILLIAMS, R. O. 2004. Spray freezing into liquid nitrogen for highly stable protein nanostructured microparticles. *European Journal of Pharmaceutics and Biopharmaceutics*, 58, 529-537.

APPENDIX

APPENDIX 2.1 PREPARATION OF [X1] TBE BUFFER

10.8g of TRIS (Hydroxymethylaminomethane) Base Ultra Pure (obtained from Sigma with 99% purity), 5.5g Boric acid (Fisher Scientific analytical reagent grade) and 0.93g EDTA (ethylenediaminetetraacetic acid) (Sigma-Aldrich grade with approximately 99% titration) was dissolved in 800mL of distilled water. The volume was further adjusted to 1L with additional distilled water.

APPENDIX 2.2 COUNTING CELLS USING A HAEMOCYTOMETER (PROTOCOL TAKEN FROM ABCAM[®])

The haemocytometer was cleaned using 70% ethanol. The shoulders of the haemocytometers was moistened and a coverslip was fixed onto it using gentle pressure and small circular motions. An indication of when the coverslip is placed correctly is by visualization of Newton's rings therefore the depth of the chamber is ensured. The cell suspension was prepared by gentle agitation of the flask containing the cells. Before the cells had a chance to settle 1mL of this suspension was taken out (using a 1mL Serological Pipette) and was placed into an eppendorf. Using a Gilson pipette 10 μ L of cell suspension was drawn up and carefully used to fill the haemocytometer by gently resting the end of the Gilson tip at the edge of the chambers allowing the sample to be drawn out of the pipette by capillary action. The haemocytometer was then placed under a microscope and the grid lines were focused using 10X objective of the microscope. Focusing on one set of

the 16 corner square (as indicated in *Figure A.1*) the number of cells in this area of 16 squares were counted using a hand tally counter.

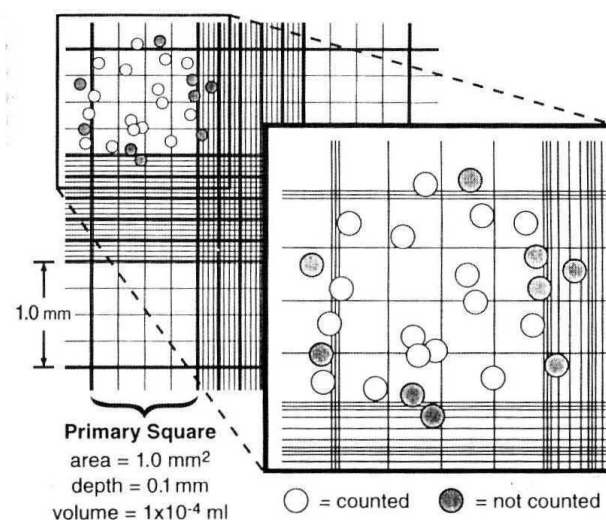


Figure A.1 Haemocytometer with cells for counting (taken from <http://www.cf.ac.uk/biosi/staffinfo/kille/Methods/Cellculture/HAEMO.html>)

The haemocytometer is designed so that the number of cells in one set of 16 corner squares is equivalent to the number of cells x 10⁴ / mL. Therefore, to obtain the cell count: The total count from 4 sets of 16 corner = (cells / ml x 10⁴) X4 squares from one haemocytometer grid.

APPENDIX 2.3 RESULTS FROM MTT ASSAY

MTT assay plates were prepared as shown in *Figure A.2a* and results are presented in *Figure A.2b*. For ease of referencing trehalose, raffinose and HPMC solutions are referenced according to %w/v where T represents trehalose, R raffinose and H HPMC.

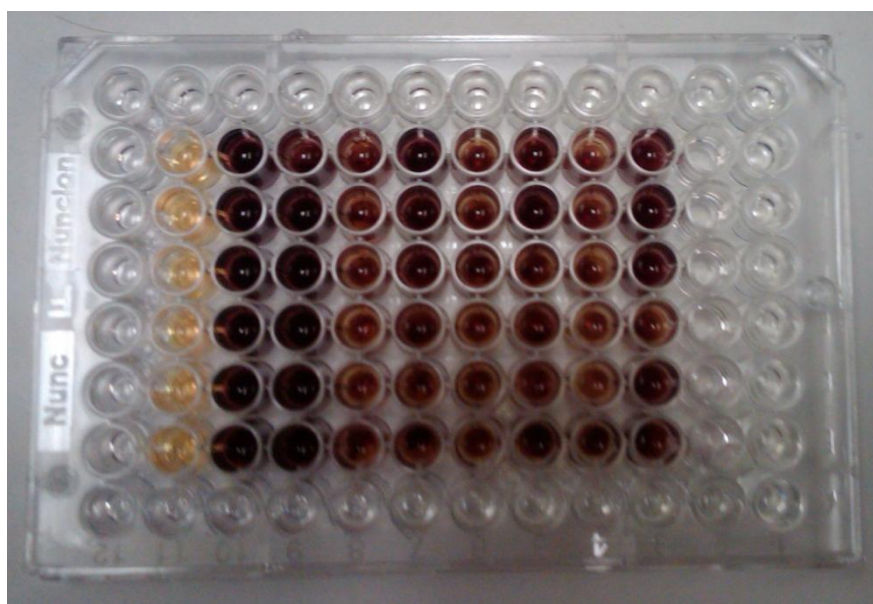
Appendix

Control solutions were referenced according to media volume in starting solution (10mL)

i.e. C6 represents control solution containing 6mL media and 4mL PBS.

	1	2	3	4	5	6	7	8	9	10	11	12											
A																							
B													CA	C6	C8.8	T10	T3	R10	R3	H2	H0.6		
C													CA	C6	C8.8	T10	T3	R10	R3	H2	H0.6		
D													CA	C6	C8.8	T10	T3	R10	R3	H2	H0.6		
E													MA	C8	C9.6	T5	T1	R5	R1	H1	H0.2		
F													MA	C8	C9.6	T5	T1	R5	R1	H1	H0.2		
G													MA	C8	C9.6	T5	T1	R5	R1	H1	H0.2		
H																							

a)



b)

Figure A.2 Schematic illustration of a 96-well plate used in an MTT assay where C = cells with media only, MA = media (RPMI – 1640) alone, C = control solutions, T = trehalose solutions, R = raffinose solutions and H = HPMC solutions, ■ = phosphate buffered saline solution

APPENDIX 2.4 PREPARING A 6-WELL PLATE

Materials

6 well plate

70% ethanol in 50mL centrifuge tube

Waste bottle

Plastic tweezers

Cover slips

Medium (complete DMEM)

Cells

Method

1. Label plates
2. Open lid of 70% ethanol
3. Take tweezers and coverslips
4. Dip 1 coverslip into 70% ethanol and then place in well
5. Repeat for all other wells
6. Add 1mL medium to wells to remove residual ethanol as this can have a negative effect on cells, and then pipette out.
7. Once this is done it is time to add the medium and then the cells
8. Unscrew medium lid
9. Take a pipette (12mL)
10. Add 2mL of medium into each well used

11. Place in 37°C incubator
12. Loosen cells
13. When this is done take loosen cells and dropwise onto coverslips
14. Shake plates gently
15. Place in incubator

APPENDIX 2.5 TRANSFECTION OF A549 CELLS

1. Ensure cells are at ~85% confluency
2. Remove medium
3. Add 5mL of trypsin
4. Swirl around cells ~15 times
5. Remove trypsin
6. Incubate at 37°C for 3-5mins
7. Add 5mL of fresh media
8. Use Haemocytometer to calculate number of cells (detailed in *Appendix 2.2*)
1000,000 cells required for successful transfection
9. Spin down cells
10. Add 1mL pre-warmed PBS twice
11. Remove PBS
12. Add 250µL EPS (Li et al '07 used FBS) and 125µg of transfer RNA (tRNA)
(10mg/mL on packaging 12.5µL of solution required), 10µg plasmid DNA, 1%
(2.5µL) DMSO
13. Mixture was incubated at room temperature for 30minutes
14. Electroporation setting U001

15. 250 μ L of serum free RPMI was added to the cells before further incubation at room temperature for 30minutes
16. Use a 6 well plate (pre-prepared *Appendix 2.3*)
17. Cells were added to 5mL of pre-warmed complete RPMI
18. Add transfected A549 cells
19. Leave plate incubated at 37°C for 2hours
20. Add 20 μ L of Sodium Butyrate into ONE well of each sample
21. Incubate for 42-48hrs

APPENDIX 2.6 TRANSFECTION OF HELA CELLS

1. Ensure cells are at ~85% confluency
2. Remove medium
3. Add 2mL PBS + EDTA solution
4. Swirl around cells
5. Incubate at 37°C for 5-10mins
6. Give a gentle “bash” to resuspend
7. Take out resuspended cells and add to an eppendorf
8. Use Haemocytometer to calculate number of cells (detailed in *Appendix 2.2*)
1000,000 cells required for successful transfection
9. Spin down cells (4000g for 10mins)
10. Wash ONCE in 1mL simple DMEM (\emptyset)
11. Spin down again
12. Take medium off and resuspend

13. (into eppendorf) Add 250 μ L EPS (electroporation solution) and 125 μ g of transfer RNA (tRNA) (*10mg/mL on packaging 12.5 μ L of solution required*), 10 μ g plasmid DNA, 2.5 μ L of 1% DMSO
14. Incubated at room temperature for 30minutes
15. Take out 250 μ L add to cuvette (discard of the rest)
16. Electroporation setting U001
17. Add 250 μ L of simple DMEM (\emptyset) added to the cuvette,
18. Taken out suspension and place in an eppendorf (using cell pipette) and incubate in eppendorf at room temperature for 30mins
19. Use a 6 well plate (pre-prepared *Appendix 2.3*)
20. Add transfected HeLa cells
21. Leave plate incubated at 37 $^{\circ}$ C for 2hours
22. Add 20 μ L of Sodium Butyrate into ONE well of each sample
23. Incubate for 42-48hrs

